

UNCLASSIFIED

AD NUMBER	
AD506043	
CLASSIFICATION CHANGES	
TO:	unclassified
FROM:	confidential
LIMITATION CHANGES	
TO:	Approved for public release, distribution unlimited
FROM:	Distribution authorized to U.S. Gov't. agencies and their contractors; Critical Technology; OCT 1969. Other requests shall be referred to Air Force Rocket Propulsion Lab., Edwards AFB, CA.
AUTHORITY	
AFRPL ltr, 9 Nov 1972; AFRPL ltr, 5 Feb 1986	

THIS PAGE IS UNCLASSIFIED

UNCLASSIFIED

AD. 506 043

CLASSIFICATION CHANGED  
TO: UNCLASSIFIED  
FROM: CONFIDENTIAL

AUTHORITY:

AFRPL Ltr, 9 Nov. 72

UNCLASSIFIED

# **SECURITY**

---

# **MARKING**

**The classified or limited status of this report applies to each page, unless otherwise marked.**

**Separate page printouts MUST be marked accordingly.**

---

THIS DOCUMENT CONTAINS INFORMATION AFFECTING THE NATIONAL DEFENSE OF THE UNITED STATES WITHIN THE MEANING OF THE ESPIONAGE LAWS, TITLE 18, U.S.C., SECTIONS 793 AND 794. THE TRANSMISSION OR THE REVELATION OF ITS CONTENTS IN ANY MANNER TO AN UNAUTHORIZED PERSON IS PROHIBITED BY LAW.

NOTICE: When government or other drawings, specifications or other data are used for any purpose other than in connection with a definitely related government procurement operation, the U.S. Government thereby incurs no responsibility, nor any obligation whatsoever; and the fact that the Government may have formulated, furnished, or in any way supplied the said drawings, specifications, or other data is not to be regarded by implication or otherwise as in any manner licensing the holder or any other person or corporation, or conveying any rights or permission to manufacture, use or sell any patented invention that may in any way be related thereto.

CONFIDENTIAL

28

AD506043  
AFRPL-TR-69-231

DEVELOPMENT AND DEMONSTRATION  
OF A  
N<sub>2</sub>O<sub>4</sub>/N<sub>2</sub>H<sub>4</sub> INJECTOR (U)

W. A. Carter and G. S. Bell

**TRW**  
SYSTEMS GROUP

REDONDO BEACH • CALIFORNIA

NO. FILE COPY

Technical Report AFRPL-TR-69-231 ✓

OCTOBER 1969

AIR FORCE ROCKET PROPULSION LABORATORY  
EDWARDS AIR FORCE BASE, CALIFORNIA

GR

CONFIDENTIAL



When US Government drawings, specifications, or other data are used for any purpose other than a definitely related Government procurement operation, the Government thereby incurs no responsibility nor any obligation whatsoever, and the fact that the Government may have formulated, furnished, or in any way supplied the said drawings, specifications, or other data, is not to be regarded by implication or otherwise, or in any manner licensing the holder or any other person or corporation, or conveying any rights or permission to manufacture, use, or sell any patented invention that may in any way be related thereto.



2



CONFIDENTIAL

(18) (19)  
AFRPL-TR-69-231

10287.000

Total Pages: 186

(6) DEVELOPMENT AND DEMONSTRATION  
OF A  
N<sub>2</sub>O<sub>4</sub>/N<sub>2</sub>H<sub>4</sub> INJECTOR (U). (8)

(9) Final rept. 1 Apr 68-15 Aug 68

(10) W. A./Carter and G. S./Bell

TRW  
SYSTEMS GROUP

REDONDO BEACH • CALIFORNIA

(15) F04611-68-C-0054

(16) AF-3058

Technical Report AFRPL-TR-69-231

(11) OCT 0 1969

(12) 182p.

AIR FORCE ROCKET PROPULSION LABORATORY  
EDWARDS AIR FORCE BASE, CALIFORNIA

In addition to security requirements which must be met,  
this document is subject to special export controls and  
each transmittal to foreign governments or foreign  
nationals may be made only with prior approval of AFRPL  
(RPOR/STINFO), Edwards, California 93523

GROUP 4

DOWNGRADED AT 3 YEAR INTERVALS;  
DECLASSIFIED AFTER 12 YEARS  
DID DOR 5200 10

This document contains information affecting the national defense  
of the United States within the meaning of the Espionage Laws,  
Title 18, U.S.C., Section 793 and 794, the transmission of which  
in any manner to an unauthorized person is prohibited by law.

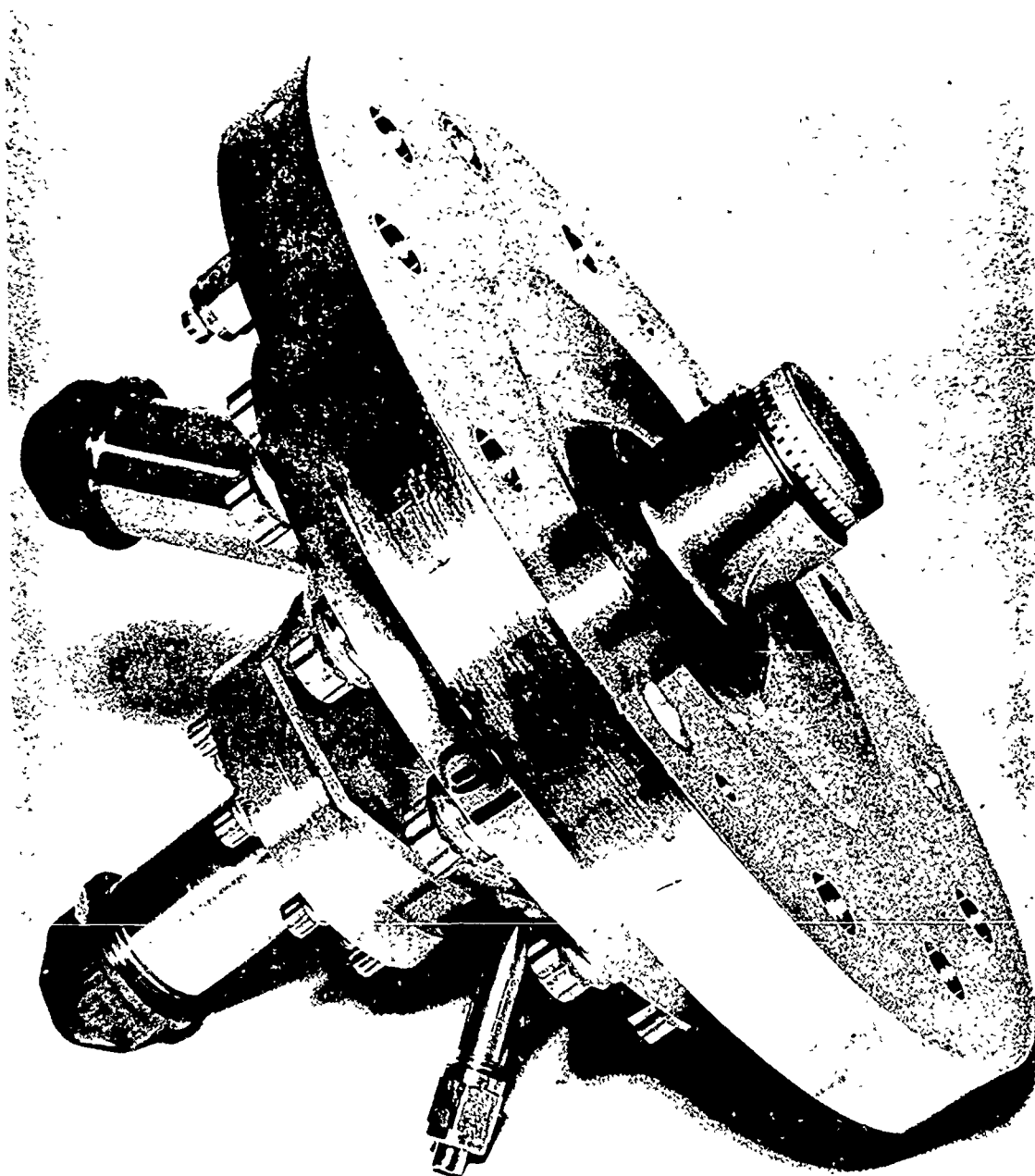
CONFIDENTIAL

1415

354 595

M-

UNCLASSIFIED



Frontispiece 3K  $\text{N}_2\text{O}_4/\text{N}_2\text{H}_4$  Single-element Coaxial Injector (U)

UNCLASSIFIED

UNCLASSIFIED

AFRPL-TR-69-231  
Page iii

FOREWORD

(U) This is the final report of work performed by TRW Systems Group, Redondo Beach, California, under Contract F04611-68-C-0054, Program Structure 750G, AFSC Project 3058, for the Rocket Propulsion Laboratory at Edwards Air Force Base, California. Mr. M. V. Rogers was the Air Force project engineer. The report covers the period 1 April 1968 through 15 August 1969, and is submitted in accordance with the requirements of Exhibit B of the contract.

(U) This technical report has been reviewed and is approved.

---

Melvin V. Rogers  
Reentry Propulsion Section

UNCLASSIFIED

(The reverse side of this page is blank)

**UNCLASSIFIED**

AFRPL-TR-69-231  
Page v

UNCLASSIFIED ABSTRACT

(U) A fifteen-month program was conducted to develop and demonstrate a single-element coaxial injector with  $N_2O_4/N_2H_4$  at the 3000 lbf thrust level. The optimum injector configuration and one variant were employed in multiple-start, long-duration ablative chamber tests. The durability of the final injector configuration was demonstrated by over 460 seconds of operation in 44 starts, including hot restarts, without discrepancies. Three basic configurations of the coaxial injector concept, with geometric variations, were tested to evaluate parameters controlling performance and injector/chamber compatibility, together with demonstrating the inherent dynamic stability of the injector. All contract design goals were met or exceeded.

**UNCLASSIFIED**

(The reverse side of this page is blank)

## TABLE OF CONTENTS

	<u>Page</u>
1. INTRODUCTION. . . . .	1
2. SUMMARY . . . . .	3
3. DESIGN, ANALYSIS, AND FABRICATION . . . . .	5
3.1 GENERAL. . . . .	5
3.2 $N_2O_4/N_2H_4$ INJECTOR DESIGN. . . . .	15
3.3 INJECTOR FABRICATION . . . . .	22
3.4 UNCOOLED THRUST CHAMBER DESIGN . . . . .	25
3.5 UNCOOLED THRUST CHAMBER FABRICATION. . . . .	28
3.6 ABLATIVE THRUST CHAMBER DESIGN . . . . .	30
3.7 INJECTOR HYDRAULICS - COMBUSTION DYNAMICS INTERACTION STUDY	30
4. TEST EVALUATION . . . . .	36
4.1 INJECTOR DEVELOPMENT COLD FLOW STUDIES . . . . .	36
4.2 EXPERIMENTAL FACILITY AND PROCEDURES . . . . .	52
4.3 INJECTOR CHARACTERIZATION TESTS. . . . .	59
5. THRUST CHAMBER MATERIALS EVALUATION . . . . .	124
5.1 TRANSIENT THERMAL ANALYSIS . . . . .	126
5.2 THERMAL STRESS ANALYSIS OF JTA INSERT. . . . .	130
5.3 EXPERIMENTAL EVALUATION. . . . .	139
6. INJECTOR RELIABILITY AND MAINTAINABILITY. . . . .	147
7. CONCLUSIONS . . . . .	149
REFERENCES. . . . .	150
APPENDICES. . . . .	151

Total No. of Pages: 186

## LIST OF FIGURES

	<u>Page</u>
1. Comparison of Stability Modes . . . . .	7
2. Coaxial Injector Orifice Geometries . . . . .	10
3. Momentum Correlation for Coaxial Injector with $N_2O_4/N_2H_4$ . . . . .	13
4. Injector Schematic Diagram . . . . .	14
5. 3K $N_2O_4/N_2H_4$ Injector Assembly . . . . .	16
6. Disassembled View of Injector Details . . . . .	17
7. Pintle Tip-Oxidizer Orifice Ring Boltup Arrangement . . . . .	19
8. Injector Oxidizer Feed Subassembly . . . . .	20
9. Injector Fuel Feed Subassembly . . . . .	21
10. Configuration 3 Injector Assembly . . . . .	23
11. Configuration 3 Oxidizer Feed Subassembly . . . . .	24
12. Uncooled Thrust Chamber Design . . . . .	26
13. Non-Directional Bomb Configuration . . . . .	29
14. Ablative Thrust Chamber Design . . . . .	31
15. Ablative Thrust Chamber Assembly . . . . .	32
16. Injector/Feed System Dynamic Model Results . . . . .	35
17. Hydraulic Characteristics of Oxidizer Orifice Ring . . . . .	37
18. Hydraulic Characteristics of Injector Fuel Circuit . . . . .	38
19. Combined Oxidizer and Fuel Injector Circuit Cold Flow . . . . .	40
20. Cold Flow Momentum Measurement Test Equipment . . . . .	42
21. Oxidizer Momentum Measurement Set-Up . . . . .	43
22. Fuel Sheet Momentum Measurement Set-Up in Operation . . . . .	44
23. Oxidizer Orifice Spray Pattern . . . . .	45
24. Oxidizer Cold Flow Momentum Test Results . . . . .	47
25. Fuel Sheet Cold Flow Momentum Test Results . . . . .	48
26. Injector Patternation Fixture . . . . .	50
27. Longitudinal Mass and Mixture Ratio Distribution . . . . . Patternation Results	53
28. 3K $N_2O_4/N_2H_4$ Engine Installation in Test Stand . . . . .	55
29. Schematic of Test Stand Feed System . . . . .	56
30. Instrumentation Schematic . . . . .	60
31. Oxidizer Orifice Ring Configurations . . . . .	62
32. Comparison of Initial and Lengthened Injector Outer . . . . . Pintle Bodies	67
33. 3K $N_2O_4/N_2H_4$ Engine Showing Pulse Gun Installation . . . . .	76

UNCLASSIFIED

AFRPL-TR-69-231

Page ix

	<u>Page</u>
34. Oscillogram from Initial Dynamic Stability Test (HA1-328) . . . . .	77
35. Characteristic Velocity Efficiency of Configuration 2 Injector . . Rings as Influenced by Slot Geometry	79
36. Characteristic Velocity Performance Change with Combustion . . . . . Chamber Length	81
37. Installation of Acrylic Thrust Chamber Section . . . . .	82
38. Configuration 2 Injector Performance Correlation with Pressure . . Drop Ratio	84
39. Configuration 2 Injector Performance Correlation with Mixture . . . Ratio	85
40. Configuration 2 Injector Performance Correlation with Momentum . . Ratio	86
41. Correlation of Chamber Pressure Characteristic Velocity with . . . Thrust-Based Characteristic Velocity	87
42. Influence of Injector Parameters on Combustion Roughness . . . . .	90
43. Power Spectral Density of Photocon Chamber Pressure Data . . . . . (HA1-328)	91
44. Wall Temperature Versus Time Trends . . . . .	95
45. Heat Flux Versus Wall Temperature . . . . .	97
46. Heat Flux Distribution in Uncooled Thrust Chamber . . . . .	99
47. Heat Flux Mixture Ratio, Combustion Chamber . . . . .	100
48. Heat Flux Vers s Mixture Ratio, Convergent Nozzle . . . . .	101
49. Heat Flux Versus Mixture Ratio, Throat . . . . .	102
50. Heat Flux Versus Mixture Ratio, Divergent Nozzle . . . . .	103
51. Heat Flux Variation with Injector Pressure Drop Ratio . . . . .	104
52. Ablative Thrust Chamber Installation on Test Stand . . . . .	108
53. Ablative Chamber Thermocouple Probes . . . . .	109
54. Thermocouple Probes During Installation into Ablative Chamber . . .	110
55. Ablative Chamber Throat Post-Test HA1-413 (16 seconds of . . . . . operation)	112
56. Ablative Chamber Throat Following Final Tests (80 seconds of . . . operation)	113
57. Chamber Pressure Versus Firing Duration for Test HA1-416 . . . . .	114
58. Theoretical Vacuum Specific Impulse for 30:1 Area Ratio, 80 . . . Percent Bell Nozzle	117
59. Theoretical Vacuum Specific Impulse for 3.5:1 Area Ratic, 15 . . . Degree Half-Angle Conical Nozzle	119
60. Injector Vacuum Specific Impulse Performance . . . . .	120
61. Location of Boundary Nodes on Throat Insert . . . . .	127
o2. Predicted Temperature Distribution Through JTA Graphite Throat . . Insert	128

UNCLASSIFIED



UNCLASSIFIED

AFRPL-TR-69-231

Page x

	<u>Page</u>
63. Predicted Temperature Distribution Through JTA Graphite Throat Insert . . . . .	129
64. Predicted Temperatures at Boundaries of Zirconia Throat Insert . . . . .	131
65. Predicted Temperatures at Boundaries of JTA Graphite Throat Insert . . . . .	132
66. Peak Stresses During Heat-Up of JTA Graphite . . . . .	136
67. Temperature Profiles Across JTA Walls During Heat-Up . . . . .	137
68. Task 3 Thrust Chambers Prior to Test (Reinforced Zirconia Insert Chamber on the Left, JTA Insert Chamber on the Right, All Ablative Chamber . . . . .	140
69. JTA Insert Chamber Post-Test . . . . .	143
70. All Ablative Chamber Post-Test . . . . .	144
71. Zirconia Insert Chamber Post-Test . . . . .	145

UNCLASSIFIED

## LIST OF TABLES

	<u>Page</u>
1. Actual discharge coefficients of oxidizer orifice rings . . . . .	41
2. Task 1a Injector Screening Test Summary . . . . .	63
3. Summary of Configuration 2 Injector Characterization Tests . . . .	69
4. Summary of Corrected Performance for Injector Configuration 2G .	88
5. Dynamic Stability Test Summary . . . . .	93
6. Summary of Heat Transfer Data . . . . .	95
7. Task 2 Ablative Thrust Chamber Test Summary . . . . .	106
8. Correlation and Summary of Injector Specific Impulse Performance	121
9. Summary of Task 3 Thrust Chamber Materials Testing . . . . .	141

## NOMENCLATURE

A	area
C	injector hydraulic interaction term (see Section 3.1.3)
C*	characteristic velocity
D,d	diameter
F	force, momentum or thrust
I <sub>sp</sub>	specific impulse
L	orifice height dimension
L*	characteristic length
M	momentum
N	number of primary orifices
O/F	mixture ratio
P	pressure
S	orifice spacing dimension (see Section 3.1.3)
V	velocity
W	orifice width dimension
$\dot{w}$	mass flow rate
$\Delta$	fuel film thickness at impingement (see Section 3.1.3)
$\Delta P_{IF}$	fuel injection pressure drop
$\Delta P_{IO}$	oxidizer injection pressure drop
$\epsilon$	expansion area ratio
$\eta$	efficiency
$\rho$	density
Subscripts	
C*	characteristic velocity
F,f	fuel or thrust
i	injector
MEAS	measured
O,o	oxidizer or stagnation
PC	based on chamber pressure
T,t	total or throat

UNCLASSIFIED

AFRPL-TR-69-231  
Page 1

## 1. INTRODUCTION

(U) Recent studies of advanced post boost propulsion systems have defined requirements for a flight-type  $N_2O_4/N_2H_4$  axial engine with the capability of operating over a wide mixture ratio range. These studies indicated that major improvements in propulsion system effectiveness could be achieved by using hydrazine as the common fuel for both the monopropellant attitude control thrusters and the bipropellant axial engine. The capability of operating the axial engine over a mixture ratio range would permit pre-selected division of the propulsion system propellant load between axial engine maneuvers and attitude control requirements, and would provide a high degree of mission flexibility within a single post boost propulsion system configuration. The axial engine should also deliver good performance, possess inherent and dynamic stability, and be capable of firing for long cumulative durations with multiple hot restarts. Additionally, the axial engine must possess reliability, ease of fabrication with a minimum of quality control, low unit cost, and the ability to withstand the post boost vibration and nuclear effects environments.

(U) Various agencies and contractors have worked on the development of stable, good performing injectors for  $N_2O_4/N_2H_4$ . However, many of these injectors had not developed in physical configurations suitable for application to a system, and little work had been done to make these injectors capable of hot restarts and compatible with state-of-the-art thrust chamber materials. Further, little work has been done to develop injector-thrust chamber assemblies for this propellant combination at the levels of chamber pressure and thrust which were defined by the advanced post boost propulsion systems studies. Therefore, an intensive development program was conducted to demonstrate the applicability of the single-element coaxial injector technique in meeting the rigorous operational requirements of the  $N_2O_4/N_2H_4$  axial engine.

(U) This report presents the results of a fifteen month program to develop and demonstrate a 3000  $lb_f$  vacuum equivalent thrust  $N_2O_4/N_2H_4$  injector operating at 300 psia chamber pressure. The major goals of this program were to demonstrate mixture ratio flexibility, dynamic combustion sta-

UNCLASSIFIED

UNCLASSIFIED

(U) bility, good performance, and injector-chamber compatibility. The program was conducted in two phases. In the initial program phase the design of the injector and associated test hardware were accomplished. The second phase comprised the major program effort and included all hardware fabrication and evaluation testing.

(U) The injector design approach selected was a building block version of a flight-type single-element coaxial injector. The building block injector concept provided the flexibility to accommodate hardware modifications with a minimum of schedule impact, yet permitted fabrication of test hardware approaching a flight-type configuration. Previous experience with  $N_2O_4/N_2H_4$  in 3000 lb<sub>f</sub> thrust sized hardware prior to the award of this program had demonstrated the inherent dynamic stability of the single-element coaxial injector concept and the achievement of the program acoustic stability goal was not considered a problem area, and in actuality was not a problem. However, the pre-contract experience had indicated that achievement of the "combustion roughness" goal would require a concerted effort. As a consequence, three different injector configurations were designed for evaluation testing for comparison with the program goals of performance, mixture ratio flexibility, "roughness", and injector-chamber compatibility.

(U) The Phase II effort consisted of three tasks. The Task I effort entailed screening of the three injector configurations in uncooled thrust chamber hardware and the selection of one configuration which was then further characterized before proceeding to the Task 2 experimental effort. Task 2 evaluated the basic compatibility of the selected injector with ablative thrust chambers and demonstrated the hot restart capability of the final injector configuration. The Task 3 effort was added to the program following the completion of Task 2 with the objective of test firing three ablative thrust chamber under a restart duty cycle to acquire comparative performance-chamber durability information with both all-ablative and throat insert configuration thrust chambers.

UNCLASSIFIED

## 2. SUMMARY

(U) An intensive experimental program was conducted to develop and demonstrate a 3000 lb<sub>f</sub> vacuum equivalent thrust N<sub>2</sub>O<sub>4</sub>/N<sub>2</sub>H<sub>4</sub> injector operating at 300 psia chamber pressure. The major goals of this program were to demonstrate mixture ratio flexibility, dynamic combustion stability, good performance, and injector-chamber compatibility. The program was conducted in two phases. In the initial program phase the design of the injector and associated test hardware were accomplished. The second phase comprised the major program effort and included all hardware fabrication and evaluation testing. The frontispiece of the report shows a pre-test view of the single-element coaxial injector produced during this program.

(U) The Phase II effort consisted of three tasks. Task 1 effort entailed screening of the three basic injector configurations in uncooled thrust chamber hardware and the selection of one configuration which was then further characterized before proceeding to the Task 2 experimental effort. Task 2 evaluated the basic compatibility of the selected injector with ablative thrust chambers and demonstrated the hot restart capability of the final injector configuration. The Task 3 effort was added to the program following the completion of Task 2 to acquire comparative performance-chamber durability information with both all ablative and throat insert configuration thrust chambers under a restart duty cycle. A total of five (5) ablative thrust chambers were tested for single burn durations in excess of 60 seconds each, followed by restarts.

(U) The following tabulation summarizes the program accomplishments and the contract design goals. All design goals were met or exceeded.

**CONFIDENTIAL**

(C)	<u>DESIGN GOAL</u>	<u>DEMONSTRATED</u>
Mixture Ratio Range	0.95 to 1.40	0.92 to 1.53
Vacuum Specific		
Impulse at Optimum Mixture	300 lb <sub>f</sub> -sec/lbm	308 lb <sub>f</sub> -sec/lbm
Ratio ( = 30:1)	minimum	at 1.2 mixture ratio
Dynamic Stability	40 millisecond recovery from 525 psi overpressure	20 millisecond recovery from overpressures rang- ing from 120 to 630 psi. Injector inherently dynamically stable.
Combustion Noise	+ 5 percent of chamber pressure	+ 5 percent
Injector/Chamber	Not	Five ablative thrust
Compatibility	Quantified	chambers tested for durations up to 90 seconds.
Injector Durability/ Operability	Not Quantified	Over 460 seconds of operation in 44 starts without discrepancies. Overall operating ex- perience of 1000 seconds in 180 starts.
Hot Restarts	Not Quantified	Pulse trains of 5 or more restarts after initial 90 seconds of operation.

**CONFIDENTIAL**

UNCLASSIFIED

AFRPL-TR-69-231

Page 5

### 3. DESIGN, ANALYSIS, AND FABRICATION

#### 3.1 GENERAL

(U) The choice of an injector concept was the single most important design decision for this program. The injector design directly affects overall dynamic stability, performance, thrust chamber life, and compatibility. Realization of the design goals for these qualities is not possible unless the injector can be made to operate in a dynamically stable manner.

(U) The selection of the injector concept was primarily predicated upon its inherent resistance to damaging modes of instability. The basic injector design is a single central element configuration wherein the fuel is injected as a continuous cylindrical sheet which impinges with oxidizer streams injected radially outward from a series of uniformly spaced slots. Part of the fuel strikes the top surface of the individual oxidizer streams and part of the fuel drops in between the oxidizer streams. The initial combustion products of the hypergolic reaction drive the propellants into each other, promoting secondary mixing. Performance is controlled through oxidizer element sizing and unit spacing as well as the fuel sheet thickness. Additional performance tuning can be accomplished by the addition of secondary oxidizer elements between the major oxidizer slots. The TRW central element injector concept has demonstrated its inherent dynamic stability in literally thousands of tests with a variety of propellants (including  $N_2O_4/N_2H_4$ ) over a wide range of thrust sizing. The injector concept has also shown it can deliver good performance and at the same time provide chamber wall compatibility control.

##### 3.1.1 Stability Considerations

(U) Storable propellant applications with pressure-fed systems involve combustion chamber pressure operation at relatively low pressures, resulting in combustion chamber geometrical sizings which may support damaging acoustic types of instability. The tangential, radial, and longitudinal modes are of concern with the tangential modes being most important (Reference 1). The single-element coaxial injector provides a fundamental approach for theoretical elimination of these modes.

UNCLASSIFIED



**UNCLASSIFIED**

(U) To arrive at a means to theoretically eliminate combustion instability it is necessary to examine the relationship between the nodes and antinodes of the acoustic vibrations associated with various instability modes and the location of possible abnormally high energy release zones which could result in sustaining combustion instability. These are given in Figure 1 indicating comparisons between distributed injection and centralized injection.

(U) The figure shows that the possible locations for abnormally high energy release in the chamber can have a dominant effect on whether or not the engine will be dynamically stable (without resorting to mechanical damping.) For example, if a large local pressure pulse is generated in a region in which the maximum compression (pressure antinode) would occur for a given acoustical mode, then that mode will probably be initiated. In inert gases, the energy supplied by the pulse will be dissipated in a few cycles through various damping processes such as turbulence, wall drag, droplet drag, and possible interference from other vibration modes which may also have been excited. However, if unburned propellant is introduced into the pressure antinode regions, the energy required to sustain the oscillations can be supplied through a rapid increase in the normal rate of combustion caused by pressure-sensitive gas reactions and increased mixing, resulting from high-velocity gases just behind the pressure front.

(U) An injector design which introduces propellant near the outer periphery of the combustion chamber can be expected to be very susceptible to the tangential modes of instability, whereas an injector having a single central element would be highly resistant to the tangential modes if fast mixing and reaction are assured by proper interlocking of oxidizer and fuel.

(U) In Figure 1a conventional multiple-orifice injection scheme is illustrated on the left side. Under stable operation, the maximum rate of energy release zone will be somewhat as shown by the solid line. Under the influence of a large pressure pulse at one side of the injector (or subsequently during unstable operation when the pressure front has just passed the left side), the energy release pattern will approximate that shown by the dotted line. The zone of maximum energy release rate moves generally toward the injector face and even closer at the peak pressure region, thus sustaining the instability.

**UNCLASSIFIED**

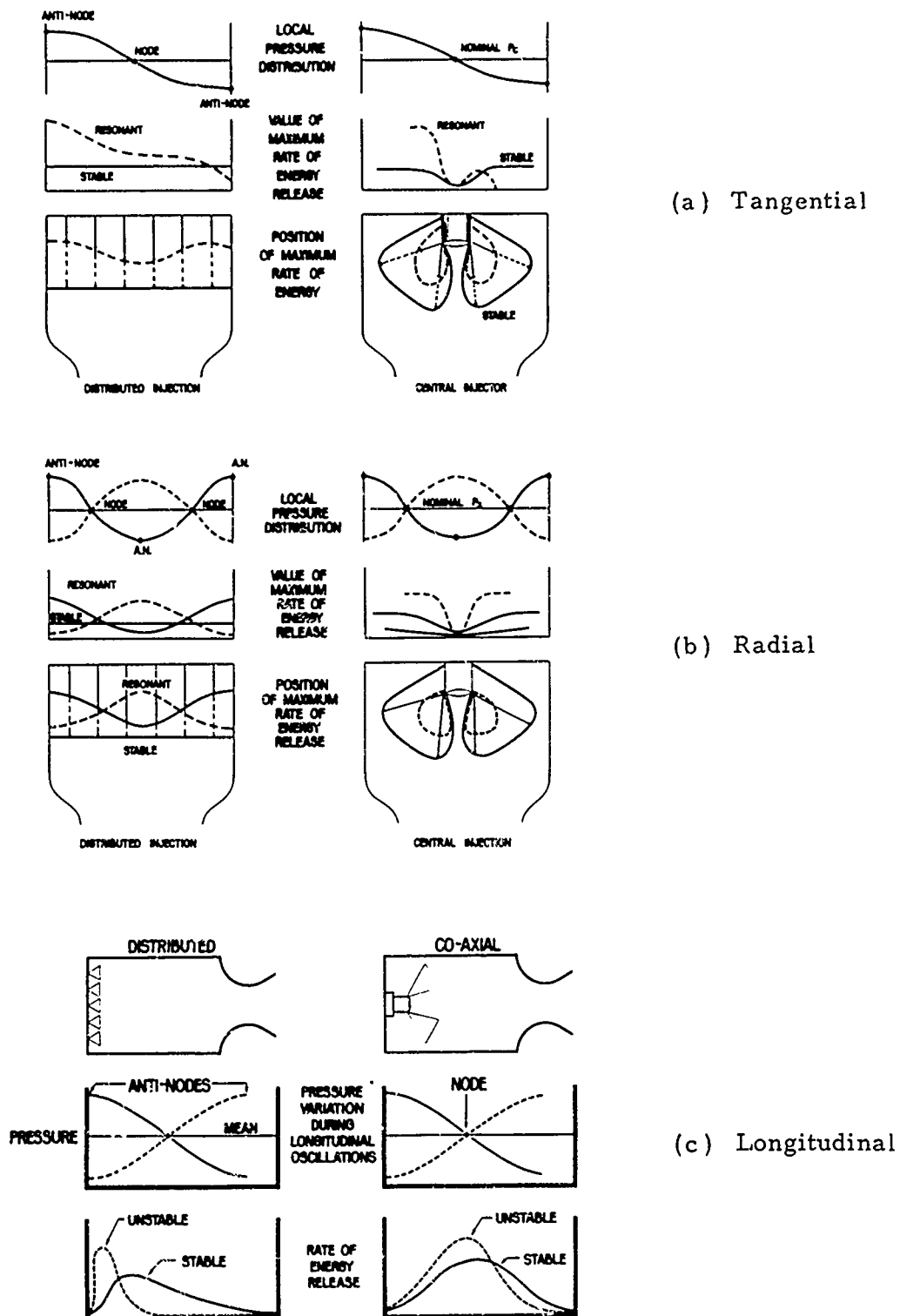


Figure 1. Comparison of Stability Modes (U)

UNCLASSIFIED

(U) A schematic diagram of the coaxial injection scheme is shown on the right side of Figure 1a, where it can be seen that under the influence of a large local pressure pulse, the zone of maximum energy release must again move toward the incoming propellants to increase the combustion rate above its normal value. In this case, it moves both toward the injector end of the chamber and inward toward the center line of the engine. It is apparent that, under these conditions, the energy would be released near the pressure node and would be very ineffective in sustaining the spinning or tangential pressure front. Therefore, any disturbance which initiates the tangential modes would be expected to damp out within a few cycles.

(U) The very high injection density near the center of the injection in the TRW design also tends to prevent the establishment of the radial mode of instability. On the right side of Figure 1b it can be seen that for the coaxial element, the normal maximum energy release zone is near the pressure node of the radial mode, and therefore does not tend to contribute effectively toward sustaining the mode. With a distributed injector some incoming propellant is at the antinode of the radial mode as shown on the left side of Figure 1b. However, in any case the radial mode is not easy to sustain.

(U) With respect to the longitudinal mode of instability, it is seen in Figure 1c that energy added close to the injector face will be most effective in sustaining the mode. For a given energy release rate, there is a maximum chamber length below which the energy is, in effect, being released at a pressure node, and therefore will not sustain longitudinal instability. However, the energy release rate is not constant, but is usually a strong function of the pressure disturbance. A high pressure front can "drive" the combustion zone back toward the injector face until the propellant injection density and/or lack of mixing is sufficient to prevent any further increase in combustion rate. For injectors using a distributed propellant source such as the one shown on the left in Figure 1c, the propellant density does not rapidly increase until very close to the injector face. Therefore, a large pressure disturbance could drive the energy release zone close to the head end of the chamber or into the antinode region and thus establish a longitudinal instability.

UNCLASSIFIED

(U) The coaxial injector resists the longitudinal mode of instability because the propellant injection density increases much more rapidly and to much higher values at a given distance from the injection ports than in injectors with a distributed source. Furthermore, the injection point is physically adjustable farther into the chamber. Thus, for a given chamber length, the stable maximum energy release occurs nearer the pressure node region and cannot be driven nearly as far toward the head end of the chamber (see the right side of Figure 1c). Since it cannot couple efficiently in this region, the engine remains stable.

### 3.1.2 Injector Element Sizing

(U) Under normal operating conditions for thrust levels above approximately 1000 lb<sub>f</sub> the oxidizer is employed as the center propellant in a coaxial injector. The fuel, therefore, is injected as a continuous sheet over the pintle tube surface. The selection of a coaxial injector pintle diameter includes consideration of:

- The ratio of pintle to selected chamber diameter to provide sufficient radial reaction time (distance) and stability considerations
- The resultant fuel sheet thickness at the design fuel orifice pressure drops
- The resulting pintle circumference from the standpoint of length available for locating the oxidizer injection orifices

(U) Injecting the oxidizer as a continuous sheet (Figure 2a) is usually not practical from a performance standpoint with the highly reactive hypergolic propellant combinations due to stream separation effects. In this figure, the arrows represent the fuel sheet flowing over the pintle tube; with the oxidizer streams flowing perpendicular to the page. Individual oxidizer streams, as shown in Figures 2b, c, and d are normally employed to obtain improved propellant interlocking (reducing separation). The physical size of the oxidizer streams and the spacing between streams become primary design variables. The oxidizer stream dimensions and velocity control, to a major extent, overall propellant mass distribution and the resultant oxidizer droplet size. Having too small a spacing between oxidizer streams (Figure 2b) precludes adequate fuel sheet penetration, while too wide a spacing (Figure 2c) allows excessive fuel penetration, resulting in fuel

UNCLASSIFIED

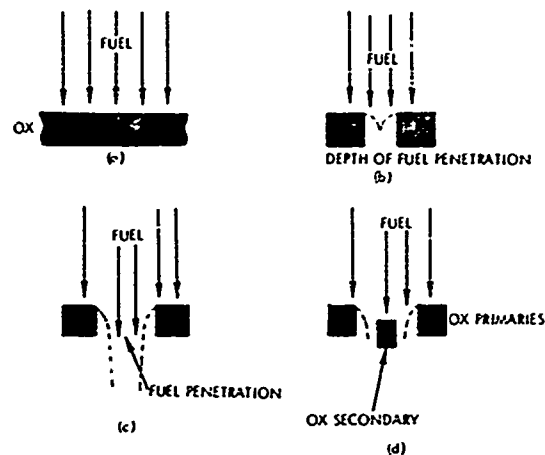


Figure 2. Coaxial Injector Orifice Geometries (U)

(U) rich gases. One approach is to separate the primary oxidizer streams and use secondary oxidizer streams to react with the fuel sheet which has purposely been allowed to penetrate (Figure 2d). This greatly increases the overall design flexibility and also reduces the effective oxidizer orifice dimensionally.

(U) Another configuration provides a secondary injection point for the fuel in the center of the pintle tip. This was accomplished by inserting a continuous tube down the center of the pintle tube, thus maintaining parent metal between the respective propellants. This secondary fuel flow is injected as a hollow cone by inserting a simple induced swirl (helix) device near the tube exit. A cone angle of  $120^\circ$  is achieved in this manner. The oxidizer orifices are then designed similar to Figure 2b or 2d, where the depth of fuel sheet penetration is controlled. The resulting oxidizer, which is deflected toward the central zone of the chamber, is then reacted with the centrally injected secondary fuel. The net result is somewhat of a "staged" combustion process (see Figure 10).

(U) In all of the configurations, the desired fuel-rich zone at the chamber walls is produced by the fuel which reacts with the top portion of the oxidizer streams.

### 3.1.3 Combustion Model of Injector

(U) The coaxial injector concept, unique for the elimination of damaging acoustic instability through geometry, embodies many of the features of

UNCLASSIFIED

(U) more conventional injecting but also has some features not readily obtained with other injectors. The injector design has performance characteristics dependent upon momentum ratios quite similar to conventional injectors.

(U) The basic atomization and mixing control for the pintle design is in the control of the hydrodynamic sheet and jet element sizes along with the use of the kinetic energy of jet interaction. It is observed that a similar process occurs for impinging jet designs, wherein a sheet is formed which then disintegrates.

(U) Dimensional arguments lead to the conclusion that the final mean drop size for a disintegrating sheet or jet should be proportional to the square root of the orifice characteristic dimension divided by the fluid velocity. This applies to any sheet-forming process. With the hypergolic propellants considered here, it is not immediately clear as to what the final actual distribution may be. If the hypergolicity is highly energetic and optimum mixing is achieved, the initially formed drops are rapidly shattered into very small drops with associated rapid combustion.

(U) To assure that peak performance can occur, it is necessary to optimize the injection hydraulics. Where liquid phase reactions are considered to be of major importance, it has been found that control of basic momentum considerations results in peak performance (Reference 2). The criteria of Reference 3 are especially applicable in either case of sheet or jet injectors.

(U) The sheet types of one-on-one elements should perform best for

$$\left( \frac{\rho_1 v_1^2}{\rho_2 v_2^2} \right) \left( \frac{d_1}{d_2} \right) \approx K$$

or in terms of mixture ratio

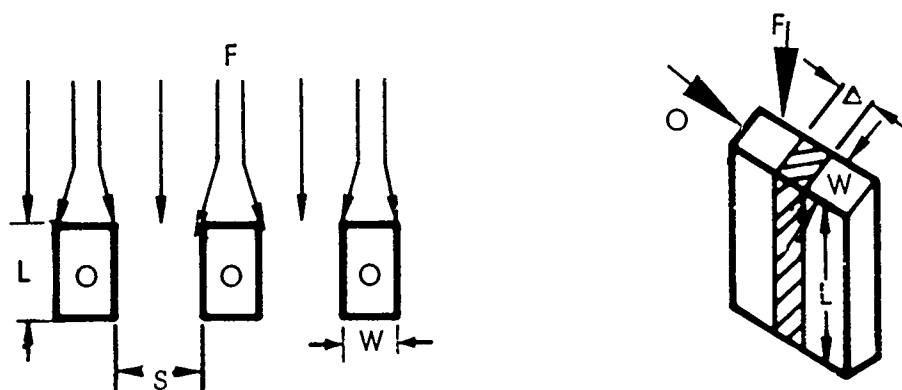
$$O/F^2 \frac{\rho_f}{\rho_o} \left( \frac{d_f}{d_o} \right)^3 \approx K$$

A simple but highly effective approach to this control is obtained through an examination of the gross dynamics of interaction of fuel and oxidizer.

UNCLASSIFIED

(U) Initial maximum mixing can be achieved only by optimum use of the available momentum forces (the product of density and area times the square of the velocity).

(U) For the single-element injector configuration, the proper areas for the fuel and oxidizer are obtained through an examination of the initial interaction mechanics. The following interaction model is envisioned.



(U) The fuel force on the oxidizer is taken as,  $F_f = \rho_f V_f^2 [\Delta W + \Delta LC]$  where  $C$  is a cross influence term to account for the side interaction. On the basis of a single reflective interaction between elements for a fuel particle a first approximation to  $C$  is taken as  $(L/V_f)(a/S) [1 - NS/D_1\pi]$  which is seen to be an estimate of the ratio of time of flight of the fuel to the dispersion of the two-phase reactants. The value of  $a$ , which is a measure of the velocity of a disturbance, is taken as that of a nearly homogeneous two-phase mixture and is estimated at 700 fps for storable propellants. The oxidizer force on the fuel is taken as,  $F_o = \rho_o V_o^2 WL$ . The final momentum ratio result for optimal momentum utilization of the slot configuration becomes

$$\frac{\rho_f V_f^2 [\Delta W + 2 \Delta LC]}{\rho_o V_o^2 WL} = 1$$

Coaxial injector designs based upon the above momentum ratio design principles provide peak performance at the optimum momentum ratios as defined above. That the coaxial pintle design will in fact peak out in performance for a given design obeying this type of behavior is illustrated in Figure 3 for  $N_2O_4/N_2H_4$ .

UNCLASSIFIED

(U) The guidelines presented by Elverum (Reference 2) and Rupe (Reference 3) can be used to provide a basis for the start of all combustion analyses. These studies indicate a maximum in performance when the liquid phase mixing occurs at essentially the combustion design mixture ratio, resulting in the individual droplets being of mixed constituents at the design mixture ratio. For this to occur to the maximum extent possible requires optimum use of the stream momentums as indicated earlier. This is particularly true if the impinging streams are highly reactive to the extent that complete liquid phase mixing cannot occur. In this case, the injector and combustion design must incorporate features to promote secondary mixing of the reactants.

(U) The basic designs are predicated upon obtaining a strong mechanical interlock of the propellants, in order that optimal liquid phase mixing can be forced to occur. To achieve this it is necessary to have a physical model of the interaction. Such a model is shown in Figure 4. The oxidizer is metered and directed outward from the center pintle in individual streams. Rectangular geometries are used because they lend themselves to ease of machining and throttling.

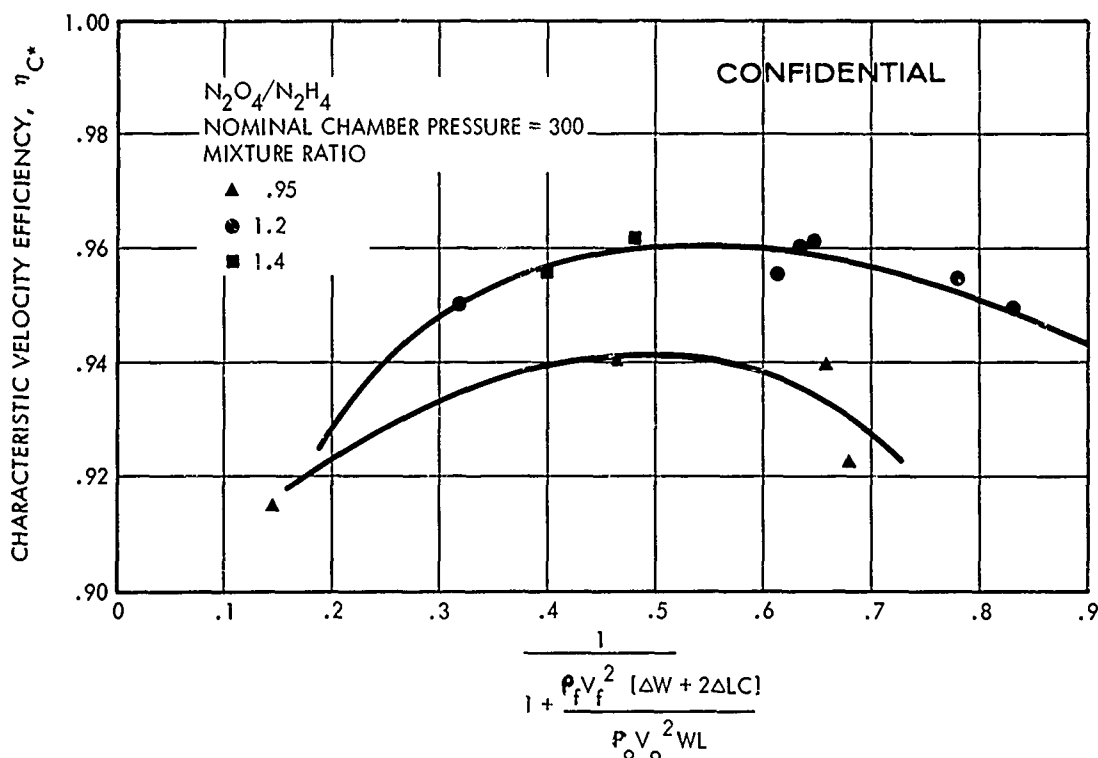


Figure 3. Momentum Correlation For Coaxial Injector With  $\text{N}_2\text{O}_4/\text{N}_2\text{H}_4$  (U)



**CONFIDENTIAL**

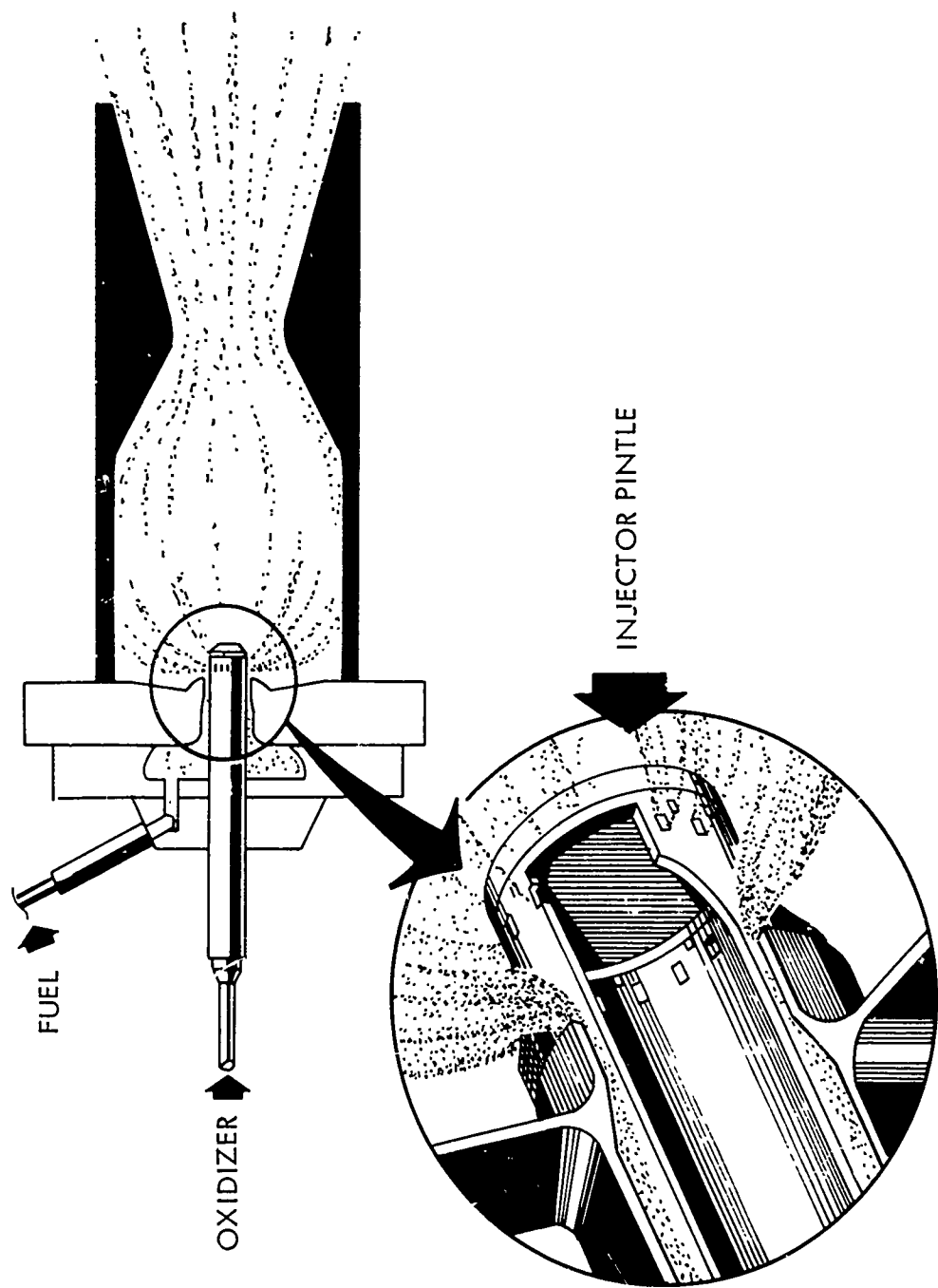


Figure 4. Injector Schematic Diagram (U)

**CONFIDENTIAL**  
(This page is unclassified)

(U) The fuel intercepts the oxidizer streams as shown, part of the fuel striking the top surface and part of it drops in between the oxidizer slots. The gross reaction scheme is illustrated in Figure 4 where reaction products drive the propellants into each other. The geometry of the system of interaction is selected on a design compromise of performance and required wall environments. Performance is controlled through oxidizer element sizing and unit spacing as well as the fuel sheet thickness. The unit spacing selection is made on the basis of achieving a fuel penetration as shown. Additional performance tuning can be accomplished by the addition of secondary oxidizer elements between the major elements.

### 3.2 $N_2O_4/N_2H_4$ INJECTOR DESIGN

(U) The specific injector configuration selected for the program was a building block version of a flight-type injector with replaceable injection elements. The building block approach provided flexibility to accommodate hardware modifications with minimum difficulty. The oxidizer injection metering slots were located in a replaceable ring structurally held between the pintle tip and the pintle sleeve which were bolted together. Oxidizer injection area variation was effected by replacing metering rings. Three variations of the basic injector were designed.

- Configuration 1 - Primary oxidizer slots only
- Configuration 2 - Primary oxidizer slots with secondary oxidizer orifices
- Configuration 3 - Primary oxidizer slots with a secondary fuel spray provided by a swirl injector in the pintle tip.

In each of the three element configurations, the fuel injection point was an annular gap whose metering area could be varied by changing shims located between the injector body and injector element sub-assemblies.

(U) The injector was a bolt-up assembly using ethylene-propylene rubber (EPR) O-ring seals on the fuel side and Teflon O-ring seals on the oxidizer side. Assembly and disassembly was accomplished rapidly by means of this bolt-up design. Figure 5 is an illustration of the basic injector assembly. Figure 6 is a disassembled view of the injector.

(U) The injector assembly consists of two basic subassemblies; the fuel and oxidizer feed subassemblies. The oxidizer feed subassembly consists of the

UNCLASSIFIED

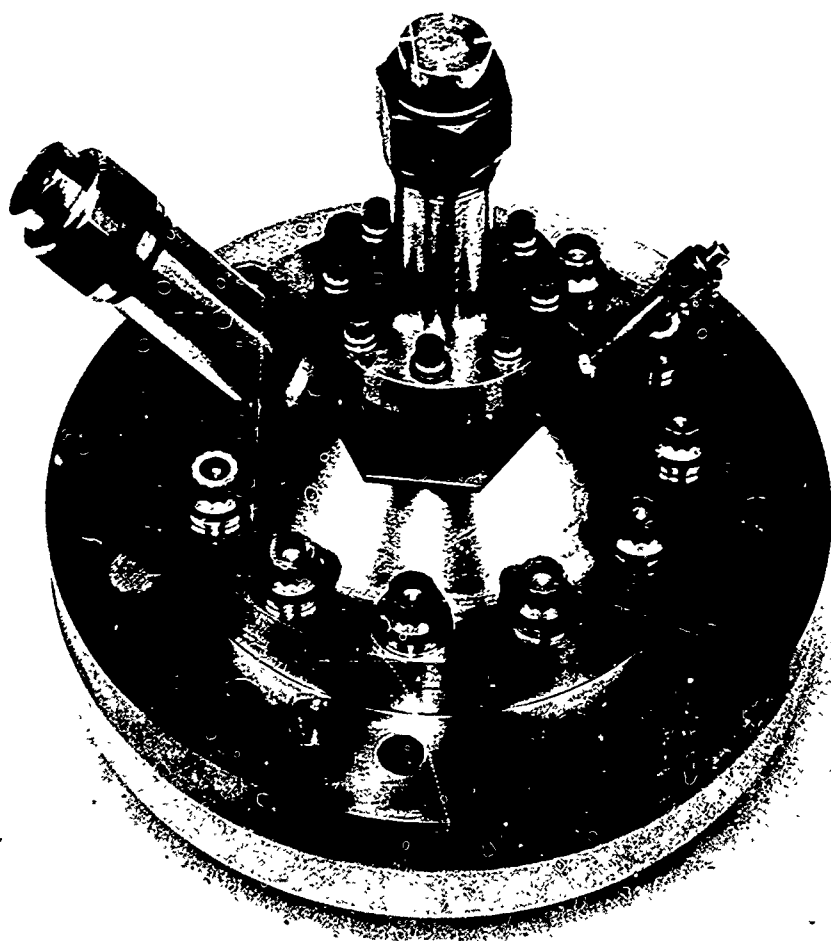
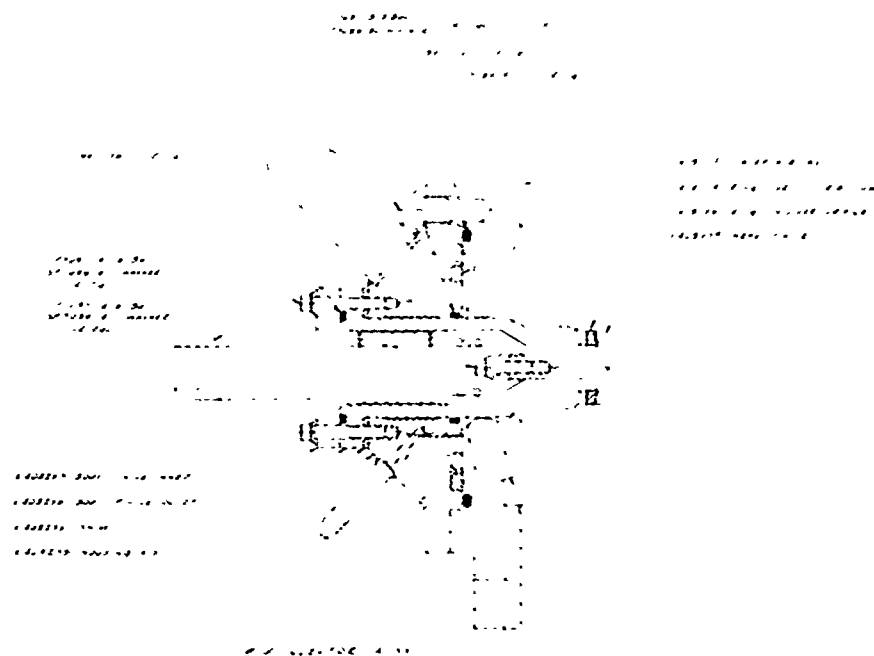


Figure 5. 3K  $N_2O_4/N_2H_4$  Injector Assembly (U)

UNCLASSIFIED

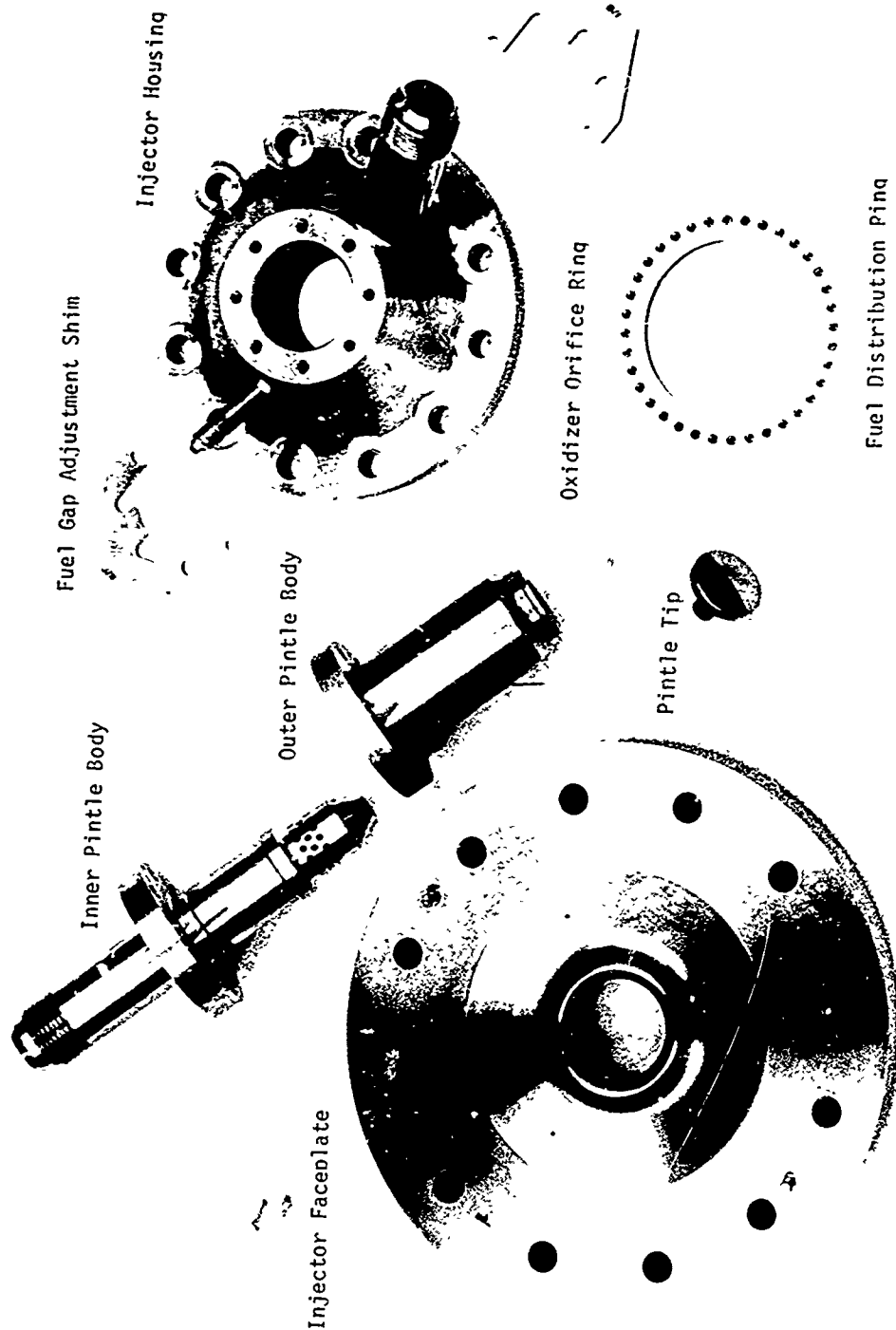


Figure 6. Disassembled View Of Injector Details (U)

**UNCLASSIFIED**

(U) inner pintle body, the outer pintle body, the orifice ring and the pintle tip. The retaining bolt is inserted into the oxidizer feed tube of the inner pintle body and threads into the pintle tip as illustrated in Figure 7. Figure 8 is a photograph and drawing of the oxidizer feed subassembly. The oxidizer is distributed radially outward from the inner pintle body through 48 holes. At an oxidizer flow rate of 5.5 lb/sec, this results in a pressure drop of 3.5 psi. The oxidizer is then metered through the oxidizer orifice ring. The maximum flow velocity in the oxidizer feed subassembly is 20 ft/sec.

(U) The fuel feed subassembly consists of the face plate and the housing with the fuel distribution ring clamped between them. The fuel feed subassembly is illustrated in Figure 9. The fuel is distributed from the inlet within the injector by means of a fuel distribution ring. The distribution is accomplished by means of 36 equally spaced holes. Water flow tests provided evidence of uniformity of fuel sheet thickness. The pressure loss due to the distribution ring is 21 psi at a fuel flow rate of 4.6 lb/sec. The maximum flow velocity in the fuel manifold is 35 ft/sec at this flow rate.

(U) The fuel gap adjustment is made by means of split shims shown previously in Figure 6. Fuel metering area variations can be effected by loosening the eight bolts securing the fuel and oxidizer subassemblies together, and installing the appropriate shims for the desired fuel gap.

(U) The oxidizer orifice ring shown in Figures 6 and 7 can be changed by removing the oxidizer feed subassembly from the injector assembly, removing the pintle retaining bolt, and withdrawing the pintle tip and oxidizer orifice ring and then reversing the process.

(U) Both the fuel gap adjustment and oxidizer orifice ring can be changed with the injector mated to the thrust chamber on the test stand. This provided injector flexibility by enabling rapid propellant orifice changes while maintaining overall firing readiness of the hardware and the test facility.

(U) Configuration 1 and 2 injector assemblies were identical with the exception of the oxidizer orifice geometry. The Configuration 1 oxidizer orifice ring had slots cut in one side of the ring only while the Configuration 2 ring had primary slots on the upstream side of the ring and secondary

**UNCLASSIFIED**

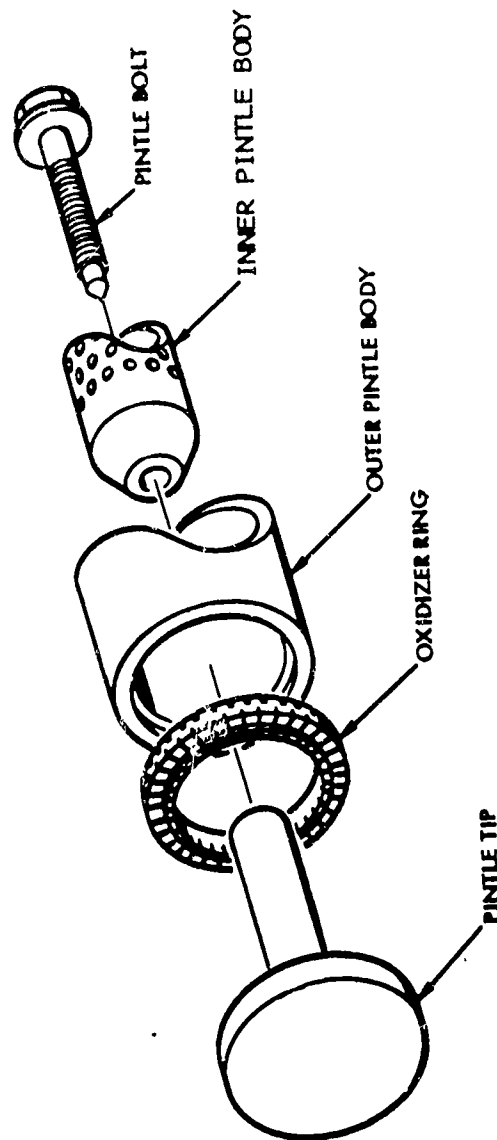


Figure 7. Pintle Tip - Oxidizer Orifice Ring Boltup Arrangement (U)

UNCLASSIFIED

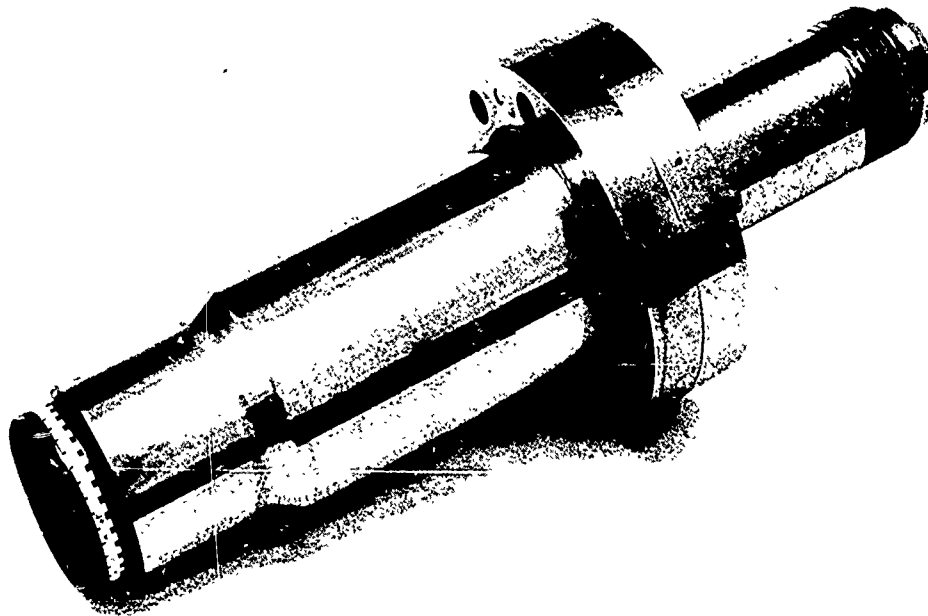
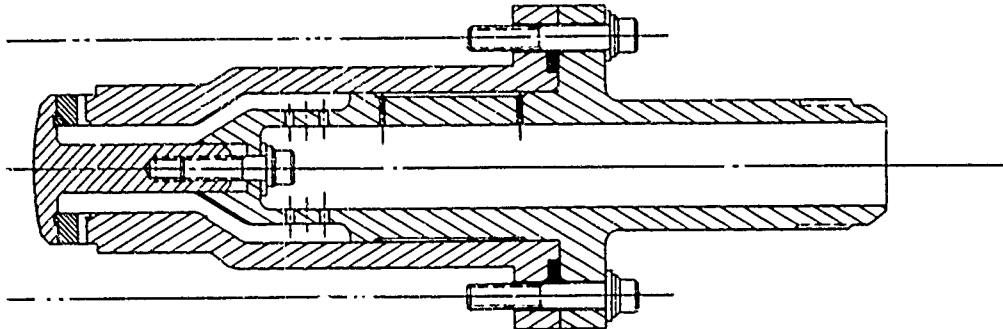


Figure 8. Injector Oxidizer Feed Subassembly (U)

UNCLASSIFIED

UNCLASSIFIED

AFRPL-1R-69-231  
Page 21

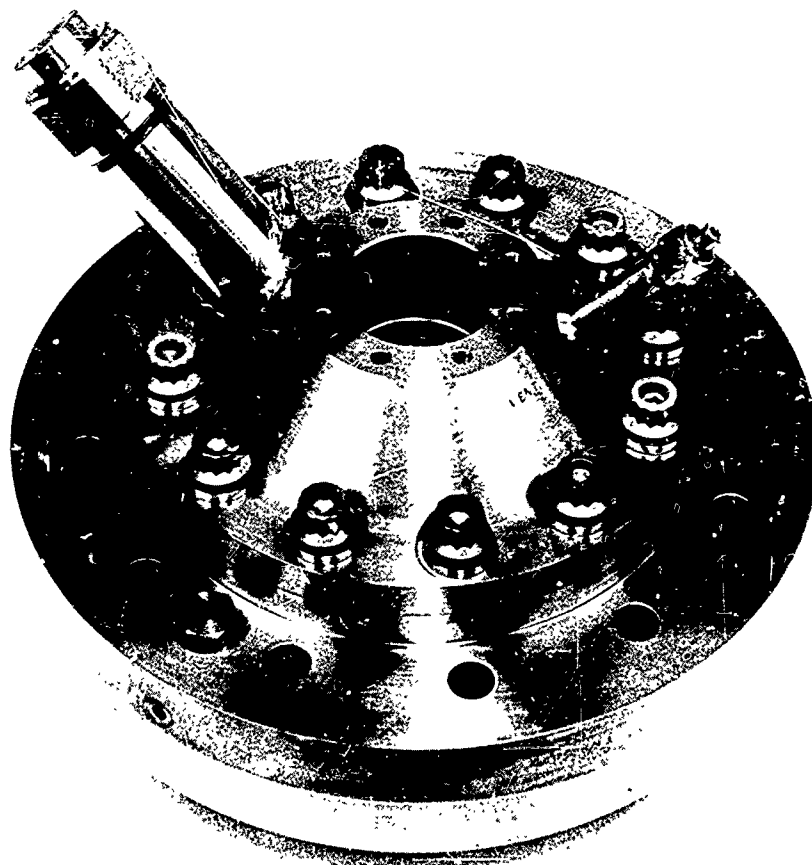
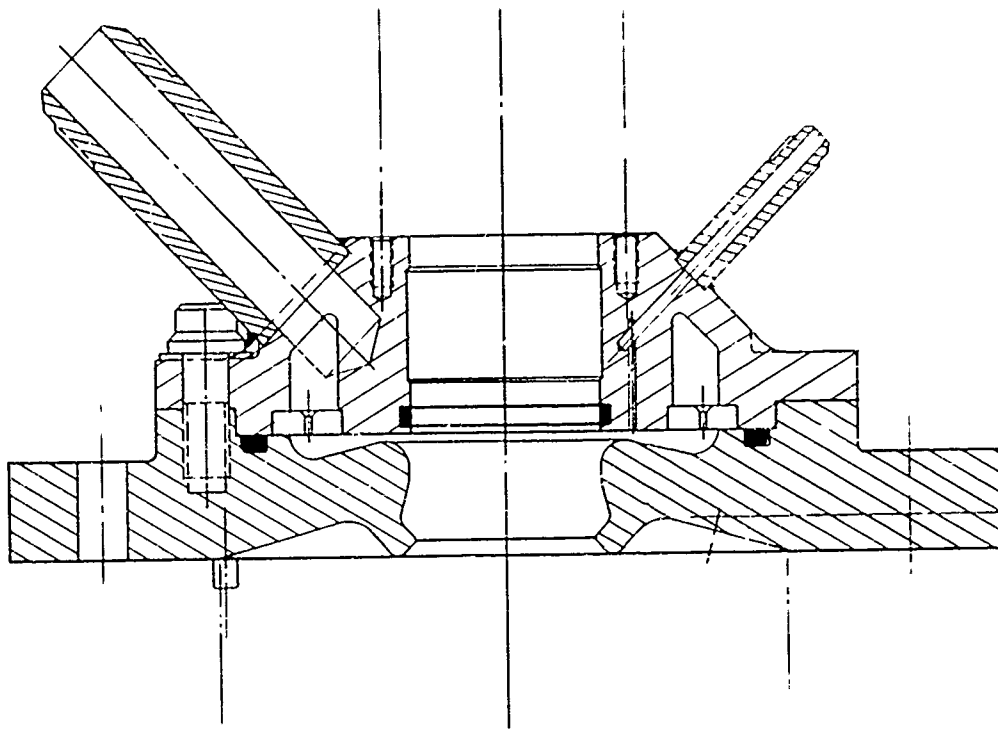


Figure 9. Injector Fuel Feed Subassembly (U)

UNCLASSIFIED



UNCLASSIFIED

(U) slots on the downstream side of the ring. Fifteen percent of the oxidizer flows through the secondary slots.

(U) Configuration 3 differed from Configurations 1 and 2 in that the entire oxidizer feed subassembly was designed such that a secondary fuel spray provided by a swirl injector in the pintle tip was incorporated. A layout drawing and photograph of the Configuration 3 injector are shown in Figure 10. The oxidizer feed subassembly for Configuration 3 is shown in Figure 11. Approximately 17 percent of the fuel flow was injected through the center swirl. The oxidizer orifice ring used with Configuration 3 was identical to Configuration 2.

### 3.3 INJECTOR FABRICATION

(U) The injector assembly was made primarily from common structural stainless steel. The face plate, and outer pintle body are fabricated from 17-4PH stainless steel hardened to H-900 condition. The inner pintle body, fuel distribution ring and housing are fabricated from 304 stainless steel. The entire injector was fabricated and assembled in less than a month.

(U) The injector fuel feed subassembly consisted of the faceplate, the fuel distribution ring and the housing. The fuel distribution ring is held in place when the housing is bolted to the face plate. The only dimensions in this assembly that are critical is the register between the face plate and the housing. The inside diameter of the face plate is  $5.7500^{+.0002}_{-.0000}$  and the outside diameter on the housing is  $5.7498^{+.0000}_{-.0002}$  leaving from .0002 to .0006 inches between the parts. The diameter of the metering surface must be held concentric to the bore of housing within about 0.0005 in. TIR. The concentricity between the fuel feed subassembly and oxidizer feed subassembly was minimized so that the fuel sheet thickness was uniform circumferentially.

(U) The oxidizer feed subassembly is assembled from the inner and outer pintle bodies. This subassembly is described in Section 3.2. The inner pintle body is fabricated from 304 stainless steel and the outer pintle body is fabricated from 17-4PH stainless steel. The outer pintle utilized 17-4PH stainless to eliminate galling when the oxidizer feed subassembly is inserted in the fuel feed subassembly.

UNCLASSIFIED

UNCLASSIFIED

AFRPL-18-09-231

Page 23

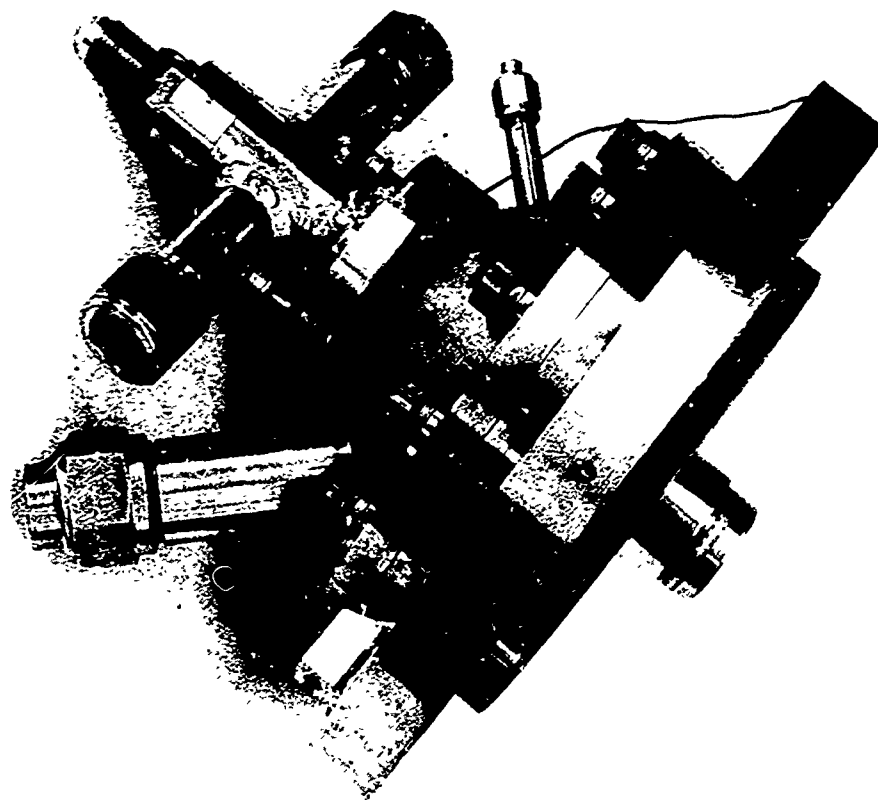
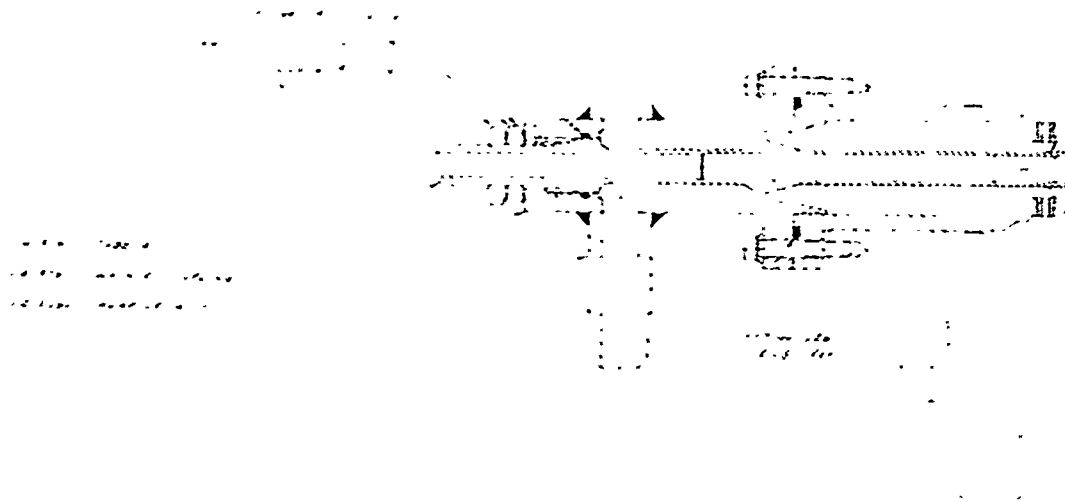


Figure 10. Configuration 3 Injector Assembly (U)

UNCLASSIFIED

UNCLASSIFIED

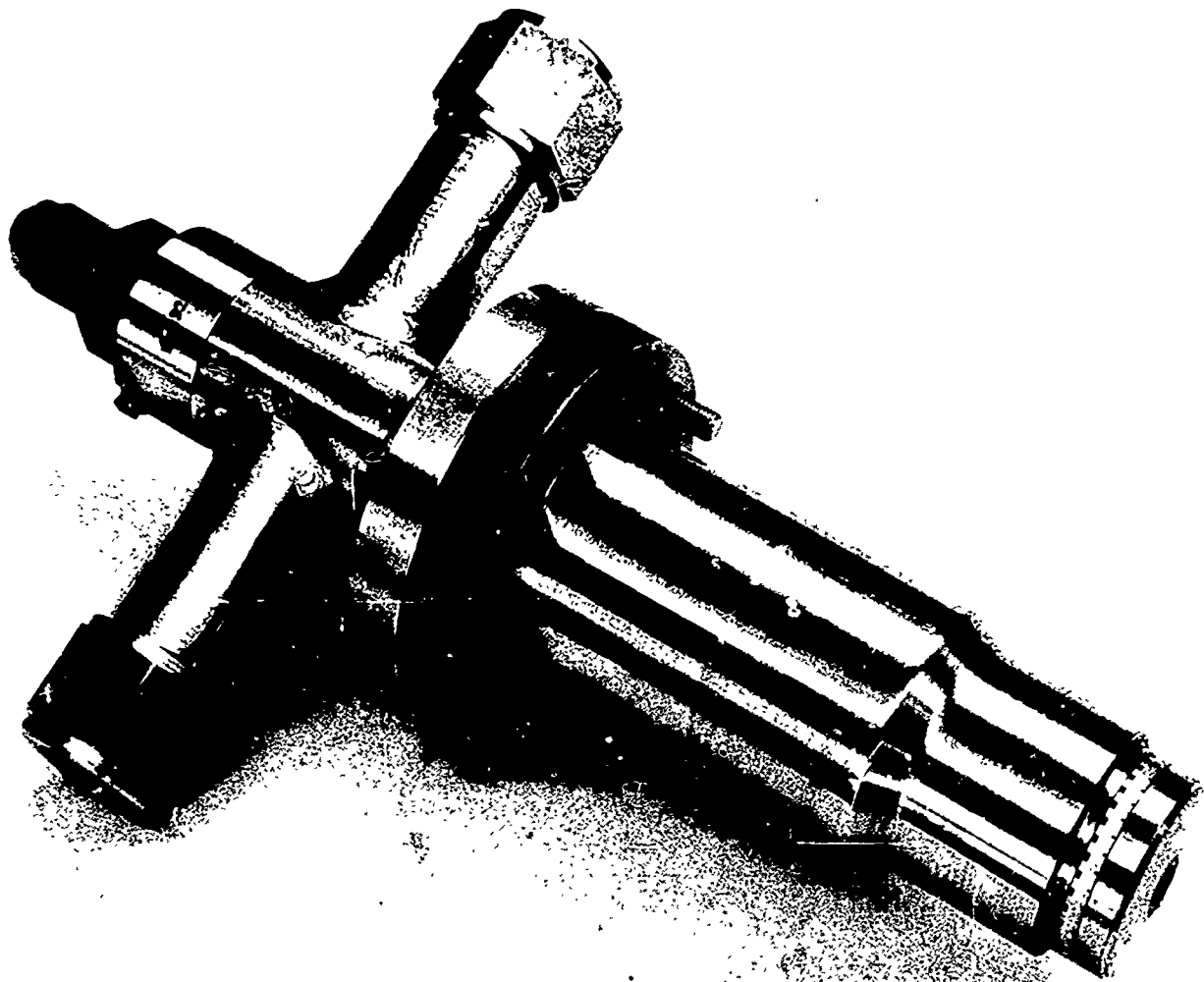


Figure 11. Configuration 3 Oxidizer Feed Subassembly (U)

UNCLASSIFIED

UNCLASSIFIED

AFRPL-TR-69-231  
Page 25

(U) The oxidizer orifice rings were fabricated from 6061 aluminum alloy. The basic blank ring was fabricated to size and then using a precision slotting saw the slots are added in accordance with the desired configuration.

(U) The pintle tip was initially fabricated from 304 stainless steel but problems arose with pintle tip erosion due to excessive heating. It was decided to incorporate a material with higher thermal conductivity. Both a nickel and columbium alloy pintle tip were made and tested. Both materials eliminated the pintle tip erosion problem and both pintle tips were used throughout the remainder of the test program. The pintle tip is bolted to the inner pintle body holding the oxidizer orifice ring between the pintle tip and outer pintle body.

### 3.4 UNCOOLED THRUST CHAMBER DESIGN

(U) The uncooled heat sink thrust chamber design utilized for Task 1 is shown in Figure 12. The chamber design employs a mild steel cylindrical chamber section and a copper (sea-level expansion) nozzle throat section. The chamber was designed to give nominal run durations of four seconds. The chamber characteristic length ( $L^*$ ) could be varied by simply changing the cylindrical spool section. The nominal  $L^*$  for the engine was 50 inches. A shorter cylindrical section which reduced the  $L^*$  to 35 inches was also fabricated and tested. The inside diameter of the chamber is six inches which results in a contraction ratio of 4.9.

(U) The nozzle incorporates a 30-degree convergence angle and a full radius throat blended into a  $15^\circ$  half angle nozzle. The nozzle expansion was truncated at an area ratio of 3.5 to give optimum expansion for test site ambient pressure.

(U) The injector was mated to the uncooled thrust chamber flange by means of twelve 1/2 inch bolts. The injector/chamber alignment is accomplished by use of two 1/4 inch dowel pins in the injector and mating holes in the chamber. Sealing at the injector/chamber interface is through use of silicone rubber O-rings. In the initial design, two O-ring seals were used to provide a redundant gas seal. Subsequently, an ablative face plate liner was added to protect the injector face plate. To accommodate the ablative liner, a step was machined in the inside diameter of the cylindrical chamber,

UNCLASSIFIED



(U) thereby eliminating the inner seal. Over one hundred tests were conducted using just the single seal and there was not one instance of a gas leak.

(U) The cylindrical section and the nozzle section of the uncooled thrust chamber are joined together by use of a ring and flange arrangement as shown in Figure 12. A steel ring with twelve clearance holes for 1/2 inch bolts is slipped over the nozzle until it engages the upper flange on nozzle. The ring is then bolted to the chamber, securing the nozzle to the cylindrical section.

(U) Sealing at the chamber/nozzle interface is through use of a crushable face seal of "Durabla" asbestos sheet gasket material. The seals are made in the form of flat rings which slip into a serrated groove about 1/8 inch deep. The nozzle section has a mating serrated tongue which compresses the gasket forming the seal. No instances of gas leakage were experience in one hundred and twenty-nine tests using this sealing method.

(U) The uncooled thrust chamber was instrumented for static and dynamic pressure measurements. Dual static pressure measurements are provided at the injector face and at the start of nozzle convergence. Dynamic pressure measurements are achieved through the use of Photocon water-cooled high frequency transducers. Five Photocon ports were provided; three near the injector end of the cylindrical section and two near the start of nozzle convergence. The cylindrical section of the thrust chamber has six fixtures through which probe type thermocouples are inserted to measure inside wall temperature. The copper nozzle contains nine calorimetric plug thermocouples to measure heat flux in the nozzle.

#### 3.4.1 Pulse Gun

(U) The pulse gun used for dynamic stability testing was a design which has been extensively used at the Air Force Rocket Propulsion Laboratory (for example see Reference 4). Operation of the pulse gun requires a 28 volt signal to a small detonating primer containing about 2 grains of explosive. The resulting explosion forces the firing pin to strike the center-fire primer of a cartridge contained in the gun breech. This percussion primer in turn ignites the gun powder charge. When sufficient pressure has been built up in the breech, the burst diaphragm ruptures and the relief of the breech pressure forms a shock which propagates down the barrel. In this

UNCLASSIFIED

(U) application, a .300 Magnum cartridge loaded with 50 grains of Hercules Bullseye gun powder was used in combination with a 20,000 psi burst disc.

#### 3.4.2 Non-Directional Bombs

(U) The bomb used to demonstrate dynamic stability was of a design for which extensive test experience at TRW has been accumulated. A sectional view of this design is shown in Figure 13. The bomb case is fabricated from Type 1 Nylon. The adaptor is machined to enable the bomb to be inserted in a Photocon transducer port. Detonation of the bomb requires a 28 volt signal to the detonating primer.

(U) The bombs were initially loaded with a #6 Hercules detonator and 7.1 grains of RDX. These bombs had an explosive force of 10 grains of RDX (12.9 grain TNT equivalent). The second lot of bombs loaded contained a #6 detonator and 22.1 grains of RDX. The total explosive force of the second lot was 25 grains of RDX (32.5 grain TNT equivalent).

#### 3.5 UNCOOLED THRUST CHAMBER FABRICATION

(U) The cylindrical section of the uncooled thrust chamber was fabricated from 1020 mild steel and the nozzle section from hot rolled Oxygen Free High Conductivity (OFHC) copper. The nozzle section was attached to the cylindrical section by means of a carbon steel ring and flange arrangement as shown in Figure 12.

(U) The cylindrical chamber section was fabricated from seamless steel tubing with one inch thick walls. Flanges for mating the injector to the chamber and for mating the nozzle were welded to the tubing. The cylindrical section was then final machined. Five ports were machined into the cylindrical section to accept Model 352A Photocon transducers. Two tangential pulse gun ports were welded to the chamber and the entry ports then drilled. Six probe type thermocouple ports were provided by welding a compression fitting to the chamber and then drilling and reaming the port. Two ports were drilled in the downstream flange for measuring downstream static chamber pressure.

(U) The nozzle section, fabricated of OFHC copper, had nine thermocouple calorimetric plugs. Three plugs were located in three rows 120 degrees apart. Three plugs were located in the convergent section, three in the geometric throat and three in the divergent section. Installation of these

UNCLASSIFIED

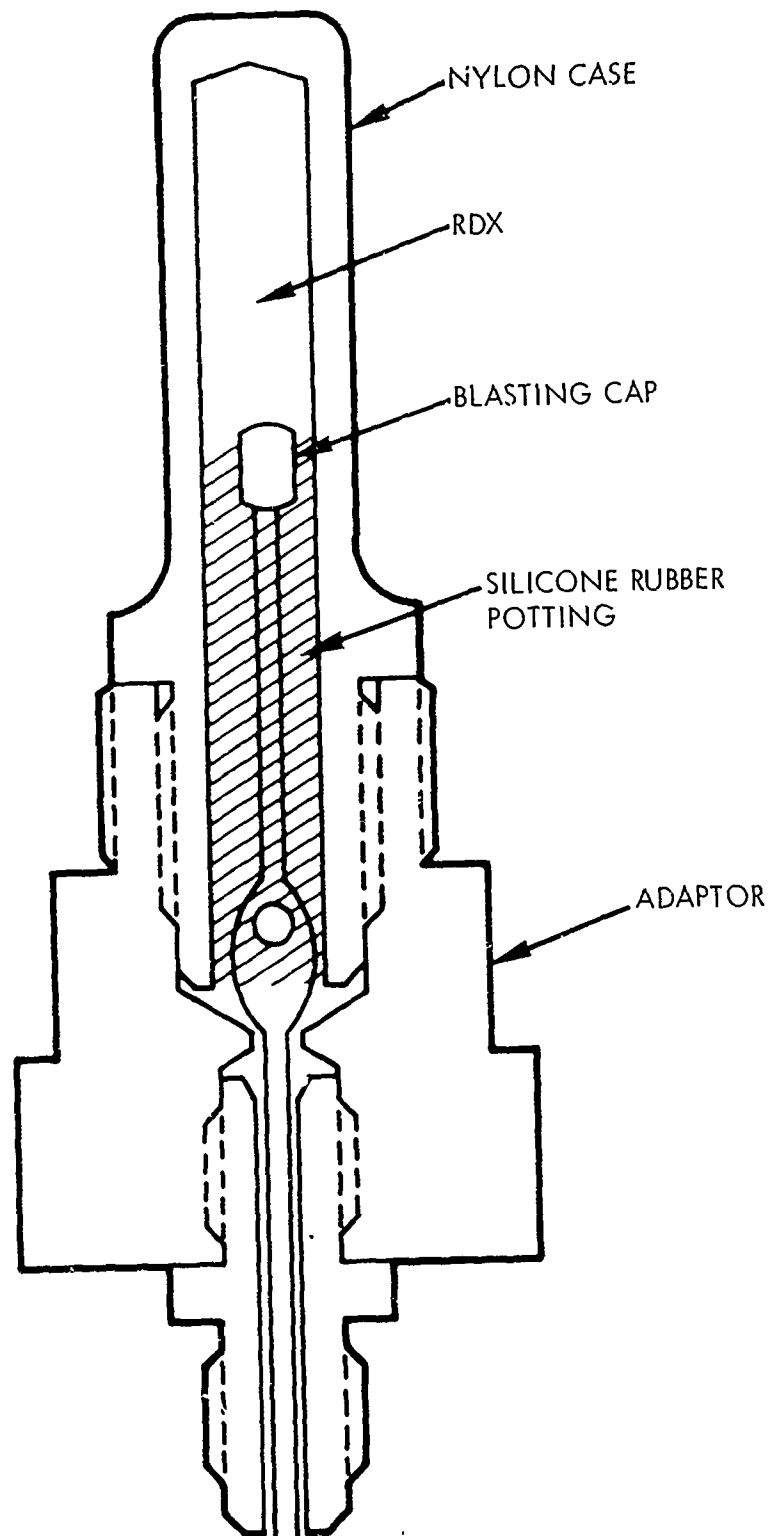


Figure 13. Non-directional Bomb Configuration (U)



UNCLASSIFIED

(U) plugs in the nozzle represented the most difficult fabrication problems, because of the difficulty in establishing a true reference point from an angle and a complex contour.

(U) Assembly of the thermocouple in the calorimetric plug was accomplished by inserting the thermocouple wire into the drilled hole in the center of the plug. The copper metal of the plug was then peened to secure the wire in the hole. Twelve holes were drilled in the exit end of the nozzle and 3/8 inch internal thread inserts installed to allow a pressure check plate to be attached.

### 3.6 ABLATIVE THRUST CHAMBER DESIGN

(U) The ablative thrust chamber designed for the Task 2 injector/chamber compatibility tests had the same inside physical dimensions as the uncooled thrust chamber. Figure 14 is a layout of the ablative thrust chamber assembly. The thrust chamber liner is made from MX 2600 silica phenolic ablative material oriented 60 degrees to the centerline. The liner is contained within a mild steel shell. The ablative thrust chamber assembly is pictured in Figure 15.

(U) Provision was made for installing thermocouples in six locations in the ablative liner. Three thermocouples 120 degrees apart are in the throat plane and three at the start of nozzle convergence. The thermocouples are made by forming the junction at the end of a plug of MX 2600 and inserting the plug in the ablative liner. The plug was then sealed with an epoxy cement.

### 3.7 INJECTOR HYDRAULICS/COMBUSTION DYNAMICS INTERACTION STUDY

(U) A non-linear hybrid-computer model of the  $3K N_2O_4/N_2H_4$  injector, combustion chamber and propellant feed system was formulated and utilized to define the degree of interaction between the engine combustion and injector assembly dynamics. Computer studies were conducted to establish the effect of various system parameters on system pressure oscillations induced by a simulated bomb perturbation within the combustion chamber. The parameters considered in this analysis included:

- Combustion Chamber Overpressure
- Oxidizer/Fuel Injector Pressure Drop
- Oxidizer/Fuel Injector Manifold Volume (Propellant Compressibility)

UNCLASSIFIED

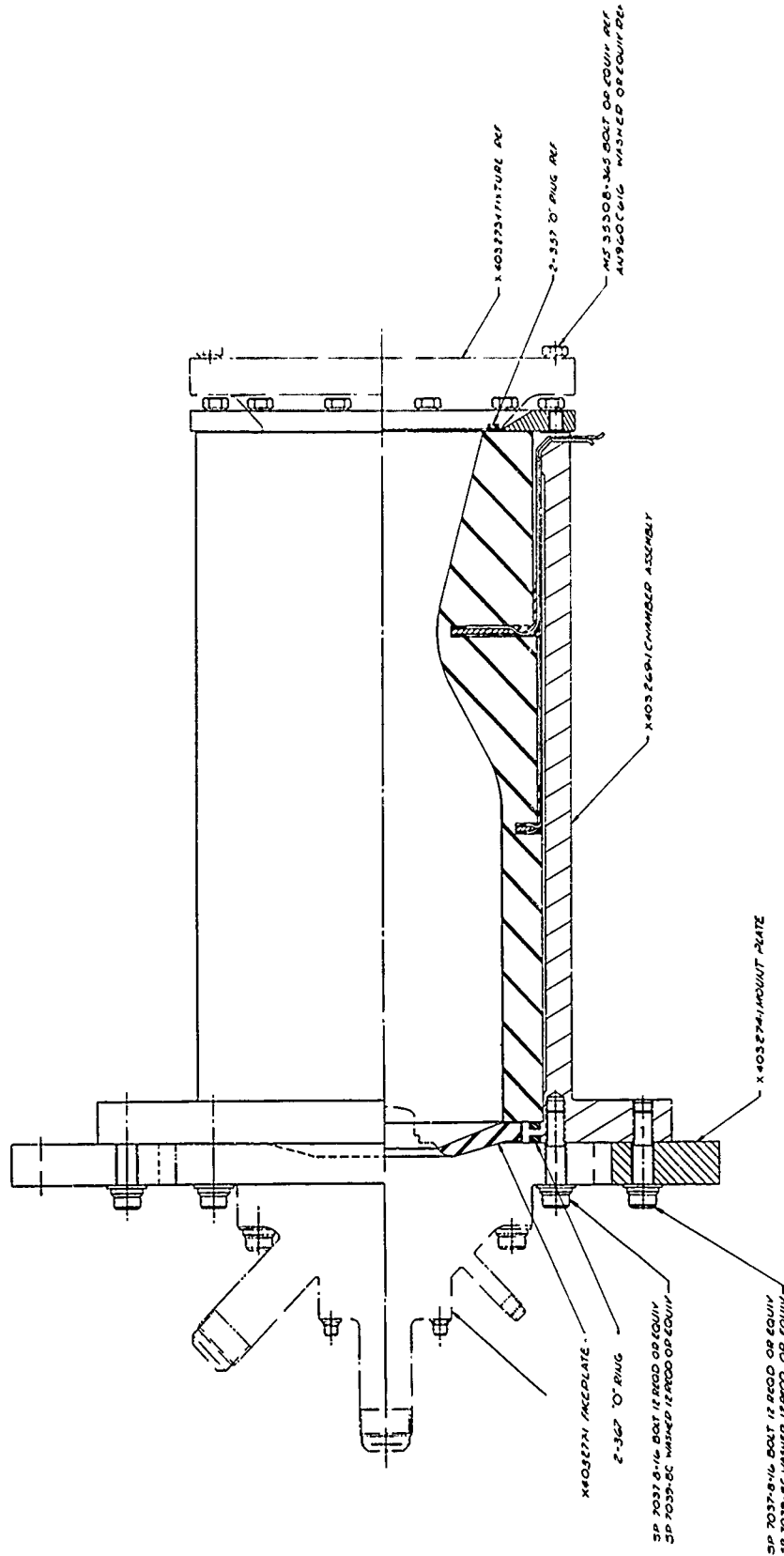


Figure 14. Ablative Thrust Chamber Design (U)

UNCLASSIFIED

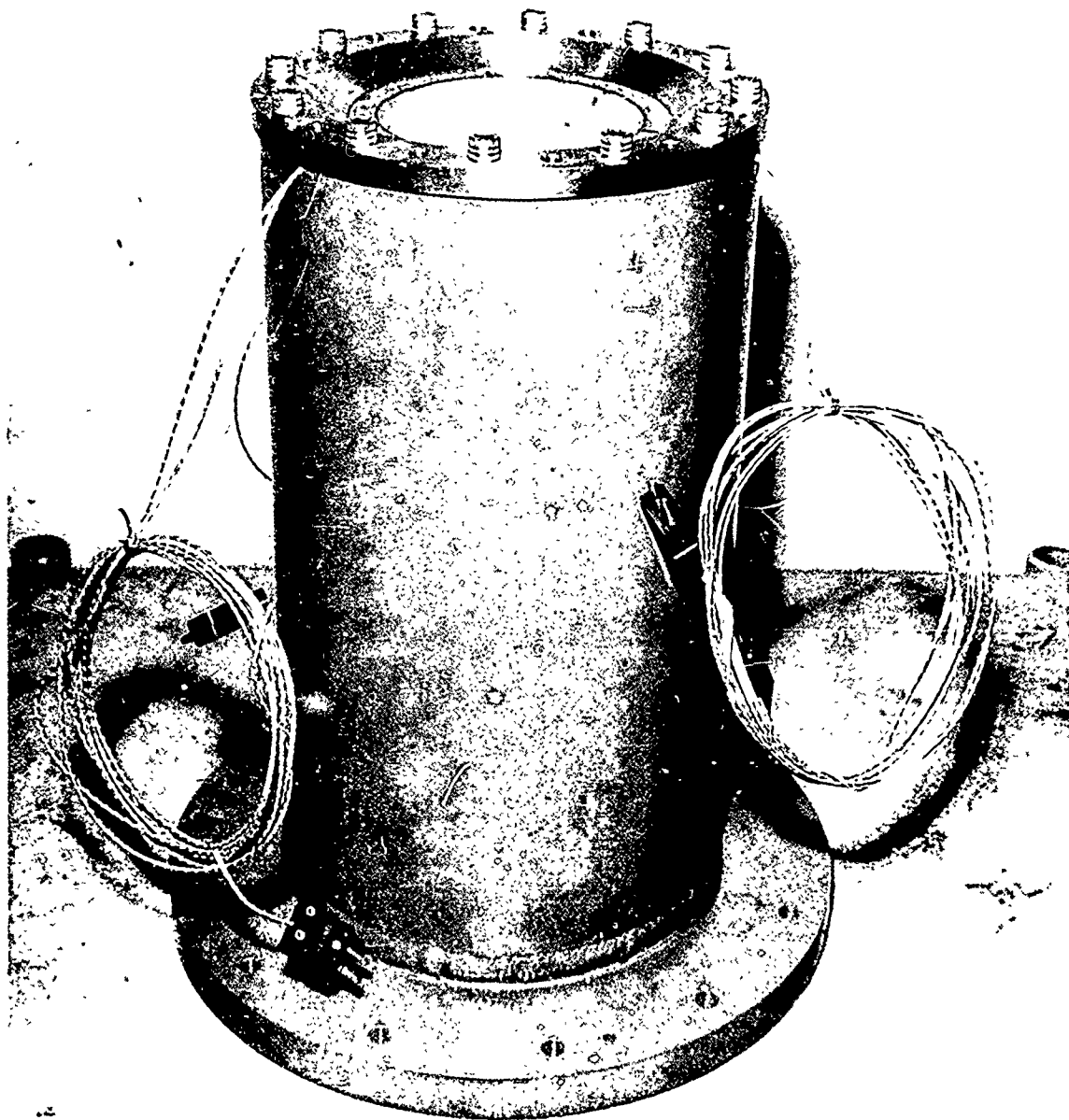


Figure 15. Ablative Thrust Chamber Assembly (U)

UNCLASSIFIED

- Oxidizer/Fuel Injector Manifold Inductance (Propellant Inertia)
- Oxidizer/Fuel Injector Time Delay

The injector time delay is defined as follows

$$\tau_{\text{injector}} = \frac{l_i A_i \rho_p}{\dot{w}_i}$$

where:

$l_i$  = distance from injector orifice to oxidizer/fuel impingement point

$A_i$  = injector orifice area

$\rho_p$  = effective propellant density

$\dot{w}_i$  = injector flow rate

(U) The results of this study established the effect of the system parameters outlined above on the pressure recovery characteristics following a simulated chamber bomb perturbation. The effect of changes in these parameters on chamber pressure amplification for a stochastic chamber pressure disturbance was not established as part of this analysis. The system response to a stochastic disturbance in the chamber pressure may indicate a different degree of sensitivity to the above system parameters.

(U) The results of the analysis effort established that the baseline 3K  $N_2O_4/N_2H_4$  engine configuration exhibits a high degree of damping in chamber pressure recovery after a simulated bomb perturbation of 490 psi (above nominal chamber pressure of 300 psia) in the combustion chamber. The high degree of stability is evident in Figure 16 which is representative of a computer run for the baseline 3K  $N_2O_4/N_2H_4$  engine configuration.

(U) Parametric studies were also made (at a nominal mixture ratio of 1.2) to determine the effect of system parameters on chamber pressure and oxidizer/fuel feed line pressure recovery characteristics after a simulated bomb perturbation in the combustion chamber. The results of these investigations were as follows:

- Increased chamber overpressure results in decreasing the effective damping and increasing the recovery time exhibited by the chamber pressure after a simulated bomb disturbance.

UNCLASSIFIED

- Oxidizer injector pressure drop is a critical parameter in stabilizing chamber pressure oscillations. Increasing the oxidizer injector pressure drop from a nominal of 120 psi tends to increase the effective damping exhibited by the chamber pressure but does not significantly decrease the recovery time.
- Engine recovery time was found to be insensitive to fuel injector pressure drop.
- Increases in the compressibility of the propellants in the injector manifold resulting from larger manifold volumes or dissolved gases in the propellant tends to destabilize the engine.
- Increases in the oxidizer inertia in the injector manifold resulting from larger effective manifold lengths or smaller effective cross-sectional manifold areas tend to stabilize the engine.
- Increases in the fuel inertia in the injector manifold resulting from larger effective manifold length or smaller effective cross-sectional areas tend to destabilize the engine.
- Increases in the oxidizer injector time delay is a stabilizing factor over a range of 1 to 50 times nominal. Above a ratio of 50 times nominal, increasing the injector time delay tends to be a destabilizing factor.
- Increases in the fuel injector time delay has a stabilizing effect on chamber pressure oscillations over an injector time delay range from 2 to 10 times nominal. Above 10 times nominal, the fuel injector time delay has a destabilizing effect on chamber pressure oscillations resulting from a bomb perturbation in the combustion chamber.
- The oxidizer injector time delay has a stabilizing effect on the chamber pressure over a larger range than the fuel injector time delay.

UNCLASSIFIED

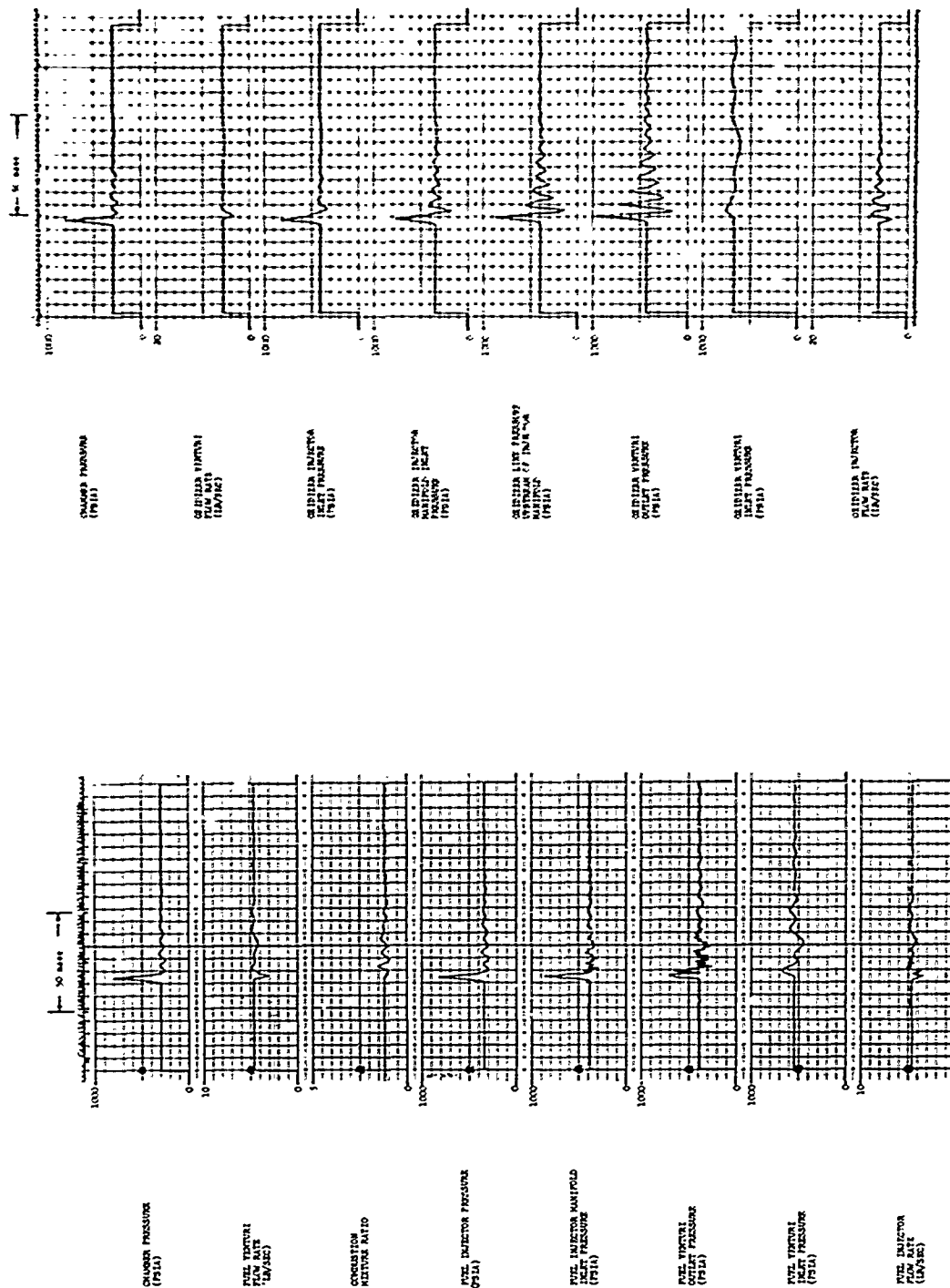


Figure 16. Injector/Feed System Dynamic Model Results (U)

UNCLASSIFIED

#### 4. TEST EVALUATION

(U) Upon completion of the Phase I analytical and design effort, two injector assemblies and sea-level expansion thrust chambers were fabricated to provide test hardware for obtaining both injector performance and heat transfer data. Both injector assemblies had the capability of accepting any of the three injection element configurations. As described earlier, the injector was designed to provide capability for hardware modification while maintaining test stand readiness.

(U) The initial experimental efforts were directed toward evaluating three injection element configurations in order to select the element which best meets the design goals of mixture ratio flexibility, dynamic stability, good performance, and injector-chamber compatibility. This effort consisted of basic cold flow studies and hot firing tests. Following this, the selected injector configuration was tested in detail to fully characterize its performance in terms of engine specific impulse, resultant thrust chamber heat transfer characteristics, combustion noise, and dynamic stability. Subsequently, a minimum effort injector/chamber compatibility test phase was conducted using near flight type ablative chambers.

##### 4.1 INJECTOR DEVELOPMENT COLD FLOW STUDIES

(U) The injector cold flow studies encompassed three parts. The basic hydraulic operating characteristics were determined from pressure drop, mass flow, and visual observations. Secondly, tests were conducted to characterize fuel and oxidizer spray uniformity through visual observations and through measurements of spray momentum. Finally, cold flow characterization for the purpose of correlating with hot firing results was attempted. With respect to the latter effort, this effort marked an initial effort at TRW to provide such characterization.

##### 4.1.1 Injector Hydraulic Characterization

(U) The initial phase of the cold flow experimental program was performed to determine flowrate-pressure drop characteristics, mass and mixture ratio distributions and overall impingement characteristics. The flowrate-pressure drop characteristics were determined using water, with results for two of the oxidizer orifice rings appearing in Figure 17 and in Figure 18

UNCLASSIFIED

UNCLASSIFIED

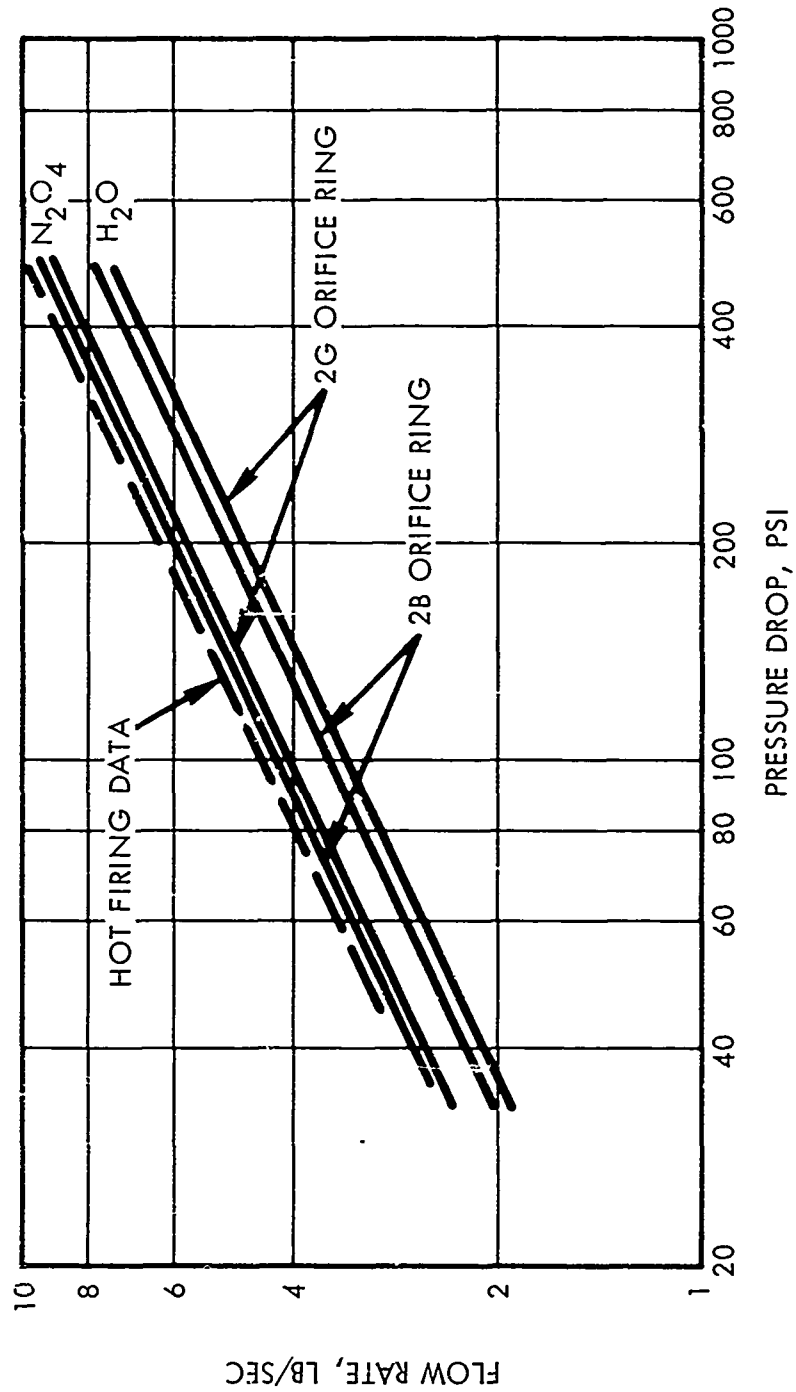


Figure 17. Hydraulic Characteristics of Oxidizer Orifice Rings (U)

UNCLASSIFIED



UNCLASSIFIED

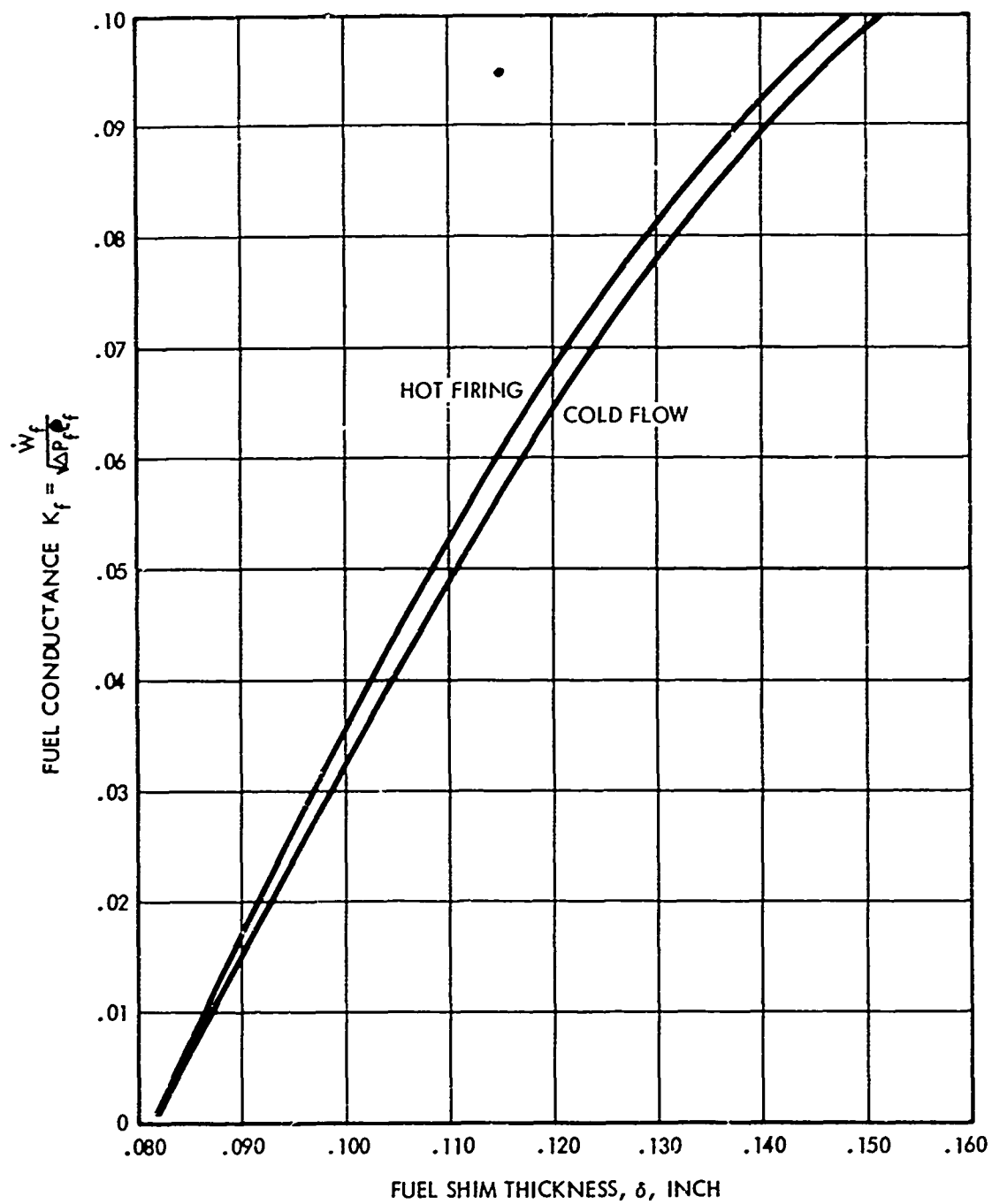


Figure 18. Hydraulic Characteristics of Injector Fuel Circuit (U)

UNCLASSIFIED

(U) for the fuel subassembly. Also plotted on Figure 17 is the equivalent curve for nitrogen tetroxide. Actual hot firing data are also plotted on these figures for comparison with cold flow data. Table 1 presents a comparison of the oxidizer orifice discharge coefficients for both hot firing and cold flow tests. In addition to overall injector pressure drop data, the various pressure drops associated with the components which comprise the overall drop were determined. These included: 1) oxidizer distribution, 2) fuel distribution, and 3) oxidizer and fuel injection gaps. This was necessary so that actual injection  $\Delta P$ 's and hence injection velocities could be determined.

(U) The overall impingement characteristics are determined visually. Figure 19 presents a photograph of the resultant spray pattern and reveals the high degree of atomization and also shows good circumferential uniformity.

#### 4.1.2 Injector Cold Flow Momentum Tests

(U) A series of cold flow tests were conducted to characterize fuel and oxidizer spray uniformity through visual observations and through measurements of spray momentum. Photographs of the test equipment are shown in Figures 20 through 23.

(U) Oxidizer Visual Observation - The oxidizer subassembly was mounted on the patternator test stand, Figure 20, and water flowed for visual observation of the oxidizer orifices. The flow rate was set at 3.86 pounds per second of water at an inlet pressure of 116.8 psig. This is the equivalent volumetric flow rate run during the hot firing test series. Visual observations are made to determine if any streams are unstable (flutter), which streams are broader or narrower than the nominal, and whether the streams are displaced vertically or circumferentially from adjacent sprays. A photograph of the oxidizer element streams at the nominal volumetric flow rate is shown in Figure 23.

(U) Fuel Sheet Visual Observation - The injector was mounted to the patternator test stand and water flowed through the fuel side. The fuel metering gap was set by inserting the appropriate shim between the fuel and oxidizer feed subassemblies. The fuel sheet was observed at three water flow rates; 3.88, 4.59 and 5.77 pounds per second.

UNCLASSIFIED

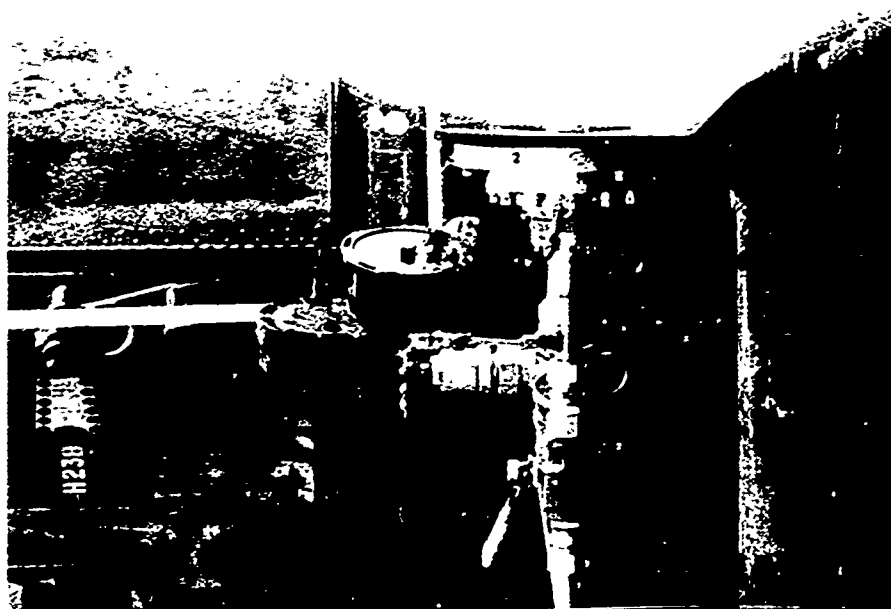


Figure 19. Combined Oxidizer And Fuel Injector Circuit Cold Flow (U)

UNCLASSIFIED

UNCLASSIFIED

AFRPL-TR-69-231

Page 41

Table 1. Actual Discharge Coefficients Of Oxidizer Orifice Rings (U)

Configuration Number	Number of Slots	Nominal Pressure Drop (psi)	Discharge Coefficient (cold flow)	Discharge Coefficient, (hot firing)
1A	36	90	0.62	0.74
1B	48	100	0.66	0.82
1C	72	90	0.74	0.84
1D	36	130	0.66	0.73
2A	36/36	90	0.71	0.74
2B	36/36	150	0.75	0.80
2C	36/36	115	0.76	0.78
2D	36/36	175	0.78	0.82
2E	36/36	150	0.80	0.80
2F	36/36	150	0.81	0.85
2G	36/36	150	0.78	0.80
2H	36/36	200	0.72	0.79
2J	36/36	150	0.79	0.80

(see Figure 31 for orifice ring geometries)

UNCLASSIFIED

UNCLASSIFIED

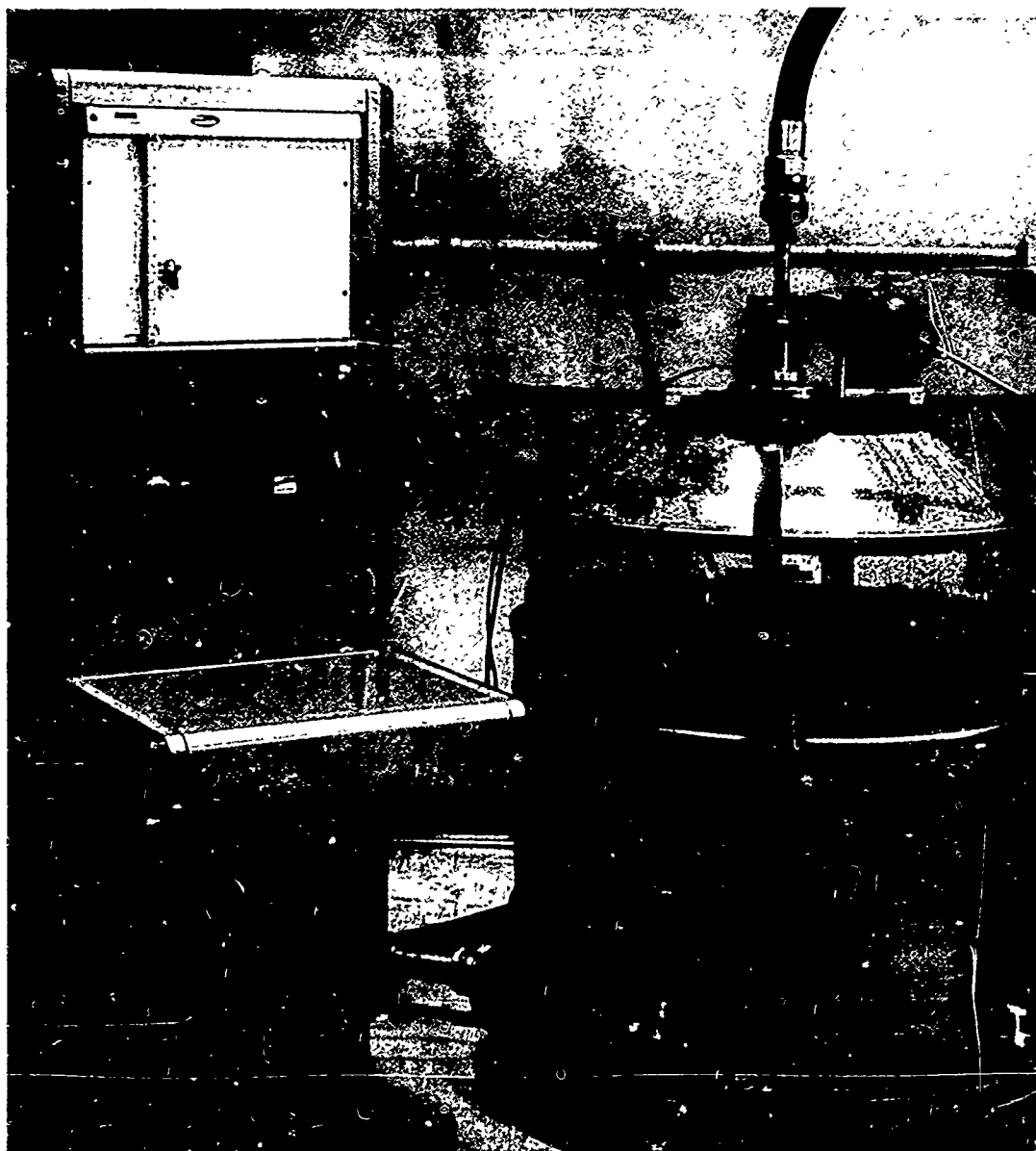


Figure 20. Cold Flow Momentum Measurement Test Equipment (U)

UNCLASSIFIED

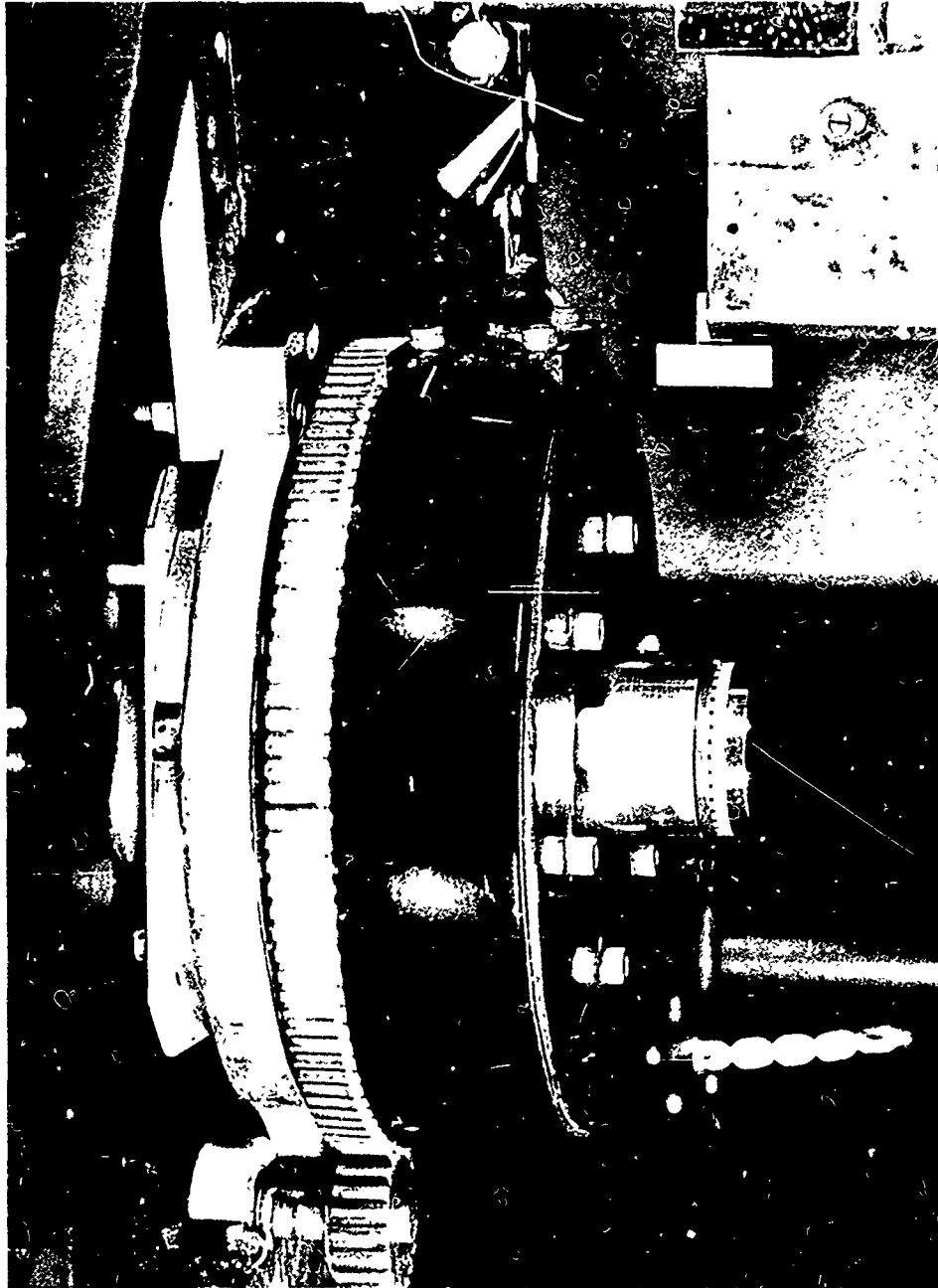


Figure 21. Oxidizer Momentum Measurement Set-up (U)

UNCLASSIFIED

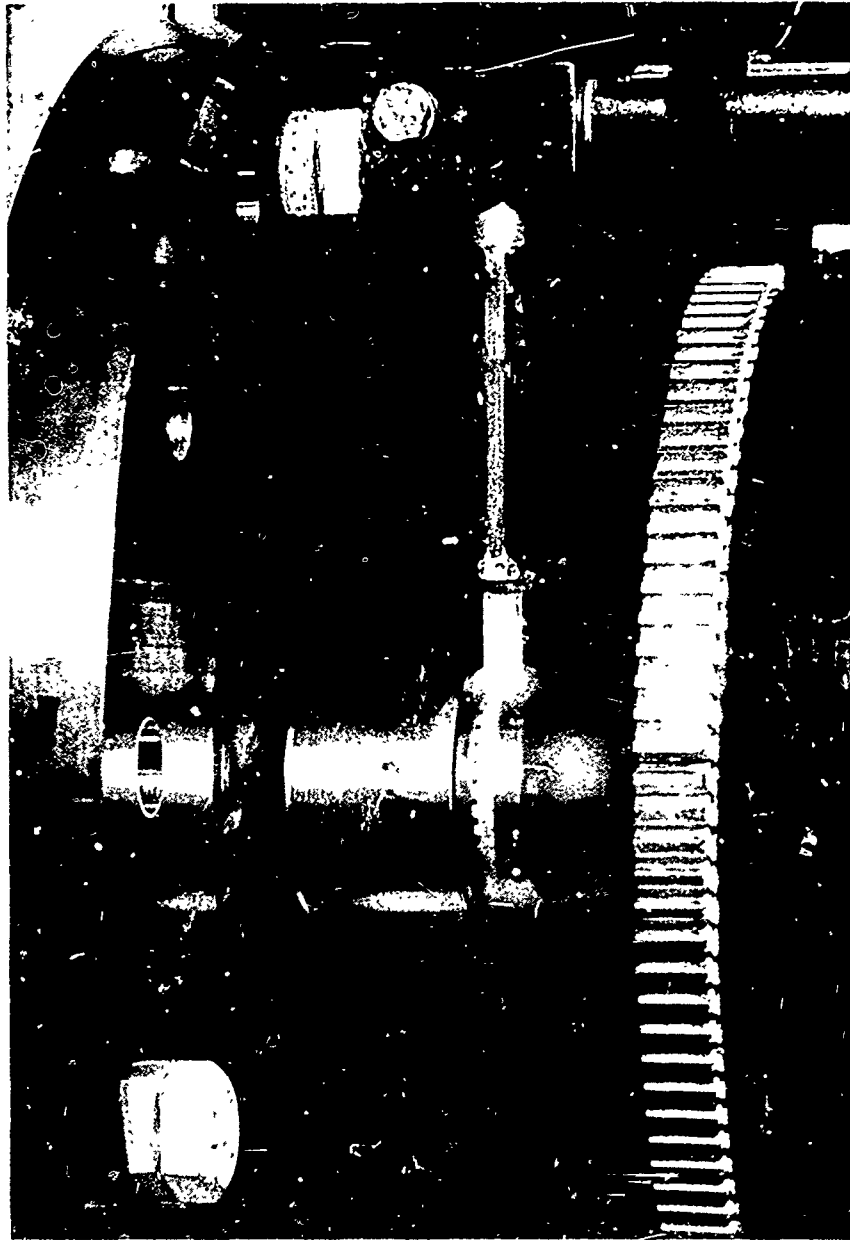


Figure 22. Fuel Sheet Momentum Measurement Set-up In Operation (U)

UNCLASSIFIED

UNCLASSIFIED

69-231

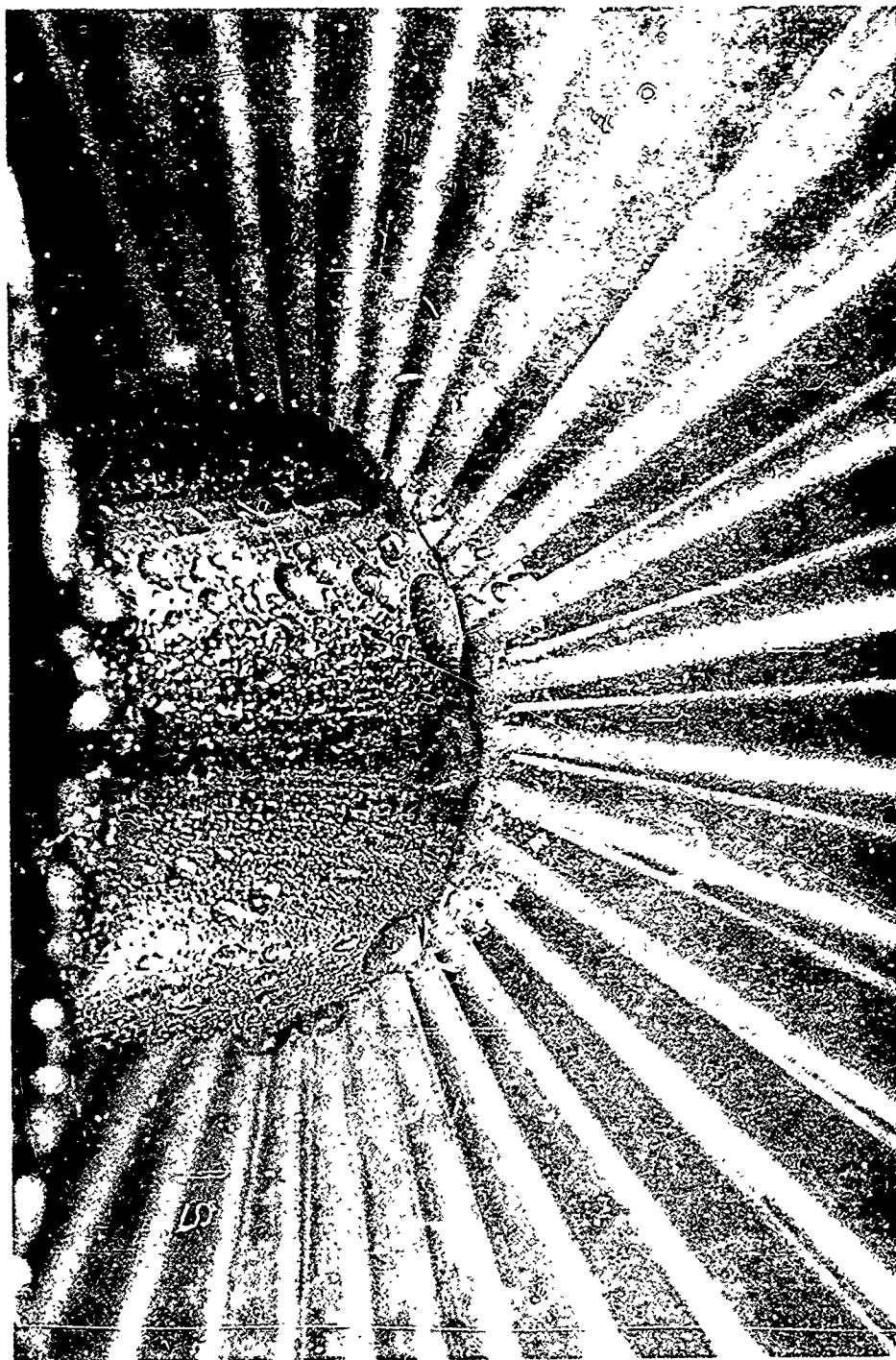


Figure 25. Oxidizer Orifice Spray Pattern (U)

UNCLASSIFIED



AD 506 043

AUTHORITY:

AFRPL

1st 5 Feb 86



UNCLASSIFIED

(U) Oxidizer Momentum Tests - The oxidizer feed subassembly was adapted to the momentum test fixture and tests were made to measure the momentum of each oxidizer spray. Figure 20 shows the complete test set up; including the patternator test stand, the momentum test fixture, and the momentum data collecting and recording equipment. Figure 21 is a close-up photograph of the oxidizer momentum probe and its drive mechanism.

(U) Briefly, the set-up and operation of the equipment is as follows: the injector assembly is mounted to the momentum carriage and drive mechanism. The probe is mounted to the carriage and aligned with the oxidizer stream. A constant drive motor turns the carriage/probe assembly around the circumference of the injector. (The probe is a strain gage instrument which measures the force of each stream as it passes through the stream). The circumferential travel (measured by a potentiometer), and the force readings are recorded on an X-Y plotter.

(U) The results of a typical oxidizer momentum test are shown in Figure 24 for the 2B orifice ring configuration. This figure shows the momentum profiles of all 36 primary and 36 secondary streams as measured at each of three radial distances from the oxidizer slots.

(U) Close-in momentum measurements are useful in assessing the overall mass flow distribution and primary/secondary flow ratios. Differences in stream direction, breakup, stability, and other variables affecting the wall environment become more apparent as the probe is moved away from the injector slots. The variation in primary oxidizer spray momentum at various distances from the injector slots is illustrated in Figure 24. As can be seen, the non-uniformity in the spray characteristics of this injector are most accentuated at a distance of 2.3 inches from the slots, which represents the chamber wall. The tests were made at a water flow rate of 3.86 pounds per second and an inlet pressure of 116.8 psig. Data was acquired at three different radial positions from the element; 0.3, 1.3 and 2.3 inches from the oxidizer slots. The probe used for these tests was 0.050 inch wide.

(U) Fuel Sheet Momentum Tests - The fuel sheet momentum fixture is shown in operation in Figure 22. An 0.074 inch wide probe was positioned under the step at the end of the injector element sleeve. Operation of the equipment was essentially the same as for the oxidizer momentum testing.

UNCLASSIFIED

UNCLASSIFIED

AFRPI-TR-69-231

Page 47

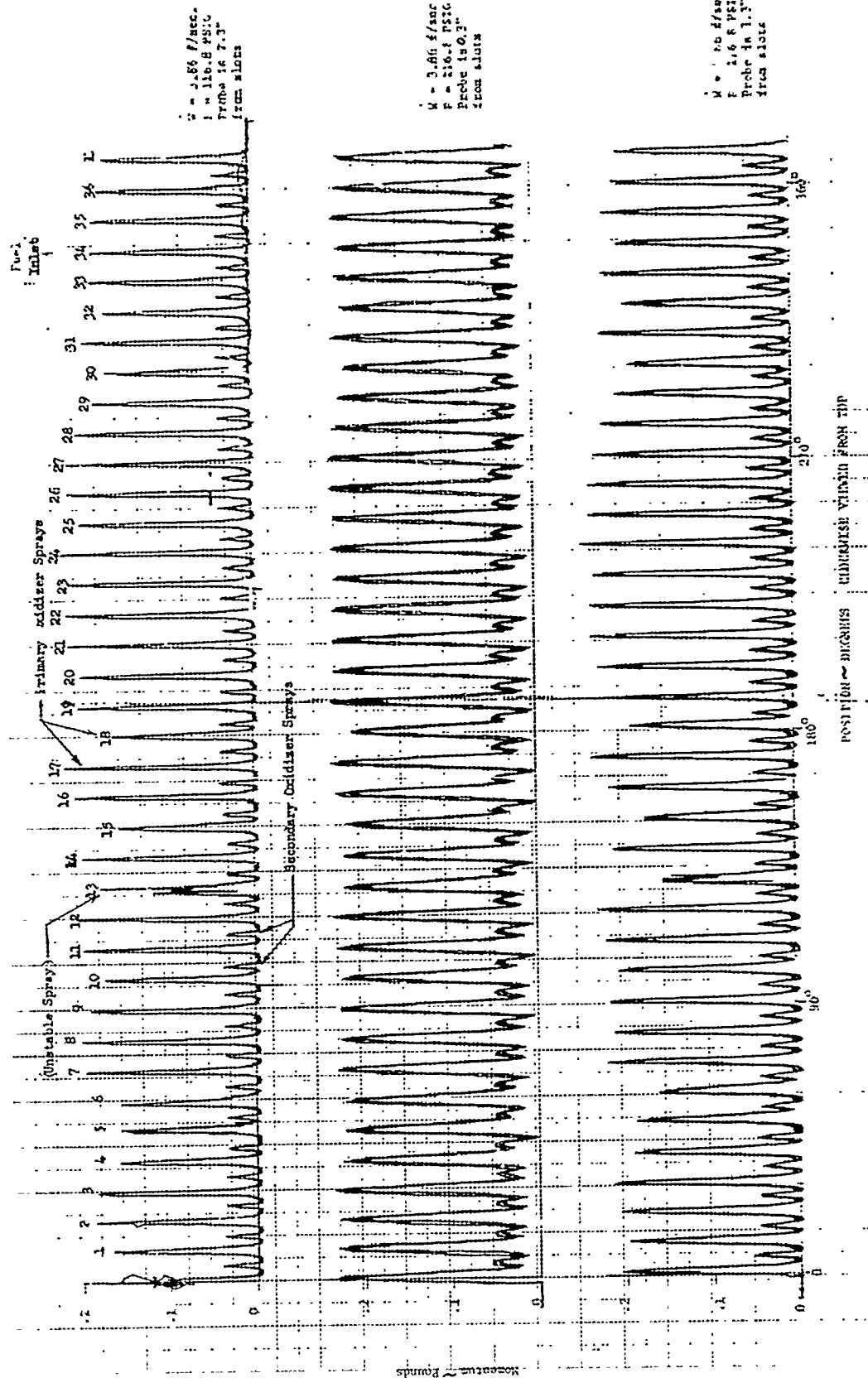


Figure 24. Oxidizer Cold Flow Momentum Test Results (U)

UNCLASSIFIED

UNCLASSIFIED

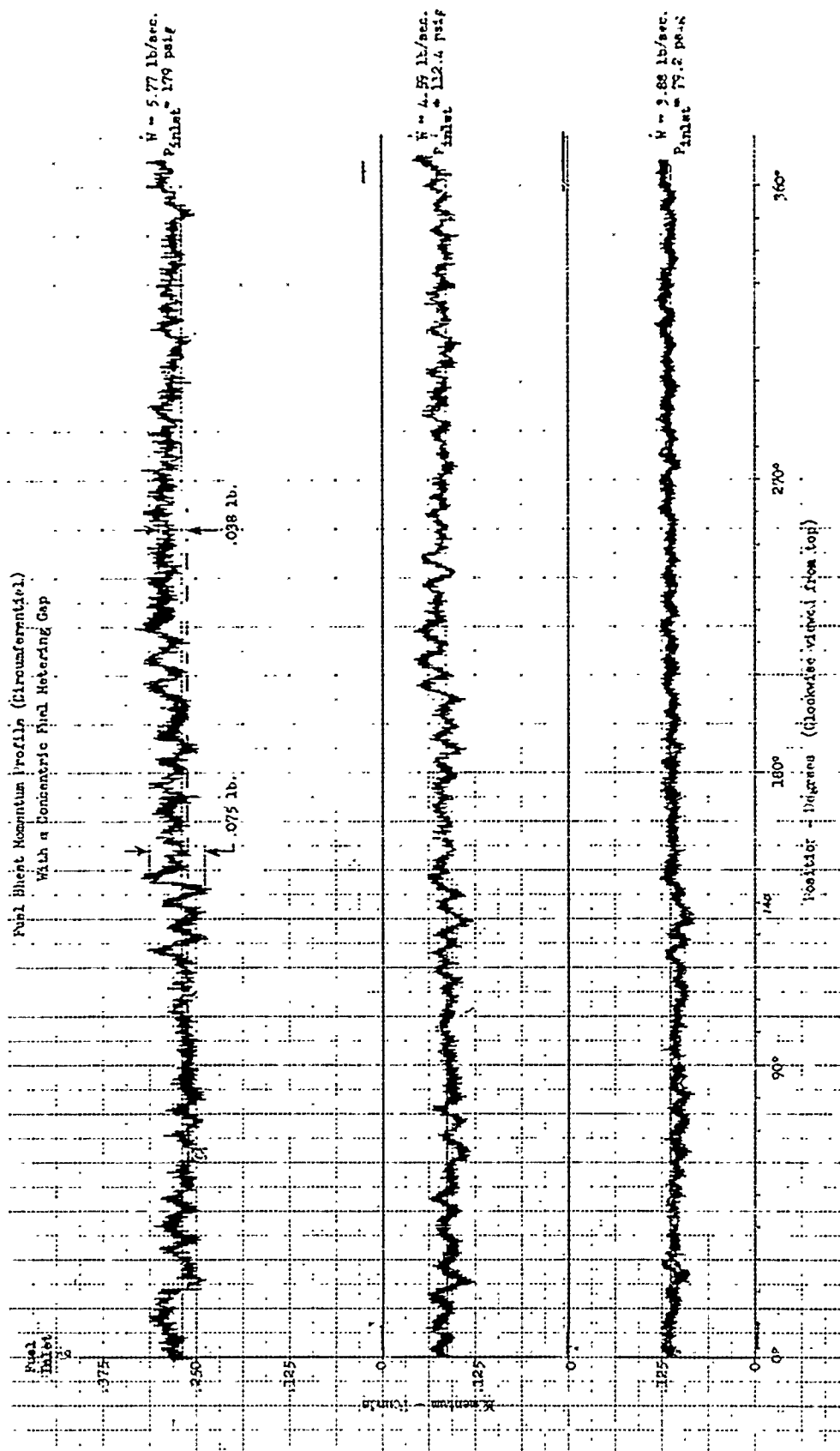


Figure 25. Fuel Sheet Cold Flow Momentum Test Results (U)

UNCLASSIFIED

(U) The testing consisted of collecting momentum data at 3 flow rates (corresponding to the three different mixture ratios for this engine), with the injector fuel sleeve concentricity maintained as accurately as possible.

(U) The results of this test are shown in Figure 25. The mass flow distribution in the fuel sheet is relatively uniform; i.e., the average momentum is approximately the same around the entire circumference of the element. A slight bias in flow does exist, however, with the high point being around 250° from the inlet and the low around 90° from the inlet. At the highest flow rate tested, this bias was in the order of 15% (.038 lb momentum).

#### 4.1.3 Cold Flow Correlation Tests

(U) An attempt was made to correlate cold flow patternation data with hot firing results. Efforts of this sort have previously been reasonably successful with conventional injectors. The TRW coaxial injector requirements for high performance follow basically those of conventional injectors, atomization and mixture ratio distribution uniformity; however, whereas impinging jet injectors may require heavy emphasis on atomization, the TRW coaxial injector requires more emphasis on mass and mixture ratio uniformity.

(U) To obtain this data, the coaxial injector requires a different approach to collection of cold flow simulants than is normally used for conventional injectors. Both circumferential and longitudinal distributions must be determined.

(U) The mass and mixture ratio distributions were obtained with the use of the apparatus shown in Figure 26. This water flow patternation fixture, developed by TRW, is located at the Capistrano Test Site's Hydraulic Laboratory. This fixture has the capability of measuring the mass and mixture ratio distribution of an injector by diverting the fluids into 1/4 inch tubes located about six inches from the injector. This equipment collects the flow from the injector in tubes spaced both circumferentially and longitudinally, resulting in a determination of the circumferential uniformity of the spray and in the mass and mixture ratio gradients through the spray fan. Mixture ratio was measured by flowing trichloroethylene through the oxidizer side and water through the fuel side.

(U) The propellant simulants of trichloroethylene and water were selected since they are reportedly immiscible and the densities are nearly those of

UNCLASSIFIED

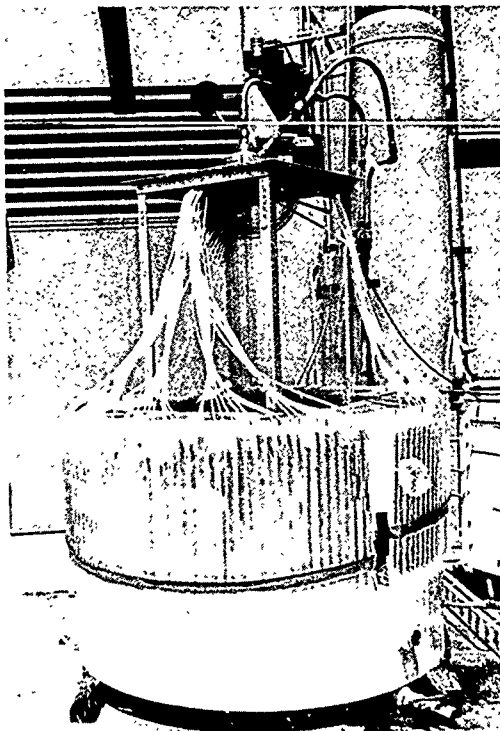
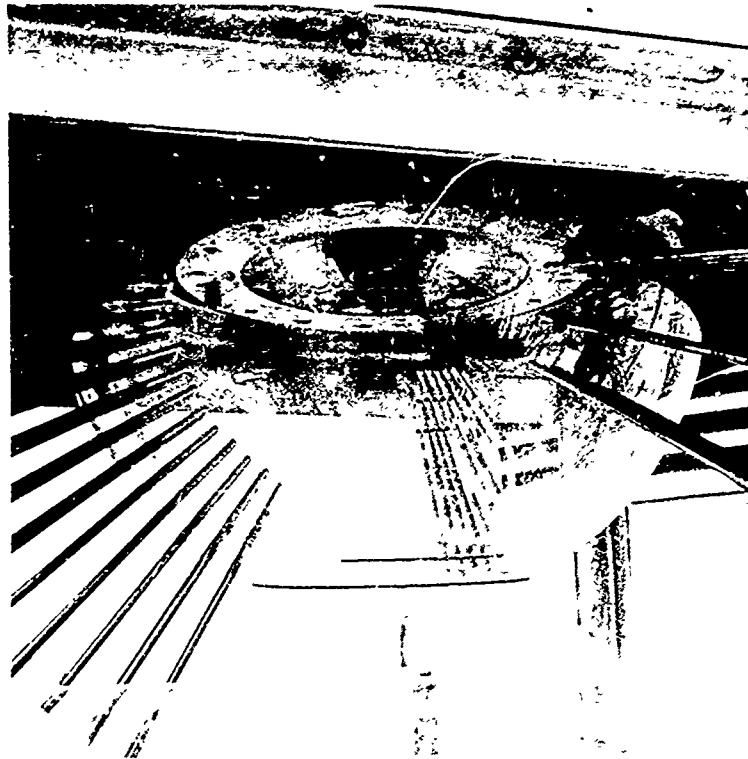


Figure 26. Injector Patterning Fixture (U)

UNCLASSIFIED

(U) the actual propellants; however, the TRW coaxial flow injectors of high performance quality provided such intimate mixing and atomization that the trichloroethylene was virtually emulsified into the water. Translation from simulant to actual propellants is made by:

$$(O/F)_{\text{propellants}} = (O/F)_{\text{sim}} \left( \left( \frac{\rho_o}{\rho_f} \right)_{\text{prop}} \left( \frac{\rho_f}{\rho_o} \right)_{\text{sim}} \right)^{1/2}$$

Because the trichloroethylene emulsified, water was used as a simulant for both propellants with a dye in the fuel. Chemical analyses were then made to measure mixture ratio in each stream tube.

(U) Circumferential distribution is found to be easily achieved with the radial flow coaxial injector and minor nonuniformities do not severely affect either the performance or wall thermal environment. Prior to hot firing, each injector was water flowed to insure basic circumferential uniformity. However, the longitudinal distribution of both mass and mixture ratio is found to be of primary importance to both performance and thermal environment. The collector used has tubes spaced  $5^\circ$  in the range from  $30^\circ$  to  $90^\circ$  from the centerline. This provides for a detailed measurement of the gradients through the resulting spray fan.

(U) A stream tube analysis can be used to determine the combustion efficiency of any injector design from the cold flow data. Several assumptions are implicit in the case of cold flow data to predict hot firing results. These are:

- no reaction effects on mixing
- no propellant vaporization effects on mixing
- no secondary mixing downstream

(U) In addition to these, if the ratio of specific heats variation is small for wide mixture ratio variation, the cold flow-hot firing correlation is quite simple. Each collector tube is taken as a stream tube having mass,  $\dot{w}_i$ , and mixture ratio,  $r_i$ . The mass in each tube is normalized with respect to the total mass sample collected,  $\dot{w}_i/\dot{w}_t$ . The tube mixture ratio can be equated to a  $C_i^*$  for that tubes. The total predicted  $C^*$  is the sum of the predicted  $C^*$ 's from each tube,  $\dot{w}_i/\dot{w}_t C_i^*$ .

**CONFIDENTIAL**

$$C^* = \sum_i \frac{\dot{\omega}_i}{\dot{\omega}_t} C_i^*$$

The predicted combustion efficiency is the ratio of the predicted  $C^*$  and the theoretical equilibrium  $C^*$  for the nominal injector mixture ratio.

$$\eta_{C^*} = C^*/C^*_{\text{theo}}$$

(C) The oxidizer elements were cold flow tested to determine the predicted combustion efficiency and expected wall environment. The mass and mixture ratio distribution for these elements, simulating a MR of 0.92, are shown in Figure 27. Using the stream tube analysis, a predicted combustion efficiency of 89.5% was determined. Actual hot firing results show a  $C^*$  efficiency of 95.5%. Additionally, the hot firing results showed that the mixture ratio adjacent to the thrust chamber wall was fuel-rich, whereas the cold flow data predicted an oxidizer-rich environment.

(U) It would appear that the reaction nature of the propellants strongly influence the results. The slotted type injector results in a fuel-oxidizer interlock system where the highly volatile fuel is confined within the initial reacting zone.

#### 4.2 EXPERIMENTAL FACILITY AND PROCEDURES

(U) The experimental facility used for testing of the  $N_2O_4/N_2H_4$  injector was the High Energy Propellant Test Stand (HEPTS) located on the northern boundary of TRW Systems Capistrano Test Site. The Capistrano Test Site (CTS) is approximately 75 miles south of the main TRW Systems complex in Redondo Beach.

(U) The High Energy Propellant Test Stand (HEPTS) is a multi-position test complex comprising a control center and two major test modules (A and B, each fitted with tank bays and two vertical open-air firing positions), plus two low-thrust altitude test positions and a complete propulsion system altitude test cell. The HEPTS A-1 cell, which was utilized for this program, contains a position for firing  $N_2O_4$ -oxidized propellants in engines rated to 15,000  $lb_f$  thrust. The HEPTS A-1 cell propellant supply is two 400-gallon, 750 psig working pressure run tanks (one each for fuel and

**CONFIDENTIAL**



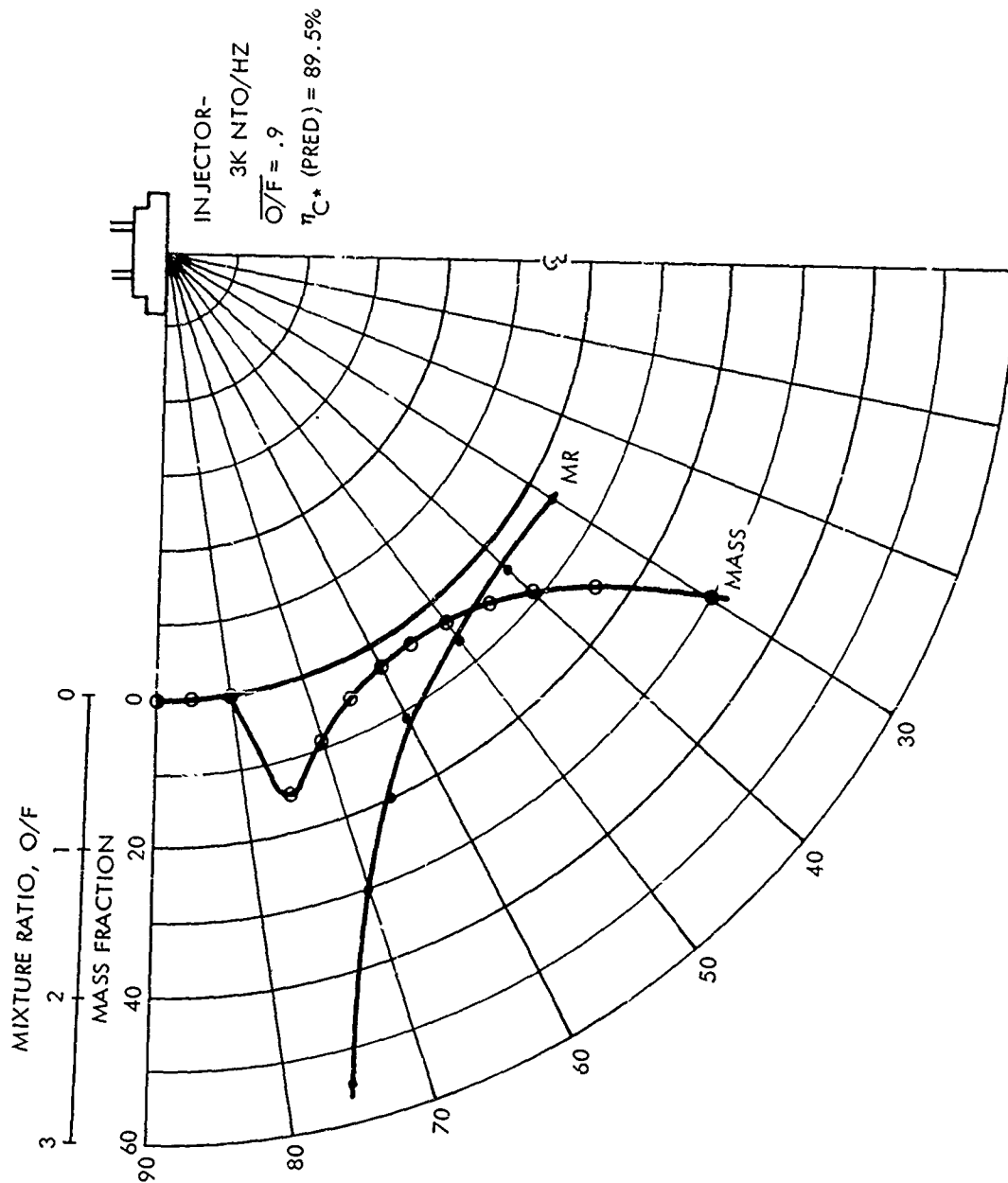


Figure 27. Longitudinal Mass And Mixture Ratio Distribution Patternation Results (U)

UNCLASSIFIED

(U) oxidizer) with 1-1/2 inch diameter lines. A nitrogen cascade system pressurizes the propellant tankage and supplies engine purges. Figure 28 illustrates the general arrangement of the HEPTS A-module with the  $N_2O_4/N_2H_4$  engine installed. Figure 29 is a schematic of the feed system.

(U) Engine test data are transmitted via twin conductor-shielded cables from the test position to the HEPTS Control Center. An SDS 925 (and/or SDS 930) computer in the Main Control Center is programmed for post-test computation of most of the important rocket engine performance parameters. Input is prerecorded tape from the digital tape recorders. It also provides engineering units reduction of parameter data recorded on the digital tape. Primary output devices are a 120-character, 10 line-per-second printer, and an 8-channel digital-to-analog converter.

#### 4.2.1 Thrust Measurement

(U) The thrust measurement stand mounted in the HEPTS A-1 cell is a double A-frame configuration bolted directly to the stand structure. (See Figure 28). The engine bolts to a yoke which transmits the force through an Ormond flexure to a dual bridge load cell (measurement load cell) firmly fixed to the stand structure. Axial location of the yoke is maintained by two flexures at 90 degrees to one another. Original alignment of the yoke is accomplished by sighting with a transit. Remote calibration is achieved using an electric motor and reduction gear arrangement with a standard load cell mounted atop the thrust stand. The gear box converts the rotary motion of the motor into translational motion of a shaft which presses down on the standard cell putting it in compression. The plate upon which the gear box is mounted floats freely above the standard cell supported on three tie rods from the main thrust yoke. As force is applied to the calibration cell, tension is placed on the tie rods which draw up on the thrust yoke, placing the measurement cell in compression equal to that on the standard cell. Calibration force levels are set by reading the standard cell output on a digital voltmeter. This calibration method has demonstrated itself to be quick, reliable, and trouble-free, allowing actual force calibrations of the thrust system with the engine installed immediately prior to testing. This thrust stand and calibrator have been tested extensively for accuracy and repeatability. Numerous calibrations were run during which the thrust stand demonstrated very low nonlinearity (approximately 0.1 percent) and

UNCLASSIFIED

UNCLASSIFIED

100-1-69-231  
100-1-69-231

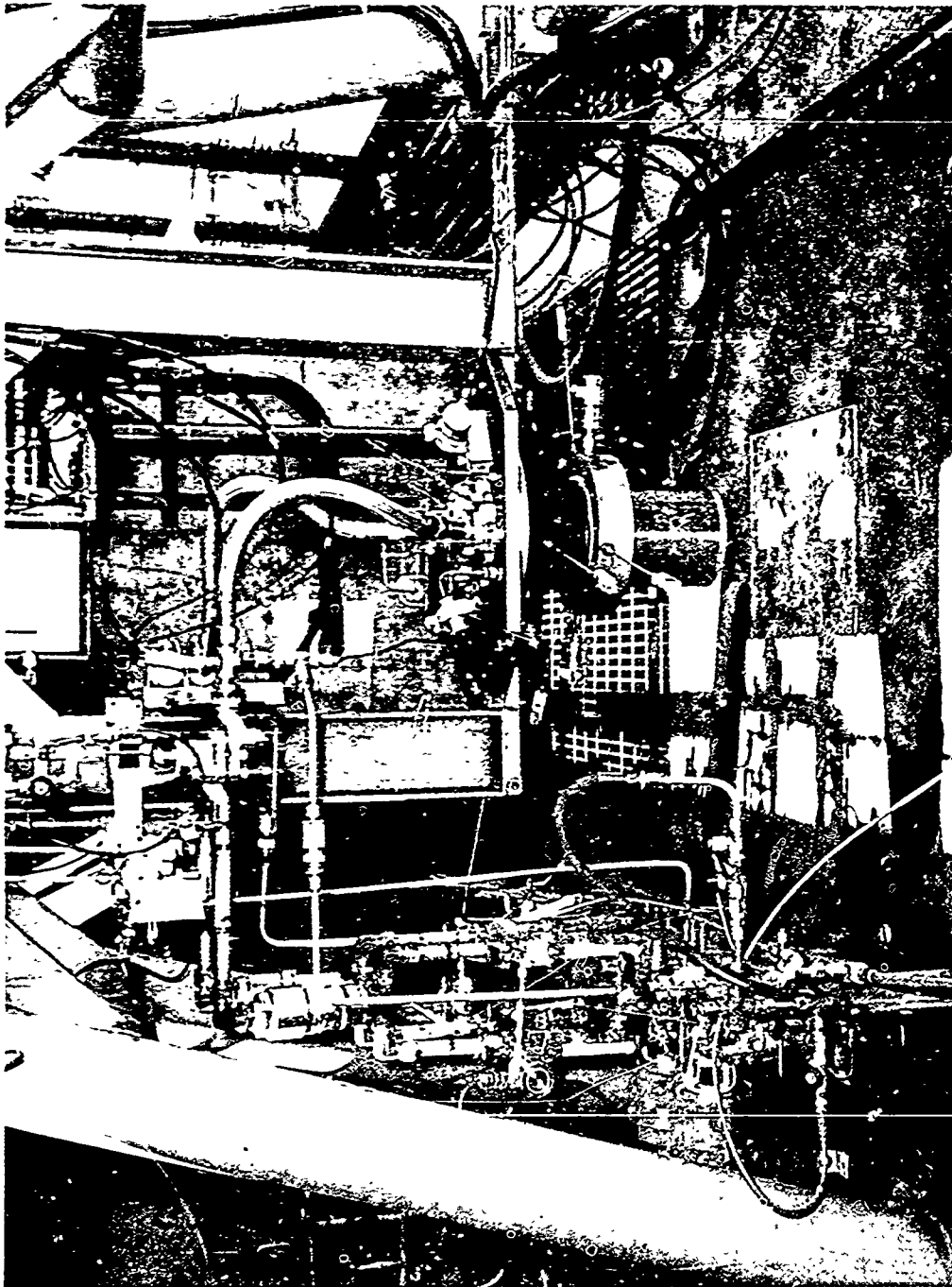


Figure 28. 3K  $N_2O_4/N_2H_4$  Engine Installation In Test Stand (U)

UNCLASSIFIED

UNCLASSIFIED

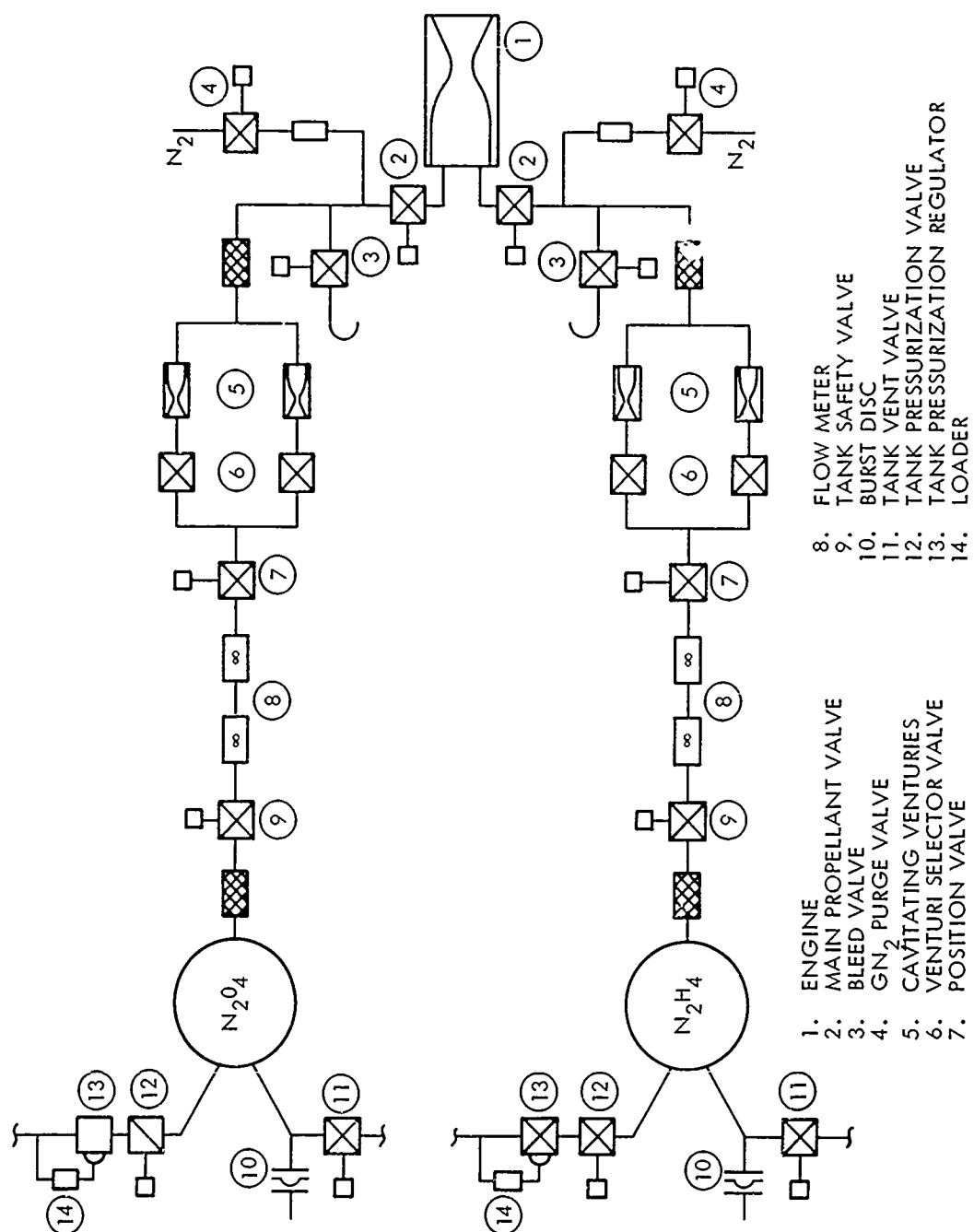


Figure 29. Schematic Of Test Stand Feed System (U)

UNCLASSIFIED

(U) hysteresis (approximately 0.1 percent). Repeatability was excellent. As a final check, an accurately known force was placed against the thrust yoke, simulating a firing. This force was reported by the system with an accuracy of better than 0.1 percent at the recorder.

#### 4.2.2 Flow Measurement

(U) Flow rate measurement of both propellants was achieved with Fischer-Porter turbine type flowmeters (10C1510A). The reliability of these meters has been such that one pair in each propellant line was used for the entire program with no problems. The calibration used up to that time was satisfactory with actual propellants. The flow calibration facility used nitrogen tetroxide and hydrazine.

(U) The flowmeter calibration facility at CTS is a closed loop system, incorporating cavitating venturis downstream of the flowmeters to prevent any effect on flow rate of receiver tank pressure rise. The system includes a 400-gallon run tank; a 300-gallon catch tank; an electronic counter for determining flowmeter revolutions; and a load cell and digital voltmeter for determining the weight of propellant transferred into the receiver tank. This weight system is dead weight calibrated prior to each flowmeter series. Error analysis of this system has indicated accuracy in determination of meter constants on the order of 0.25 percent.

#### 4.2.3 Pressure Measurement

(U) All pressure transducers used on the program were Taber-Teledyne strain gage transducers with the exception of three Photocon Model 352A transducers to measure high frequency chamber pressure fluctuations. These transducers were dead weight calibrated on a regular three-month basis or more frequently if there is evidence of erratic operation.

#### 4.2.4 Injector Performance Data Reduction

(U) All raw performance data are recorded on digital tape and reduced by means of the Capistrano Test Site SDS 925 digital computer on a run-to-run basis. The test firings are characterized by two performance parameters: delivered specific impulse ( $I_{sp}$ ) and characteristic exhaust velocity ( $C^*$ ). The characteristic exhaust velocity is computed by:

# UNCLASSIFIED

$$C^* = \frac{P_o A_T g_o}{\dot{w}_T}$$

$P_o$  = nozzle stagnation pressure, psia

$A_T$  = nozzle throat area, in<sup>2</sup>

$g_o$  = gravitational constant, 32.174 ft/sec<sup>2</sup>

$\dot{w}_T$  = total propellant weight flow, lb/sec

- (a) Each of the parameters within the  $C^*$  equation is computed as follows. The nozzle stagnation pressure ( $P_o$ ) is computed from measured nozzle entrance chamber static pressure ( $P_{CD}$ ) by  $P_o/P_{CD} = 1.009$ . (The  $P_o/P_{CD}$  ratio is determined from classical gas dynamic relationships for total to static pressure ratio as a function of contraction ratio and gas specific heat ratio.) The nozzle static pressure ( $P_{CD}$ ) is computed from the average of two measurements. The injection head end static chamber pressure,  $P_{CH}$ , is also recorded to empirically define the  $P_{CD}/P_{CH}$  ratio to permit  $C^*$  determination in the ablative thrust chamber test where  $P_{CD}$  is not directly measured.
- (b) The propellant flow rates are computed from the average of a pair of turbine flowmeters. The actual flow rate is computed from the frequency output of the meter, the calibration factor, and the propellant densities based on measured propellant temperatures.
- (c) The nozzle throat area is computed from the average of three throat diameter measurements taken prior to each test.
- (d) The combustion efficiency ( $\eta_{C^*}$ ) is determined by dividing the computed  $C^*$  by the theoretical equilibrium characteristic exhaust velocity at the appropriate run nozzle stagnation pressure and oxidizer-to-fuel mixture ratio. The variation of the theoretical equilibrium  $C^*$  with nozzle stagnation pressure and mixture ratio is provided as a tabular input to the data reduction program.
- (e) The engine specific impulse ( $I_{sp}$ ) was computed on the basis of the measured thrust and total propellant weight flow.

$$I_{sp} = \frac{F, \text{ measured thrust, lb}}{\dot{w}_T, \text{ measured total flow rate, lb/sec}}$$

# UNCLASSIFIED

UNCLASSIFIED

AFRPL-TR-69-231

Page 59

(U) The measured thrust is determined from the load cell output and the pre-run calibration. The measured specific impulse data were also corrected to vacuum conditions by adding to the measured thrust a correction equal to the product of the nozzle exit area times the ambient pressure.

(U) All parameters affecting either the hydraulic or the combustion performance of the injector were measured redundantly to insure the validity of all measurements. The redundantly measured parameters were: oxidizer injection pressure, fuel injection pressure, head end chamber pressure, downstream chamber pressure, oxidizer flow rate, fuel flow rate, oxidizer temperature, and fuel temperature.

#### 4.3 INJECTOR CHARACTERIZATION TESTS

(U) Phase II of the  $N_2O_4/N_2H_4$  Injector Program, Injector Development and Demonstration, initially consisted of two tasks. Task 1 entailed development of the injector for mixture ratio flexibility, stability, performance and compatibility using uncooled thrust chamber hardware. Three injector element configurations were evaluated for comparison with program goals in Task 1a. The selected injector configuration was then characterized fully during Task 1b. The Task 2 effort evaluated the basic compatibility of the selected injector configuration with ablative thrust chambers through a long duration firing followed by hot restart. The Task 2 results are discussed subsequently in Section 4.3.3.

(U) The engine assembly used for the injector characterization tests consisted of the basic injector as described in section 3.2 and the uncooled thrust chamber described in 3.4. Figure 28 is a photograph of the engine installed in the HEPTS-A1 position prior to the first test (HA1-284). The first phase of testing, the injector element screening tests, (HA1-284 through HA1-326) was conducted using a chamber cylindrical section without pulse gun ports and a copper nozzle without thermal instrumentation. All subsequent testing was conducted using the fully instrumented thrust chamber assembly. Figure 30 is the instrumentation schematic for the uncooled engine assembly showing relative position of the instrumentation.

##### 4.3.1 Task 1a - Injector Element Screening Tests

(U) The primary objective of this task was to evaluate each of three injector element configurations and to select the one which most closely achieved

UNCLASSIFIED

UNCLASSIFIED

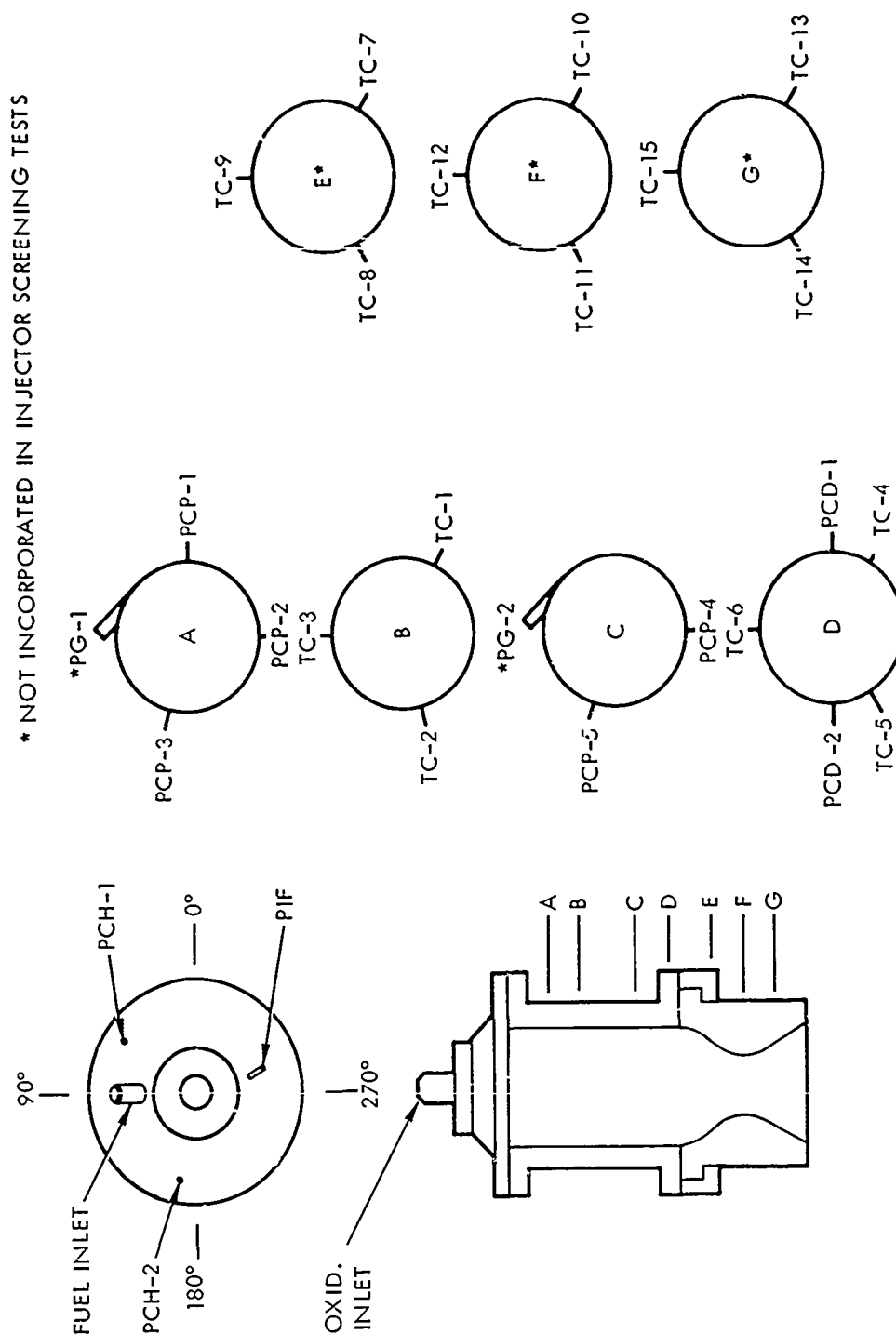


Figure 30. Instrumentation Schematic (U)

UNCLASSIFIED



(U) the program goals. As discussed previously, the three injector element configurations were:

- Configuration 1 - Primary oxidizer slots
- Configuration 2 - Primary oxidizer slots with secondary oxidizer orifices
- Configuration 3 - Primary and secondary oxidizer slots with a secondary fuel spray provided by a swirl injector in the pintle tip

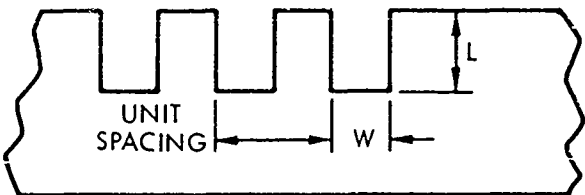
For each configuration shown above, variations in geometry were also tested. For configuration 1, three variations in the number of slots were tested. Configuration 1 included 36, 48, and 72 slot versions. Configuration 2 orifice rings all utilized 36 primary and 36 secondary slots with 15 percent of the oxidizer flow through the secondary slots. Configuration 3 used an orifice ring with 36 primary and 36 secondary slots and provided 17 percent of the fuel flow injected as a conical spray through the pintle tip. Figure 31 presents the oxidizer orifice dimensions for all elements tested.

(C) A total of 43 tests were conducted during the screening phase of Task 1. Each injector element was tested at three mixture ratios covering the range 0.95 to 1.40. Eighteen tests were conducted on configuration 1, 20 tests on Configuration 2 and five tests on Configuration 3. Table 5 is a tabulation of the 45 tests performed during Task 1a. All performance values quoted in this table are "as measured" (see Section 4.2.4). The test series on each oxidizer orifice ring was conducted at a fixed oxidizer flow rate (fixed oxidizer pressure drop) with the fuel flow rate varied to accommodate the desired mixture ratio changes, which in turn resulted in variations in total propellant flow rate (and chamber pressure). As the fuel injection pressure drop could also be varied at a constant flow rate by changing the shim thickness, the performance influences of mixture ratio, injection pressure drop, and pressure drop ratio could be rapidly appraised.

(C) Of the 18 tests conducted on the configuration 1 orifice ring, eleven were with the 36 slot ring, 3 with 48 slot ring and 4 with 72 slot ring. The characteristic velocity efficiency ( $\eta_{C*}$ ) varied from .788 to .892. The initial tests with the 36 slot ring resulted in low performance. The oxidizer pressure drop was low. It was anticipated so the ring was modified to give a higher oxidizer pressure drop ( $\Delta P_{IO}$ ). The performance was increased about 5 percent for the same ratio of oxidizer to fuel pressure drop ( $\Delta P_{IO}/\Delta P_{IF}$ ).

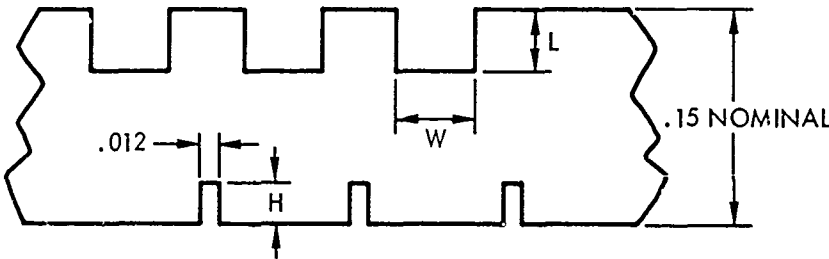
**CONFIDENTIAL**

PRIMARY ORIFICES, CONFIGURATION 1



	NUMBER OF SLOTS	NOMINAL PRESSURE DROP, PSI	PERCENT OPEN	RING DIAMETER, IN.	UNIT SPACING, IN.	W, IN.	L, IN.
1-A	36	90	35	1.50	.131	.052	.065
1-B	48	100	35	1.50	.098	.040	.055
1-C	72	90	35	1.50	.065	.025	.059
1-D	36	130	35	1.50	.131	.052	.056

36 PRIMARY AND 36 SECONDARY ORIFICES,  
CONFIGURATION 2



	NOMINAL PRESSURE DROP, PSI	PERCENT OPEN	PERCENT SECONDARY FLOW	RING DIAMETER, IN.	W, IN.	L, IN.	H, IN.
2-A	90	35	15	1.50	.052	.056	.042
2-B	150	35	15	1.50	.052	.040	.031
2-C	115	35	17	1.50	.052	.047	.042
2-D	175	35	15	1.50	.052	.037	.024
2-E	150	40	15	1.50	.058	.036	.031
2-F	150	35	15	1.40	.052	.040	.031
2-G	150	25	15	1.50	.035	.059	.031
2-H	180	25	15	1.50	.037	.052	.024
2-I	150	25	15	1.60	.037	.057	.031

NOTE: PERCENT OPEN IS THE RATIO OF SLOT WIDTH TO UNIT SPACING

Figure 31. Oxidizer Orifice Ring Configurations (U)

**CONFIDENTIAL**  
(This page is unclassified)

CONFIDENTIAL

Table 2. Task 1a Injector Screening Test Summary (U)

Date	Run No.	Injector Configuration	O/F	$\dot{W}_T$	$\Delta P_{IO}$	$\Delta P_{IF}$	$P_o$	$F_{(meas)}$	$C_{PC}^*$ (meas)	$t_C^*$	Remarks
6-21-68	HAL-284	1A	1.182	9.75	86	70	249	1912	4745	.823	Test Aborted - Loose Ox Ring.  CONFIDENTIAL
6-21	-285	1A	1.375	10.27	107	65	260	2004	4728	.820	
6-24	-286	1A	0.953	10.09	75	65	268	2090	4905	.841	
6-24	-287	2A	1.201	10.25	93	66	262	2067	4736	.821	
6-24	-288	2A	1.397	10.42	108	65	264	2074	4675	.811	
6-24	-289	2A	0.963	10.13	76	64	270	2123	4930	.845	
6-27	-290	2C	1.195	10.29	111	73	297	2318	5345	.928	
6-27	-291	2C	---	---	---	---	---	---	---	---	
6-27	-292	2C	1.396	10.47	138	72	308	2404	5433	.943	
7-1	-293	2C	0.966	10.21	92	58	287	2231	5210	.894	
7-2	-294	2C	1.228	10.19	109	60	291	2224	5288	.907	
7-2	-295	2C	1.409	10.42	129	57	296	2314	5263	.915	
7-2	-296	2C	0.958	10.14	92	80	289	2272	5283	.906	
7-2	-297	1B	1.209	10.27	104	75	255	1978	4602	.800	
7-2	-298	1B	1.422	10.40	124	70	257	1964	4583	.814	
7-2	-299	1B	0.959	10.17	82	90	258	2000	4704	.807	
7-8	-300	2C	1.440	10.29	134	69	280	2148	5046	.896	
7-8	-301	2C	1.414	10.33	130	66	301	2327	5396	.938	

CONFIDENTIAL

**CONFIDENTIAL**

Table 2. Task 1a Injector Screening Test Summary (U)

Date	Run No.	Injector Configuration	O/F	$\dot{W}_T$	$\Delta P_{10}$	$\Delta P_{IF}$	$P_o$	$F_{(meas)}$	$C^*_{PC (meas)}$	$r^*_C$	Remarks
7-8	IA1-302	2C	1.414	10.34	138	89	304	2351	5448	.946	CONFIDENTIAL
7-8	-303	2C	1.414	10.36	138	122	299	2328	5350	.930	
7-9	-304	1C	1.407	10.22	110	88	259	1965	4686	.815	
7-9	-305	1C	1.191	10.07	90	100	251	1903	4605	.788	
7-9	-306	1C	0.948	10.06	70	98	255	1947	4692	.802	
7-9	-307	1C	1.383	10.94	136	97	278	2126	4688	.812	
7-18	-308	1D	1.195	10.12	122	95	278	2175	5073	.870	
7-18	-309	1D	1.369	9.50	125	73	265	2064	5139	.892	
7-18	-310	1D	0.978	11.10	128	142	302	2421	5017	.858	
7-18	-311	1D	1.193	10.13	128	166	270	2120	4910	.841	
7-19	-312	1D	1.204	10.09	131	142	270	2105	4927	.844	
7-19	-313	1D	1.198	10.12	134	120	273	2120	4967	.850	
7-19	-314	1D	1.191	10.14	129	91	278	2160	5057	.865	
7-19	-315	1A	1.212	10.14	106	116	271	2094	4918	.843	

**CONFIDENTIAL**

**CONFIDENTIAL**

Table 2. Task 1a Injector Screening Test Summary (U)

Date	Run No.	Injector Configuration	O/F	$\dot{W}_T$	$\Delta P_{IO}$	$\Delta P_{IF}$	$P_o$	$F_{(meas)}$	$C^*_{PC} (meas)$	$r_C^*$	Remarks
7-19	316	2B	1.205	10.18	149	90	304	2356	5499	.940	CONFIDENTIAL
7-19	317	2B	1.438	9.43	149	66	281	2159	5490	.958	
7-19	318	2B	0.958	11.22	149	154	316	2508	5782	.885	
7-19	319	2B	1.214	10.17	153	111	301	2354	5459	.932	
7-22	320	2B	1.215	10.08	151	90	305	2335	5574	.956	
7-22	321	2B	1.208	10.14	153	67	306	2371	5563	.955	
7-22	322	3	1.214	10.09	146	64	302	2340	5508	.944	
7-22	323	3	---	---	---	---	---	---	---	---	
7-22	324	3	---	---	---	---	---	---	---	---	
7-23	325	3	1.407	9.44	106	55	276	2087	5362	.932	
7-23	326	3	0.958	11.29	119	143	330	2617	5369	.918	

Low  $P_C$  Shutdown  
Test Aborted

**CONFIDENTIAL**

**CONFIDENTIAL**

(U) During the initial tests, a 304 stainless steel pintle tip was used. Post test inspection of the pintle tip revealed the tip was warping, allowing leakage between the pintle and the orifice ring. Additional stainless steel pintle tips were fabricated but post test inspection revealed some pintle tip erosion in addition to the warping. In order to eliminate the pintle tip erosion, materials with higher thermal conductivity were investigated. Both nickel 200 and a columbium alloy C-103 pintle were fabricated and subsequently tested. The columbium tip was aluminide coated for oxidation protection at elevated temperatures. Both the nickel and columbium pintle tips individually eliminated the problems of erosion and warping.

(U) An ablative face plate liner was designed and fabricated when it was determined that the injector face plate was heating to the point where it was distorting, causing a shift in the fuel pressure drop during the test. The ablative liner was fabricated from MX2625 random oriented silica phenolic material. Use of the ablative liner eliminated the faceplate heating problem and the resultant  $\Delta P_{IF}$  shift. Because of the addition of the ablative liner for the faceplate, it was necessary to increase the length of the outer pintle body to extend beyond the ablative liner. Figure 32 shows a comparison of the initial and final (lengthened) outer pintle body.

(C) The first three tests with the configuration 2 orifice ring resulted in  $C^*$  efficiencies of 0.811 to 0.845. The oxidizer pressure drop was lower than expected for this ring. The ring was modified to increase the oxidizer pressure drop and the range of performance subsequently increased to 0.894 to 0.943.

(C) Five tests, of which 2 yielded no data, were conducted on Configuration 3. The performance of configuration 3 ranged from a  $C^*$  efficiency of 0.918 to 0.944. Although the performance was only slightly lower than configuration 2, the combustion roughness was greater.

**CONFIDENTIAL**

(C) The first of the five configuration 3 tests (HA1-322) were at a 1.2 mixture ratio and were satisfactory. The next three tests were targeted for a 1.4 mixture ratio, however only the third test achieved steady state operation. The first test (HA1-323) at 1.4 mixture ratio was aborted by the low chamber pressure safety circuit due to the excessively long start transient with the lower fuel flow rate and larger fuel manifold priming volume. The following tests (HA1-324) was aborted at ignition by rupture of the flexible fuel feed line. The propellant line, which had been hydrostatically proof tested to 1500 psig, ruptured as a result of an apparent detonation

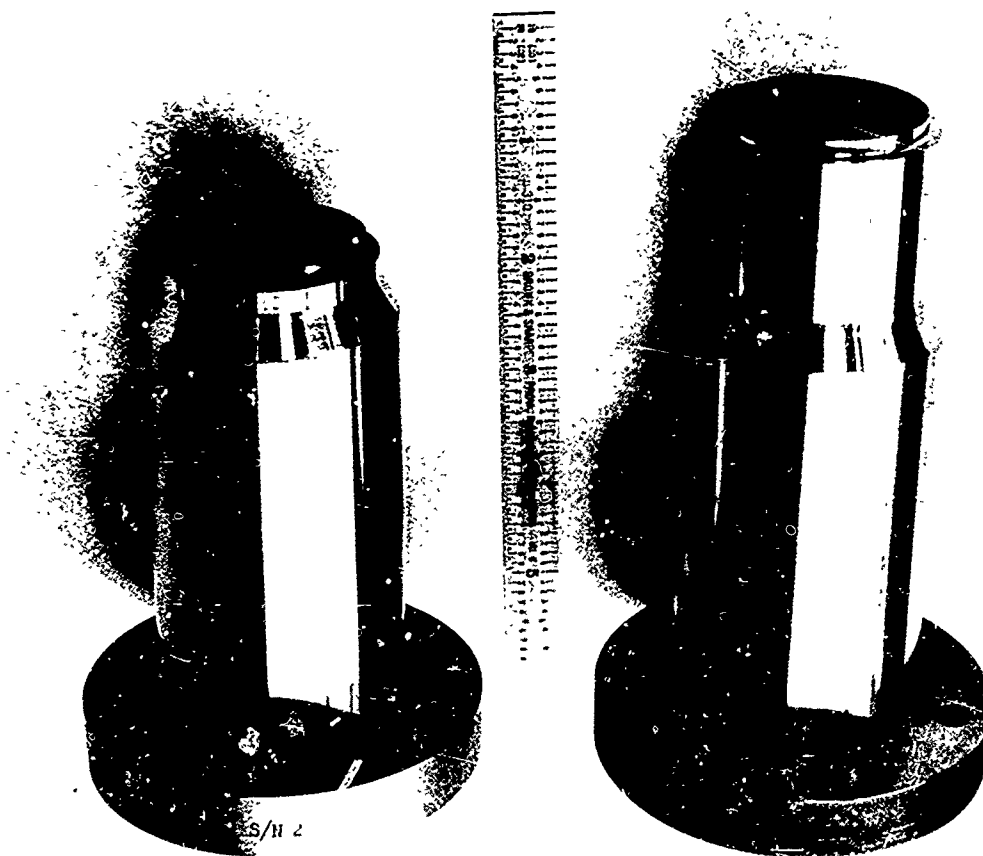


Figure 32. Comparison Of Initial And Lengthened Injector Outer Pintle Bodies (U)

**CONFIDENTIAL**

(C) in the injector fuel manifold at ignition. The detonation was probably due to either residual contamination from the previous test or oxidizer vapors migrating into the manifold from the oxidizer lead flow. The injector housing flange was slightly deformed under the fuel inlet tube. However, the injector was still operable with all sealing integrity maintained. The final two swirl injector tests (HA1-325 and -326) were satisfactorily conducted at mixture ratios of 1.4 and 0.95 respectively.

(U) On the basis of the 43 test firings during the injector screening phase, the configuration 2 injector was selected as the configuration which best met the program requirements and was selected to be more fully characterized during Task 1b. In addition to performance considerations, the configuration 2 injector was preferable on an overall operability basis.

#### 4.3.2 Task 1b - Selected Injector Element Characterization Tests

(U) The objective of this task was to characterize configuration 2, selected during Task 1a, in terms of the effect of operating parameters on performance, stability, heat rejection and combustion roughness. Eighty-five tests were conducted during this phase of the program (Table 3).

(U) The first two tests conducted (HA1-327 and -328) were intentional duplicates of previous tests except that -328 was a dynamic stability rating test using a pulse gun as the excitation device. Figure 33 presents a view of the engine pre-test HA1-328 prior to installing the loaded pulse gun in the upper tangential port (the lower pulse gun with burst disc installed was used as a plug). A 50 grain charge of Hercules Bullseye powder was used to produce the dynamic disturbance. The real time recorded oscillograph from HA1-328 is presented as Figure 34. The  $\Delta P/P_c$  overpressure was 1.75 and the engine completely recovered within 20 msec. The measured peak-to-peak roughness level relative to each of the three Photocon transducer traces were 32, 35, and 53 psi. The program roughness goal was  $\pm$  5 percent of chamber pressure which corresponds to 30 psi peak-to-peak.

(C) A total of 13 tests during Task 1b were conducted on the orifice ring used during Task 1a. Of the 13 tests, four tests were dynamic stability tests using the pulse gun as the excitation method. The remainder of the

**CONFIDENTIAL**



Table 3. Summary of Configuration 2 Injector Characterization Tests (U)

Date	Run No.	Orifice Confg.	O/F	$\dot{W}_T$	$\dot{W}_{OX}$	$\dot{W}_F$	$\Delta P_{10}$	$\Delta P_{IF}$	$P_0$	$F_{(meas)}$	$C_{PC}$ (meas)	$r_{C_{PC}}^*$	Remarks
7-24-68	HAI-327	2B	1.195	10.15	5.53	4.62	148	125	304	2332	5478	.938	Dynamic Stability Test
7-24	-328	2B	1.197	10.22	5.57	4.65	152	128	305	2347	5472	.938	
8-5	-329	2B	0.921	11.09	5.32	5.77	148	220	326	2572	5440	.925	
8-6	-330	2B	1.098	10.60	5.55	5.05	148	101	320	2532	5623	.960	CONFIDENTIAL
8-6	-331	2B	0.936	11.16	5.40	5.75	146	126	332	2648	5515	.945	
8-6	-332	2B	0.932	11.15	5.38	5.77	140	72	334	2660	5574	.955	
8-6	-333	2D	---	---	---	---	---	---	---	---	---	---	Aborted due to Low $P_c$ device
8-6	-334	2D	---	---	---	---	---	---	---	---	---	---	Aborted due to Low $P_c$ device
8-6	-335	2B	0.945	11.20	5.44	5.76	151	192	327	2584	5371	.921	Dynamic Stability Test
8-6	-336	2B	0.945	11.19	5.44	5.75	149	128	331	2614	5493	.940	
8-7	-337	2B	1.380	9.32	5.41	3.92	137	58	276	2139	5490	.951	
8-7	-338	2B	1.418	9.23	5.41	3.82	155	69	274	2116	5522	.960	Dynamic Stability Test
8-7	-339	2B	1.423	9.23	5.42	3.81	139	69	272	2107	5499	.956	
8-7	-340	2B	1.175	10.02	5.41	4.61	155	100	298	2322	5533	.946	
9-5	-341	2D	1.205	9.96	5.44	4.52	170	96	305	2352	5620	.961	Combustion Gas Sample Test
9-5	-342	2D	1.419	9.20	5.40	3.80	167	67	276	2115	5504	.957	
9-5	-343	2D	1.411	9.20	5.39	3.82	163	69	276	2117	5504	.957	

CONFIDENTIAL

Table 3. Summary of Configuration 2 Injector Characterization Tests (U)

Date	Run No.	Orifice Config.	$\dot{Q}/F$	$\dot{W}_T$	$\dot{W}_{OX}$	$\dot{W}_F$	$\Delta P_{IO}$	$\Delta P_{IF}$	$P_0$	$F_{(meas)}$	$C_{PC}^*$ (meas)	$C_{PC}^*$	Remarks
9-6-68	111-344	2D	0.947	11.08	5.39	5.69	180	156	336	2618	5550	.949	CONFIDENTIAL
9-6	-345	2D	1.117	9.97	5.39	4.58	169	115	303	2343	5552	.949	
9-6	-346	2D	1.172	9.96	5.38	4.59	165	71	302	2343	5540	.947	
9-6	-347	2D	1.170	9.98	5.38	4.60	164	151	280	2165	5140	.880	
9-6	-348	2F	1.186	10.05	5.45	4.60	130	123	266	2050	4847	.828	
9-6	-349	2F	1.357	9.50	5.47	4.03	127	95	265	2005	5102	.883	
9-6	-350	2F	1.192	10.14	5.51	4.52	127	51	295	2286	5327	.912	
9-6	-351	2F	1.185	10.17	5.51	4.65	129	83	286	2198	5136	.878	
9-6	-352	2B	1.190	10.13	5.50	4.63	160	128	304	2342	5489	.939	
9-9	-353	2E	1.166	9.96	5.36	4.60	131	109	289	2235	5351	.915	
9-9	-354	2E	1.444	9.20	5.43	3.76	142	72	270	2075	5426	.946	
9-9	-355	2E	0.940	11.14	5.40	5.74	143	173	314	2448	5200	.892	
9-9	-356	2E	1.157	10.12	5.43	4.69	159	160	286	2196	5130	.880	
9-9	-357	2E	1.166	10.16	5.47	4.69	147	58	303	2355	5505	.941	
9-10	-358	2G	1.211	10.06	5.51	4.55	152	111	307	2370	5609	.960	
9-10	-359	2G	1.188	10.16	5.52	4.65	152	117	310	2401	5617	.961	
9-10	-360	2G	1.470	9.20	5.48	3.72	149	74	275	2099	5500	.962	

CONFIDENTIAL

**CONFIDENTIAL**

AFRPL-TR-69-231

Page 71

Table 3. Summary of Configuration 2 Injector Characterization Tests (U)

Date	Run No.	Orifice Config.	O/F	$\dot{W}_T$	$\dot{W}_{OX}$	$\dot{W}_F$	$\Delta P_{IO}$	$\Delta P_{IF}$	$P_0$	$F_{(meas)}$	$C_{PC}^*$ (meas)	$\eta_{CPC}^*$	Remarks
9-10-68	HAL-361	2G	0.954	11.28	5.50	5.77	148	221	326	2354	5325	.914	<b>CONFIDENTIAL</b>  Dynamic Stability Test Dynamic Stability Test Short L* Chamber Short L* Chamber Short L* Chamber Short L* Chamber Short L* Chamber Acrylic Chamber Test Oxidizer Ring Did Not Seal
9-10	-362	2G	1.200	10.06	5.49	4.57	147	154	305	2357	5582	.955	
9-10	-363	2G	1.199	10.12	5.52	4.60	146	64	306	2372	5552	.950	
9-10	-364	2G	1.408	10.27	6.01	4.26	176	126	311	2419	5578	.968	
9-10	-365	2G	1.342	10.53	6.04	4.50	183	146	322	2494	5618	.971	
9-11	-366	2G	1.211	10.95	6.00	4.95	184	185	337	2593	5601	.959	
9-11	-367	2G	1.228	10.93	6.03	4.91	181	189	337	2587	5610	.961	
9-11	-368	2G	1.394	10.29	5.99	4.30	175	140	314	2386	5554	.963	
9-11	-369	2G	1.210	10.14	5.55	4.59	151	107	303	2306	5445	.932	
9-11	-370	2G	1.489	9.37	5.61	3.77	152	72	274	2053	5327	.933	
9-11	-371	2G	0.970	11.36	5.59	5.77	159	180	319	2457	5117	.875	
9-19	-372	2G	1.201	10.06	5.49	4.57	156	143	286	2192	5207	.891	
9-19	-373	2G	1.203	10.11	5.52	4.59	148	60	293	2271	5308	.908	
9-19	-374	2G	1.198	10.08	5.49	4.59	146	117	300	2322	5447	.932	
9-20	-375	2F	1.196	10.09	5.50	4.60	95	117	258	1945	4670	.797	
9-20	-376	2F	1.426	9.39	5.52	3.87	137	82	265	2004	5134	.893	
9-20	-377	2F	1.181	10.14	5.49	4.65	141	119	268	2040	4834	.826	

**CONFIDENTIAL**

CONFIDENTIAL

Table 3. Summary of Configuration 2 Injector Characterization Tests (U)

Date	Run No.	Orifice Config.	O/F	$\dot{W}_T$	$\dot{W}_{OX}$	$\dot{W}_F$	$\Delta P_{IO}$	$\Delta P_{IF}$	$P_0$	$F_{(meas)}$	$C_{PL}^*$ (meas)	$C_{PC}^*$	Remarks
9-20-68	HA1-378	2F	0.943	11.34	5.50	5.84	144	179	307	2371	4960	.851	CONFIDENTIAL
9-24	-379	2G	0.937	11.24	5.44	5.80	175	146	336	2605	5476	.940	
9-24	-380	2G	0.948	11.26	5.48	5.78	159	145	331	2562	5381	.926	
9-24	-381	2G	0.945	11.25	5.46	5.78	149	99	337	2631	5463	.940	
9-24	-382	2G	0.947	11.26	5.47	5.78	133	54	329	2559	5339	.915	
9-24	-383	2G	0.946	11.20	5.45	5.76	159	143	326	2514	5322	.913	
9-24	-384	2G	1.196	10.02	5.48	4.56	154	92	303	2328	5522	.944	
9-24	-385	2G	1.425	9.29	5.46	3.83	149	65	279	2118	5498	.956	
9-24	-386	2H	1.197	10.05	5.57	4.57	195	109	310	2360	5655	.967	
9-24	-387	2H	1.472	9.23	5.49	3.73	188	72	277	2104	5502	.962	
9-24	-388	2H	1.080	10.53	5.47	5.06	191	129	325	2505	5644	.965	
9-24	-389	2H	0.951	11.25	5.49	5.77	187	168	338	2612	5489	.941	
9-25	-390	2H	1.217	10.07	5.53	4.54	202	172	297	2275	5358	.924	
9-25	-391	2H	1.231	10.02	5.53	4.49	198	174	308	2364	5676	.964	
9-25	-392	2H	---	---	---	---	---	---	---	---	---	---	
9-25	-393	2H	1.234	9.94	5.49	4.45	210	175	306	2339	5639	.967	
9-30	-394	2H	1.267	9.93	5.55	4.38	204	184	304	2332	5592	.961	

Dynamic Stability Test

CONFIDENTIAL

Table 3. Summary of Configuration 2 Injector Characterization Tests (U)

Date	Run No.	Orifice Config.	O/F	$\dot{W}_T$	$\dot{W}_{OX}$	$\dot{W}_F$	$\Delta P_{IO}$	$\Delta P_{IF}$	$P_0$	$F_{(meas)}$	$C_{PC}^*$ (meas)	$'C_{PC}^*$	Remarks
9-30-68	HA1-395	2H	1.255	9.96	5.55	4.42	194	185	303	2328	5544	.952	Dynamic Stability Test
9-30	-396	2H	0.961	11.34	5.56	5.78	204	190	351	2719	5630	.964	Dynamic Stability Test
9-30	-397	2H	0.957	11.36	5.56	5.81	199	198	351	2718	5629	.965	Fuel Venturi Out of Cavitation
9-30	-398	2H	1.708	8.80	5.55	3.25	181	120	254	1907	5259	.945	Fuel Venturi Out of Cavitation
9-30	-399	2H	1.696	8.81	5.54	3.27	186	121	260	1959	5381	.967	Fuel Venturi Out of Cavitation
10-1	-400	2H	1.406	9.55	5.58	3.97	192	164	286	2186	5460	.948	Dynamic Stability Test
10-1	-401	2H	1.401	9.54	5.56	3.97	200	203	282	2145	5391	.935	Dynamic Stability Test
10-1	-402	2H	1.399	9.53	5.56	3.97	203	207	284	2170	5440	.944	Dynamic Stability Test
10-1	-403	2I	1.215	10.10	5.54	4.56	156	99	310	2376	5620	---	No Digital Data
10-1	-404	2I	1.463	9.32	5.54	3.78	---	---	281	2136	5520	---	No Digital Data
10-1	-405	2I	0.951	11.34	5.53	5.81	164	162	341	2645	5485	.941	Dynamic Stability Test
10-1	-406	2I	1.200	10.13	5.53	4.61	159	161	302	2300	5440	.931	Dynamic Stability Test
10-1	-407	2I	1.205	10.16	5.56	4.61	128	72	290	2231	5191	.888	Data Not Valid, Loose Pintle Tip
10-2	-408	2I	1.198	10.14	5.52	4.61	158	99	311	2400	5583	.955	CONFIDENTIAL
10-2	-409	2I	1.460	9.30	5.52	3.78	154	56	280	2190	5473	.956	CONFIDENTIAL
10-2	-410	2I	1.194	10.11	5.50	4.61	154	63	310	2392	5590	.956	CONFIDENTIAL
10-2	-411	2G	1.261	10.05	5.60	4.44	156	105	306	2355	5544	.952	Run Without Cavitating Venturi

**CONFIDENTIAL**

(C) tests on the ring were to obtain performance as a function of both mixture ratio and injection pressure drop ratio ( $\Delta P_{IO}/\Delta P_{IF}$ ). The injector was operated over a mixture ratio range of 0.92 to 1.42 and a  $\Delta P_{IO}/\Delta P_{IF}$  range of 0.77 to 3.11. Characteristic velocity efficiencies varied from 0.92 to 0.96 for these 13 tests.

(C) An oxidizer ring (2-D) was then tested which increased the oxidizer pressure drop to a nominal 170 psi. The geometry of the slots (ratio of total slot width to circumference) was the same for this ring as the 2-B ring. Nine tests (HA1-333, 334 and 341 through 347) covering the mixture ratio range of 0.947 to 1.419 were conducted on this configuration. Two of the tests were aborts due to a malfunction in the low pressure shutdown timing device. The performance of the injector using this orifice ring varied from 0.880 to 0.961. One test (HA1-347) was extremely low in performance compared to the rest of the tests with the ring. The  $C^*$  efficiency for the ring varied from 0.947 to 0.961 for 6 of the 7 tests. The low performance on the one test may have been due to a loosened pintle tip as the test in question was the last in the 2-D ring series.

(U) During this test series, combustion gas samples were taken to verify the chemical environment along the wall. The wall environment was determined by this technique to be fuel-rich, which was also verified photographically in a subsequent test using a Fastax camera viewing through an acrylic plastic chamber section. The sampling ports (located at chamber station D, Figure 30) were connected to one-liter bombs and a vacuum pump with stainless steel lines. The sampling apparatus was evacuated and maintained below 5 torr until the firing when a solenoid valve was actuated upon for the sampling duration. Adjustable throttle valves in each sampling line were previously calibrated to result in a pressure less than one atmosphere in the sample bomb at the end of the preset sampling time period. The sample bombs were then sealed by closing hand valves and removed from the apparatus. The gas samples were analyzed by both infrared spectroscopy and gas chromatography in a controlled temperature chamber maintained at 200°F. The resulting gas composition did not permit determination of an equivalent mixture ratio and the presence of carbon dioxide and carbon

**CONFIDENTIAL**

**CONFIDENTIAL**

AFRPL-TR-69-231

Page 75

monoxide suggested atmospheric contamination (although oxygen was not detected). However, other investigators (for example, reference 5) have determined that a positive molar ratio of hydrogen to nitrogen is all that is necessary to establish the fuel-rich condition of the gases. The measured molar ratio of hydrogen to nitrogen was the order of 0.4 which is clearly a fuel-rich condition. As the intent of the limited gas sampling tests was only to determine if a fuel-rich condition existed, further sampling tests were not made.

(U) Four tests (HA1-348 through -351) were conducted in which the pintle diameter was decreased from 1.50 inch to 1.40 inch. The objective of this series was to determine the effect of the venting distance (distance from oxidizer orifice to impingement) on combustion roughness. There was a noticeable increase in combustion roughness ( $\pm 12$  to  $\pm 25\%$  of chamber pressure) and a decrease in performance by increasing the vent distance.

(C) Subsequently, a series of eight tests (HA1-403 through -410) were run in which the pintle diameter was increased to 1.60 inch, thereby decreasing the vent distance behind impingement. One test, HA1-407, was run with the pintle tip loose which reduced the  $C^*$  efficiency to 0.88 due to leakage between the orifice ring and the pintle tip. Excluding test number HA1-407, the performance for this series varied from 0.931 to 0.956. Combustion roughness decreased to  $\pm 6 \frac{1}{2}\%$  of chamber pressure at  $\Delta P_{IO}/\Delta P_{IF}$  of 1.1.

**CONFIDENTIAL**

**CONFIDENTIAL**

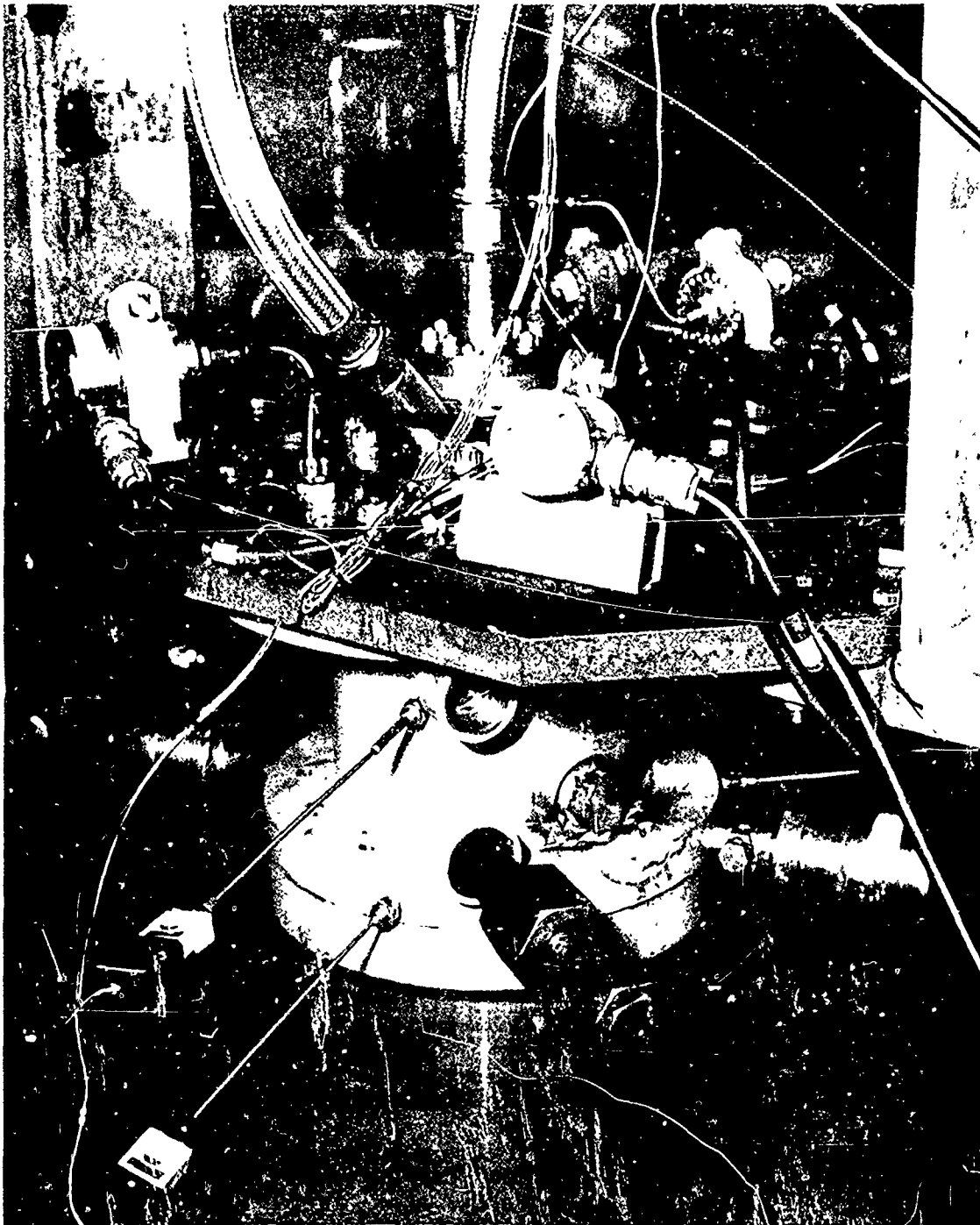


Figure 33. 3K N<sub>2</sub>O<sub>4</sub>/N<sub>2</sub>H<sub>4</sub> Engine Showing Pulse Gun Installation (U)

**CONFIDENTIAL**  
(This page is unclassified)



**CONFIDENTIAL**

AFRPL-IR-69-231  
Page 77

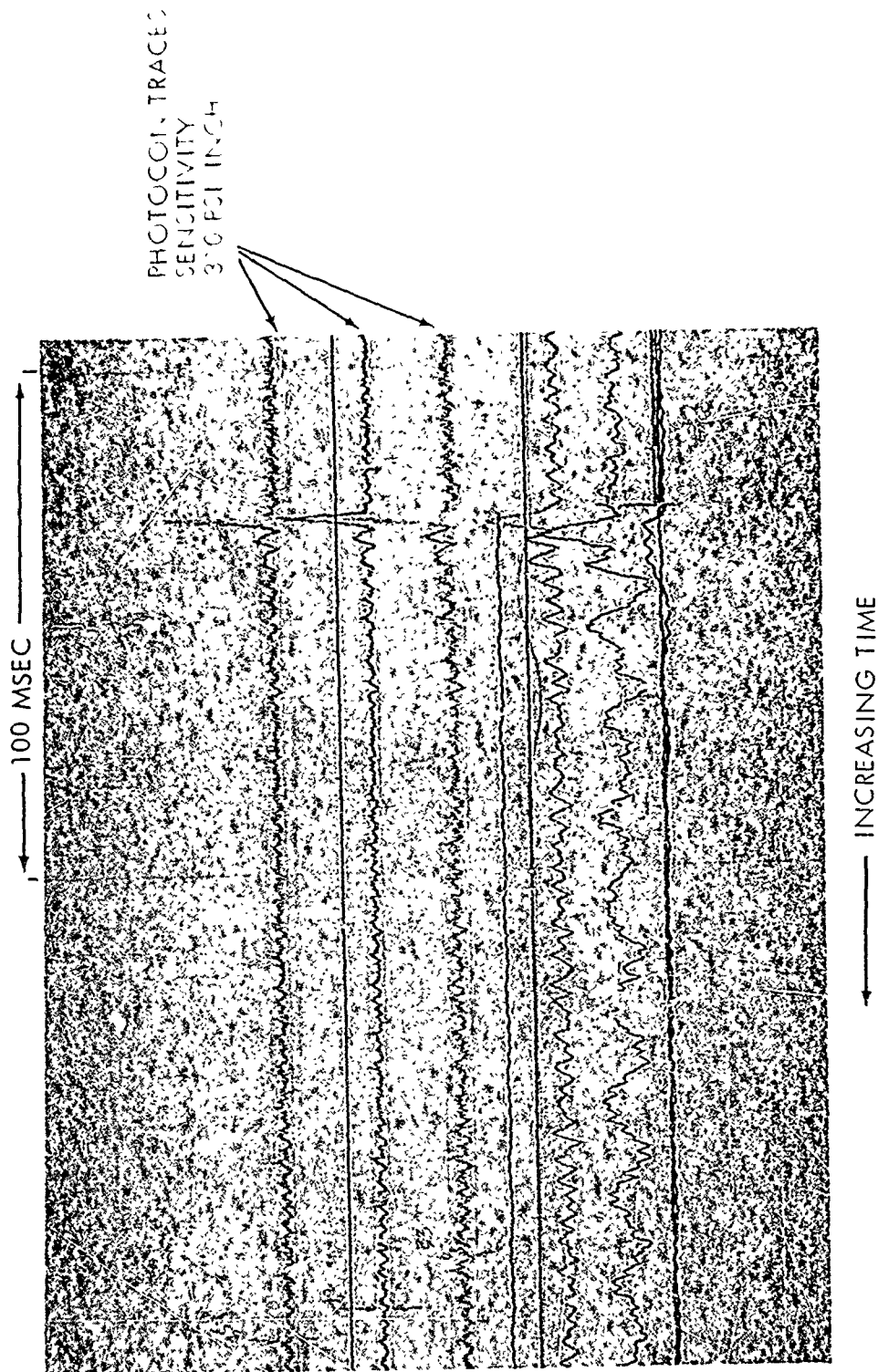


Figure 34. Oscillogram From Initial Dynamic Stability test (HAI-528) (U)

**CONFIDENTIAL**  
(This page is unclassified)

**CONFIDENTIAL**

(C) Another group of tests (HA1-353 through -363) were conducted to evaluate the effect of slot geometry on injector performance. The first five tests (HA1-353 through -357) were performed using the 2-E ring configuration. This oxidizer ring resulted in a nominal oxidizer pressure drop of 150 psi at a flow rate of 5.5 lb/sec of  $N_2/O_4$ . This ring had a slot width to unit width ratio of 0.40 (or 40% open) compared with 0.35 for the 2-B ring which was the baseline configuration. Characteristic velocity efficiency of the 2-E ring varied from 0.89 to 0.94. The next orifice ring tested (2-G) had a slot configuration which was 25% open and an oxidizer pressure drop of 150 psi. The  $C^*$  efficiency of this ring was 0.90 to 0.96 over the range of  $\Delta P_{IO}/\Delta P_{IF}$  of 0.77 to 3.25 and a mixture ratio of 0.95 to 1.40. Figure 35 compares the characteristic velocity efficiency of the three oxidizer orifice ring configurations as a function of  $\Delta P_{IO}/\Delta P_{IF}$  for three slot width to unit width ratios. Since the 25% open configuration yielded approximately 2% higher  $C^*$  efficiency at the lower  $\Delta P_{IO}/\Delta P_{IF}$  ratios and was equivalent at the high end of the range, the majority of the remaining Task 1b tests were conducted on oxidizer orifice configurations which were 25% open.

(C) Five tests were conducted on the 2-G ring with the total flow rate increased to give a nominal oxidizer pressure drop of 180 psi. The performance on the five runs varied only 1%, from 96 to 97 percent of theoretical shifting equilibrium  $C^*$ . The objective of testing at the higher flow rate was to evaluate combustion roughness at the higher oxidizer pressure drop. Combustion roughness ( $\Delta P/P_c$ ) varied from  $\pm 5$  to  $\pm 8$  percent. Tests number HA1-367 and -368 were dynamic stability tests using a 13.5 grain omni-directional bomb inserted in the side of the thrust chamber. The tests were conducted at mixture ratios of 1.2 and 1.4 respectively. The bomb resulted in over pressures of approximately 125 psi from which the engine recovered in 10 msec.

**CONFIDENTIAL**

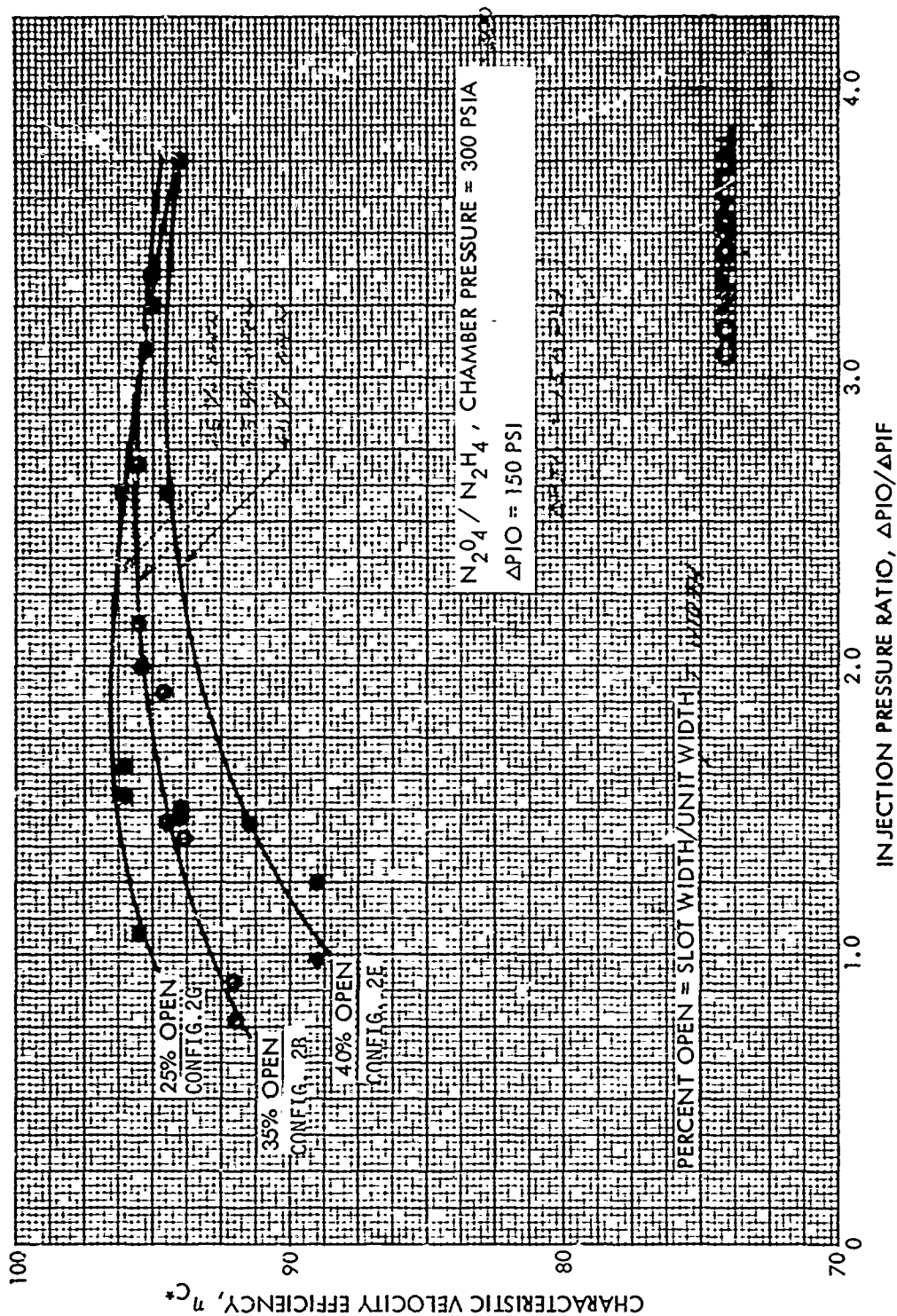


Figure 35. Characteristic Velocity Efficiency Of Configuration 2 Injector Rings  
As Influenced By Slot Geometry (U)

**CONFIDENTIAL**

(C) A series of five tests was conducted on the engine using the 2-G orifice configuration and the thrust chamber characteristic length ( $L^*$ ) reduced to 35 inches. This was accomplished by removing the cylindrical spool section of the thrust chamber assembly and inserting a cylindrical section which was three inches shorter. No attempt was made to optimize the injector for the shortened chamber as only the effect of the shortened chamber on performance was desired. The five tests encompassed the mixture ratio range of 0.97 to 1.47 and the  $\Delta P_{IO}/\Delta P_{IF}$  range of 1.0 to 3.6. The measured characteristic velocity efficiency decreased 3 percent over the longer chamber. Figure 36 compares the measured performance of the injector with both the 50 inch and the 35 inch  $L^*$  chambers.

(U) Following the series with the reduced  $L^*$  chamber, a single test (HA1-374) was conducted in which the ignition and one second of steady state operation were photographed through an acrylic plastic chamber section. A Fastax camera operating at 5000 frames per second was used to photograph the combustion process. Figure 37 is a side view of the thrust chamber assembly looking through the acrylic section. The acrylic section was "frosted" after the test but otherwise was not damaged.

(C) Test numbers HA1-386 through -402 were conducted using the 2-H orifice ring which was 25% open with a nominal oxidizer pressure drop of 200 psi. The  $C^*$  efficiency of this ring varied about 4 percent (0.924 to 0.967) over the mixture ratio range of 0.95 to 1.4 and a  $\Delta P_{IO}/\Delta P_{IF}$  range of 1.1 to 3.4. Combustion roughness for this ring varied from  $\pm 4$  to  $\pm 10$  percent. Of the 17 tests conducted on the 2-H configuration, 3 tests were dynamic stability tests using both bombs and pulse guns as the triggering mechanism. The three stability tests were conducted at mixture ratios of 0.96, 1.2 and 1.4. In each case the engine recovered from the pressure spike within 20 milliseconds.

#### Injector Performance (Characteristic Velocity Efficiency)

(U) The configuration 2 injector, selected from the tests of Task 1a, was subjected to eighty-five tests during Task 1b in addition to the twenty-two tests performed during Task 1a. The injector performance ( $C^*$  efficiency) was evaluated as a function of the oxidizer

**CONFIDENTIAL**

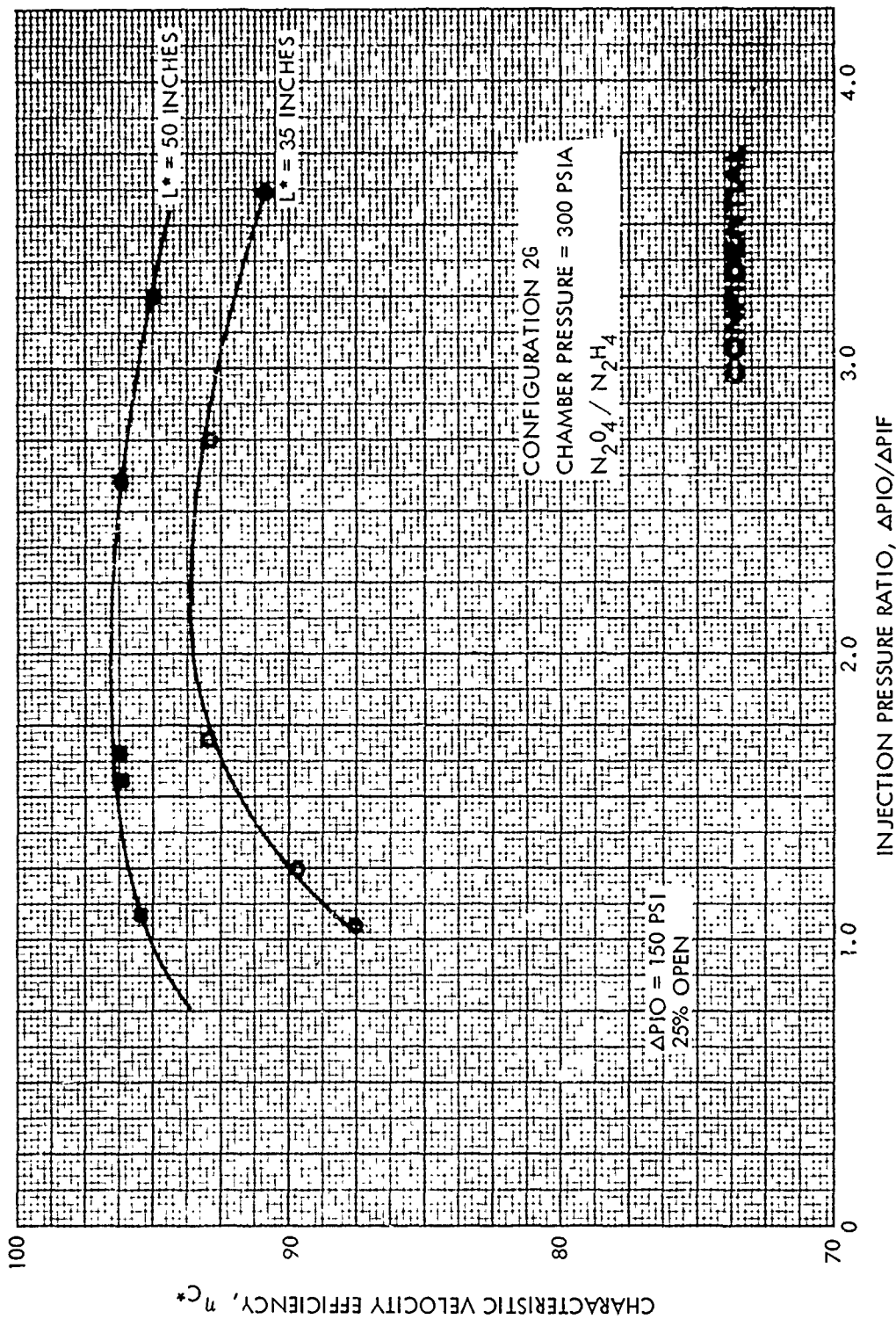


Figure 36. Characteristic Velocity Performance Change With Combustion Chamber Length (U)

**CONFIDENTIAL**

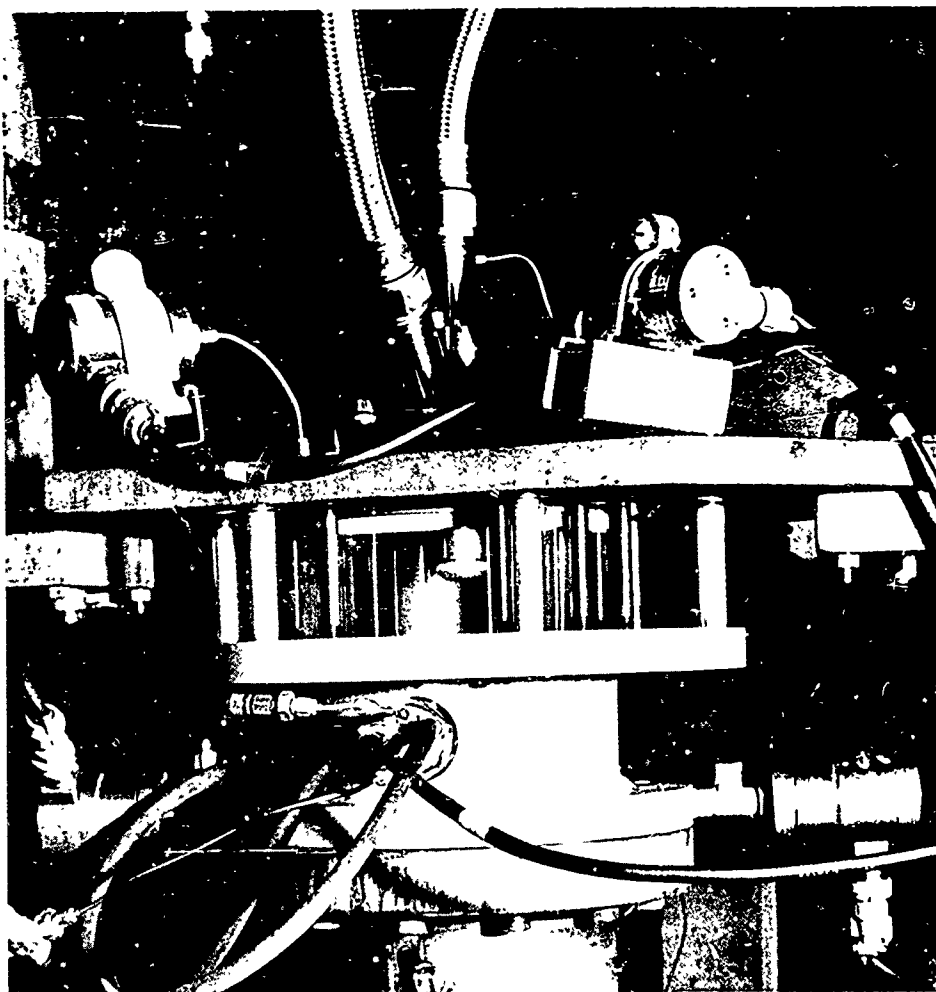


Figure 37. Installation of Acrylic Thrust Chamber Section (U)

**CONFIDENTIAL**  
(this page is unclassified)

(U) pressure drop, distance from orifice to impingement, slot geometry, oxidizer-to-fuel pressure drop ratio and mixture ratio.

(U) The effect of oxidizer injection pressure drop ( $\Delta P_{IO}$ ) on characteristic velocity efficiency is shown in Figure 38, for an orifice ring with 25% open slot geometry and  $\Delta P_{IO}$  of 150 and 200 psi. Both curves show the injector to be quite insensitive to injection pressure drop ratio.

(U) The next figure, Figure 39, also illustrates the relative insensitivity of the injector to wide changes in operating parameters. Measured  $C^*$  efficiency is presented as a function of mixture ratio for oxidizer pressure drops of 150 and 200 psi. This figure also shows that at the higher oxidizer pressure drop, performance is less sensitive to changes in mixture ratio. Figure 40 illustrates the effect of momentum ratio on measured  $C^*$  efficiency for  $\Delta P_{IO}$  of 150 and 200 psi.

(U) Figure 41 presents a comparison of corrected characteristic velocity efficiency computed from chamber pressure and a corresponding  $C^*$  computed from the thrust measurement for the 2-G orifice ring configuration. The excellent agreement is thus a strong verification of overall data consistency. The heat rejection, friction, nozzle throat diameter change, and nozzle discharge coefficient corrections to measured characteristic velocity (defined in section 4.2.4) are defined in Appendix A together with the corresponding factors to derive characteristic velocity from thrust. Table 4 presents the measured and corrected data used in preparing Figure 41. The average correction to measured characteristic velocity efficiency, which is the generally quoted performance parameter in this report, was 0.1 percent.

#### Combustion Noise

(U) One goal of the program was to limit the "combustion roughness" level to  $\pm 5$  percent of steady state chamber pressure. Combustion roughness was defined as the maximum peak-to-peak measured amplitude.

Each test was conducted using three Photocon 352A dynamic pressure transducers located as shown in Figure 30. The oscillograph trace of these three transducers was then measured to determine the combustion roughness.

CONFIDENTIAL

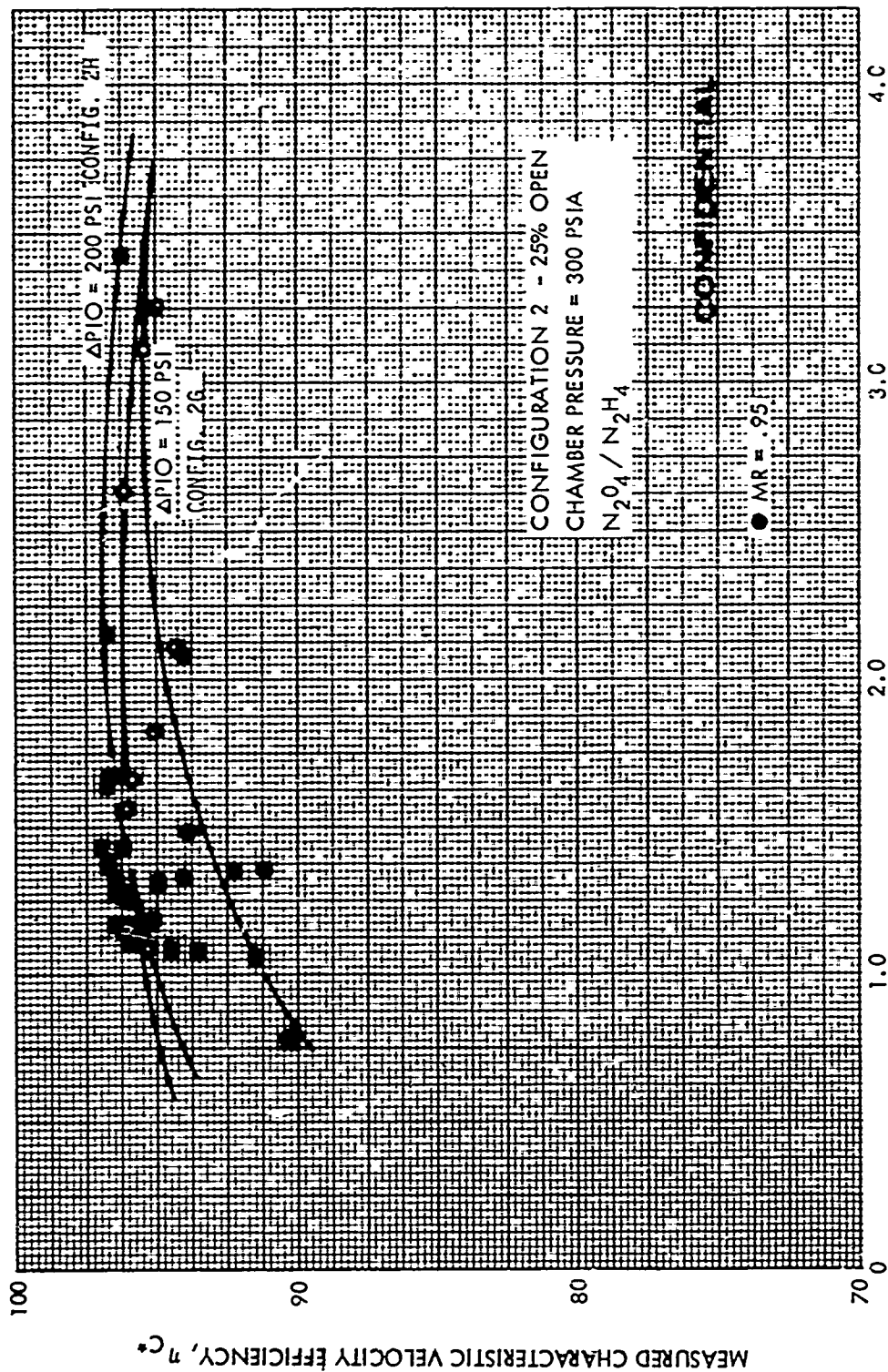


Figure 38. Configuration 2 Injector Performance Correlation With Pressure Drop Ratio (1)

CONFIDENTIAL



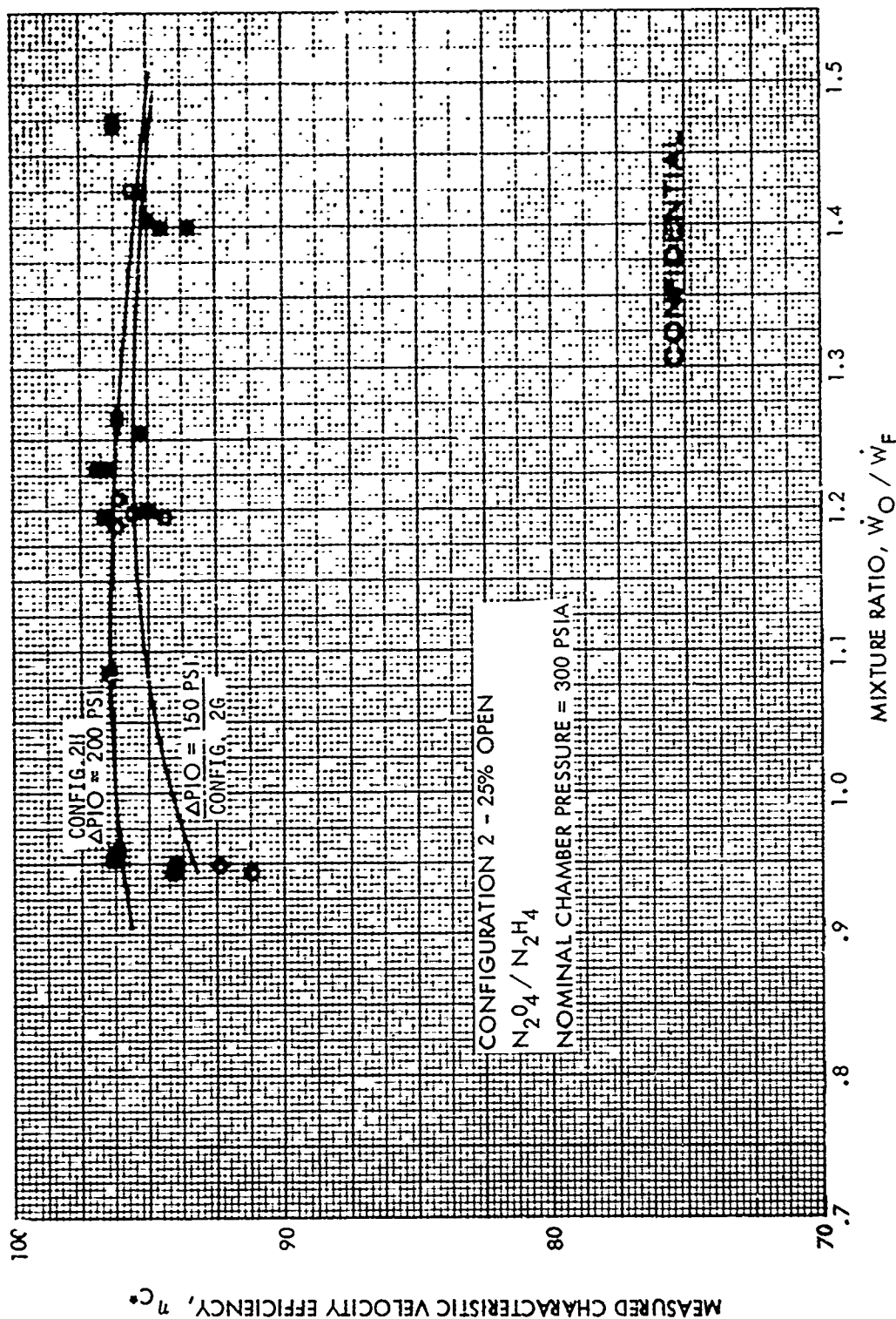


Figure 39. Configuration 2 Injector Performance Correlation With Mixture Ratio (U)

CONFIDENTIAL

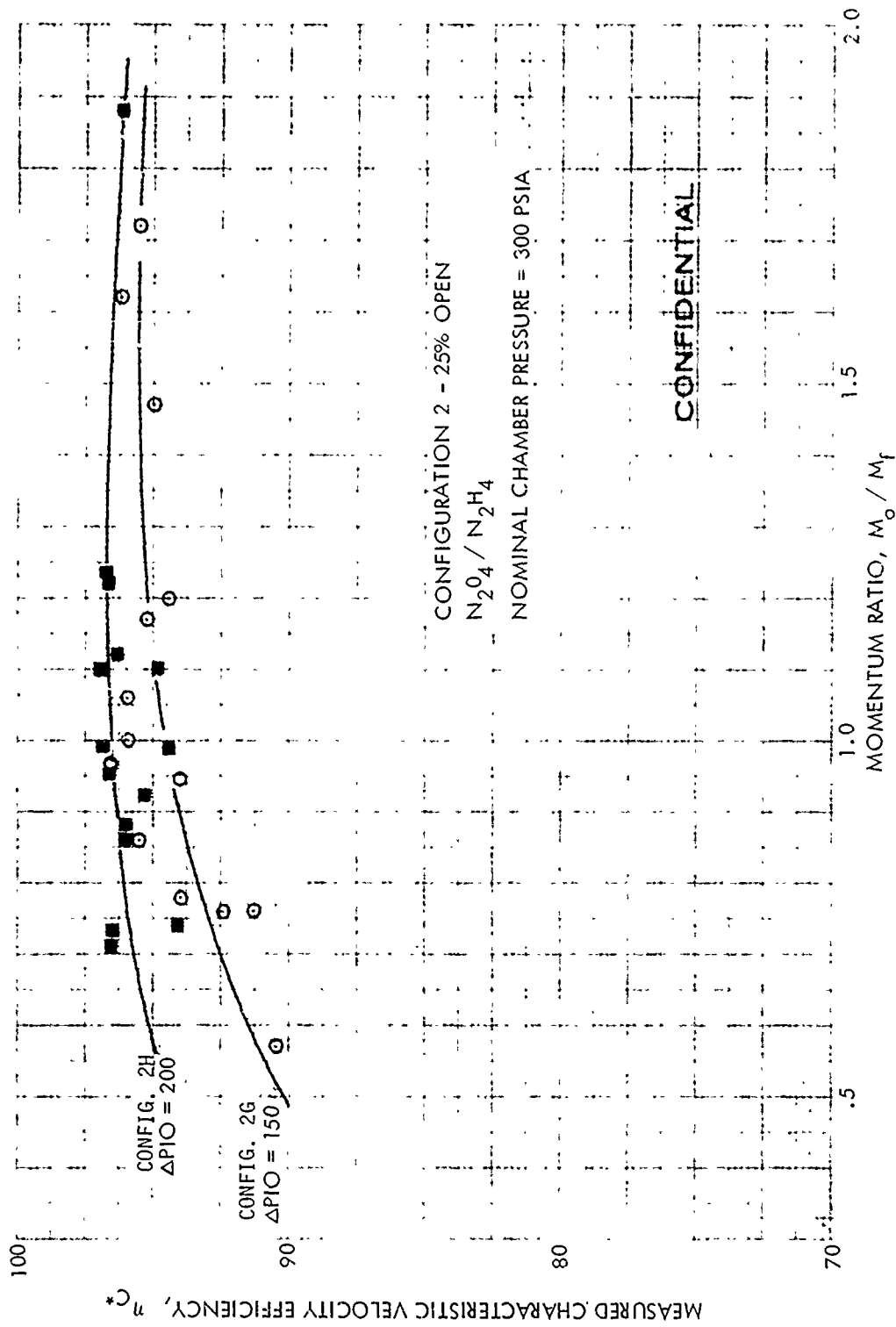


Figure 40. Configuration 2 Injector Performance Correlation With Momentum Ratio (II)

CONFIDENTIAL

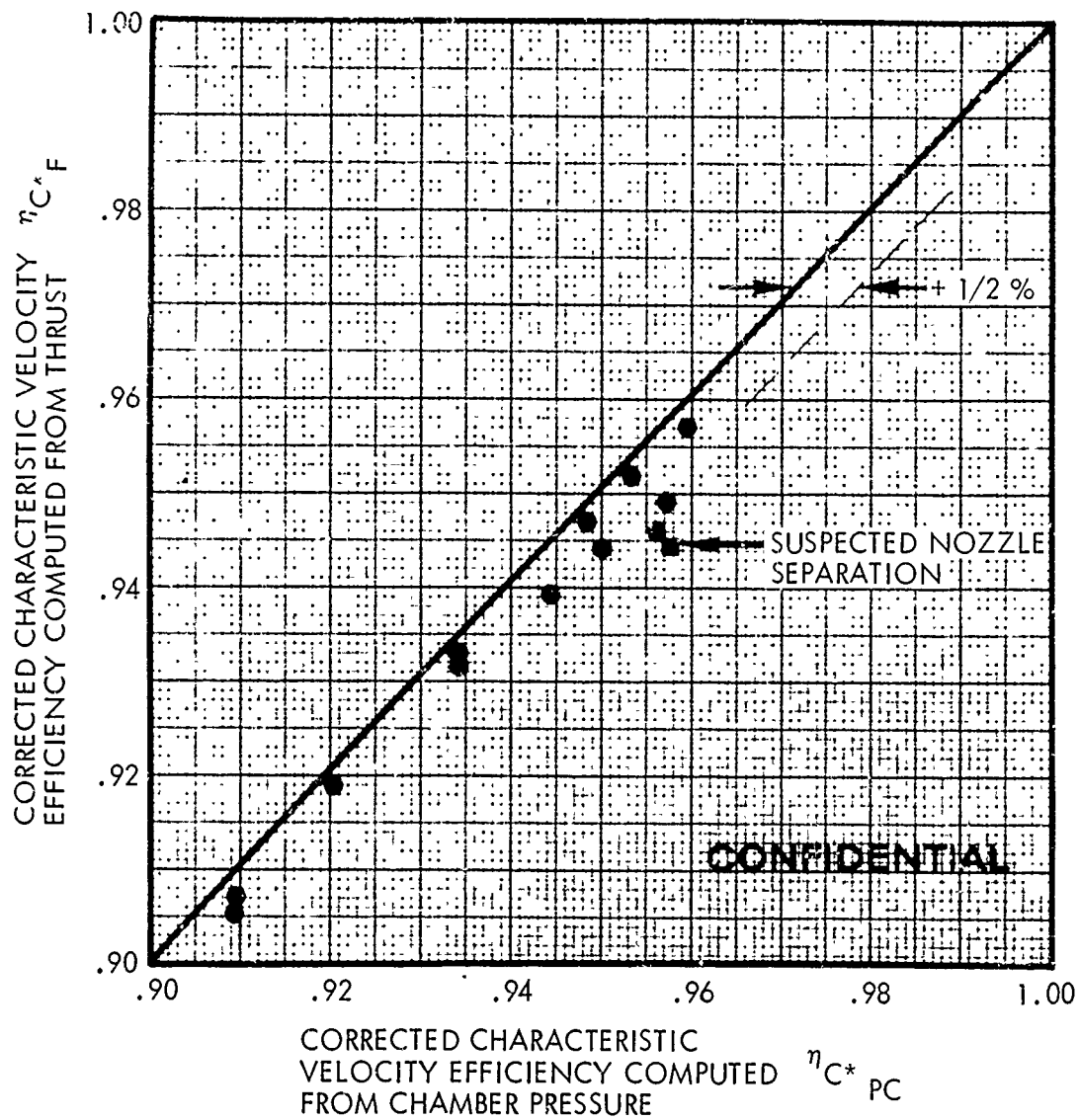


Figure 41. Correlation Of Chamber Pressure Characteristic Velocity With Thrust-Based Characteristic Velocity (U)

CONFIDENTIAL

Table 4. Summary of Corrected Performance for Injector Configuration 2G (U)

Run No.	MR	$\omega$ T lb/sec	$\Delta P_{I0}$ Psi	$\Delta P_{IF}$ Psi	$P_0$ Psi	$F_{MEAS}$	Measured		Corrected		Corrected		Remarks
							$C^* P_c$ ft/sec	$C^* F$ ft/sec	$C^* P_c$ ft/sec	$C^* F$ ft/sec	$\eta_{C^* P_c}$	$\eta_{C^* F}$	
HA1-358	1.211	10.06	152	111	307	2370	5609	5350	5603	5532	.957	.947	CONFIDENTIAL
-359	1.188	10.16	152	117	310	2401	5617	5400	5610	5584	.959	.957	
-360	1.470	9.20	149	74	273	2099	5469	5220	5475	5409	.956	.946	
-361	.954	11.28	148	221	326	2534	5325	5125	5313	5289	.909	.906	
-362	1.200	10.06	147	154	305	2357	5582	5380	5576	5553	.953	.952	
-363	1.199	10.12	146	64	306	2372	5552	5350	5546	5532	.948	.947	
-379	.937	11.24	175	146	336	2605	5476	5280	5462	5444	.934	.933	
-380	.948	11.26	159	145	331	2562	5381	5200	5368	5361	.920	.919	
-381	.945	11.25	149	99	337	2631	5463	5280	5450	5444	.934	.932	
-382	.947	11.26	133	54	329	2559	5339	5195	5326	5356	.912	.919	
-383	.946	11.20	159	143	326	2514	5322	5120	5310	5279	.909	.905	Poor agreement
-384	1.196	10.02	154	92	303	2328	5522	5300	5522	5480	.944	.939	
-385	1.425	9.29	149	65	273	2118	5498	5220	5495	5438	.956	.946	
-411	1.261	10.05	156	105	306	2355	5544	5320	5543	5501	.950	.944	

CONFIDENTIAL

(U) The combustion noise was found to be controlled by oxidizer injection pressure drop and by the ratio of oxidizer-to-fuel pressure drop. Figure 42 shows the effect of oxidizer pressure drop and  $\Delta P_{IO}/\Delta P_{IF}$  on combustion roughness for the 25% open configuration.

(U) Since the injector performance is relatively insensitive to  $\Delta P_{IO}/\Delta P_{IF}$  in the range from 1.0 to 2.0, the best compromise in terms of both parameters is to operate the injector at a  $P_{IO}/P_{IF}$  ratio as close to unity as possible. As shown in Figure 42, the goal of  $\pm 5\%$  can be achieved by operating at an oxidizer pressure drop of 150 psi and  $\Delta P_{IO}/\Delta P_{IF}$  of about 1.1, or by operating at an oxidizer pressure drop of 200 psi and  $\Delta P_{IO}/\Delta P_{IF}$  of approximately 1.8.

(U) A power spectral density (PSD) analysis was conducted on the three Photocon transducer outputs for test number HA1-328. The results of the PSD are shown in Figure 43 where  $\text{psi}^2/\text{cps}$  versus frequency are plotted. The analysis also showed that the root-mean-square values of roughness varied from 17.2 psi to 10.6 psi and that the predominant frequency of the engine was 300 cps. (Figure 34 presents a reproduction of the oscillogram for test HA1-328. The corresponding peak-to-peak roughness values were 53 psi to 32 psi.) The 300 cps predominant frequency was characteristic of the test program. Possible propellant feed system influence or the combustion noise was evaluated by conducting duplicate tests both with and without cavitating venturis installed. No differences in combustion operating characteristics could be discerned when the feed system hydraulic characteristics were altered. Other investigators (for example, references 5 and 6) have also observed comparable combustion frequencies with  $\text{N}_2\text{O}_4/\text{N}_2\text{H}_4$  and concluded that this phenomenon was associated with the fundamental liquid phase mixing and combustion kinetics of this propellant combination.

#### Dynamic Stability

(U) During Task 1b testing, a total of ten dynamic stability tests were conducted and in each case the engine recovered from the overpressure within 29 milliseconds. Of the ten tests, four tests used only the pulse gun for excitation, three tests were performed using only non-directional bombs, and the remaining three tests were performed using both bombs and pulse guns for excitation during a single test. When both bombs and pulse guns are used on the same test, the bomb was detonated first, approximately 500 msec after steady state chamber pressure was attained and the pulse gun was triggered one second later.

UNCLASSIFIED

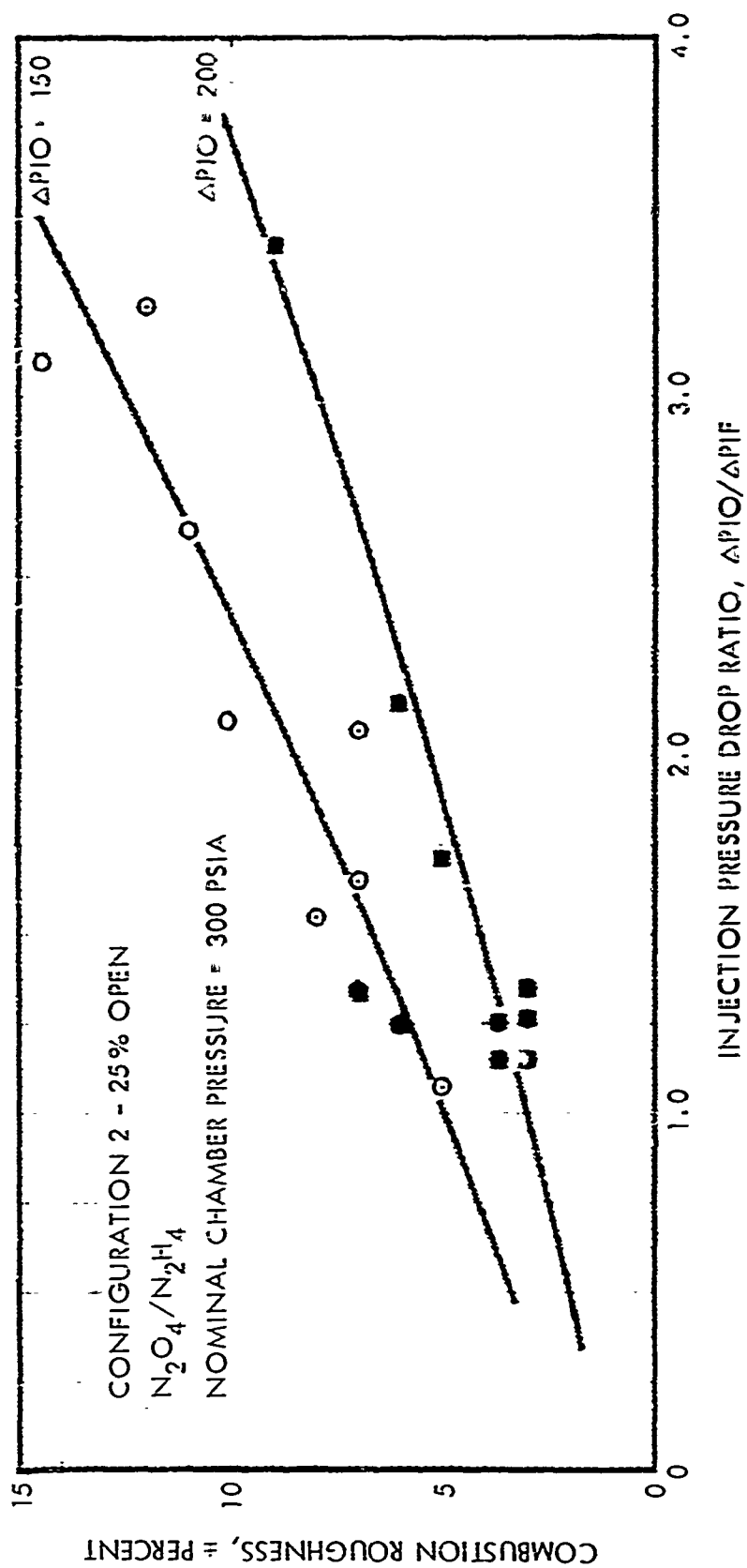


Figure 42. Influence of Injector Parameters on Combustion Roughness (11)

UNCLASSIFIED

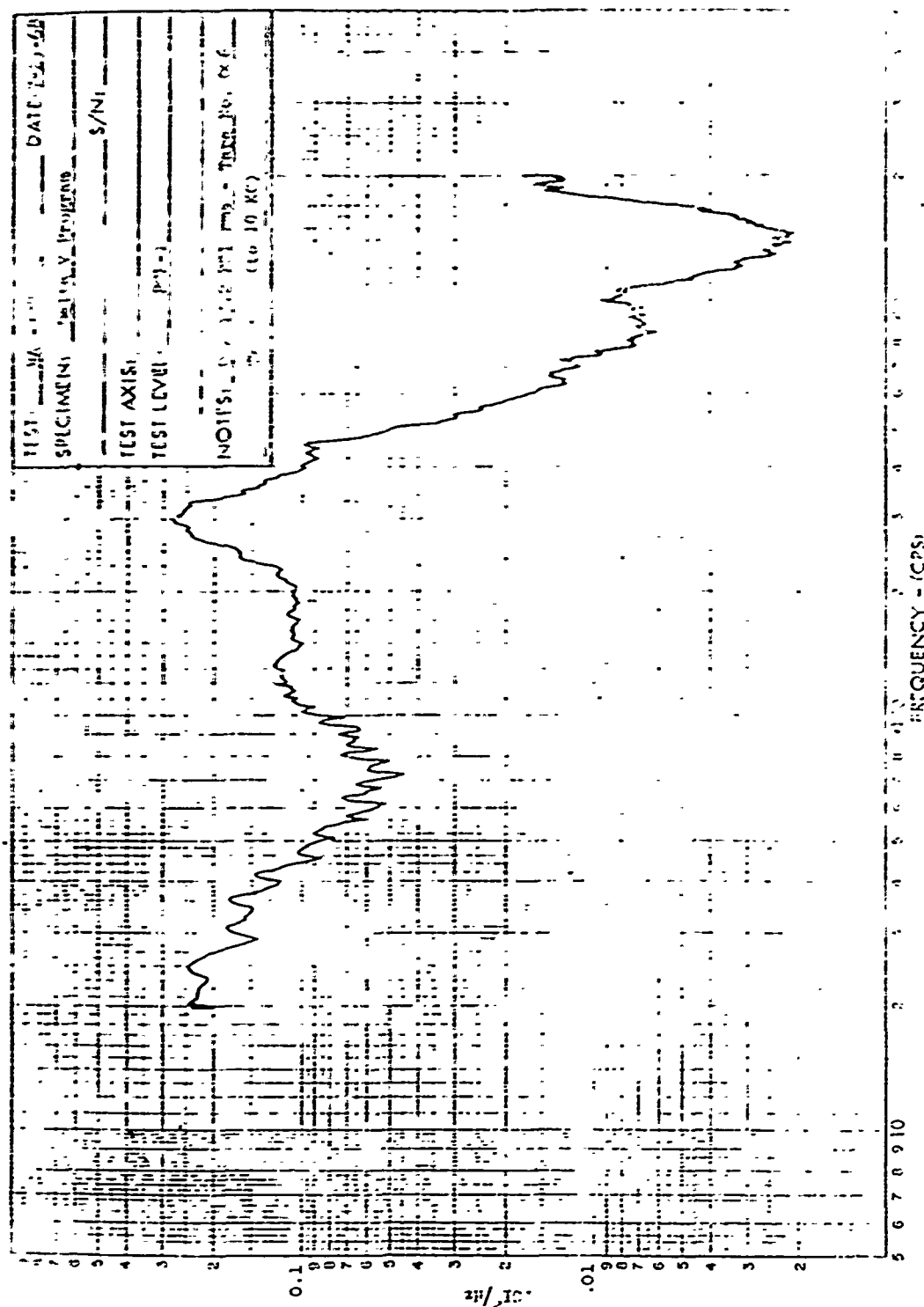


Figure 43. Power Spectral Density of Photocon Chamber Pressure Data (JN1-528) (1)

(See Figure 34 for Corresponding Oscillogram.)

**CONFIDENTIAL**

(U) The first two tests (HA1-367 and -368) using bombs as the excitation device were performed with a 13 grain TNT equivalent charge. The overpressure produced by the bomb in these tests was about 125 psi. These bombs were sized based upon previous tests using a similar injector and thrust chamber configuration. Since the overpressure was less than anticipated, another lot of bombs was loaded using the correlation developed by Rocketdyne in Reference 7. Subsequent tests incorporated a 32.5 grain TNT equivalent bomb in order to produce a larger overpressure. The next three tests in which bombs were used (HA1-395, -397 and -402) resulted in overpressures of 240 to 330 psi. These overpressures were below the value anticipated based upon the correlation of Reference 7. In the Rocketdyne correlation, there was no strong influence of case thickness on shock amplitude whereas earlier reports indicated a profound effect on shock amplitude with case thickness. The pulse gun with a 50 grain charge of Hercules Bullseye powder resulted in higher recorded overpressures. Table 5 lists the dynamic stability tests and the associated overpressures.

#### Thermal Characteristics

(C) Detailed analyses of the engine thermal data were conducted for a series of firings encompassing a mixture ratio range of 0.92 to 1.47 at an operating chamber pressure of 300 psia  $\pm$  10%. The analyses used heat sink test data reduction to determine heat flux and gas side recovery temperatures. The oxidizer orifice configurations analyzed were the 2-B and 2-G orifice rings.

(U) The heat sink engine was instrumented with thermocouples as shown previously in Figure 30. Two different types of thermocouples were used: Nanmac pencil probes (T/C-1 to 6) were used in the cylindrical section of the combustion chamber to measure inside wall temperature and copper calorimeter plugs (T/C-7 to 15) were used in the copper nozzle section to measure the heat flux.

(U) A transient heat flux data analysis program was utilized to reduce the test data for the Nanmac pencil probes. The test data for the calorimeter plugs was reduced using a transient analysis technique developed for a one dimensional calorimeter plug. To account for the heat losses between the calorimeter plug web and the chamber wall, a simulated two dimensional thermal model was constructed for each calorimeter plug. The results

**CONFIDENTIAL**



TABLE 5. DYNAMIC STABILITY TEST SUMMARY (U)

Run No.	Configuration		$P_o$ (psia)	$\eta_c^*$	$\Delta P$ (psia)	Excitation
	Run No.	O/F				
HA1-328	2-B	1.20	305	0.938	525	Pulse Gun (See Figure 34)
HA1-336	2-B	0.95	331	0.940	350	Pulse Gun
HA1-339	2-B	1.42	272	0.956	370	Pulse Gun
HA1-340	2-B	1.18	298	0.946	400	Pulse Gun
HA1-367	2-G	1.23	337	0.961	120	Bomb (13 grain)
HA1-368	2-G	1.39	314	0.963	125	Bomb (13 grain)
HA1-393	2-H	1.23	306	0.967	---	Bomb (13 grain) Did not det.
HA1-395	2-H	1.26	303	0.952	300/630	Bomb (32.5 grain)/Pulse Gun
HA1-397	2-H	0.96	351	0.965	280/280	Bomb (32.5 grain)/Pulse Gun
HA1-402	2-H	1.40	282	0.935	330/405	Bomb (32.5 grain)/Pulse Gun

**CONFIDENTIAL**

(U) obtained for the one-dimensional calorimeter plugs were then corrected to account for the two-dimensional heat losses. The gas side convective film coefficients and recovery temperatures were derived, for both the Nanmac probes and calorimeter plugs, from the slope of the heat flux wall temperature curves.

(U) A summary of the heat flux data as a function of wall temperature is presented in Table 6 for the various thrust chamber stations for the configuration 2-B and 2-G injector elements. Typical wall temperature - time response and heat flux - wall temperature curves are shown in Figures 44 and 45 respectively. These curves illustrate the trends which were exhibited for all runs. The initial increase of heat flux with wall temperature is caused by the transient response of the engine.

#### Combustion Chamber

(U) For the upstream combustion chamber thermocouple location. (Station B, Figure 30) an average recovery temperature of  $2560^{\circ}\text{F}$  was indicated with a corresponding convective film coefficient of  $1.46 \times 10^{-3} \text{ Btu/sec-in}^2\text{-}^{\circ}\text{F}$  for both the configuration 2-B and 2-G oxidizer orifice rings. At the downstream combustion chamber thermocouple location, the average recovery temperature was  $3080^{\circ}\text{F}$  with a corresponding convective film coefficient of  $1.27 \times 10^{-3} \text{ Btu/sec-in}^2\text{-}^{\circ}\text{F}$ . The lower recovery temperature and corresponding higher film coefficient at the upstream combustion chamber location compared with the downstream location was probably due to incomplete combustion and high turbulence at this location.

#### Throat

(U) At the throat the calculated recovery temperature from the calorimeter plug data was found to be less than  $2000^{\circ}\text{F}$  for all tests analyzed. This value was considered to be unrealistically low and was probably due to the lack of agreement between the assumptions used in the data analysis technique and the actual conditions. The analysis assumes that the time-temperature response at the inside and back surfaces of the calorimeter plug is the same. The results of the analysis indicated that this was not the case due to high heat loads imposed at the throat.

#### Heat Flux Distributions

(U) The heat flux distribution as a function of axial distance in the thrust

**CONFIDENTIAL**  
(This page is unclassified)

Table 6. Summary Of Heat Transfer Data (U)

RUN Number	Pressure  P <sub>0</sub>	Pressure Correction Factor (300/P <sub>0</sub> ) <sup>.8</sup>	ΔP/F Ratio	Mixture Ratio O/F	HEAT FLUX NORMALIZED TO 300 PSIA - (BTU/IN <sup>2</sup> -SEC-1)															
					Combustion Chamber T/C-1			Combustion Chamber T/C-6			Converging Section T/C-8			Throat T/C-12						
					700	900	1000	INNER WALL TEMP °F	INNER WALL TEMP °F	INNER WALL TEMP °F	INNER WALL TEMP °F	INNER WALL TEMP °F	INNER WALL TEMP °F	INNER WALL TEMP °F	Diverging Section T/C-14 INNER WALL TEMP °F					
Injector Configuration 2-B																				
329	330	.9256	.770	.92	Not Analyzed			*	*	*	3.28	2.32	2.04	4.04	3.53	3.20	*	*	*	
332	339	.9068	3.11	.93				2.14	2.19	2.21	2.21	2.21	2.21	2.31	*	*	*	2.34	2.34	2.40
335	326	.9359	.910	.94				2.33	2.33	2.24	2.24	3.61	3.05	2.56	4.84	4.07	3.54	2.06	2.12	2.17
331	335	.9154	1.46	.94				2.21	2.23	2.22	2.22	3.42	2.92	2.57	4.58	4.14	3.74	2.23	2.29	2.33
336	336	.9134	1.49	.94				2.11	2.11	2.09	2.09	3.15	2.69	2.33	4.40	3.88	3.47	2.49	2.15	2.06
330	301	.9244	2.00	1.10				2.21	2.20	2.14	2.14	3.47	2.64	2.22	5.05	4.53	4.10	2.26	2.50	2.82
340	302	.9947	1.91	1.18				2.30	2.32	2.25	2.25	3.23	2.92	2.72	5.57	5.43	5.08	2.49	2.54	2.50
337	279	1.060	3.35	1.38				2.22	2.21	2.18	2.18	2.98	2.81	2.38	5.30	4.66	*	2.71	2.42	2.38
338	278	1.063	2.15	1.42				2.17	2.20	2.10	2.10	2.72	1.96	1.88	5.16	4.73	4.44	2.50	2.37	2.02
339	277	1.066	2.68	1.42				2.29	2.26	2.22	2.22	2.98	2.69	2.30	5.33	5.10	4.67	2.68	2.51	2.40
Injector Configuration 2-G																				
379	339	.9068	1.47	.937	2.29	2.49	2.38	2.39	2.58	2.45	3.17	3.13	2.49	5.69	5.08	4.59	2.29	2.22	2.01	
381	340	.9048	2.07	.945	2.18	2.06	2.01	*	*	*	3.45	3.12	2.62	4.81	4.76	4.48	2.34	2.33	2.26	
383	329	.9283	1.37	.946	2.45	2.31	2.23	*	*	*	3.63	3.55	3.20	5.44	4.87	4.34	2.14	2.09	2.00	
380	334	.9125	1.35	.948	2.52	2.52	2.39	2.51	2.64	2.60	3.65	3.15	2.50	5.78	4.97	4.38	2.01	2.01	2.16	
361	326	.9357	.77	.954	2.41	2.40	2.34	2.08	2.24	2.16	3.77	3.70	3.18	*	*	*	2.62	2.21	2.25	
384	306	.9843	2.11	1.196	*	*	*	*	*	*	3.39	3.62	3.50	5.67	6.14	5.85	2.53	2.41	2.24	
363	308	.9795	3.25	1.199	1.93	1.84	1.72	2.16	2.20	2.16	3.70	3.83	3.59	*	*	*	2.70	2.74	2.74	
362	308	.9795	1.08	1.20	2.16	2.05	1.96	2.20	2.22	2.16	3.62	3.48	3.34	*	*	*	2.84	2.79	2.64	
358	310	.9743	1.65	1.211	1.87	1.87	1.85	2.11	2.17	2.24	3.78	3.77	3.49	6.09	5.38	4.92	2.86	2.75	2.71	
365	325	.9380	1.43	1.342	2.17	1.90	1.83	2.13	2.11	2.07	3.92	3.79	3.61	*	*	*	2.74	2.53	2.65	
364	314	.9642	1.62	1.402	1.85	1.74	1.63	2.03	2.02	1.96	3.71	3.83	3.67	*	*	*	2.97	2.75	2.46	
385	282	1.051	3.10	1.425	*	*	*	*	*	*	3.36	3.30	3.17	6.14	6.20	5.84	2.44	2.49	2.47	
360	278	1.063	2.68	1.47	1.62	1.59	*	1.62	1.60	*	3.17	3.00	2.39	5.66	5.71	5.53	2.83	2.91	2.73	

\* Bad data or no data recorded

UNCLASSIFIED

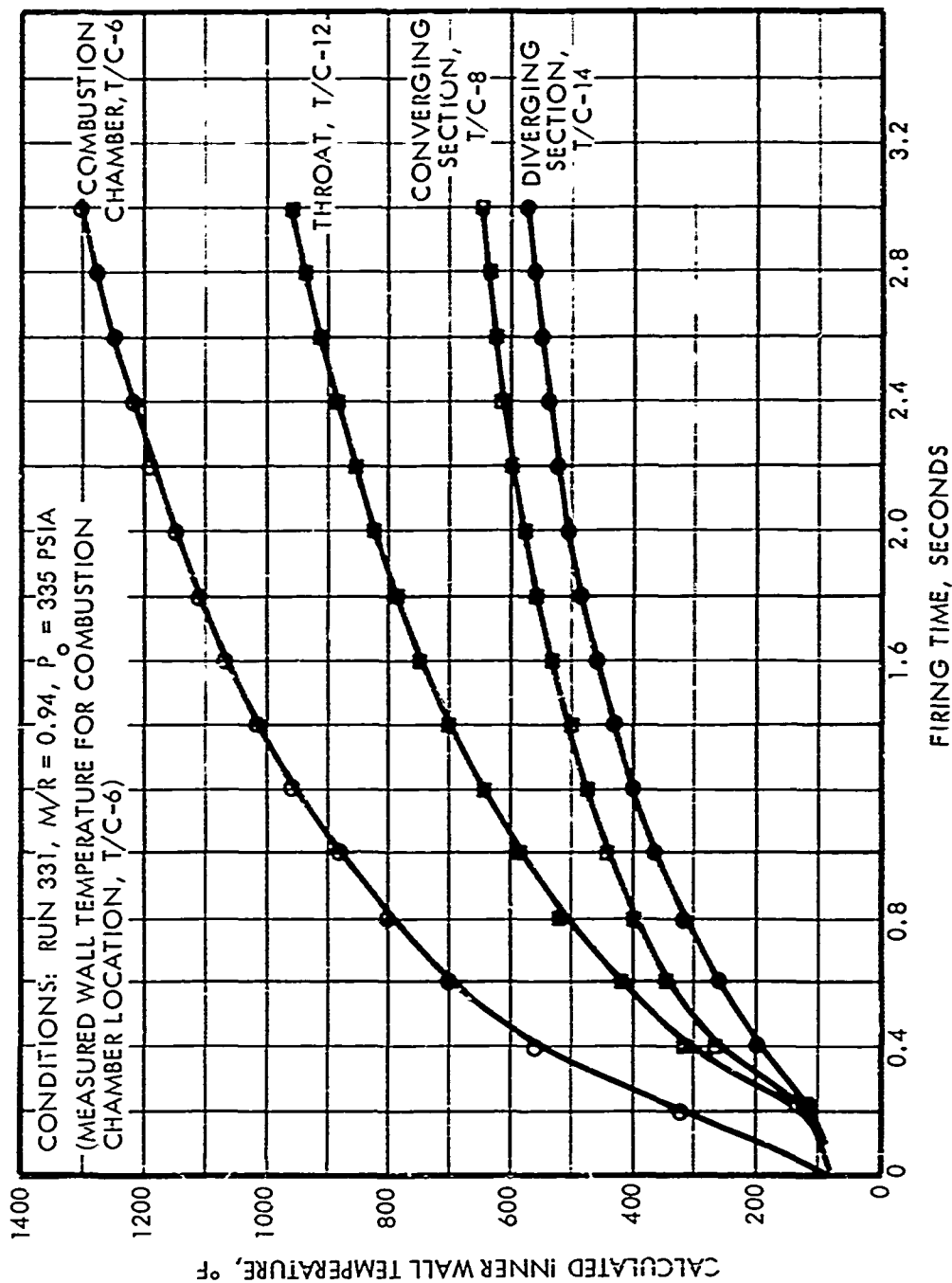


Figure 44. Wall Temperature Versus Time Trends (U)

UNCLASSIFIED

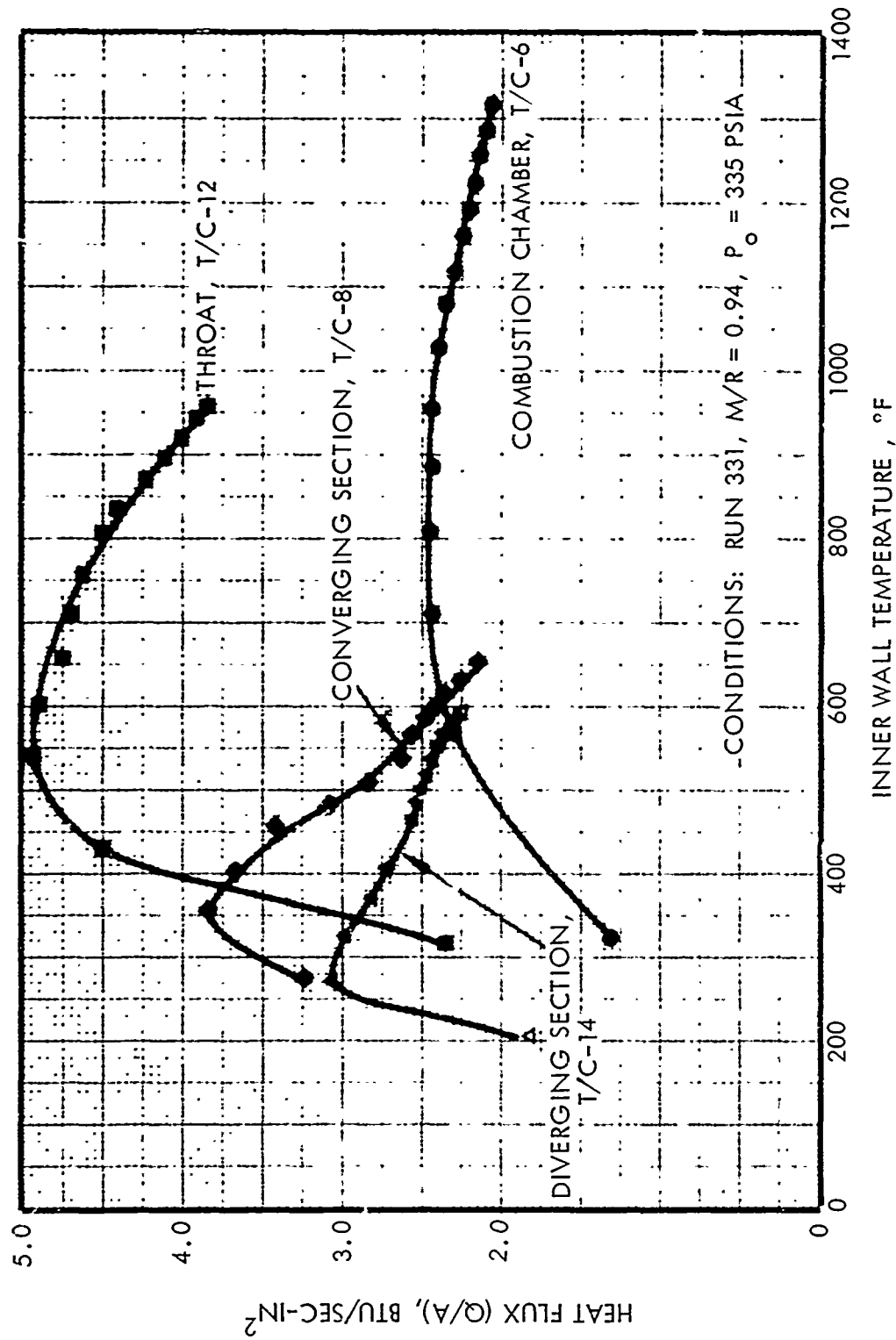


Figure 45. Heat Flux Versus Wall Temperature (U)

UNCLASSIFIED

(U) chamber is presented in Figure 46 at a firing time of 2.4 seconds. For comparison, the heat flux prediction based upon the Bartz equation from Reference 8 for a recovery temperature of 3000°F is also shown. The Bartz equation predicted a 25% higher heat flux at the throat and a 50% lower heat flux in the combustion chamber than was obtained from the test results. The agreement in the convergent and divergent sections was within 15%.

(U) An asymmetric radial heat flux distribution was found for the convergent and divergent section of the nozzle. The maximum heat loads were found to occur along a line located 180° from the fuel inlet (at T/C-8 and T/C-14). The asymmetric radial heat flux distribution was confirmed by the ablative chamber results obtained in Task 2 where the maximum temperature response or maximum heat load was also found to occur at a circumferential location 180 degrees from the fuel inlet.

#### Heat Flux Correlation

(U) The heat flux was calculated at selected wall temperatures to determine the effect of varying chamber conditions and injector configurations upon the heat flux. For comparison purposes, the heat flux data was normalized to a pressure of 300 psia by multiplying by a factor of  $(300/P_o)^{0.8}$ . A summary of the normalized heat flux data at selected wall temperatures is presented in Table 6.

(U) The effect of mixture ratio upon heat flux is presented graphically in Figures 47 through 50. For the combustion chamber location downstream, no noticeable trend was found between heat flux and mixture ratio. For the converging-diverging section and the throat, the heat flux was found to increase sharply up to mixture ratio of 1.2 and level off at higher mixture ratios.

The effect of  $\Delta P_{IO}/\Delta P_{IF}$  on heat flux is illustrated in Figure 51 for the throat region. No strong dependence upon  $\Delta P_{IO}/\Delta P_{IF}$  was observed except at the throat where there was an increase in heat flux with increasing  $\Delta P_{IO}/\Delta P_{IF}$  independent of the mixture ratio.

UNCLASSIFIED

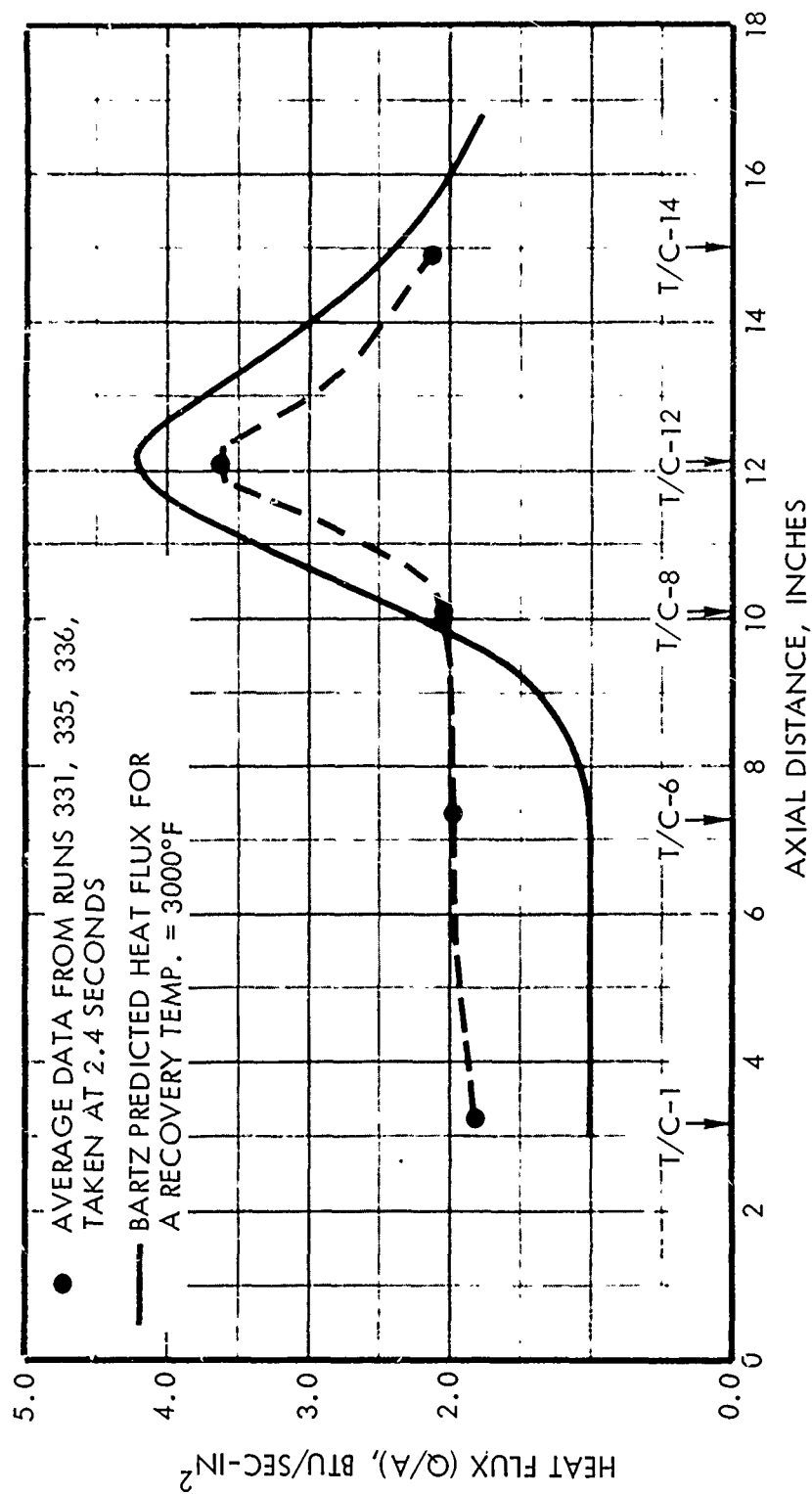


Figure 46. Heat Flux Distribution in Uncooled Thrust Chamber (U)

UNCLASSIFIED

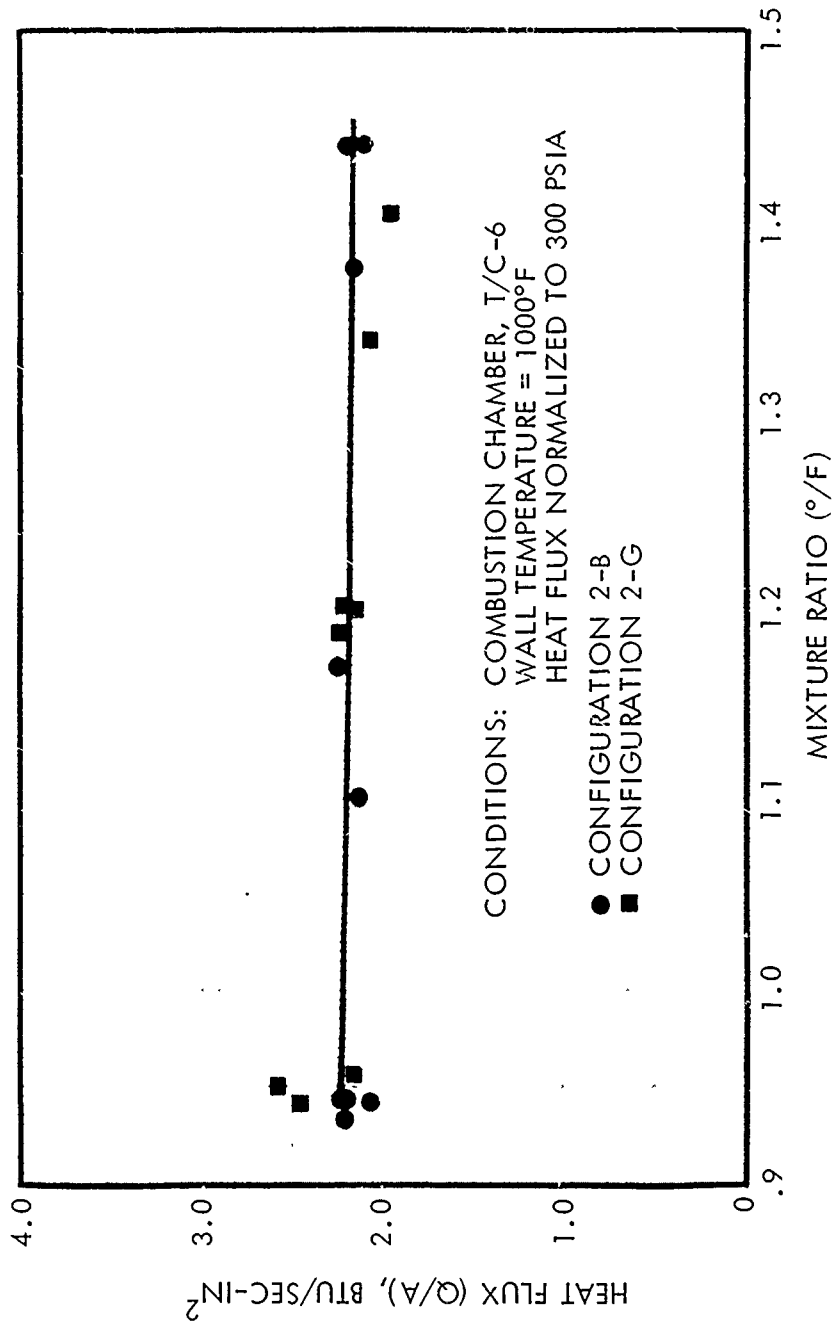


Figure 47. Heat Flux Versus Mixture Ratio, Combustion Chamber (U)

UNCLASSIFIED



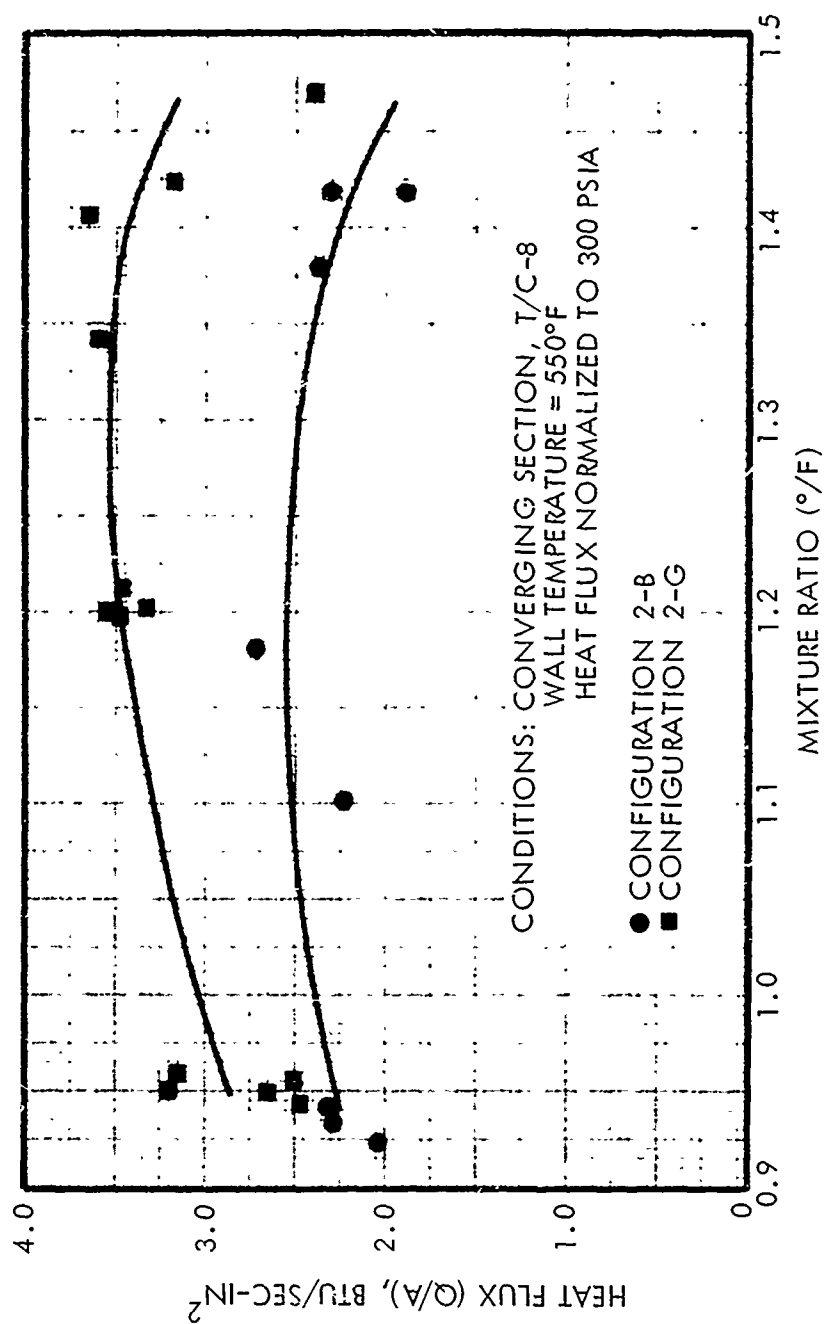


Figure 48. Heat Flux Versus Mixture Ratio, Convergent Nozzle (U)

UNCLASSIFIED

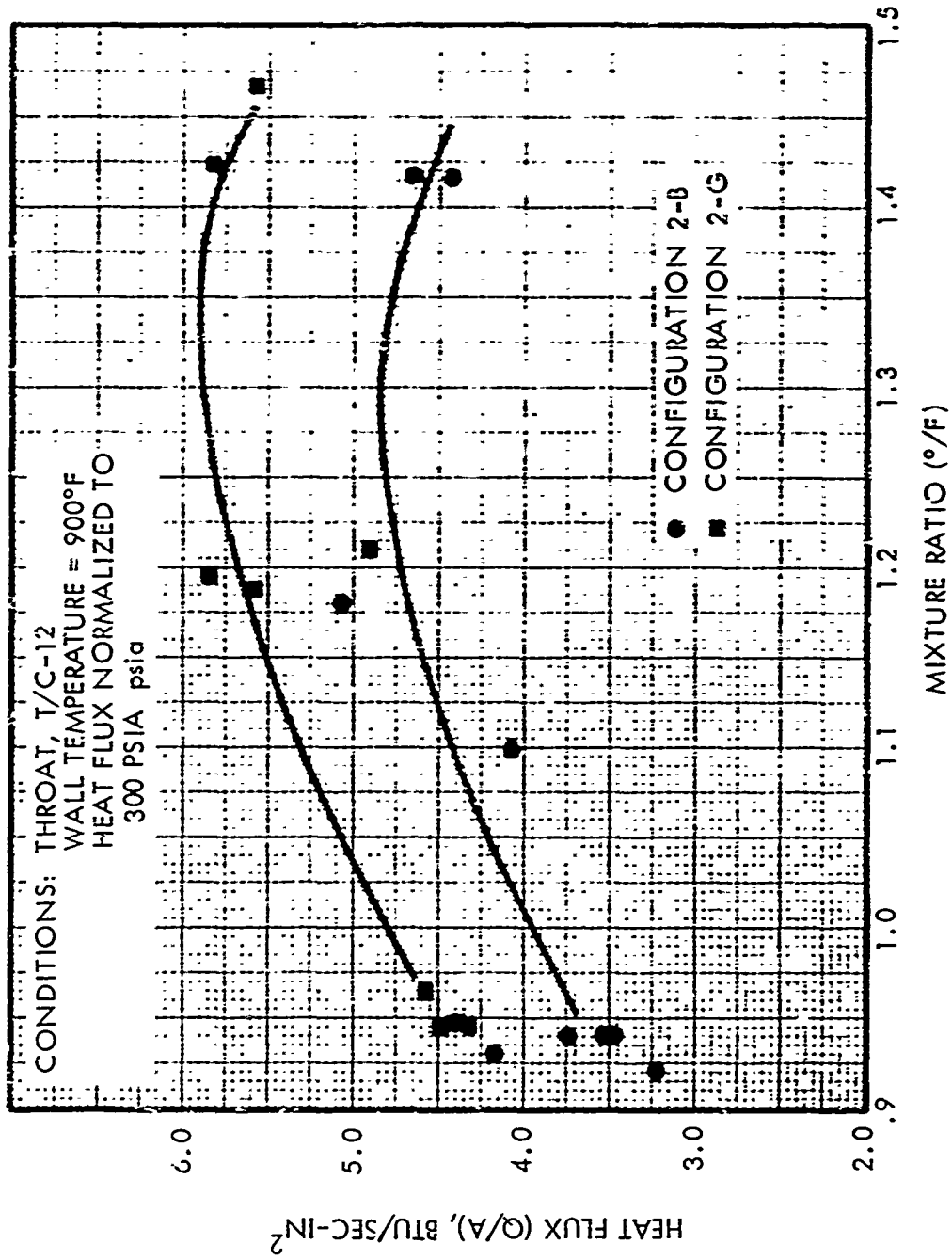


Figure 49. Heat Flux Versus Mixture Ratio, Throat (U)

UNCLASSIFIED

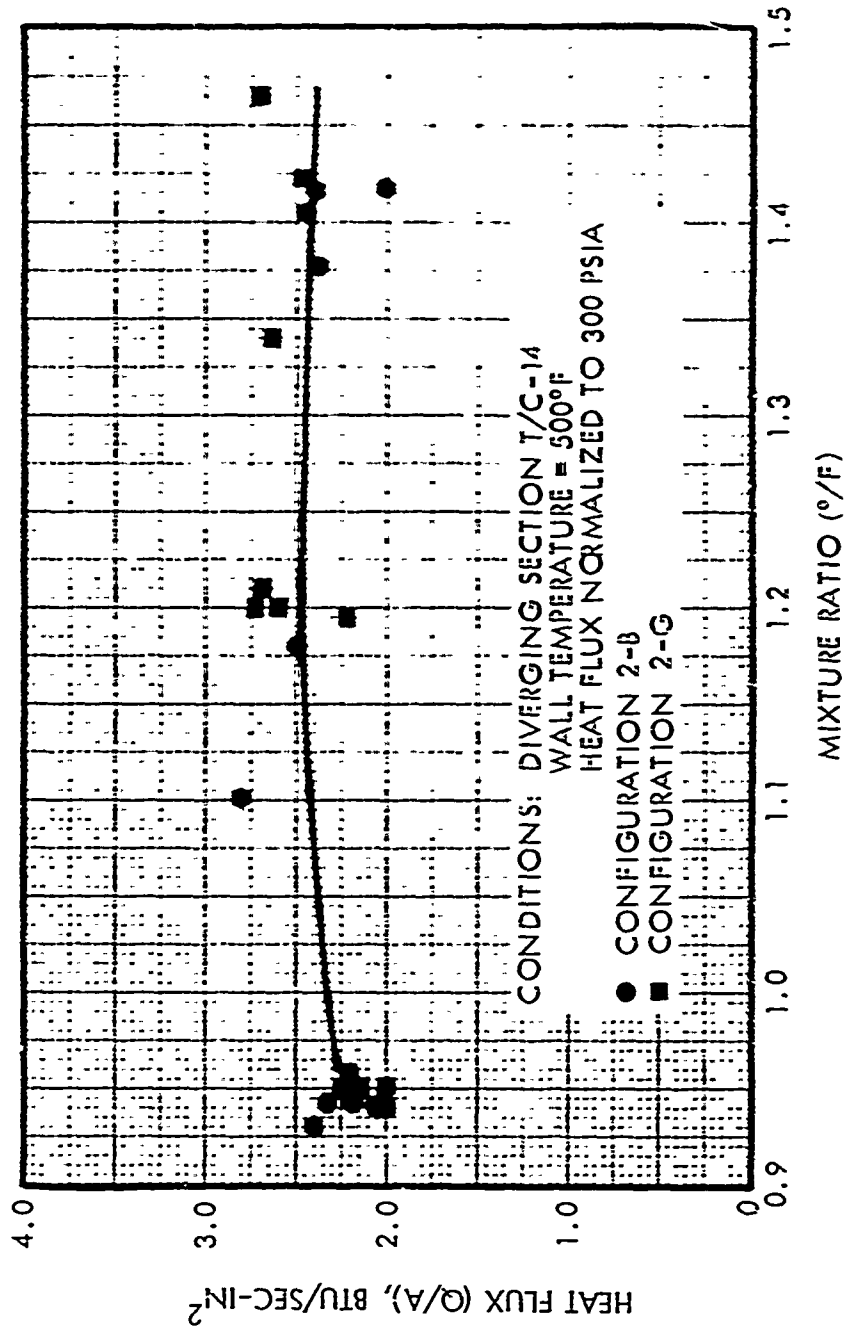


Figure 50. Heat Flux Versus Mixture Ratio, Divergent Nozzle (II)

UNCLASSIFIED

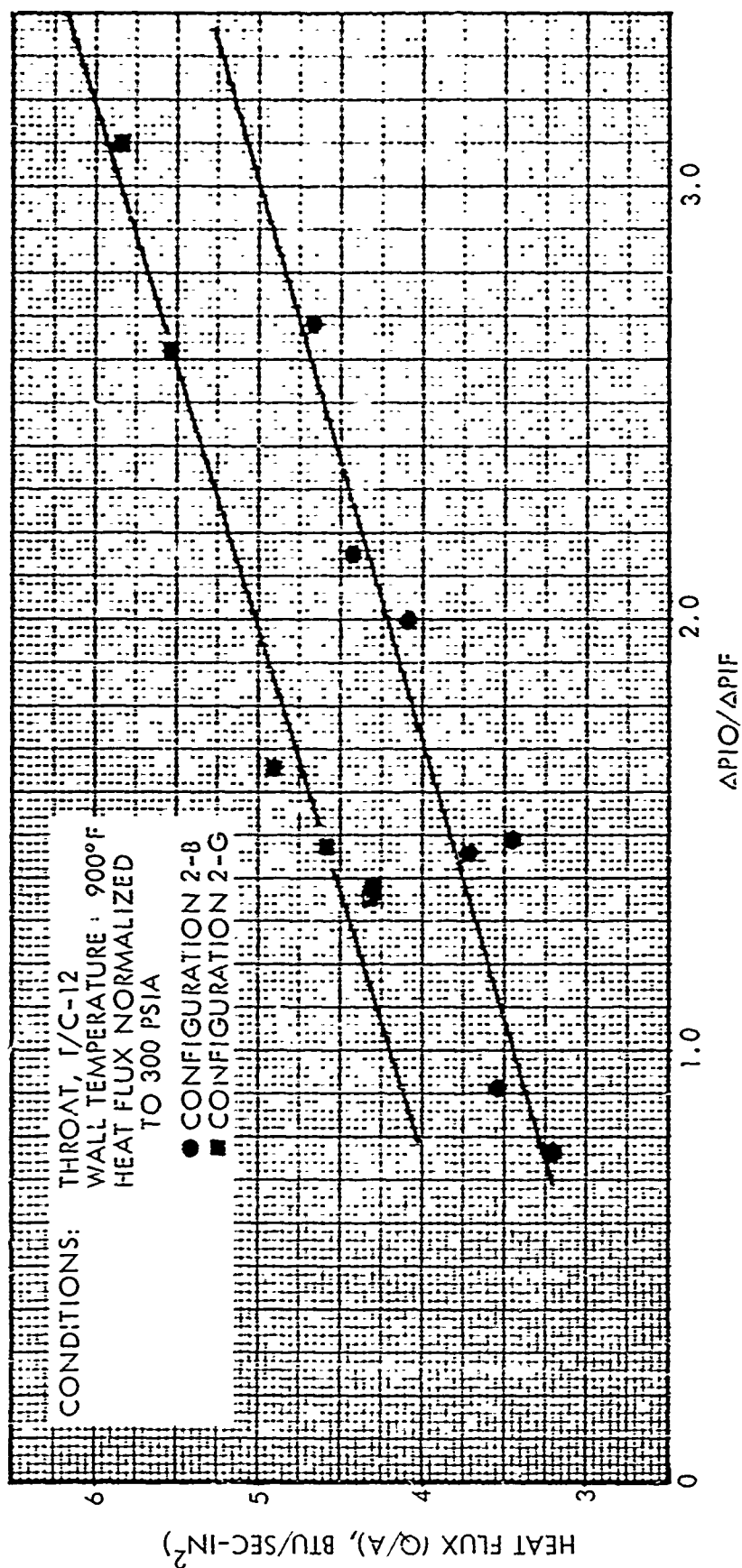


Figure 51. Heat Flux Variation With Injector Pressure Drop Ratio (U)

UNCLASSIFIED

(U) Injector configuration 2-G (25% open) resulted in higher heat fluxes at the convergent and throat sections than did configuration 2-B (35% open). No discernable difference in the heat flux in the combustion chamber and divergent section was noted for the two configurations (see Figure 47 and 48).

(U) Although the recovery temperatures at the throat associated with injector configurations 2-B and 2-G could not be directly obtained from the calorimeter plugs, the recovery temperature can be inferred from comparison of the measured throat heat fluxes of a common wall temperature (see Figure 49) and defining a common value for the film coefficient. Assuming the film coefficient to be equal to the theoretical Bartz value, the calculated recovery temperature for configuration 2-B was 3000°F at a mixture ratio of 1.20. The corresponding recovery temperature value for configuration 2-G was 3500°F.

(U) The major conclusions derived from the thermal analysis were:

- In the converging-diverging sections and the throat, the heat flux was found to increase up to a mixture ratio of 1.2 and then level off. No noticeable trend was found in the cylindrical portion of the combustion chamber.
- The  $\Delta P_{IO}/\Delta P_{IF}$  ratio did not exhibit a large effect upon the heat flux with the two oxidizer elements analyzed except at the throat.
- Substantially higher heat fluxes were obtained when operating with injector Configuration 2-G as compared with 2-B in both the convergent and throat regions.

#### 4.3.3 Task 2 - Injector/Chamber Compatibility

(U) The objective of this task was to evaluate the compatibility of the selected injector configuration with an ablative thrust chamber through a single long duration burn followed by a hot restart. Two ablative chambers were fabricated to evaluate the injector/chamber compatibility. Table 7 summarizes the ablative chamber firings. All Task 2 testing employed the 2-G oxidizer orifice ring configuration.

(U) Since the ablative engine tests required hot restarts, the HEPTS A-1 test stand was re-plumbed to close-couple the fire valves to the engine. The fire valves were relatively slow response Annin valves, and were mounted directly on the injector to minimize the priming volume. The revised test

UNCLASSIFIED

Table 7. Task 2 Ablative Thrust Chamber Test Summary (U)

	<u>On Time</u>	<u>Off Time</u>
Chamber No. 1	16 seconds	Complete cooldown
	60 seconds	600 second heat soakback
	4 seconds	✓(End of Testing)
Chamber No. 2	60 seconds	30 seconds
	1 second	15 seconds
	1 second	15 seconds
	35 seconds	(End of Testing)

UNCLASSIFIED

(J) stand configuration is shown in Figure 52 with the ablative engine mounted on the thrust stand.

(U) The instrumentation for the injector/chamber compatibility tests was identical to the instrumentation for the previous test series except for thrust chamber instrumentation. Chamber pressure measurements were made through ports in the injector face and corrected to nozzle stagnation pressure. There were no dynamic pressure measurements taken with the ablative engine. Thermal data were taken at three circumferential locations 120 degrees apart and at two axial stations. The axial location of the thermocouples was near the start of nozzle convergence and at the geometric throat.

(U) The thermocouple assembly was a 1/4 inch diameter plug of MX2600 silica phenolic with slots on two sides of the plug. There is resin-glass insulation on individual wires along sides of the plug with bare wire across the end of the plug. The thermocouple wire was cemented into the slots with low expansion cement and the plug was then potted into the hole in the liner with epoxy cement. The thermocouple plugs extend into the ablative liner to within 0.3 inch of the inside surface. Figure 53 illustrates the thermocouples during assembly prior to cementing the wire in the slots. Figure 54 shows how the thermocouple plugs were inserted into the ablative liner. The groove along the side of the liner carries the wire to the outside of the metal shell.

#### Experimental Results

(U) The Task 2 effort began with a test stand checkout run using heat sink hardware. The checkout run was necessary because the stand had been re-plumbed as described earlier. The checkout run (HA1-412) disclosed no variation in the system from previous tests. All Task 2 tests were conducted with cavitating venturis in the propellant feed system to maintain constant flow rates so that chamber pressure was directly proportional to throat area as a cross check of post-test diametral measurements.

(U) The ablative engine assembly with S/N-1 ablative liner was then mounted on the stand. The initial test (HA1-413) using the ablative

UNCLASSIFIED

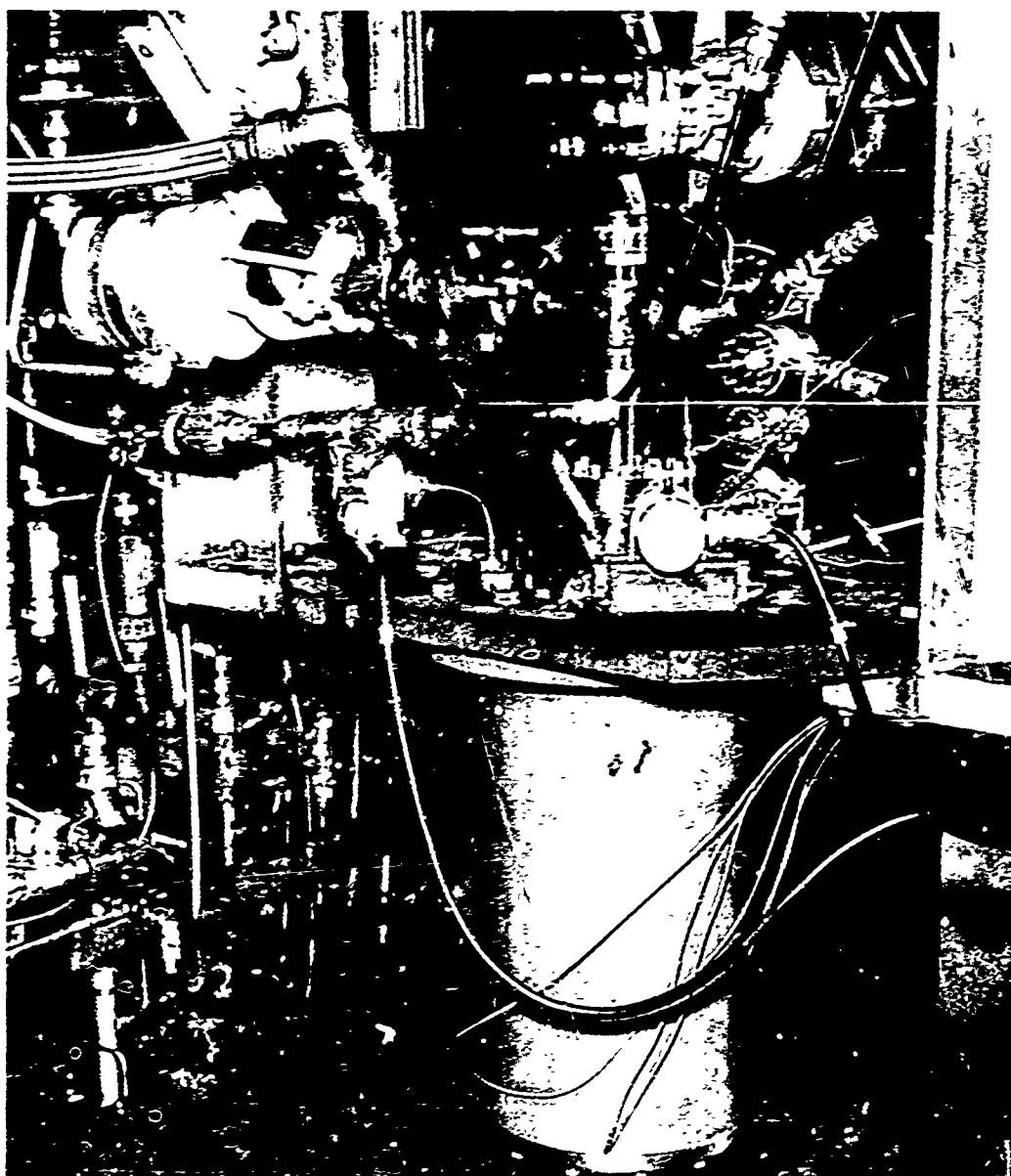


Figure 52. Ablative Thrust Chamber Installation on Test Stand

UNCLASSIFIED



UNCLASSIFIED

AFRPL-IR-69-231  
Page 109



Figure 53. Ablative Chamber Thermocouple Probes (U)

UNCLASSIFIED

UNCLASSIFIED

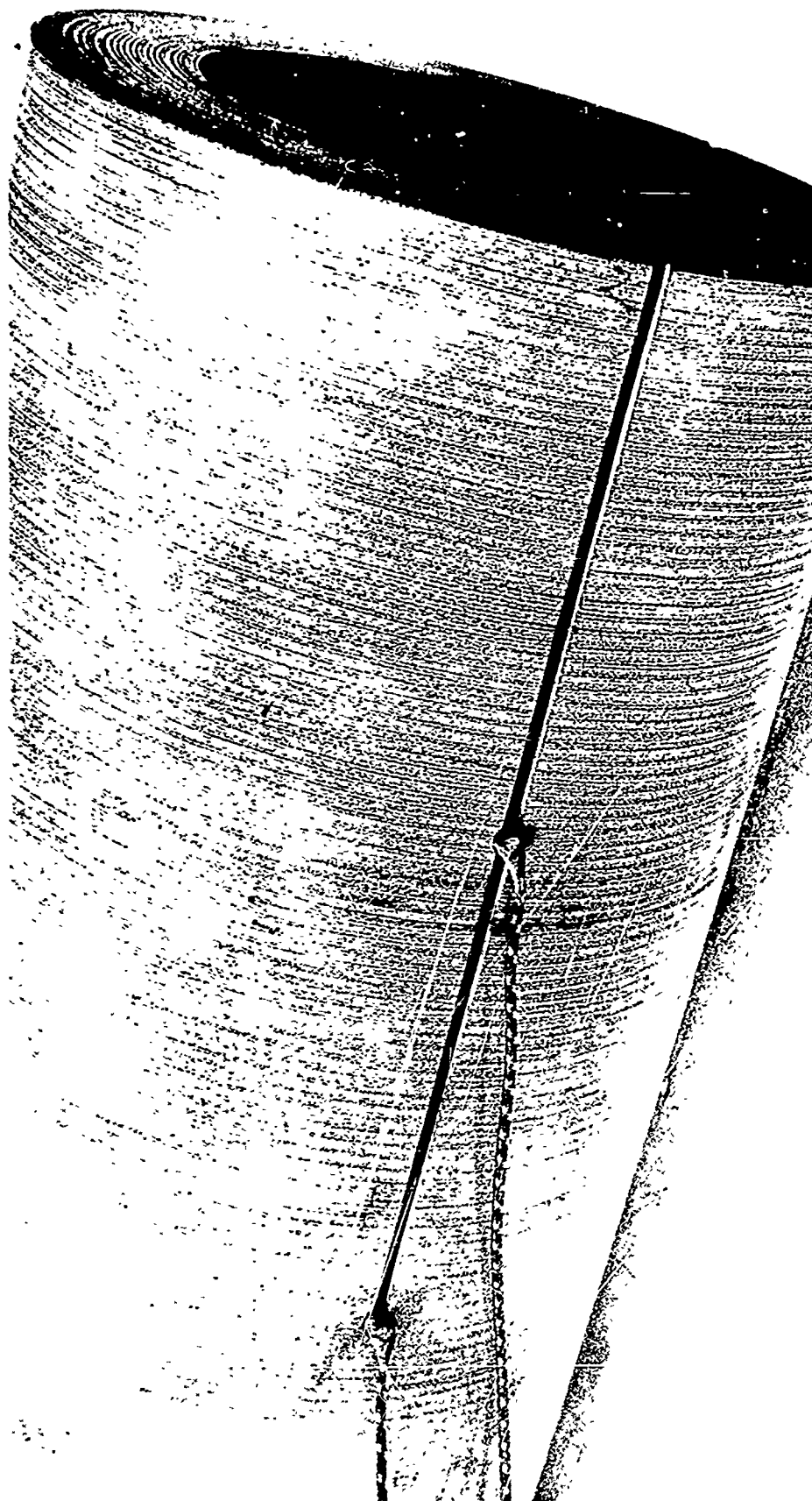


Figure 54. Thermocouple probes During Installation Into Ablative Chamber (U)

UNCLASSIFIED

(C) engine was targeted for a mixture ratio of 1.4 and a nominal duration of 16 seconds. The actual mixture ratio was 1.49 and the measured characteristic velocity efficiency was 97 percent. Post-test inspection of the ablative liner revealed erosion of the throat. However, there were no streaks evident. Figure 55 is a Post HA1-413 view of the ablative chamber viewing from the injector end into the throat. The head end area of the ablative liner showed evidence material delamination near the point where propellant impingement occurs. Post test measurements were taken on the chamber at four axial locations. The throat diameter measured 2.90 inches (average of three measurements) after test HA1-413. This is an erosion of 0.097 inches during the 16 second run.

(C) After post test measurements and photographs were taken, the thrust chamber assembly was again mounted on the stand. Another test was performed using the same ablative chamber (S/N-1). Test HA1-414 had a target mixture ratio of 1.2 and a target duration of 60 seconds with a soak period of 600 seconds followed by a hot restart of 4 second duration. Actual mixture ratio was 1.20 and the characteristic velocity efficiency for this test was measured as 0.955. Post test inspection of the chamber revealed two rather light streaks as shown in Figure 56. The two areas of asymmetric erosion, that corresponded to the  $180^{\circ}$  and  $250^{\circ}$  (clockwise from the fuel inlet) locations which were identified during the uncooled thrust chamber testing (see section 4.3.2, Thermal Characteristics). It was found that the thermocouple plugs began to leak hot gas when the char layer reached the plug which was 0.3 inch from the inside surface. The post test throat diameter measurement was 3.14 inches (average of three measurements) for a net erosion of 0.212 inches during the 60 second run and 4 second restart after a 600 second heat soakback.

(C) The second ablative chamber assembly was subjected to a multiple restart duty cycle consisting of an initial 60 second duration firing, a 30 second soakback, two (2) pulses of 1 second on and 15 seconds off, and concluding with another long duration firing. The chamber pressure characteristics during the initial 60 seconds of operation are illustrated in Figure 57. The mixture ratio was 1.19 and the measured characteristic velocity efficiency was 97 percent. The firing was prematurely terminated during the third restart after 35 seconds

**CONFIDENTIAL**



Figure 55. Ablative Chamber Throat Post-test (16 seconds of operation ) (U)

**CONFIDENTIAL**  
(this page is unclassified)

UNCLASSIFIED

ADP-18-09-211  
Page 11

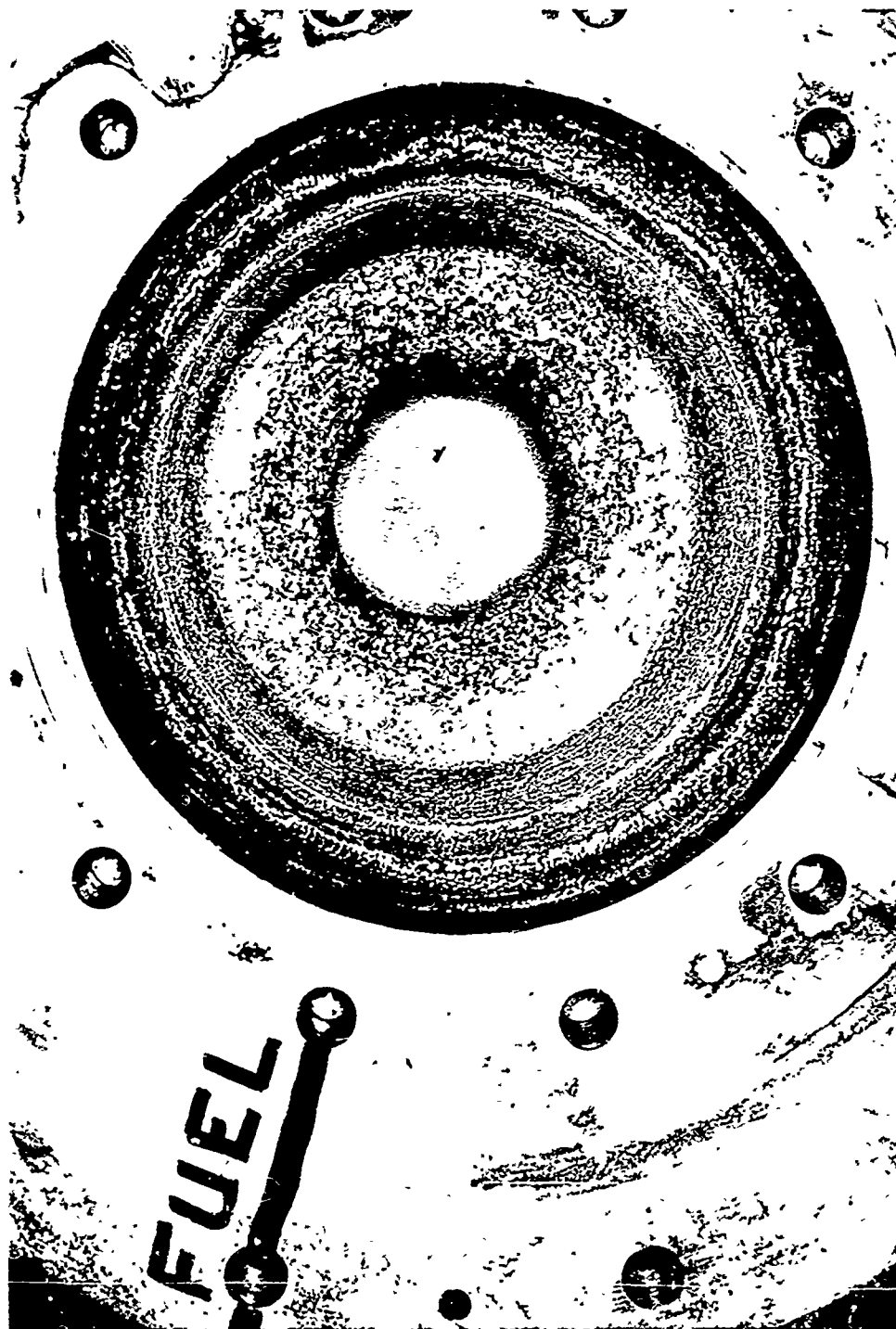


Figure 56. Ablative Chamber Throat Following Final Tests (80 seconds of operation) (U)

UNCLASSIFIED

THIS REPORT HAS BEEN DELIMITED  
AND CLEARED FOR PUBLIC RELEASE  
UNDER DOD DIRECTIVE 5200.20 AND  
NO RESTRICTIONS ARE IMPOSED UPON  
ITS USE AND DISCLOSURE.

DISTRIBUTION STATEMENT A

APPROVED FOR PUBLIC RELEASE,  
DISTRIBUTION UNLIMITED.

UNCLASSIFIED

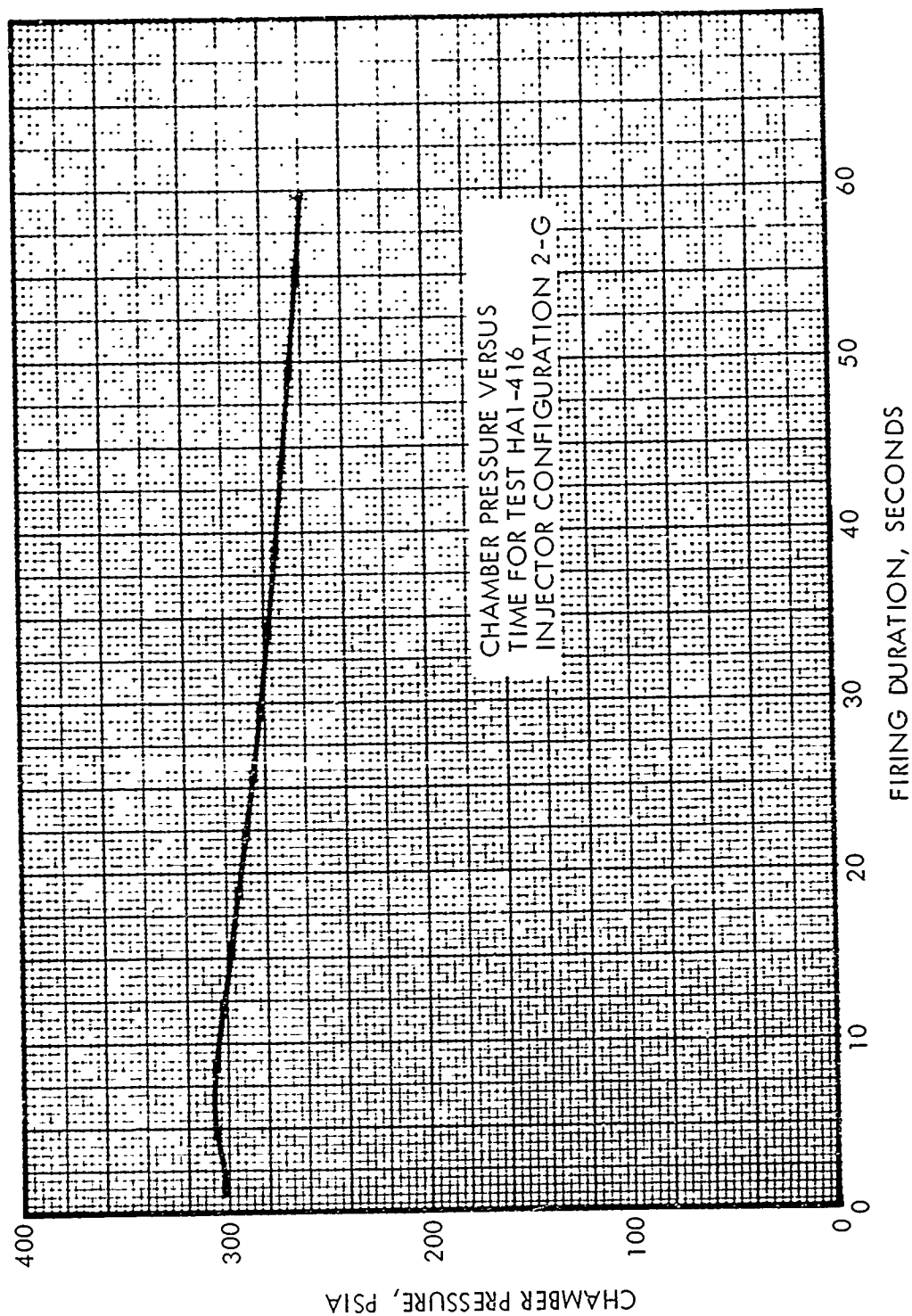


Figure 57. Chamber Pressure Versus Firing Duration for Test HAI-416

UNCLASSIFIED

(C) following an abrupt drop in chamber pressure caused by loss of the injector pintle tip. The oxidizer-contacting side of the columbium pintle tip was not aluminide coated and the long cumulative exposure to  $N_2O_4$  during the Task 1b and Task 2 testing embrittled the columbium which resulted in structural failure of the pintle tip. (Subsequent testing in Task 3 employed a completely aluminide coated pintle tip which was successfully operated without incident for a cumulative operating time greater than 330 seconds obtained in 23 starts, of which 11 were hot re-starts.) The post-test throat diameter was 2.98 inches for a net erosion of 0.136 inches during the 97 seconds of cumulative operation with three hot restarts.

(U) The experimental and analytical temperature profiles and erosion depths from the ablative chamber tests were compared to determine the recovery temperature at the throat. The analytical results were obtained using a simulated thermal model programmed for a Charring and Dimensional Ablation Program. A calculated Bartz film coefficient of  $2.1 \times 10^{-3}$  Btu/sec-in<sup>2</sup>-°F was used at the throat. Although the technique is dependent upon the choice of convective coefficient, experience has shown that at the throat, the theoretical Bartz prediction was in reasonable agreement with the values obtained from the Task 1 test data reduction. The results of the data matching indicated that the recovery temperature in the throat region was in the range of 3300°F to 3800°F. The agreement with the 3500°F value derived from the uncooled thrust chamber data (Section 4.3.2) was considered extremely good considering the variety of factors which could adversely influence the data correlation.

(U) The objectives of establishing the basic compatibility of the injector with an ablative thrust chamber through a long duration test, followed by a hot restart to demonstrate satisfactory operation of the hydrazine fuel under restart conditions, were amply demonstrated during the Task 2 testing. Two ablative thrust chamber liners were subjected to different extremes of firing conditions utilizing the highest performing injector configuration evaluated under the program. Although throat erosion was encountered on both thrust chambers, the overall results at the high injector performance levels tested were very encouraging considering the program approach of directly proceeding from short duration uncooled thrust chamber hardware testing to long duration, multiple start ablative chamber testing without intermediate testing stages.



**CONFIDENTIAL**

#### 4.3.4 Injector Predicted Altitude Performance

(U) As stated previously, all test firings were conducted with a low area ratio nozzle with expansion to ambient pressure conditions. The contract performance goals are stated in terms of vacuum expansion of a 30:1 area ratio nozzle which requires that a prediction of altitude performance be made on the basis of the low area ratio test data. The ICRPG Performance Standardization Working Group procedure (Reference 9) for considering the five acknowledged loss mechanisms (kinetics, divergence, mixture ratio distribution, incomplete combustion, and viscous effects and heat transfer) was followed for these performance predictions.

(U) Figure 58 presents the theoretical performance of  $N_2O_4/N_2H_4$  at an area ratio of 30:1 as a function of mixture ratio. The performance decrements between the equilibrium specific impulse and the two dimensional Kinetic specific impulse corrected for boundary layer effects for a 3000°F chamber wall environment is shown to be strongly influenced by mixture ratio. The nozzle contour selected for the analysis was an 80 percent bell contour with a 2.7 inch throat diameter, and with the upstream and downstream throat radii of curvature equal to the throat diameter. The divergence efficiency of this contour was .9875. The equilibrium performance and axisymmetric kinetic performance parameters were obtained from TRW developed computer programs (References 10 and 11, respectively) which are the ICRPG industry references. The performance loss from combined friction and heat transfer was calculated on a computer program developed by JPL (Reference 8). Figure 58 also illustrates the range of performance loss incurred through two-zone expansion of a cool zone at the chamber wall (3000°F) which surrounds a higher mixture ratio core. The two-zone flow losses are presented in terms of outer zone flow-to-total flow versus overall throughput mixture ratio. (The Two Dimension Kinetic Corrected for Viscous Losses curve is also the zero outer zone flow condition for the two-zone expansion losses comparison.)

(U) The lower temperature, fuel-rich environment adjacent to the thrust chamber wall which is requisite to injector-compatibility is conventionally provided by film cooling (or boundary layer cooling) in multi-element injectors. However, the single-element coaxial injector developed under this

**CONFIDENTIAL**

(This page is unclassified)

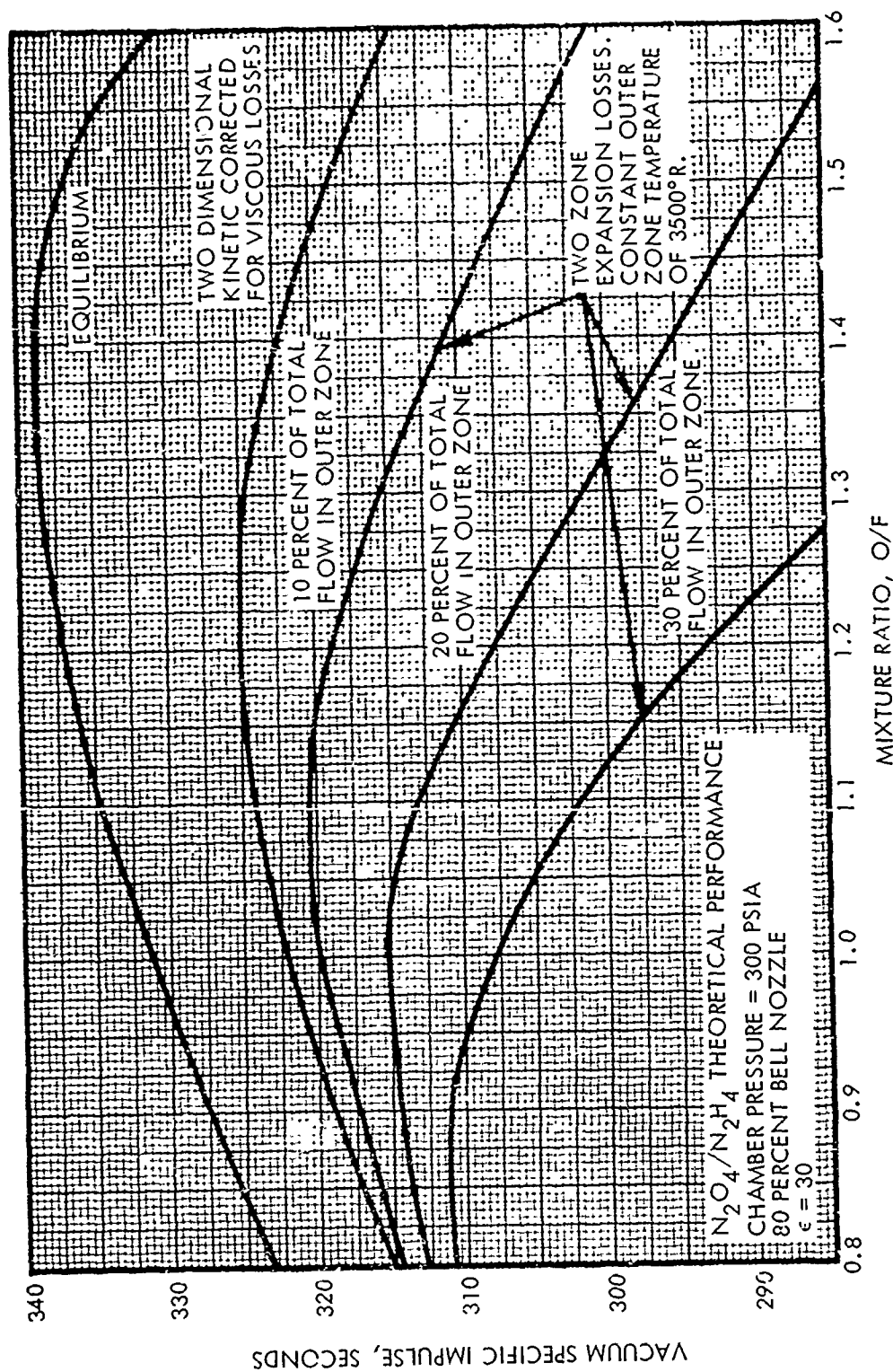


Figure 58. Theoretical Vacuum Specific Impulse For 30:1 Area Ratio, 80 Percent Bell Nozzle (U)

**CONFIDENTIAL**

(U) program accomplished the necessary wall environment control by geometrical spacing of the oxidizer slots and by balance of the fuel and oxidizer injection momenta, without recourse to supplemental film cooling (see section 4.3.2). As a consequence, the division of the total injector throughput between the cool zone adjacent to the thrust chamber wall and the remaining hot, high performance inner core cannot be directly measured. Water flow patternation of the injector was attempted to establish mass and mixture ratio distributions but did not add any insight (see section 4.1.3). In fact the cold flow distribution study predicted an oxidizer-rich wall environment, however, gas sampling of the combustion products and high speed photography of the combustion process conclusively demonstrated that the wall environment was fuel-rich (see section 4.3.2). Therefore, measurement of the characteristic velocity performance under this program is a composite evaluation of both combustion efficiency (or energy release efficiency) and mixture ratio distribution. It should also be noted that the assigned division of losses between actual combustion efficiency and mixture ratio distribution has a small overall effect in correlating characteristic velocity data. However, the effects on correlating specific impulse are not trivial as shown in Figure 58.

(U) The theoretical performance of the test nozzle configuration (3.5:1 area ratio 15 degree half-angle cone) for both equilibrium flow and two dimension kinetic with boundary layer corrections is presented as Figure 59.

(C) In the absence of specific determinations of mixture ratio distribution and energy release efficiency which are necessary to rigorously follow the ICRPG prediction procedure, the measured specific impulse data were corrected by the ratio of the theoretical two dimensional kinetic performance with boundary layer losses for the 30:1 nozzle divided by the comparable kinetic performance for the 3.5:1 test nozzle at the identical mixture ratio. The results of this correlation are presented in Figure 60 for both the 2-B and 2-G injector configurations operating in a fixed orifice mode. The measured, uncorrected specific impulse test data and the corresponding predicted 30:1 area ratio expansion specific impulse values are summarized in Table 8. The ablative thrust chamber performance values from both Tasks 2 and 3 are also presented in Table 8 and in Figure 60.

**CONFIDENTIAL**

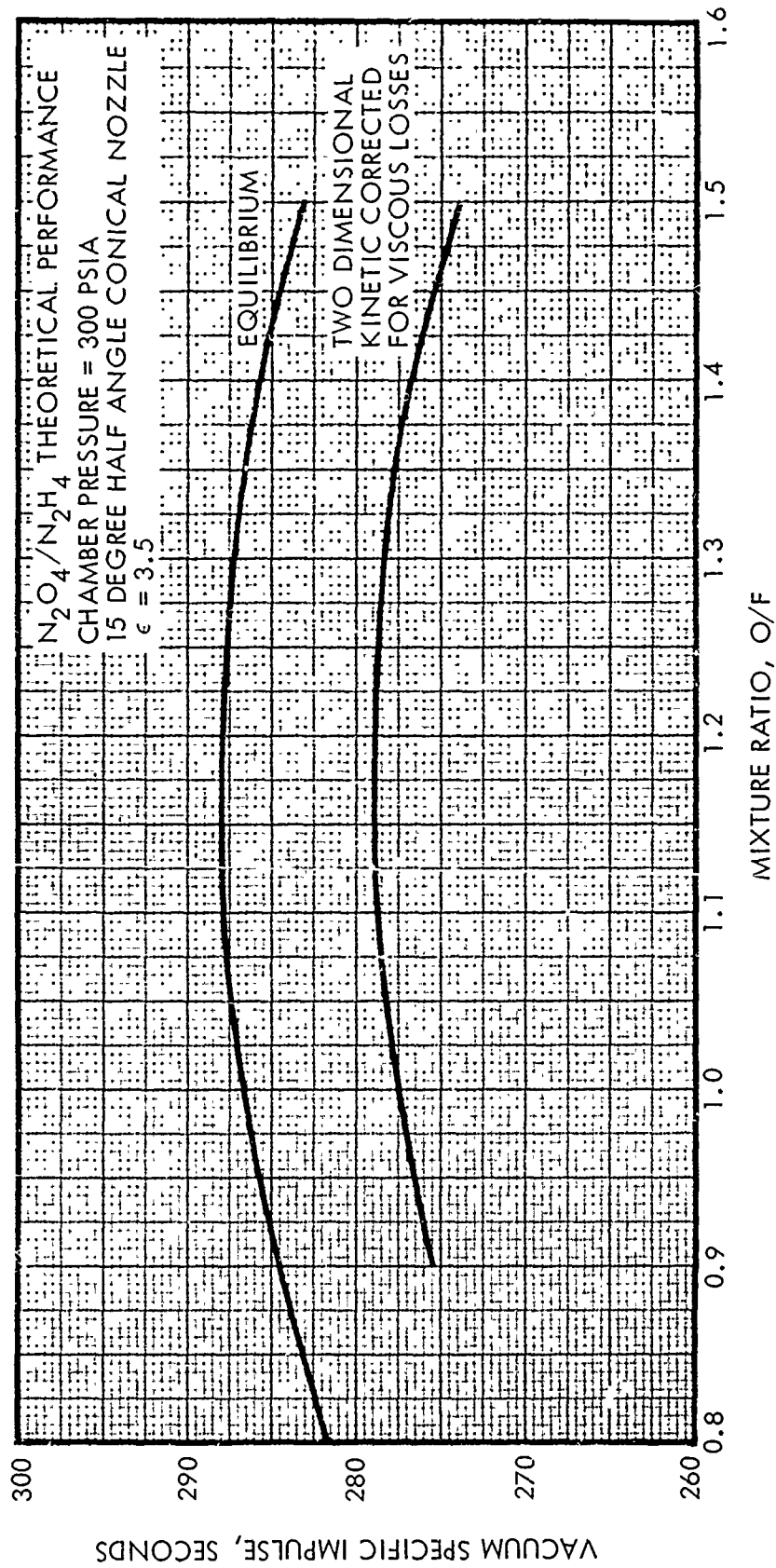


Figure 59. Theoretical Vacuum Specific Impulse for 3.5:1 Area Ratio, 15 Degree Half Angle Conical Nozzle (U)

**CONFIDENTIAL**

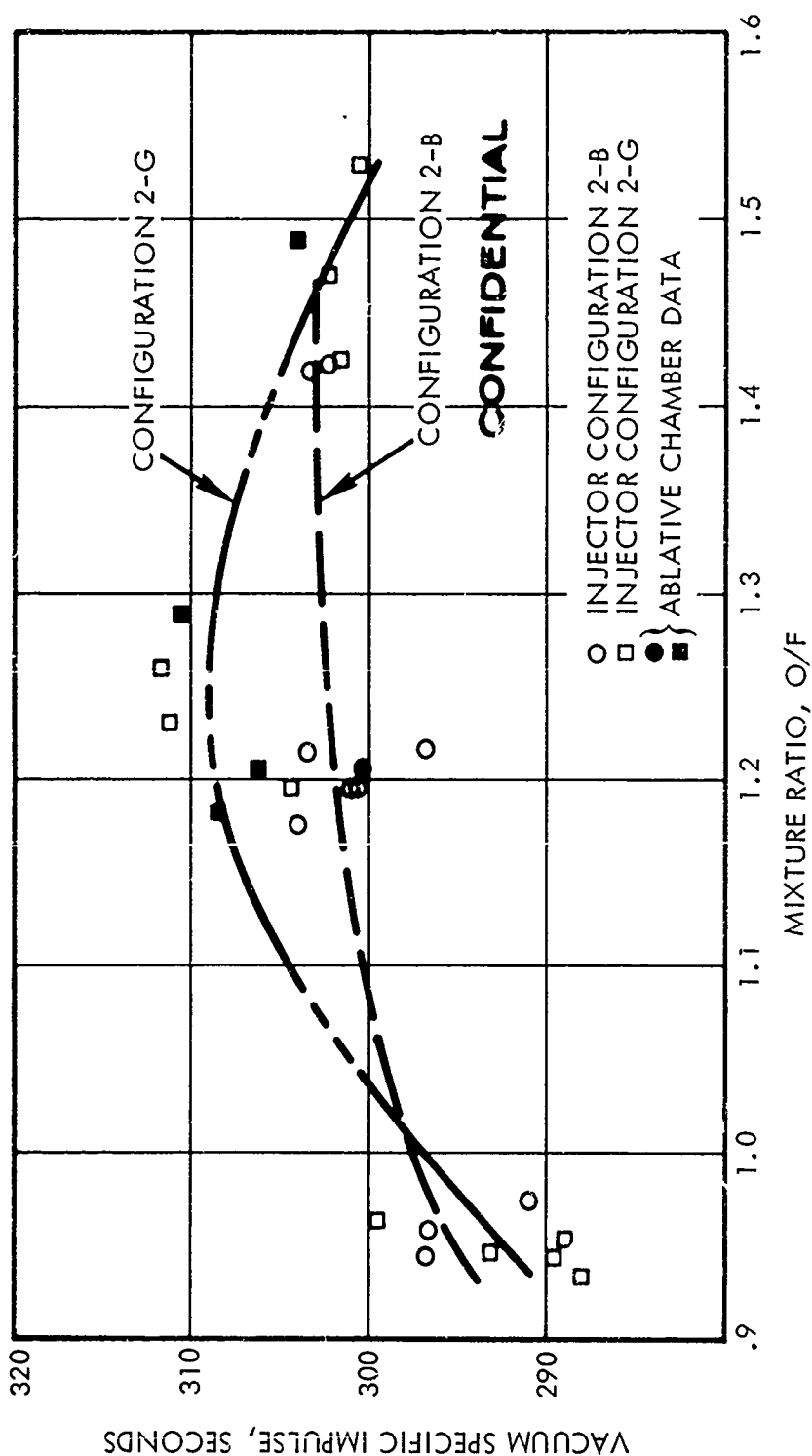


Figure 60. Injector Vacuum Specific Impulse Performance (U)

**CONFIDENTIAL**

CONFIDENTIAL

Table 8. Correlation and Summary of Injector Specific Impulse Performance (U)

Run Number	Injector Configuration	Mixture Ratio	Measured C*	Vacuum Test Nozzle	Isp* (c = 3.5:1) Isp; (c = 30:1)	Predicted Vacuum	Comments
HA1-318	2-B	.958	5182	256.2	296.6		
-320	2-B	1.215	5574	260.5	303.4		
-327	2-B	1.195	5478	258.3	301.0		
-328	2-B	1.197	5472	258.0	300.6		
-335	2-B	.945	5371	256.5	296.8		
-338	2-B	1.418	5522	260.7	303.4		
-339	2-B	1.423	5499	259.8	302.3		
-340	2-B	1.175	5533	260.8	304.0		
-358	2-G	1.2:1	5609	264.4	308.0		
-359	2-G	1.188	5617	264.7	308.5		
-360	2-G	1.470	5500	259.7	302.2		
-361	2-G	.954	5325	250.4	289.9		
-379	2-G	.932	5476	257.6	298.0		
-380	2-G	.948	5381	253.2	293.1		
-383	2-G	.946	5322	250.3	289.7		
-384	2-G	1.196	5522	261.1	304.3		
-385	2-G	1.425	5498	259.2	301.6		
-413	2-G	1.489	5563	261.3	304.0		Ablative chamber**
-414	2-G	1.204	5573	259.2	302.0		Re-fire of ablative chamber**
-416	2-G	1.184	5695	264.6	308.4		Ablative chamber**
-496	2-B	1.217	5213	254.8	296.8		
-497	2-B	.975	5100	251.0	291.0		
-500	2-G	1.231	5510	267.3	311.2		

CONFIDENTIAL

CONFIDENTIAL

CONFIDENTIAL

Table 8. Correlation and Summary of Injector Specific Impulse Performance (U)

Run Number	Injector Configuration	Mixture Ratio	Measured $C^*$	Vacuum Test Nozzle $I_{sp}^*$	Predicted Vacuum $I_{sp}$ ( $\epsilon = 30:1$ )	Comments
HA1-501	2-G	1.260	5499	267.9	311.7	
-502	2-G	1.530	5305	254.4	300.6	
-504	2-G	.964	5340	258.6	299.5	
-507	2-G	1.207	5485	262.8	306.2	Ablative chamber**
-508	2-G	1.201	5506	257.5	300.0	Ablative chamber**
-510	2-G	1.206	5645	263.2	306.6	
-511	2-G	1.290	5619	267.1	310.7	Ablative chamber**

CONFIDENTIAL

\*  $I_{sp}$  test data are not corrected for heat transfer losses.  
 \*\*Ablative chamber data slice intervals correspond to the same operating duration as the uncooled thrust chamber tests.

CONFIDENTIAL

(C) The ablative thrust chamber data slice intervals correspond to the same operating durations as the uncooled thrust chamber hardware data points. The test data have not been corrected for heat transfer losses. It is evident from Figure 60 that both of the injector configurations exceed the 300 second specific impulse goal at mixture ratio values of 1.2 and greater. At the 1.2 mixture ratio, the nominal performance of the 2-G configuration is 308 seconds and the nominal performance of the 2-B configuration is 302 seconds.

(C) Evaluation of measured injector performance data and prediction of altitude specific impulse for a 30:1 area ratio nozzle results in the following conclusions:

- Both the 2-B and 2-G injector configurations exceed the contract performance goal at mixture ratios of 1.2 and greater.
- The 2-G injector performance is 7 percent higher than configuration 2-B at the optimum mixture ratio of 1.2.
- The performance of injector configuration 2-B is nearly independent of mixture ratio over an operating range of 1.2 to 1.4.



**CONFIDENTIAL**

## 5. THRUST CHAMBER MATERIALS EVALUATION

(U) The Task 3 Thrust Chamber Materials Evaluation effort was added to the program following the completion of the brief Task 2 injector-chamber compatibility test activity. The objective of this activity was to acquire comparative performance-chamber durability information on all-ablative and throat insert configuration thrust chambers test fired for a common restart duty cycle.

(U) The experimental performance and heat transfer results obtained under Tasks 1 and 2 indicated that the 2-G and the 2-B injector configurations differed approximately 2-percent in delivered performance while the throat heat transfer rates and, consequently, wall recovery temperature differed approximately 20-percent. The recovery temperature at the throat for the 2-G configuration (the higher performing configuration) was approximately 3500°F while the recovery temperature for the 2-B configuration was approximately 3000°F. The differences in performance and heat rejection resulted from variations in oxidizer orifice geometry which affect the forced mixing characteristics of the injector. Dimensional ablation of a soft throat ablative thrust chamber is predicted as non-existent for recovery temperatures up to 3000°F, whereas significant erosion is predicted for recovery temperatures greater than 3400°F. At the higher recovery temperatures, throat inserts can provide an additional margin of erosion resistance. The approach of this effort was to (1) evaluate the performance of the 2-B configuration injector with an all ablative thrust chamber, and (2) to evaluate candidate throat insert materials using the 2-G configuration which had been tested previously with all-ablative chambers in Task 2.

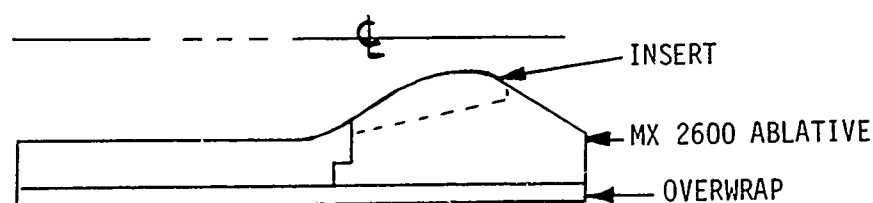
(U) Coincident with the completion of the Task 2 compatibility testing, TRW was conducting an extensive literature and laboratory test evaluation of thrust chamber materials for the Lunar Module Descent Engine Ablative Chamber-Injector Compatibility Improvement Study under contract NAS 9-8229. The results of the comprehensive materials survey, which are reported in Reference 12, revealed a very limited choice of candidate throat insert materials which were available in physical sizes necessary for this program and had also been previously evaluated in rocket engine firings. It was significant that none of the candidate materials had been tested at

**CONFIDENTIAL**

(This page is unclassified)

the chamber pressure and hardware size of this program. Two materials were selected for evaluation in Task 3: JTA graphite and a zirconia reinforced with tungsten-rhenium fibers. The reinforced zirconia material had been developed under a NASA-Lewis Research Center Program (Reference 13 ) and was singularly successful in multiple test firings conducted by NASA-LeRC at 100 psi chamber pressure with  $N_2O_4/50-50 N_2H_4$ -UDMH.

(U) The overall configuration of the three ablative chambers fabricated in Task 3 (one all-ablative and two ablative chambers with throat inserts) were identical to the Task 2 ablative chambers and the same chamber liner retainer hardware was used for testing (see Section 3.6). The general design approach of the Task 3 thrust chambers is illustrated in the following sketch. All three chambers were fabricated with a bonded tongue and groove joint and a glass overwrap.



(U) The throat insert configuration was selected by the reinforced zirconia supplier based on his previous test experience and the specific operating conditions of this program. A thermal stress analysis of the zirconia insert was not performed. The JTA graphite insert configuration was analyzed for thermal-mechanical behavior and is discussed in Section 5.2.

(U) The zirconia insert matrix material was a fine texture zirconia partially stabilized with 2.85% MgO. The reinforcement was 7 volume percent of 2-mil diameter x 1/8" long chopped wire of W-3% Re alloy randomly oriented in the matrix. The insert was fabricated by isostatic pressing at 30,000 psi around a removable metal core. A vacuum cycle of 4 hours at 4000°F was used for sintering the compact. The density of the machined insert was measured by water displacement at 5.9 g/cc which was 90% of theoretical density.

UNCLASSIFIED

(U) The JTA graphite insert was machined from a billet of Union Carbide processed material with the axis of symmetry coincident with the extrusion direction.

#### 5.1 TRANSIENT THERMAL ANALYSIS

(U) The thermal behavior of a reinforced zirconia thrust insert and a JTA throat insert of identical geometry were analyzed to define the temperature gradients for subsequent evaluation of the thermal stress behavior of the JTA insert material. A two-dimensional model of the insert, the surrounding ablative material and the mild steel enclosure was formulated on a Thermal Analyzer Program. Figure 61 shows a sketch of the modelled region and some of the nodes at the interface between the hard throat insert and the surrounding ablative material. The total thermal model was quite detailed and consisted of 158 nodes.

(U) Based on the thermal data reduction studies of Task 2 (see Section 4.3.3), a recovery temperature of 3500°F was used, and it was assumed that the convective heat transfer coefficient was adequately approximated by the standard Bartz relation. The duty cycle investigated consisted of a 90 second burn, a 15 second soak, and a final 5 second burn.

(U) Figure 62 shows the temperature distribution through the zirconia throat insert at various time intervals through the test duty cycle and soakback. It can be seen that initially, due to the low conductivity of the zirconia, there will be a very steep gradient near the inside surface (i.e., gas side surface).

(U) Figure 63 shows the temperature distribution through the JTA parallel graphite throat insert at various time intervals through the test duty cycle. Because of the much higher conductivity of the JTA along the shear planes, as compared to the zirconia, the thermal gradients through the insert are much less steep.

UNCLASSIFIED

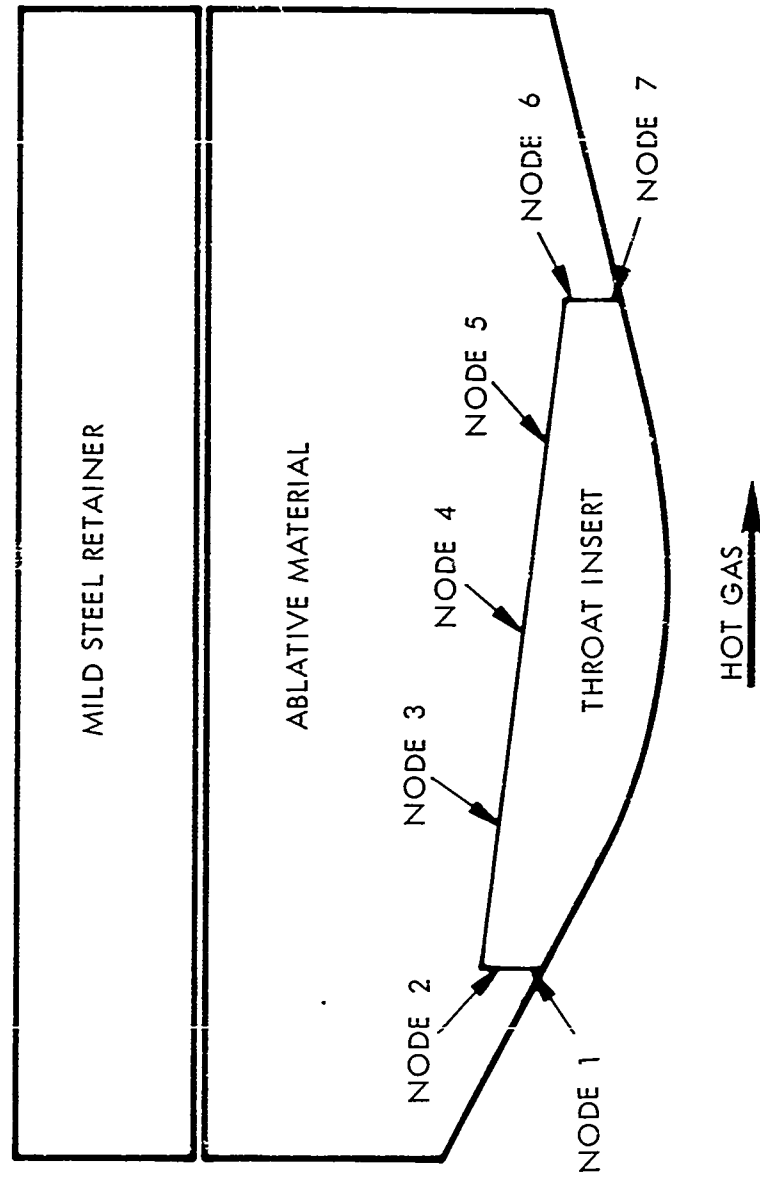


Figure 61. Location of Boundary Nodes on Throat Insert

UNCLASSIFIED

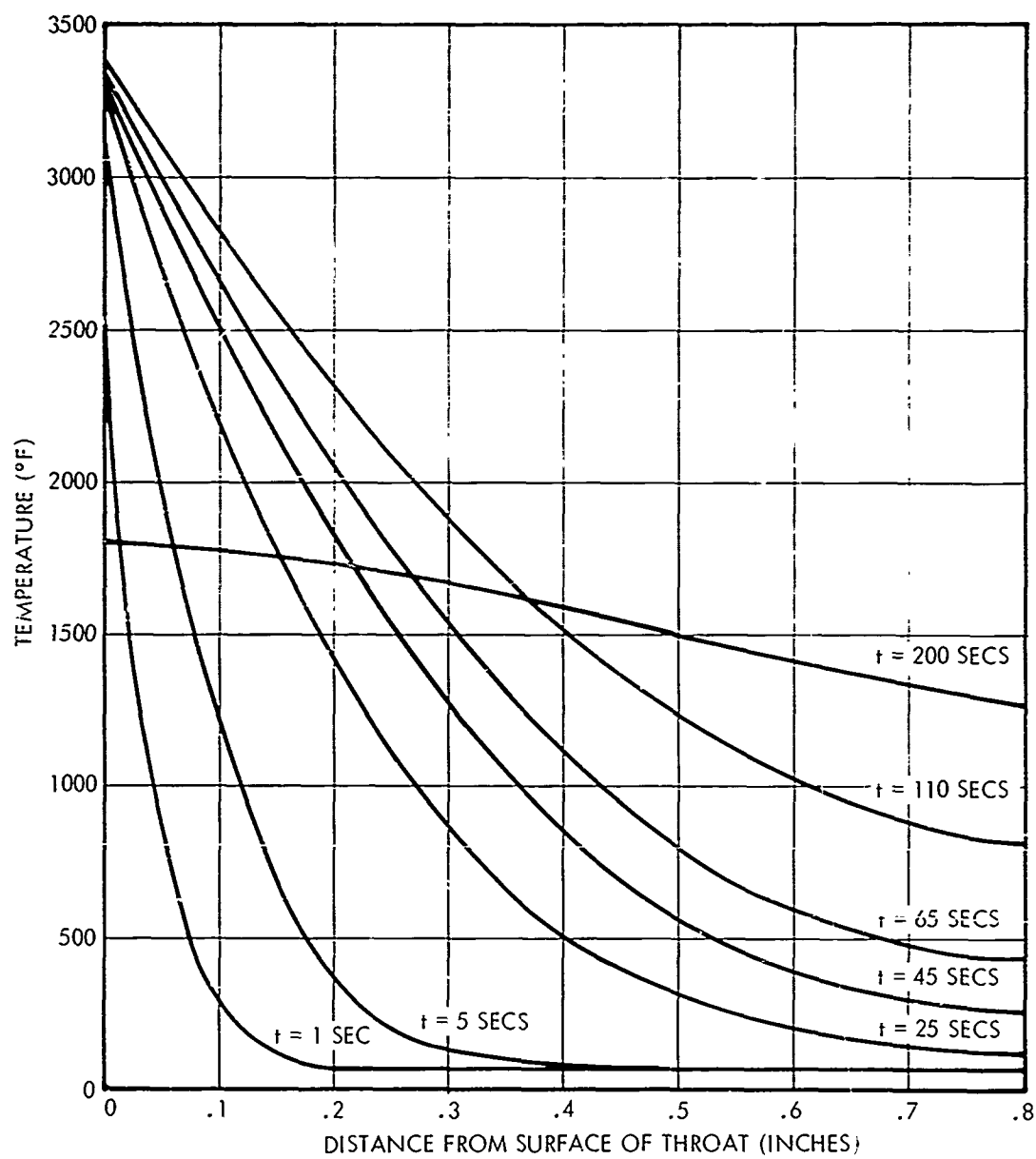


Figure 62. Predicted Temperature Distribution Through Zirconia Throat Insert (U)

UNCLASSIFIED

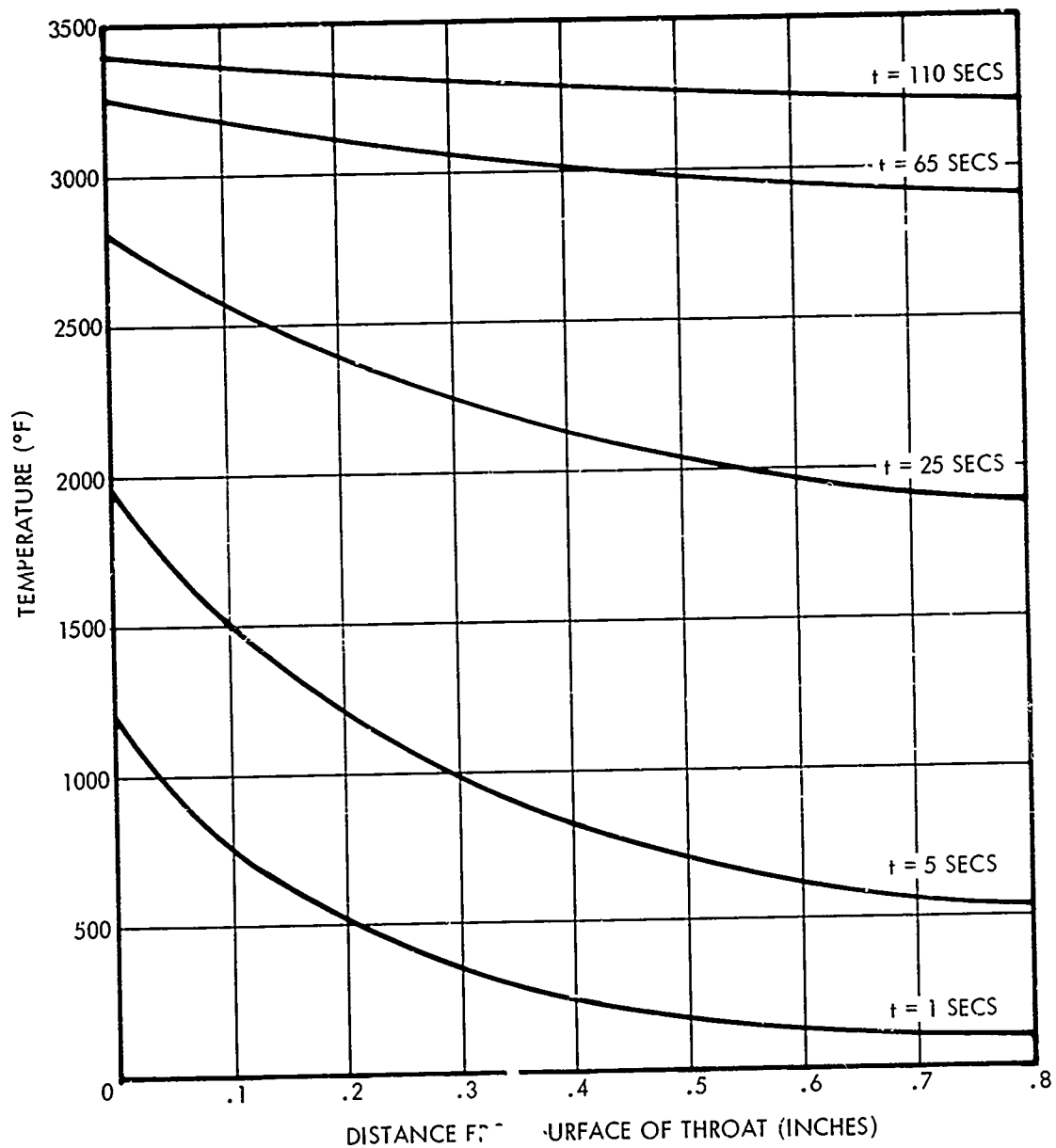


Figure 63. Predicted Temperature Distribution Through JTA Graphite Throat Insert (U)

UNCLASSIFIED

(U) In order to determine the thermal adequacy of the interface between the insert and the surrounding MX 2600 ablative material, temperatures at the interface are presented in Figure 64 for the zirconia insert. During the firing, nodes 1 and 7, located close to the gas-side surface, are predicted to heat up to greater than 3300°F. None of the other interface nodes exceed 2000°F.

(U) Figure 65 shows the predicted interface temperature results for the graphite insert during the test duty cycle. Nodes 1 and 7 rise in temperature slightly less rapidly than for the zirconia insert but exceed 3400°F at the end of the duty cycle. The other nodal locations at the interface approach 3300°F at the end of the duty cycle.

## 5.2 THERMAL STRESS ANALYSIS OF JTA INSERT

(U) A combined experimental and analytical study was conducted to provide information on the probable mechanical behavior of a JTA throat insert. Fracture of the insert due to large thermal stresses or cyclic heating was the primary concern.

(U) Laboratory thermal stress tests were performed on three hollow cylindrical test samples. The heating rates employed and the temperature differentials achieved were comparable to those calculated for an actual JTA throat insert. Each sample was subjected to several heating pulses, all starting from room temperature. The induced thermal stresses and deformations were calculated using the best available stress-strain data for JTA. These calculated stresses were compared with the tensile and compressive strengths of JTA as well as with the calculated stresses based on the predicted temperatures in the thrust chamber insert during a standard heating pulse.

### 5.2.1 Experimental Results

(U) The JTA used to determine the thermal shock behavior of this material was obtained from Union Carbide in 1965 and had been stored at TRW since that time. No details are available concerning the prior history of the material.

UNCLASSIFIED

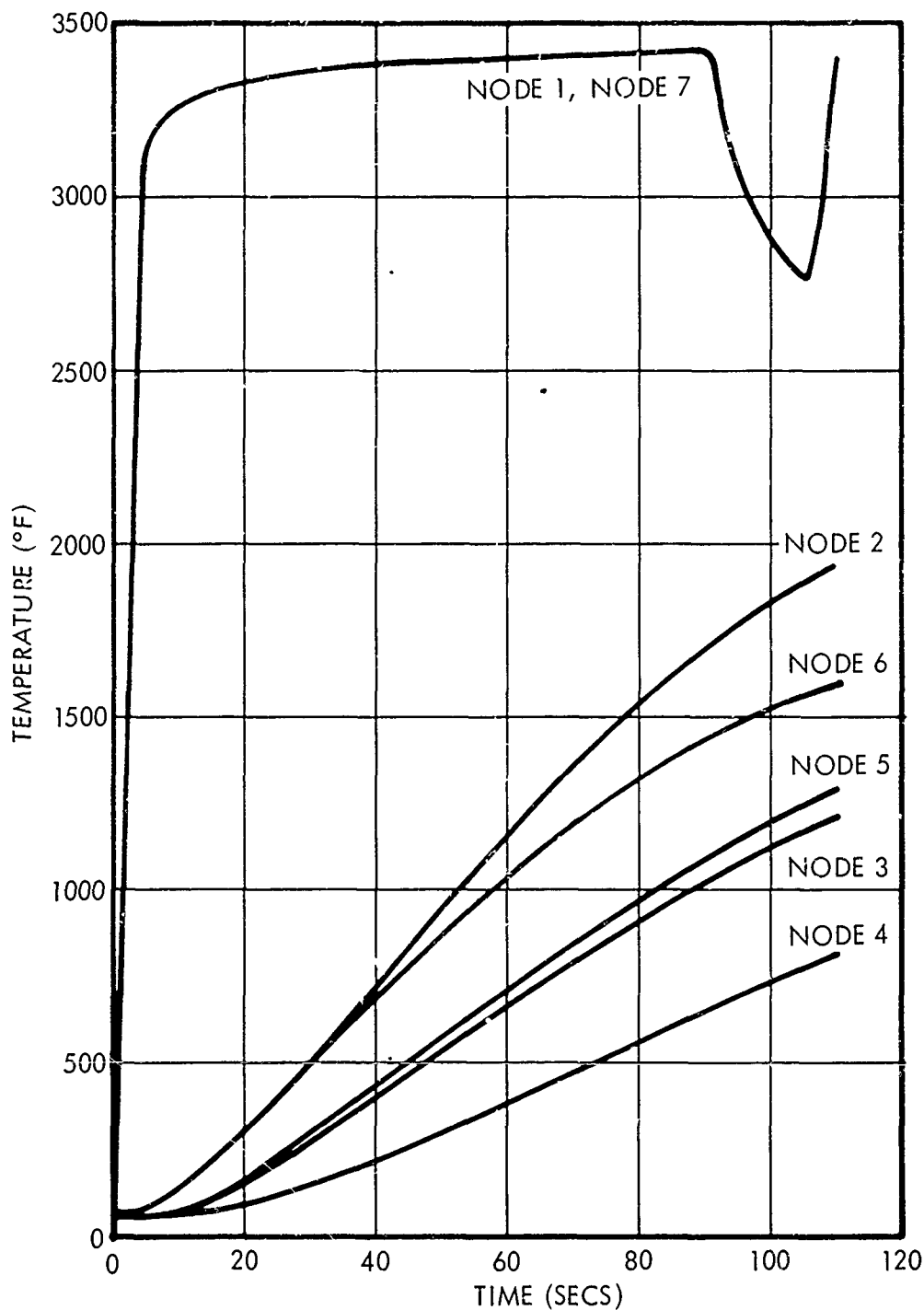


Figure 64. Predicted Temperatures at Boundaries of Zirconia Throat Insert (U)



UNCLASSIFIED

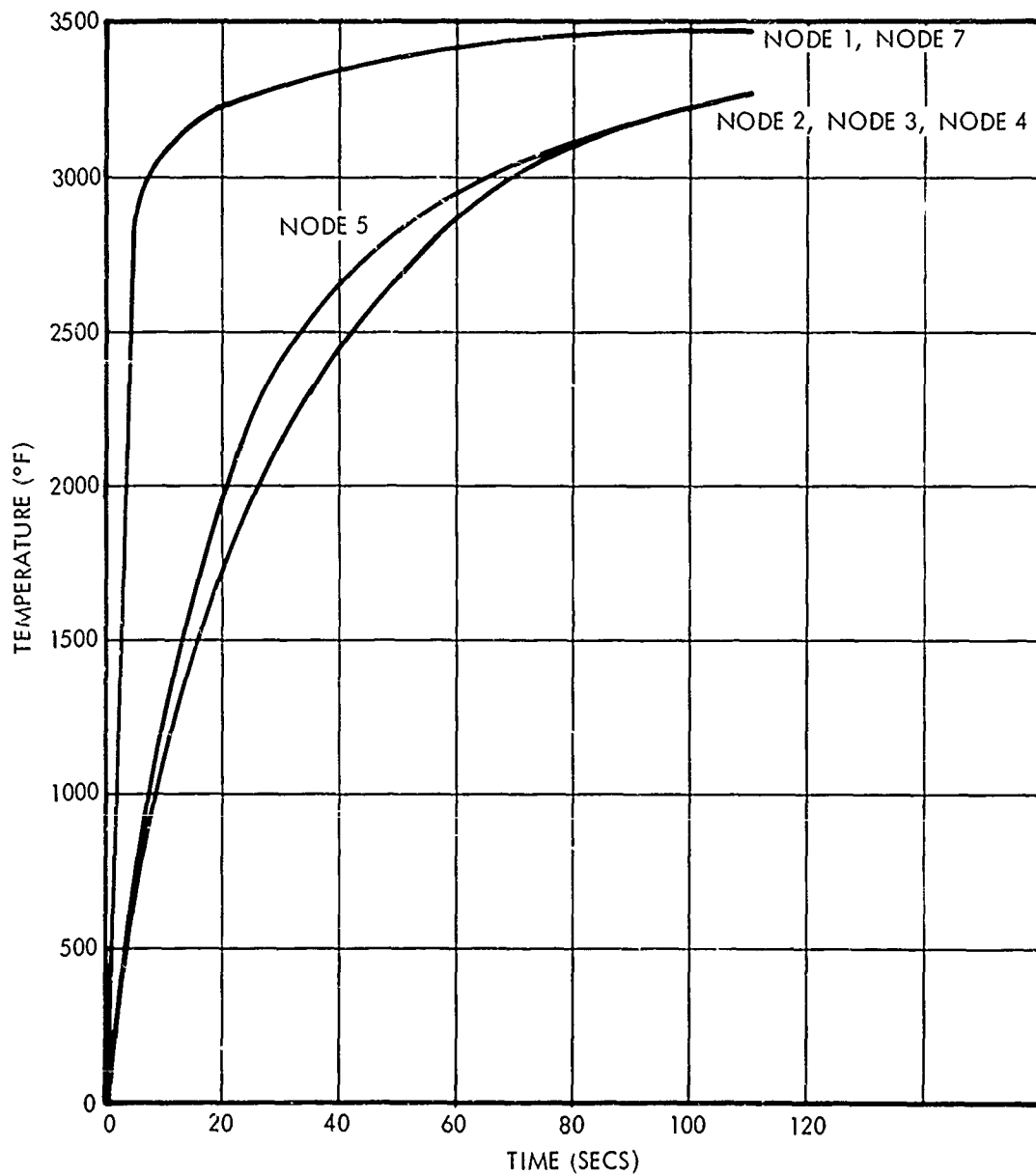


Figure 65. Predicted Temperatures at Boundaries of JTA Graphite Throat Insert (U)

UNCLASSIFIED

(U) Three thermal stress test samples were machined from the original piece obtained; the dimensions of the hollow cylinder test samples were 1/2" high, 1" I.D. and 2" O.D. The samples were heated from the I.D. by electron bombardment as in tests of other materials run and reported previously. In the case of JTA, however, the inside surface of each of the test samples was coated with a thin Ta layer prior to testing to reduce the emissivity and to attempt to keep low melting point constituents at the I.D. from causing difficulties with the electron beam. The Ta formed a TaC layer during bakeout upon reacting with carbon in the JTA.

(U) After coating, three W-W + 26% Re thermocouples were attached to the sample by first spot welding Ti tabs to the samples, then spot welding the thermocouples to the tabs. This procedure was used since it had been established that the thermocouples could not be welded directly to the samples.

(U) The three thermocouples were located at positions near the I.D. (generally about 0.050" from the inside surface), about half way through the wall and near the O.D. The I.D. thermocouple readings do not truly reflect the actual I.D. temperature since they are placed about 50 mils from the surface. However, placing the thermocouple junction directly on the I.D. would result in serious recording problems; based on previous studies the locations chosen were found to be the most acceptable compromise.

(U) The samples were tested by electron bombardment of the I.D. surfaces. During the course of the test, the sample was monitored by recording the three thermocouple outputs, the diameter change and the power supply output. Both analog and digital records of each of the runs were made.

(U) During a typical test run, the electron beam power raises to a preset level, referred to as the peak power over a time span of the order of 0.1 second. As the I.D. of the sample radiates to the filament, the characteristics change, resulting in a gradual lowering of the output power until the power shutdown. This shutdown is accomplished either manually or automatically at a preset time. The power is recorded both as an analog trace

# UNCLASSIFIED

(U) and as a digital output, the digital portion recorded as KW. For the specimen geometry used in this study,  $1 \text{ KW} = .415 \text{ BTU/in}^2 \text{ sec.}$

(U) All three samples survived all of the test cycles without fracturing during the heat-up portion of the cycles but fracture of all three samples was induced during cooling by controlling the temperature histories. Peak power inputs ranged from 18 KW to 75.4 KW or 7.45 to  $31.4 \text{ BTU/in}^2 \text{ sec.}$

(U) Although no effort was made to obtain sample dimension changes to determine if plastic deformations occurred during testing, there is reason to suspect that plastic deformation did take place in JTA resulting in the cracks observed at the I.D. in all three samples. In all cases, the samples did not fracture completely through the wall. This type of cracking is typically found in thermal stress samples that have undergone plastic deformation during testing and which crack due to the stress reversal which occurs at the I.D. after the peak temperature gradients have passed.

(U) The details of each of the tests run for the three samples is given in Appendix B.

## 5.2.2 Stress Analysis

(U) Stresses in both the laboratory specimens and the JTA insert were calculated using a TRW Systems computer program which can be applied either to thin annular discs (plane stress) or long hollow cylinders (plane strain) subjected to an arbitrary radial temperature distribution. By comparing the solutions obtained from these two extreme cases, estimates also can be made of the stresses induced in axially symmetric bodies of intermediate length. Both plasticity and anisotropy are taken into account in the analysis, and all of the material properties are treated as functions of temperature.

(U) The material properties used in the analysis were taken from Reference 14. The coefficients of thermal expansion are fairly well defined but the stress-strain behavior of JTA is subject to interpretation, particularly in regard to plasticity and stress reversal effects. For purposes

# UNCLASSIFIED

of comparison, two sets of stress-strain data were used to calculate the stresses in the insert:

- (1) Plastic. An elastic modulus in the r- $\theta$  direction of  $10.6 \times 10^6$  psi, with a yield stress of 10 ksi, and a modulus in the axial (z) direction of  $4 \times 10^6$  psi, with a yield stress of 7 ksi. The complete stress-strain curves which were used are shown in Figure 66.
- (2) Elastic. An r- $\theta$  elastic modulus of  $7.5 \times 10^6$  psi and an axial modulus of 2.8 psi, with the material assumed to be completely elastic (dashed lines in Figure 66).

In both cases, the Poisson's ratios were taken as .28 for  $\nu_{r\theta} = \nu_{\theta r}$ , and .14 for  $\nu_{z\theta}$  and  $\nu_{zr}$  (stress applied in z direction).

(U) Temperature profiles through the wall during the third heating pulse of Specimen B (43 KW, 5.9 seconds) are shown in Figure 67. Using the plane stress (thin disc) analysis with the "plastic" stress-strain curves, the maximum circumferential tensile stress at the specimen O.D. was calculated to occur at about 2 seconds and to have a magnitude of 11.3 ksi. The peak compressive stress at the I.D. occurred at about 1 second and was 26.0 ksi. These two calculated stress values correspond almost exactly to the published values for the tensile and compressive strength of JTA. As has been pointed out, however, no tensile failures were observed during heat-up in any of the thermal stress tests.

(U) Calculated temperature profiles through the wall of the thrust chamber JTA insert at the throat section also are shown in Figure 67. The temperature differential across the wall of the insert is greatest at about 5 seconds and is equal to about  $1420^\circ$  ( $1950^\circ\text{F}$  to  $530^\circ\text{F}$ ). In comparison at 2 seconds in the thermal stress specimen, the temperature differential across the wall is about  $2150^\circ$  ( $3070^\circ\text{F}$  to  $920^\circ\text{F}$ ).

(U) When these data are used to calculate the peak O.D. tensile stresses in the insert, values ranging from 9 to 14 ksi are obtained, as shown in Figure 66, depending upon whether the plane stress or the plane strain analysis is employed, and also depending upon which stress-strain curves are used. Generally, however, the stresses in the JTA insert will be slightly lower than in the thermal stress specimens. Calculated on the

UNCLASSIFIED

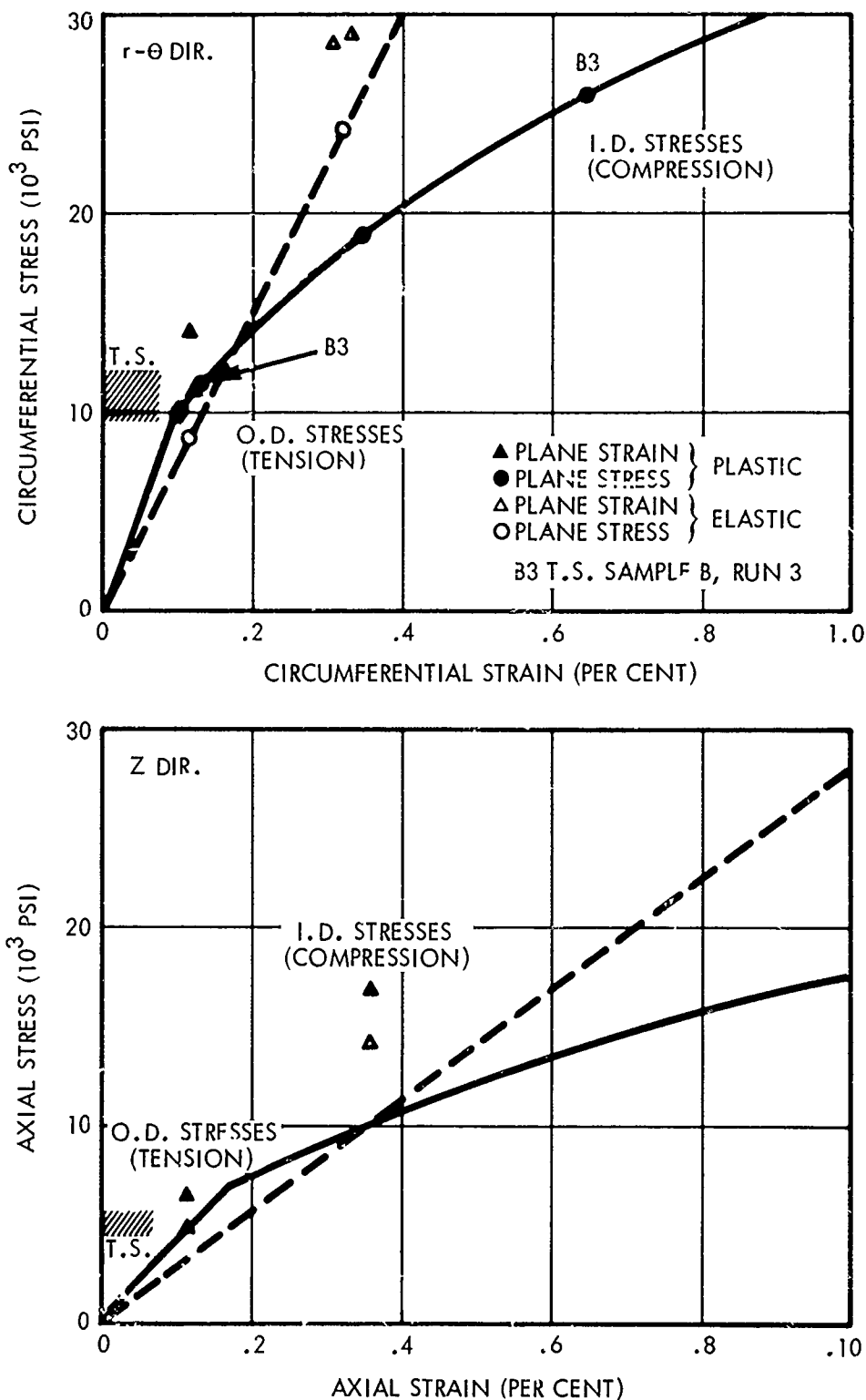


Figure 66. Peak Stresses During Heat-up of JTA Graphite (U)

UNCLASSIFIED

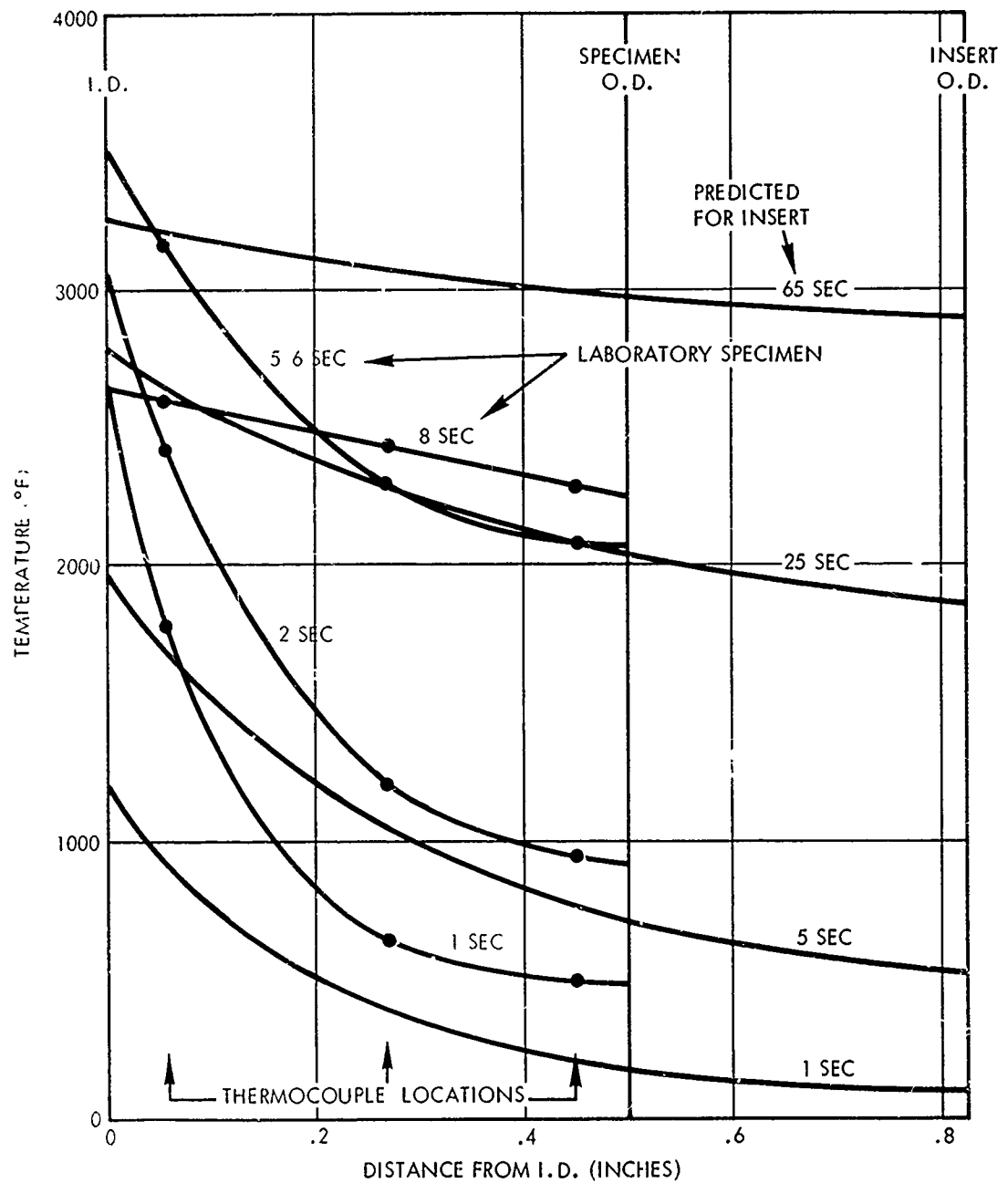


Figure 67. Temperature Profiles Across JTA Walls During Heat-Up (U)

UNCLASSIFIED

(U) same basis as for the thermal stress specimen, the peak O.D. tensile stress in the insert (at 5 seconds) is 10.0 ksi compared to 11.3 ksi in the thermal stress specimen. The peak compressive stress at the insert I.D. is 19 ksi (compared to 26 ksi). The amount of plastic flow at the insert I.D. is only about half as much as in the thermal stress specimen, which means that the probability of cracking at the I.D. is lower.

(U) When the plane strain analysis is used, tensile stresses of 5 to 6 ksi are predicted in the axial direction (at the insert O.D.). The tensile strength of JTA in the axial direction is also in the neighborhood of 5 to 6 ksi.

(U) A comparison between the calculated stresses in the laboratory thermal stress specimens and the thrust chamber insert (based upon measured temperatures and predicted temperatures, respectively) indicates that the laboratory specimens were subjected to a slightly more severe thermal stress environment than the thrust chamber insert is expected to see. There are many unknowns, however, and many factors which could work to produce a less favorable result. The fact that one set of calculated stresses is based upon temperatures obtained from thermocouple measurements while the other is based upon temperatures predicted by a thermal analysis is a difference which is certain to introduce some error into the comparison. Also, the fact that the insert is relatively longer in axial dimension than the thermal stress specimen may cause the circumferential stresses to be slightly higher than indicated by the plane stress comparison and result in axial stresses in the insert more like those predicted by the plane strain analysis. Since the calculated maximum tensile stresses in all cases are right on the borderline of the tensile strength of the material (both circumferential and axial) any such errors or unaccounted-for differences between the two cases could be the cause of a difference in outcome for the thrust chamber insert from that which was predicted.

UNCLASSIFIED

### 5.3 EXPERIMENTAL EVALUATION

(U) The originally planned test duty cycle was 90 seconds on, 15 seconds off, and a 5 second restart and the thermal analyses (see Section 5.1) were made on this basis. However, in the interest of obtaining the maximum of technical information from this task, the AFRPL recommended that the duty cycle be changed to 90 seconds on, 25 seconds off, followed by multiple restarts of 3 seconds on and 8 seconds off. Evaluation of the previously conducted thermal analysis indicated that the JTA insert chamber that had been fabricated to a one-restart design configuration would not survive multiple restarts due to excessively high temperatures at the JTA-ablative interface (see Figure 65). The all-ablative and reinforced zirconia insert thrust chambers did not appear to be similarly limited and the multiple restart duty cycle was adopted for these two units. The original single restart duty cycle was retained for the JTA insert chamber configuration. Figure 68 presents a pre-firing photograph of the three ablative thrust chambers.

(U) A series of six calibration and check-fire tests was conducted with both the 2-B and 2-G oxidizer orifice rings in the same injector in uncooled-chamber hardware. These tests were conducted using the mixture ratio-injector pressure drop ratio matrix employed during Task 1. The performance results were directly comparable to the Task 1 data, as was expected. The time span between completion of Task 2 testing and the start of Task 3 was six months. This series of checkout tests verified both injector and facility operability.

(U) The target injector operating conditions for all three thrust chambers was a mixture of 1.2 with an injection pressure drop ratio ( $\Delta P_{IO}/\Delta P_{IF}$ ) of 1.5. The 2-G configuration oxidizer orifice ring was used for testing the two chambers with throat inserts and the 2-B configuration ring was employed for the all ablative chamber testing. A summary of the Task 3 test results is presented in Table 9. The facility valving configuration was the same as that used during Task 2 (see Figure 52).

(U) The JTA insert chamber (unit 1) was tested for 90 seconds followed by a 5 second restart using the 2-G oxidizer orifice ring. Post-test evaluation of unit 1 revealed cracking of the insert (Figure 69). The instrumentation movies of the test revealed the loss of small particles early in



UNCLASSIFIED

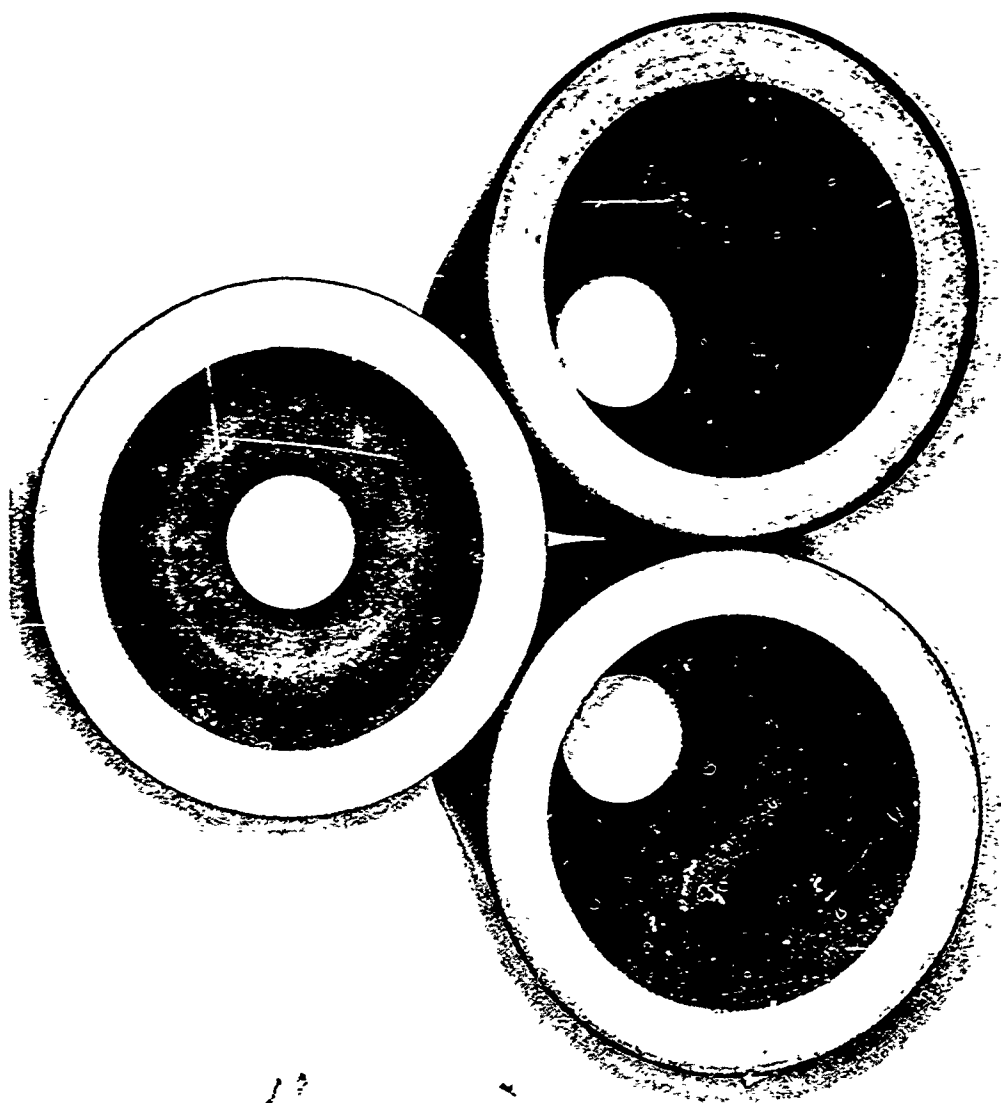


Figure 68. Task 3 Thrust Chambers Prior to Test (Reinforced zirconia insert chamber on the left, JTA insert chamber on the right, all ablative chamber on top.) (U)

UNCLASSIFIED

Table 9. Summary Of Task 3 Thrust Chamber Materials Testing (U)

<u>Order of Testing</u>	<u>Throat Configuration</u>	<u>Injector Configuration</u>	<u>Test Duty Cycle</u>	<u>Comments</u>
Unit 1	JfA	2-G	90 seconds on/15 seconds off, 5 second restart	Insert eroded (see text for discussion)
Unit 2	All Ablative	2-B	90 seconds on/25 seconds off, 5 pulses of 3 seconds on/8 seconds off	No erosion
Unit 3	Reinforced Zirconia	2-G	90 seconds on/25 seconds off, 5 pulses of 3 seconds on/8 seconds off	Insert failed during initial burn.

UNCLASSIFIED

the long duration burn. The square erosion pattern evident in Figure 69 could not be correlated with any injector flow pattern (the injector fuel inlet orientation is noted on Figure 69) and could not be explained. The average decay rate after the initial 10 seconds of operation was 0.5 psi/second. Post-test throat measurements were not made.

(U) Unit 2 (the all ablative chamber) was tested for 90 seconds on, 25 second soak, followed by five restart pulses of 3 seconds on, and 8 seconds off using the 2-B oxidizer orifice ring. The results of this test were highly encouraging as the post-test throat area was slightly less than the pre-test throat area. A post-firing view of the throat as viewed from the nozzle exit is presented in Figure 70. A very slight streak approximately 180° from the injector fuel inlet is evident in Figure 70. However, the operating chamber pressure and the post-test throat diameter measurements both indicated a net shrinkage of the throat.

(U) The reinforced zirconia insert chamber configuration using the 2-G orifice ring was also tested for 90 seconds on, 25 second soak, followed by five restart pulses of 3 seconds on and 8 seconds off. Ejection of particles from the insert was visually observed almost immediately after ignition. A rapid decay in chamber pressure began at approximately 6 seconds elapsed time, and within 35 seconds elapsed time the chamber pressure dropped 95 psi. As the chamber pressure stabilized somewhat with only a 10 psi decrease between 35 seconds and 60 seconds elapsed time, the pre-set duty cycle was allowed to run to completion. A post-firing view of the throat region is presented as Figure 71.

(U) A post-firing evaluation of the zirconia insert material was conducted to determine the failure mechanism. (The location of the sample is identified by an arrow in Figure 71.) The previous zirconia test history at NASA-LeRC, with both smaller and larger throat diameter inserts, at a nominal 100 psia chamber pressure and significantly higher gas recovery temperatures was excellent and the failure on this program was unexpected. Both metallographic and electron probe analyses of the insert material were conducted to compare the zirconia of this program with those previously tested at NASA-LeRC. Unfortunately, the real-time decision to allow the test to continue until the completion of the pre-set duty cycle obscured the cause of the insert failure by allowing the residual ragged edges of the insert to see the full stagnation conditions. The laboratory evaluation results indicated only that the

UNCLASSIFIED

UNCLASSIFIED

AFRPL-1R-69-231  
Page 143

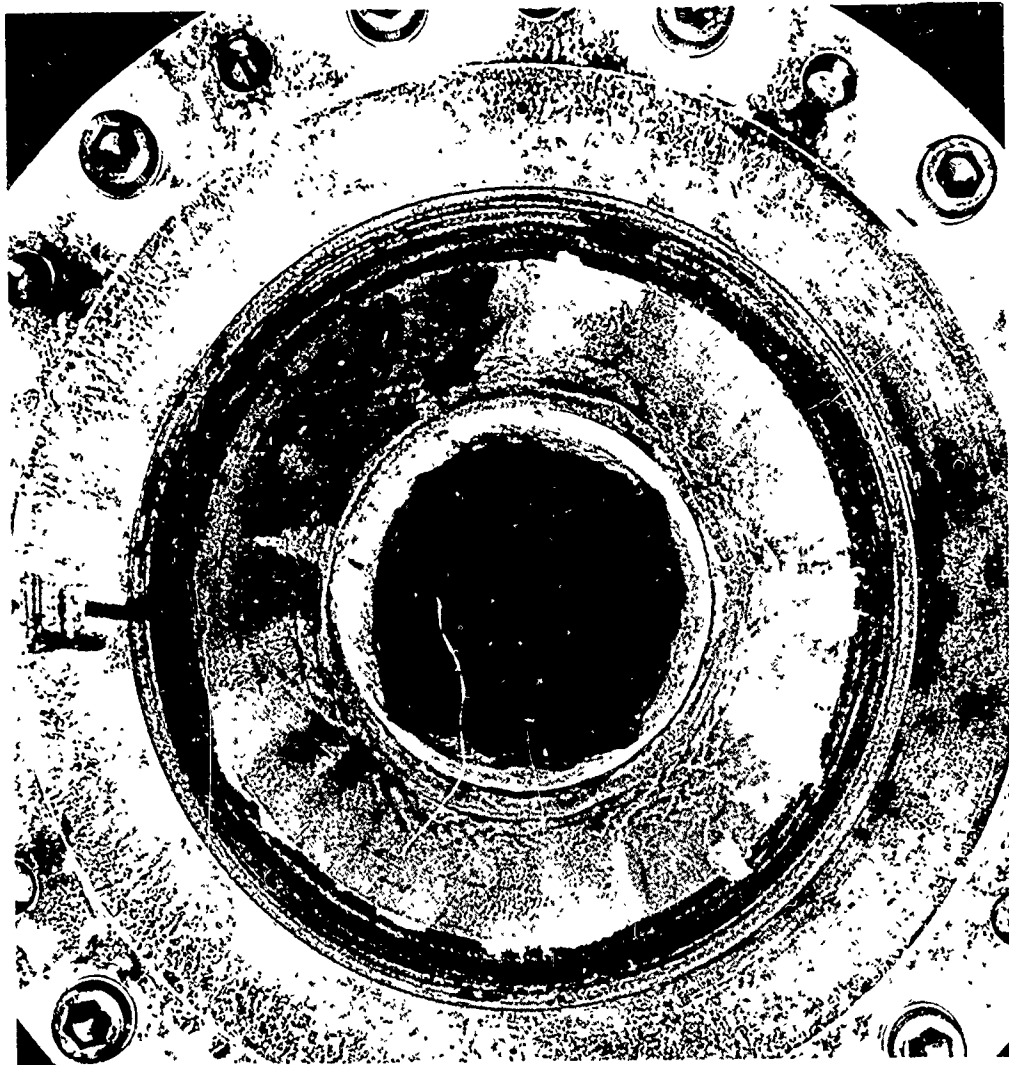


Figure 69. JTA Insert Chamber Post Test (U)

UNCLASSIFIED

UNCLASSIFIED

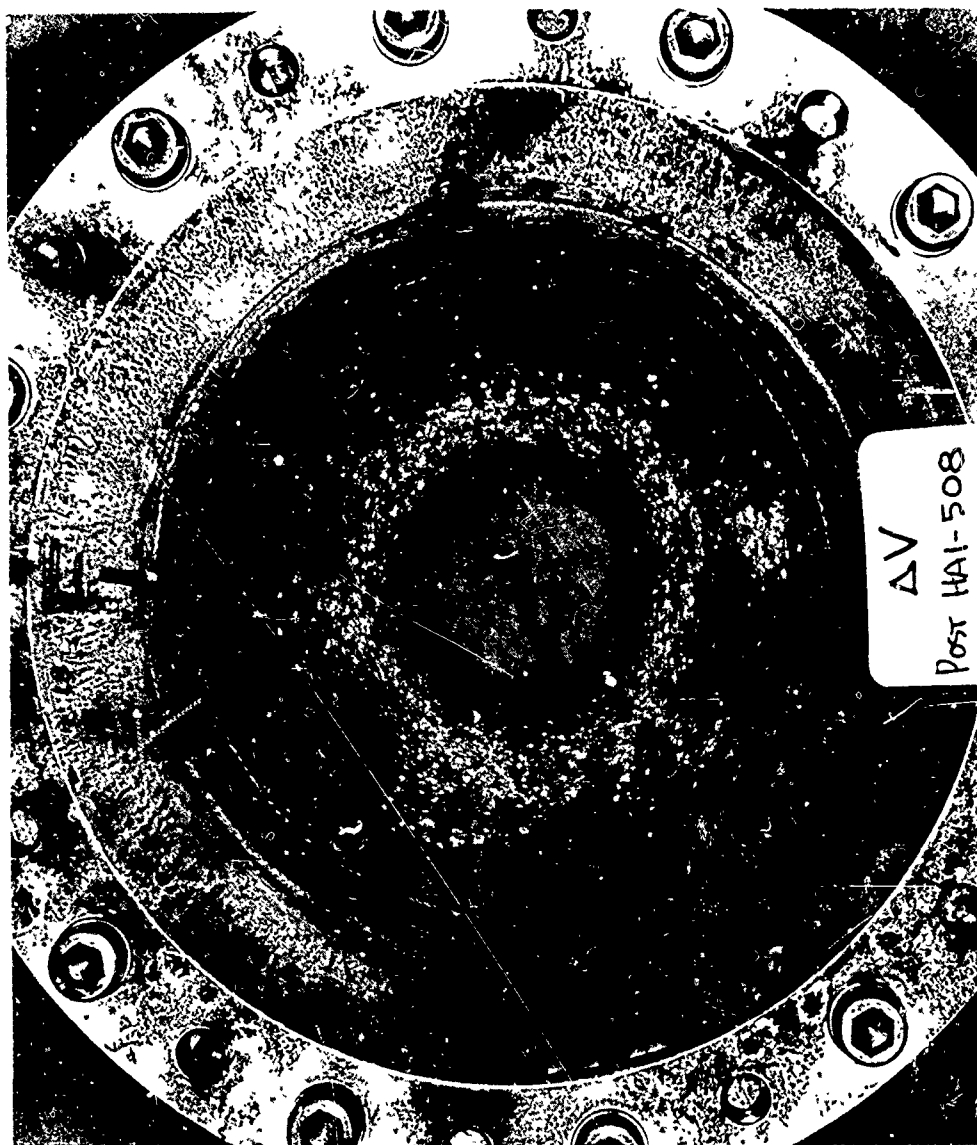


Figure 70. A11 Ablative Chamber Post Test (U)

UNCLASSIFIED

UNCLASSIFIED

AFRPL-TR-69-231  
Page 145

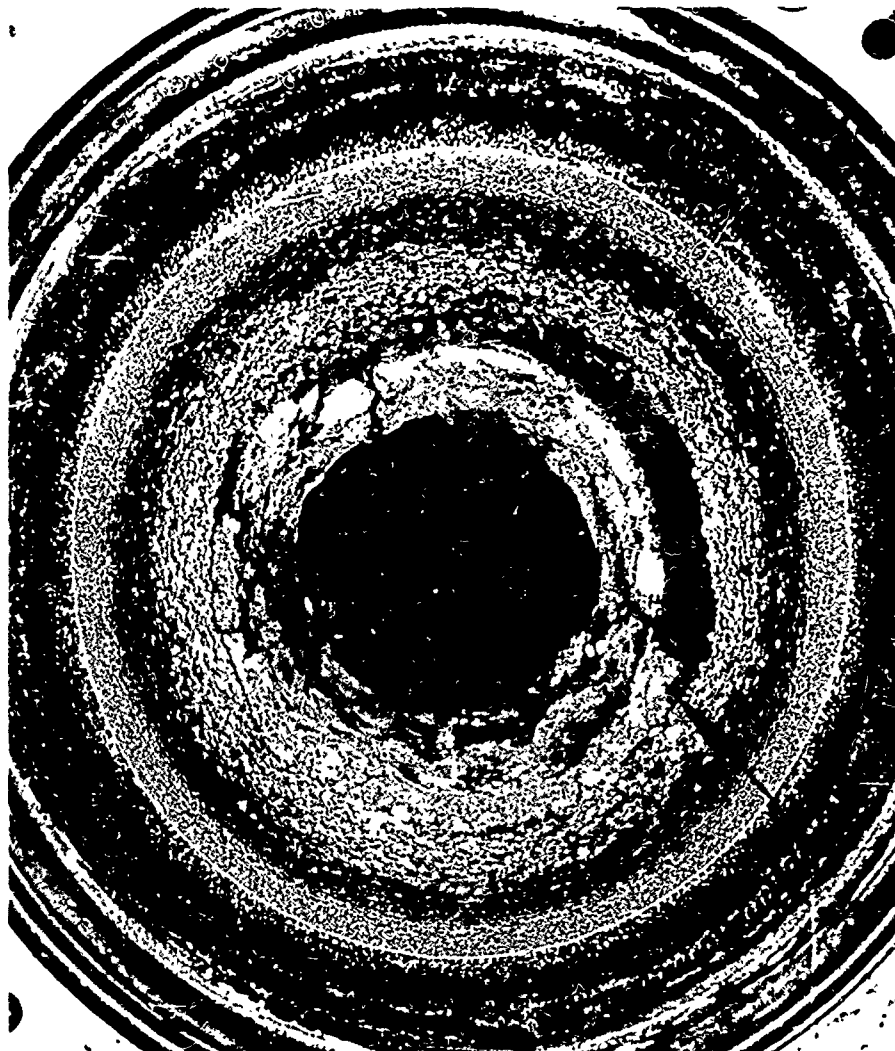


Figure 71. Zirconia Insert Chamber Post-Test (U)

UNCLASSIFIED

UNCLASSIFIED

(U) specimen analyzed had been exposed to temperatures approaching stagnation conditions. Therefore, it must be concluded that the substantial difference in hot firing performance of reinforced zirconia resulted from the 300 psia chamber pressure of this program.

(U) The results of the Task 3 chamber testing demonstrated that a performance/chamber durability match of the 2-B injector configuration and an all ablative thrust chamber configuration is achievable and verified the Task 1 chamber wall environment prediction. A comparable performance/chamber durability match with the 2-G injector configuration will require additional injector tuning and thrust chamber material evaluation. The overall results were highly encouraging due to the demonstrated state-of-the-art capability improvements in chamber operating lifetime at 300 psia chamber pressure in 3,000 lb<sub>f</sub> thrust size hardware and at high combustion performance levels.

UNCLASSIFIED

6. INJECTOR RELIABILITY AND MAINTAINABILITY

(U) Previous sections of this report have discussed the program achievements in relation to the performance, mixture ratio variability, dynamic stability, and injector-chamber compatibility goals. The potential utilization of this injector concept in an advanced weapons system application additionally requires that the reliability and maintainability inherent in the design approach be demonstrated as early as possible in the development cycle. This section presents an evaluation of the program accomplishments in relation to the reliability (operability and durability) of the injector hardware and associated maintainability history.

(U) The formal demonstration of specific reliability levels and maintainability characteristics was not a goal of the  $N_2O_4/N_2H_4$  injector development program. However, attainment of the required program goals did entail a large number of engine firings on slightly varying engine configurations and accumulated long operating duration experience for an exploratory development program. The successful completion of a large number of engine starts on very similar configurations does indicate what reliability levels could be expected from a production program where field utilization missions require a large number of starts.

(U) The overall program test history was as follows:

	Number of Starts (Tests)	Cumulative Duration
Heat Sink Thrust Chamber Hardware (Tasks 1 and 3)	143	430 seconds
Ablative Thrust Chambers (Tasks 2 and 3)	21	480 seconds
Company-Sponsored Tests Subsequent to Task 3	<u>16</u>	<u>120 seconds</u>
	180	1030 seconds



**UNCLASSIFIED**

(U) All injector configurations except Configuration 3 (the swirl concept) were considered similar enough to be representative of the selected configuration for the purposes of reliability evaluation. Two (2) malfunctions occurred during the 175 applicable test starts which were chargeable to the injector. Two (2) chargeable failures in 175 engine starts demonstrates a start probability  $> .984$  at a 50% confidence level based on binomial sampling techniques. Inclusion of the two chargeable engine failures probably presents too conservative an estimate of reliability levels to be expected from a production program since they are attributable to the bolt-up pintle configuration. One-piece construction would be utilized in a production program thereby eliminating this particular failure mode and enhancing maintainability procedures by emphasizing simplicity, and ease of part installation, inspection, and removal. By the elimination of these failure modes an engine start probability  $> .996$  at a 50% confidence level could be expected in a development program. The test experience acquired during the Task 3 and company-sponsored firings accumulated over 460 seconds of injector operation in 44 starts (20 of which were restarts) without injector discrepancies of any nature is an excellent demonstration of injector durability, operability, and restartability.

(U) It is also equally significant that no acoustic combustion instabilities, either self-triggered or induced, were encountered during this program. (The coaxial injector concept has never experienced acoustic combustion instability with any propellant combination at any hardware size.)

(U) The injector developed under this program was specifically designed for flexibility and ease of maintenance which permitted complete disassembly and re-assembly in a manner of minutes. However, once a specific oxidizer orifice element is selected, the injector is singularly free of service requirements and remains in a ready state. The injector was routinely purged, flushed, and re-purged at the conclusion of each test series and stored in a non-controlled environment until required for the next test series. The longest period of storage was six (6) months. The storage life of the existing hardware is limited only by the life of the O-ring seals. The storage life of an all-welded injector design would be virtually unlimited.

**UNCLASSIFIED**

## 7. CONCLUSIONS

(U) The major conclusions drawn from the  $N_2O_4/N_2H_4$  Injector Development and Demonstration Program are as follows:

1. The program met or exceeded all contract goals for performance, mixture ratio variability, dynamic stability, and injector/chamber compatibility.
2. Multiple hot restarts with the hydrazine fuel were successfully demonstrated.
3. Injector steady state/restart durability was conclusively demonstrated.
4. The injector design conditions controlling the thrust chamber wall environment were defined and verified by long-duration ablative chamber tests.
5. The overall versatility of the single-element coaxial injector as an engine development tool was confirmed.

UNCLASSIFIED

REFERENCES

1. Weiss, R. R., "An Introduction to Combustion Instability in Liquid Rocket Engines," Technical Report AFRPL-TR-66-150, July 1966.
2. Elverum, G., and Staudhammer, P., "The Effect of Rapid Liquid Phase Reactions on Injector Design and Combustion in Rocket Motors," Progress No. 30-4, Jet Propulsion Laboratory, Pasadena, California.
3. Rupe, J., "On The Dynamic Characteristics of Free Liquid Jets and a Partial Correlation with Orifice Geometry," JPL Technical Report No. 32-207, 1962.
4. AFRPL-TR-69-14 "Influence of Storable Propellant Liquid Rocket Design Parameters on Combustion Instability." Jan. 1969, C.J. Abbe, C. W. McLaughlin, & R. R. Weiss.
5. Houseman, J., "Combustion Effects in Sprays", CPIA Publication No. 183, December 1968, pages 255-261.
6. Lawver, B.R., "An Experimental Study of the  $N_2O_4/N_2H_4$  Jet Separation Phenomena", CPIA Publication No. 183, December 1968, pages 263-270.
7. AFRPL-TR-68-18, "Improvement of Bombs and Pulse Guns as Stability Rating Devices," March 1968. Rocketdyne Div., North American Rockwell Corp.
8. Elliot, D. G., Bartz, D. R., and Silver, S., "Calculation of Turbulent Boundary-Layer Growth and Heat Transfer in Axisymmetric Nozzles," JPL Technical Report No. 32-387, 15 February 1963.
9. J. L. Pieper, "ICRPG Liquid Propellant Thrust Chamber Performance Evaluation Manual," CPIA Report No. 178, September 1968.
10. Kliegel, J.R., "One Dimensional Reacting Gas Nonequilibrium Performance Program," TRW Systems Report No. 02874-6003-R000, March 1967 (revised September 1967).
11. Kliegel, J. R. and Quan, V., "Axisymmetric Reacting Gas Nonequilibrium Performance Program," TRW Systems Report No. 02874-6004-R000, March 1967 (revised September 1967).
12. TRW Report 11602-6022-R0-00, "Materials Survey for the Apollo Lunar Module Descent Engine Ablative Chamber - Injector Compatibility Improvement Study," March 1969, R. E. Parsons et al.
13. NASA CR-54984, "Improved Throat Insert for Ablative Thrust Chambers," D. N. Crump et al, September 1968.
14. S. A. Bortz, "Properties of JTA Graphite," AFML-TR-68-178, July 1968.

UNCLASSIFIED

## APPENDIX A

## CALCULATION OF ENGINE PERFORMANCE

(U) The index of engine performance for the experimental program will be the corrected characteristic velocity ( $C^*$ ) or characteristic velocity efficiency ( $\eta_{C^*}$ ) for the sea level tests and the corrected specific impulse ( $I_{sp}$ ) for the altitude tests. The  $C^*$  is calculated by two independent methods, one based on the measurement of chamber pressure and the other on the measurement of thrust. The  $I_{sp}$  is calculated from the measurement of thrust and propellant flow rates. Details of the computational procedures and of the applied corrections are given in the following sections.

### 1. CHARACTERISTIC VELOCITY-CHAMBER PRESSURE TECHNIQUE

(U) Characteristic velocity based on chamber pressure is defined by the following:

$$\eta_{C^*} = \frac{(P_c)_o (A_t)_{\text{eff}} g_c}{(\dot{w}_T) (C^*)_{\text{theo}}} \quad (\text{A-1})$$

where

- $(P_c)_o$  = stagnation pressure at the throat
- $(A_t)_{\text{eff}}$  = effective thermodynamic throat area
- $g_c$  = conversion factor (32.174 lbf-ft/lbf-sec<sup>2</sup>)
- $\dot{w}_T$  = total propellant weight flow rate
- $(C^*)_{\text{theo}}$  = theoretical characteristic velocity based on shifting equilibrium

Values calculated from Equation (A-1) are referred to as "corrected"  $C^*$  efficiencies, because the factors involved are obtained by application of suitable influence factor corrections to measured parameters. Stagnation pressure at the throat is obtained from measured static pressure at start of nozzle convergence by assumption of isentropic expansion, effective throat area is estimated from measured geometric area by allowing for geometrical radius changes during firing and for nonunity discharge coefficient, and chamber pressure is corrected to allow for energy losses

UNCLASSIFIED

(U) from combustion gases to the chamber wall by heat transfer and friction.

Equation (A-1) may therefore be written as follows:

$$\eta_{C^*} = \frac{P_c A_t g_c f_p f_{TK} f_{DIS} f_{FR} f_{HL} f_{KE}}{(\dot{w}_o + \dot{w}_f) (C^*)_{theo}} \quad (A-1)$$

where

- $P_c$  = measured static pressure at start of nozzle convergence, psia
- $A_t$  = measured geometric throat area, in<sup>2</sup>
- $g_c$  = conversion factor (32.174 lbf-ft/lbm-sec<sup>2</sup>)
- $\dot{w}_o$  = oxidizer weight flow rate, lb/sec
- $\dot{w}_f$  = fuel weight flow rate, lb/sec
- $(C^*)_{theo}$  = theoretical C\* based on shifting equilibrium calculations, ft/sec
- $f_p$  = influence factor correcting observed static pressure to throat stagnation pressure
- $f_{TR}$  = influence factor correcting for change in throat radius during firing
- $f_{DIS}$  = influence factor correcting throat area for effective discharge coefficient
- $f_{FR}$  = influence factor correcting measured chamber pressure for frictional drag of combustion gases at chamber wall
- $f_{HL}$  = influence factor correcting measured chamber pressure for heat losses from combustion gases to chamber wall
- $f_{KE}$  = influence factor correcting C\* values to account for finite chemical reaction rates

Methods of estimation of the various correction factors are described in the following paragraphs.

#### 1.1 Pressure Influence Factor ( $f_p$ )

(U) Measured static pressure at start of nozzle convergence is converted to stagnation pressure at the throat by assumption of effectively no combustion in the nozzle and application of the isentropic flow equations, with contraction ratio ( $A_c/A_t$ ) and shifting-equilibrium specific heat ratios ( $\gamma$ ). Frozen-equilibrium specific heat ratios usually make the influence correction factor about 1/2 percent larger. Hence, the value

UNCLASSIFIED

(U) employed with shifting equilibrium is the more conservative. Figure A-1 shows the influence factor as a function of contraction ratio.

### 1.2 Throat Radius Influence Factor ( $f_{TR}$ )

(U) Temperature gradients produced at the solid metal nozzle wall result in thermal stresses which affect throat radius, with the result that the geometric throat diameter ambient measurement is not the same as that which exists during firing.

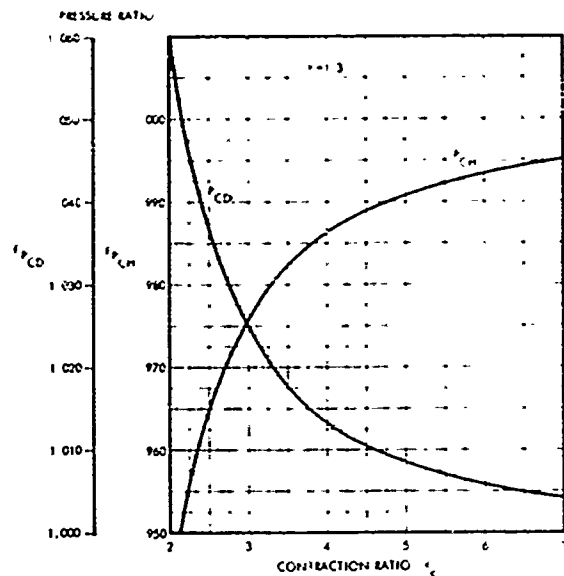


Figure A-1 Momentum Correction

(U) For certain types of nozzles thermal penetration of the nozzle wall at the initiation of firing is small with respect to the wall thickness, hence the outer wall diameter is unchanged. The inner wall material will therefore expand toward the center, resulting in a decrease in throat diameter. As heat penetrates throughout the nozzle wall, the outer diameter will also increase, allowing outward expansion of the inner portion and consequent increase in throat diameter. Therefore, throat diameter during firing is a function of time, as well as of the physical properties of the throat material and the temperature and pressure of the combustion gases.

(U) The actual computation is based upon integration of transient thermal stress equations for a hollow cylinder. A relatively simple expression results by assuming parabolic temperature distribution.

#### 1.2.1 Thermal Effects

(U) Since performance is influenced also by throat area changes, attention should be directed primarily to this zone of the thruster. With monomaterial construction, the throat effects can be analyzed with reasonable accuracy. It can be shown that throat shrinkage and expansion

UNCLASSIFIED

(U) effects for such nozzles can be estimated from the following for parabolic temperature distributions:

$$dr = \alpha \left[ \frac{1+\nu}{1-\nu} \right] \frac{T_i - T_o}{(R_o - R_i)^2} \left[ \frac{R_o^2 R_i}{2} - \frac{2}{3} R_o R_i^2 + \frac{R_i^3}{4} - \frac{R_o^4}{12 R_i} \right] \quad (A-3)$$

where

$R_i$  = inner wall radius

$R_o$  = outer wall radius

$\alpha$  = coefficient of linear expansion of wall material

$\nu$  = Poisson's ratio of wall material

$T_i$  = Temperature of inner wall

$T_o$  = Temperature of outer wall

The temperature distribution is given by

$$T = a + br + cr^2 \quad (A-4)$$

and is estimated by the method of Reference D-1. The throat shrinkage effects manifest themselves at the initiation of firing. For long steady-state firings, the throat size may actually increase, depending upon the temperature distribution and resultant stresses. Plastic as well as elastic deformations are readily included, as well as gas pressure effects.

(U) For chambers employing thin wall throats the thermal growth is more easily obtained from the thermal expansion based on the temperature change from ambient temperature. The change in throat area can be written as:

$$A_{th} = \frac{\pi}{4} (2 + \alpha \Delta T) (\alpha \Delta T) D^2$$

where

$\Delta A^*$  = change in throat area due to thermal growth

$\alpha$  = average thermal expansion coefficient

$\Delta T$  = temperature rise from ambient conditions

$D$  = throat diameter at ambient conditions

UNCLASSIFIED

(U) The throat area correction factor is as follows:

$$f_{TR} = 1 + \frac{\Delta A_{th}}{A_{th}}$$

$$= (1 + \alpha \Delta T)^2 \quad (A-6)$$

(U) The thermal expansion coefficient for copper is  $\alpha_{Cu} = 9.8 \times 10^{-6}$  in/in-°F, assuming an ambient temperature of 70°F, the throat area correction factor becomes

$$f_{TR} = \left[ 1 + 9.8 \times 10^{-6} (T_{th} - 70) \right]^2 \quad (A-7)$$

This equation was used to generate the curve in Figure A-2.

### 1.3 Throat Discharge Coefficient Influence Factor ( $f_{DIS}$ )

(U) The discharge coefficient is defined as the ratio of actual flow rate through the throat to the theoretical maximum, based on geometric throat area and ideal, uniform, one-dimensional flow with no boundary layer.

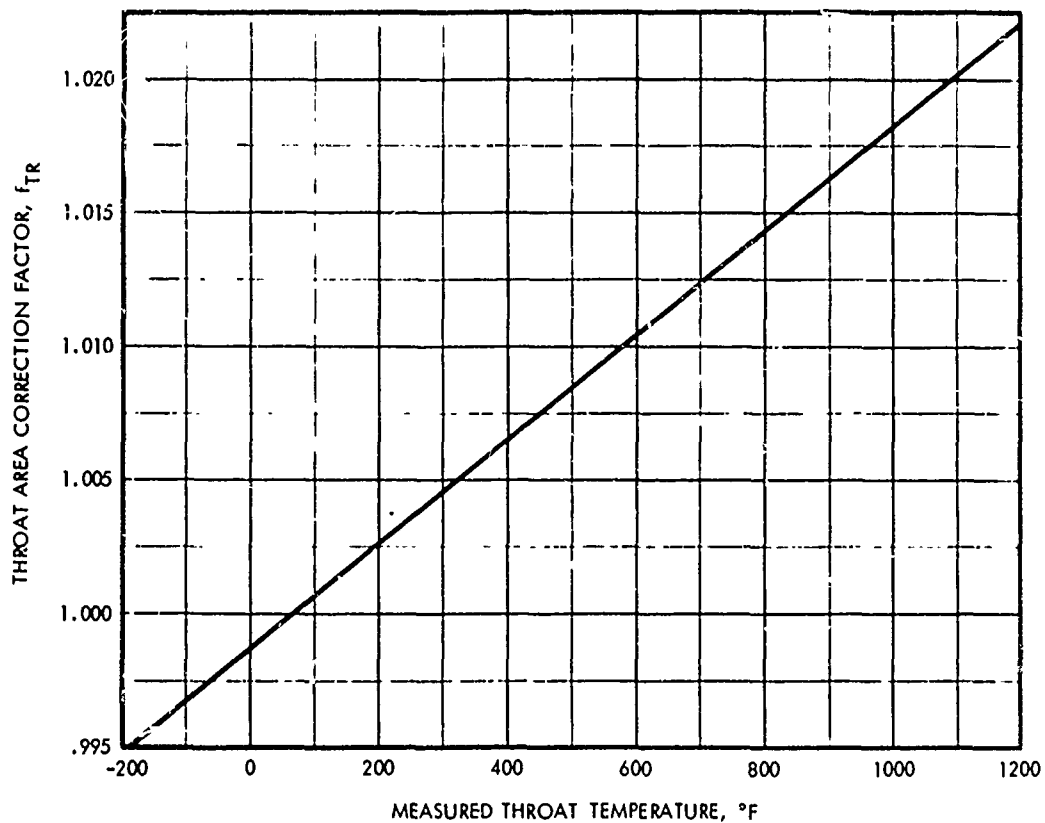


Figure A-2 Throat Area Correction Factor



UNCLASSIFIED

(U) The discharge influence coefficient may be estimated in two ways: one based on calculations made from a theoretical, inviscid flow model of combustion products, and the other based on a correlation of results obtained in various experimental study results of air flow through nozzles of similar geometry.

### 1.3.1 Theoretical Model

(U) Total mass flow rate is given by

$$\dot{m} = \int_0^A \rho V dA \quad (A-8)$$

where

$\rho$  = gas density

$V$  = gas velocity

$A$  = cross-sectional area

Theoretical maximum flow rate at the throat is

$$\dot{m}_{\max} = \int_0^{A_t} \rho^* V^* dA \quad (A-9)$$

where

$A_t$  = geometric area of the throat

$\rho^*$  = sonic gas density

$V^*$  = sonic gas velocity

For ideal, uniform, parallel flow, Equation (A-8) becomes

$$\dot{m}_{\max} = \rho^* V^* A_t \quad (A-10)$$

The discharge coefficient is then

$$C_D = \frac{\dot{m}}{\dot{m}_{\max}} = \int_0^A \left( \frac{\rho}{\rho^*} \right) \left( \frac{V}{V^*} \right) \left( \frac{dA}{A_t} \right) \quad (A-11)$$

### 1.3.2 Empirical Value

(U) Experimental conical nozzle discharge coefficients obtained with air by various investigators are plotted in Figure A-3 against the indicated geometric parameter. Data sources also are listed in Figure A-3.

UNCLASSIFIED

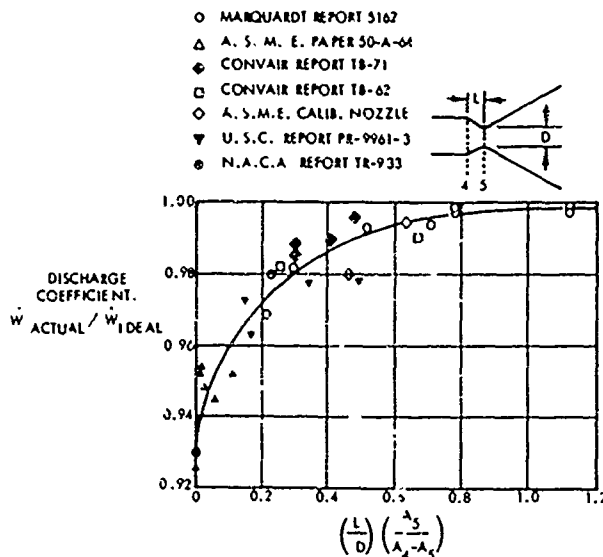


Figure A-3. Conical Nozzle  
Discharge Coefficient

(U) The values obtained by both methods are found to be in excellent agreement.

#### 1.4 FRICTIONAL DRAG INFLUENCE FACTOR ( $f_{FR}$ )

(U) Calculations of  $C^*$  based on chamber pressure are concerned with chamber phenomena up to the nozzle throat. Drag forces to this point are small enough to be considered negligible, so that the factor  $f_{FR}$  may be taken to be unity.

#### 1.5 Energy Loss Influence Factor ( $f_{HL}$ )

(U) Chamber pressure and thrust are decreased by heat transfer from the combustion gases to the walls of a thrust chamber. This enthalpy loss is substantially reduced in ablative chambers and is effectively recovered in a regeneratively cooled chamber.

(U) The effect on  $C^*$  of enthalpy loss by heat transfer can be estimated from a loss of chamber enthalpy. This is determined from a two station energy balance, one at the start of nozzle convergence and the other at the throat which

$$\frac{1}{2} V_c^2 + H_c = \frac{1}{2} V_t^2 + H_t + \dot{Q}_{conv} \quad (A-12)$$

where

- $V_c$  = gas velocity at chamber exit
- $V_t$  = gas velocity at nozzle throat
- $H_c$  = gas enthalpy at chamber exit
- $H_t$  = gas enthalpy at nozzle throat
- $\dot{Q}_{conv}$  = heat loss in nozzle convergence

Velocity at the throat is given by:

$$V_t = [V_c^2 + 2(H_c - H_t - \dot{Q}_{conv})]^{1/2} \quad (A-13)$$

UNCLASSIFIED

With negligible nozzle inlet velocity

$$V_t = [2(H_c - H_t - \dot{Q}_{conv})]^{1/2} \quad (A-14)$$

Logarithmic differentiation of Equation (A-14) gives

$$\frac{dV_t}{V_t} = 1/2 \frac{d(H_c - H_t - \dot{Q}_{conv})}{(H_c - H_t - \dot{Q}_{conv})} = 1/2 \left( \frac{dH_c - dH_t}{H_c - H_t - \dot{Q}_{conv}} \right) \quad (A-15)$$

Substitution of enthalpy definition into Equation D-15 gives:

$$\frac{dV_t}{V_t} = 1/2 \left( \frac{c_{pc} dT_c - c_{pt} dT_t}{H_c - H_t - \dot{Q}_{conv}} \right) \quad (A-16)$$

With constant  $C_p$  between the two stations,

$$\frac{dV_t}{V_t} = 1/2 \left( \frac{c_p dT_c}{H_c - H_t - \dot{Q}_{conv}} \right) 1 - \left( \frac{dT_t}{dT_c} \right) \quad (A-17)$$

If the specific heat ratio,  $\gamma$ , is assumed constant,

$$\frac{dT_t}{dT_c} = \frac{T_t}{T_c} \quad (A-18)$$

Substituting Equation (A-18) into Equation (A-17), replacing differentials by incrementals, and noting that  $C^*$  is proportional to gas velocity at the throat gives:

$$\frac{\Delta V_t}{V_t} = \frac{\Delta C^*}{C^*} = 1/2 \left( \frac{c_p \Delta T_c}{H_c - H_t - \dot{Q}_{conv}} \right) 1 - \left( \frac{\Delta T_t}{T_c} \right) \quad (A-19)$$

Total heat loss to the chamber walls, in Btu per pound of propellant, is obtained by summation of observed heat fluxes over the appropriate areas:

$$\text{Heat loss} = \frac{\sum(q/A) A}{\dot{w}_T} \quad (A-20)$$

where

- $q/A$  = experimentally observed heat flux
- $A$  = area applicable to each  $q/A$  value
- $\dot{w}_T$  = total propellant flow rate

UNCLASSIFIED

If this heat loss is equated to the change in enthalpy of the gas in the combustion chamber,  $c_p \Delta T_c$ , then substitution in Equation (A-19) gives:

$$\frac{\Delta C^*}{C^*} = 1/2 \left[ \frac{\Sigma(q/A)A}{\dot{w}_T} \right] \left[ \frac{1 - (T_t/T_c)}{H_c - H_t - Q_{conv}} \right] \quad (A-21)$$

The applicable influence factor is

$$f_{HL} = 1 + \frac{\Delta C^*}{C^*} = 1 + 1/2 \left[ \frac{\Sigma(q/A)A}{\dot{w}_T} \right] \left[ \frac{1 - (T_t/T_c)}{H_c - H_t - Q_{conv}} \right] \quad (A-22)$$

(U) An alternate expression can be obtained from the basic  $C^*$  definition:

$$C^* = \frac{\sqrt{RT_c}}{\Gamma} \quad (A-23)$$

Logarithmic differentiation of this yields:

$$\frac{dc^*}{c^*} = \frac{1}{2} \frac{dT_c}{T_c} \quad (A-24)$$

Substituting incrementals from differentials in Equation (A-24) gives:

$$\frac{\Delta c^*}{c^*} = \frac{1}{2} \frac{\Delta T_c}{T_c} \quad (A-25)$$

Equating  $\Delta T_c$  with the heat loss from Equation (A-20) results in the following:

$$\frac{\Delta c^*}{c^*} = \frac{1}{2} \left[ \frac{\Sigma(q/A)A}{\dot{w}_t} \right] \left[ \frac{1}{c_p T_c} \right] \quad (A-26)$$

The applicable influence factor is:

$$f_{HL} = 1 + \frac{1}{2} \left[ \frac{\Sigma(q/A)A}{\dot{w}_t} \right] \left[ \frac{1}{c_p T_c} \right] \quad (A-27)$$

where

$c_p$  = specific heat at constant pressure

UNCLASSIFIED

(U) Although derived independently it can be shown that these two expressions, Equations (A-22) and (A-27), are nearly equivalent.

### 1.6 Influence Factor for Chemical Kinetics ( $f_{KE}$ )

(U) The effect of finite chemical reaction rates is to produce a  $C^*$  less than the corresponding theoretical equilibrium values. A TRW Systems developed one-dimension nonequilibrium reacting gas computer program is employed with reaction rate constants selected for the propellant system. The fluid mechanical and chemical equations are integrated from the inlet section by an implicit technique.

## 2. CHARACTERISTIC VELOCITY-THRUST TECHNIQUE

(U) The alternate determination of  $C^*$  efficiency is based on thrust:

$$\eta_{C^*} = \frac{F_{vac} g_c}{(C_F)_{vac} \dot{w}_T C^*_{theo}} \quad (A-28)$$

where

- $F_{vac}$  = measured thrust corrected to vacuum conditions  
by the equation:  $F_{vac} = F + P_a A_e$
- $F$  = measured thrust, lbf
- $P_a$  = ambient pressure, psia
- $A_e$  = area of nozzle exit, in<sup>2</sup>
- $g_c$  = conversion factor (32.174 lbf-ft/lbf-sec<sup>2</sup>)
- $(C_F)_{vac}$  = theoretical shifting thrust coefficient (vacuum)
- $\dot{w}_T$  = total propellant flow rate, lbf/sec
- $C^*_{theo}$  = theoretical shifting-equilibrium characteristic  
velocity, ft/sec

Values of vacuum thrust are obtained by applying corrections to sea-level measurements. With these values, which include allowances for all important departures from ideality, theoretical thrust coefficients may be used for calculation of  $C^*$ .  $C_F$  efficiency is taken as 100 percent if there is no combustion in the nozzle, if chemical equilibrium is maintained in the nozzle expansion process, and if energy losses from the combustion gases are accounted for.

UNCLASSIFIED

(U) Applicable influence factors for measured thrust are specified in the following equation:

$$\eta_{C^*} = \frac{(F + P_a A_e) g_c \phi_{FR} \phi_{DIV} \phi_{HL} \phi_{KE}}{(C_F)_{theo} (\dot{W}_o + \dot{W}_f) (C^*)_{theo}} \quad (A-29)$$

where

- $F$  = measured thrust, lbf
- $P_a$  = ambient pressure, psia
- $A_e$  = area of nozzle exit, in<sup>2</sup>
- $g_c$  = conversion factor (32.174 lbf-ft/lbm-sec<sup>2</sup>)
- $(C_F)_{theo}$  = theoretical shifting thrust coefficient (vacuum)
- $\dot{W}_o$  = oxidizer flow rate, lbm/sec
- $\dot{W}_f$  = fuel flow rate, lbm/sec
- $(C^*)_{theo}$  = theoretical shifting equilibrium characteristic velocity, ft/sec
- $\phi_{FR}$  = influence for frictional losses
- $\phi_{DIV}$  = influence factor for nozzle divergence
- $\phi_{HL}$  = influence factor for heat losses to chamber and nozzle walls
- $\phi_{KE}$  = influence factor correcting  $C^*$  and  $C_F$  values to account for finite chemical reaction rates

The influence factors in Equation (A-29) are applied to vacuum thrust  $(F + P_a A_e)$  instead of to measured static thrust ( $F$ ) because, for convenience, the factors are readily calculated as changes in efficiency based on theoretical vacuum parameters. The total influence factor is then of the form  $\Delta F/F_{vac}$ .

(U) Implicit in the use of theoretical  $C_F$  values are corrections to geometric throat area and to measured static chamber pressure at start of nozzle convergence. Therefore, calculation of corrected  $C^*$  efficiency from thrust measurement includes all the previously described corrections plus an additional one to account for nonparallel nozzle exit flow. However, because  $(C_F)_{theo}$  is essentially independent of small changes to chamber pressure and contraction ratio which are involved in corrections to  $P_c$  and  $A_t$ , these corrections are of no practical significance in calculation of  $C^*$  from thrust measurements.

UNCLASSIFIED

## 2.1 Influence Factor for Frictional Drag ( $\phi_{FR}$ )

(U) This factor corrects for energy losses caused by viscous drag forces on the thrust chamber walls. Its magnitude is estimated by a boundary layer analysis utilizing the integral momentum equation for turbulent flow, which accounts for boundary layer effects from the injector to the nozzle exit by suitable description of the boundary layer profile and local skin friction coefficient. A computer program is used to carry out a numerical integration of the equation, including effects of pressure gradient, heat transfer, and surface roughness. The program requires a potential nozzle flow solution obtained from variable-property, axisymmetric method of characteristics calculation of the flow field outside the boundary layer; corresponding properties for the subsonic combustion chamber flow field are also calculated.

## 2.2 Influence Factor for Nozzle Divergence ( $\phi_{DIV}$ )

(U) The one-dimensional theoretical performance calculations assume that flow at the nozzle exit is uniform and parallel to the nozzle axis. The influence factor,  $\phi_{DIV}$ , allows for nozzle divergence (i. e., for nonaxial flow) and for nonuniformity across the nozzle exit plane. It is calculated by a computer program which utilizes the axisymmetric method of characteristics for a variable-property gas. Computation begins with a transonic input near Mach 1, providing a characteristic line for use in the analysis of the supersonic portion of the nozzle. The resulting pressures are integrated over the given geometry to give the geometric efficiency.

## 2.3 Influence Factor for Heat Loss ( $\phi_{HL}$ )

(U) To obtain the heat loss influence factor from measured thrust the approach is identical to that taken previously from the pressure measurement, except that the nozzle losses must also be included. With constant specific heat and gamma from start of nozzle convergence to exit, Equation (D-22) becomes

$$\phi_{HL} = 1 + \frac{1}{2} \left[ \frac{\sum \left( \frac{q}{A} \right) A}{\dot{w}_T} \right] \left[ \frac{1 - T_e/T_c}{H_c - H_e - Q_{nozzle}} \right] \quad (A-30)$$

UNCLASSIFIED

(U) when "e" corresponds to the exit condition, and the summation occurs over the entire combustion.

An alternate can also be derived as in Equation (D-27). This equation becomes

$$\phi_{HL} = 1 + \frac{1}{2} \left[ \frac{\sum (q/A)A}{w_T} \right] \left[ \frac{1}{c_p T_e} \right] \quad (A-31)$$

#### 2.4 Influence Factor for Chemical Kinetics ( $\phi_{KE}$ )

(U) The effect of finite chemical reaction rates is to produce a  $C^*$  and  $C_F$  less than the corresponding theoretical equilibrium values. A TRW Systems developed one-dimensional nonequilibrium reacting gas computer program is employed with reaction rate constants selected for the propellant system. The fluid mechanical and chemical equations are integrated from the inlet section by an implicit technique.

### 3. DELIVERED SPECIFIC IMPULSE AND THRUST COEFFICIENT

(U) Specific impulse is defined by the following:

$$I_{sp}(\text{vac}) = \frac{F_{\text{vac}}}{\dot{w}_t} \quad (A-32)$$

where

$F_{\text{vac}}$  = measured thrust corrected to vacuum conditions  
by the equation:  $F_{\text{vac}} = F_{\text{meas}} + P_a A_e$

$F_{\text{meas}}$  = measured thrust, lbf

$\dot{w}_t$  = total propellant flowrate, lbm/sec

$P_a$  = ambient pressure, psia

$A_e$  = area of nozzle exit, in<sup>2</sup>

(U) The thrust coefficient is a measure of the nozzle performance and is given by

$$C_F(\text{vac}) = \frac{F_{\text{vac}}}{P_c A_t} = \frac{I_{sp}(\text{vac})}{C^*} g_c \quad (A-33)$$



UNCLASSIFIED

APPENDIX B

JTA THERMAL STRESS SPECIMENS TEST LOG

(U) The following paragraphs describe the individual test conditions of the three laboratory thermal stress specimens.

Sample A

(U) This sample was given six runs ranging in peak power input from 18 to 67.3 KW. The first three runs were all fairly long in duration compared to the last three. After the third run, the melted area at the I.D. precluded further testing, so the I.D. was removed by machining and recoated with Ta prior to the other three runs. Details of the six runs are given below.

Run 1

The sample was run for 14.5 seconds with a peak power of 18 KW. At power shutdown, the inside thermocouple was reading 3410°F while the outside was 2930°F. No fracture of the sample was observed, either visually or by studying the circumferential extensometer trace.

Run 2

Because of arcing, the initial heat-up of the sample was slower than in Run 1 even though the peak power was 23 KW. The test duration was 43.5 seconds at which time the center thermocouple was at 3350°F and the outer thermocouple at 3150°F; the inside thermocouple shorted during the test run. No fracture was observed.

Run 3

The test time for this run was 19.6 seconds with a peak power of 27.5 KW. The inside thermocouple again shorted, this time at 10.3 seconds into the run when the temperature was 3220°F. At power shutdown, the center thermocouple was at 3230°F and the outside thermocouple at 3040°F. After this run, the sample

UNCLASSIFIED

was removed from the test chamber and examined. No evidence of fracture was noted. Previously molten material as discussed above was observed on the I.D. of the sample.

After post-test examination, the TaC layer was removed by machining, the sample was re-coated and testing continued.

#### Run 4

In an attempt to initiate fracture in this sample, the power supply was pre-set to shut down when the maximum temperature gradient existed. From previous tests, this time was determined to be 1.6 seconds. The re-coated sample ran better than had been expected so that at 1.6 seconds, the  $\Delta T$  had already reached a maximum and was decreasing. Peak power was 62.2 KW.

Melting was observed at 0.7 seconds when the I.D. thermocouple was reading 1880°F. At power shutdown, the I.D. thermocouple reading was 2240°F, the middle was 1260°F and the O.D. was 910°F. Visual observation of the cooled sample from outside the test chamber revealed no cracking.

#### Run 5

The same time was used for this run as the previous run, 1.6 seconds, with a peak power of 67.3 KW. Melting began at 0.4 seconds when the I.D. thermocouple reading was 1260°F.

At power shutdown, the I.D. thermocouple reading was 2110°F, the center was 1220°F and the O.D. was 890°F. No discontinuities were found in the extensometer trace, although visual observation of the sample indicated that perhaps a crack existed. Based on the extensometer data, it was decided to give the sample at least one more run before opening the test chamber.

UNCLASSIFIED

Run 6

The sample was run for 1.09 seconds with a peak power of 65.2 KW. Melting was observed at 0.5 seconds when the I.D. thermocouple was 1550°F. At power shutdown, the I.D. thermocouple reading was 2000°F, the center was 970°F, and the O.D. was 630°F.

Again the extensometer showed no discontinuities indicative of cracking but it was decided to open the test chamber for a close visual observation. Two very fine cracks were found extending from the I.D. to a depth of about 0.1 inch. One of the cracks was in the position identified after Run 5 as a possible crack site. It is therefore highly likely that at least one of the cracks was present prior to the last run.

Sample B

(U) The five runs on this sample ranged in peak power from 32 KW to 60 KW. As in the previous test sample, melting occurred which lowered the input power at the onset of melting. A single crack was observed after the fifth run. The details of each of the five runs are given below.

Run 1

The first run was the longest in duration on this sample, 16.5 seconds, with a peak power level of 32 KW. Heat-up was relatively slow. At 3.5 seconds, instability in the power trace indicative of melting was observed. At that time, the inside thermocouple was 2690°F. The inside thermocouple shorted out before the completion of the run. At power shutdown, the center thermocouple was at 3120°F while the O.D. thermocouple was 3090°F.

Run 2

The initial heat-up on this run was quite good with a peak power of 40 KW. The test was terminated at 3.0 seconds due to melting and the resultant power supply instability. At power shutdown, the I.D. thermocouple was 2550°F, the center was 1520°F and the O.D. was 1260°F.

UNCLASSIFIED

Run 3

The run duration was 5.9 seconds with a peak power of 43 KW. Melting was observed at 1.3 seconds when the I.D. thermocouple was at 2140°F. At power shutdown, the I.D. thermocouple reading was 3160°F, the center was 2320°F and the O.D. was 2090°F.

Run 4

This run had the highest peak power, 60 KW, of the five runs on this sample. Melting started at 0.6 seconds. No I.D. temperature information was obtained due to shorting of the thermocouple. At power shutdown (6.8 seconds) the center thermocouple was 2650°F while the O.D. was 2370°F.

Run 5

This run was intended to be at 80 KW. However, the heat-up was very poor with melting occurring at 0.7 seconds so the maximum desired power level was never reached. The maximum power level was about 50 KW. The power was shut down at 14.9 seconds when the I.D. thermocouple was 3570°F, the center was 3160°F and the O.D. was 2990°F.

After the fifth run, visual examination through the bell jar test chamber showed that the sample had cracked. The crack had not been observed prior to the fifth run, although no discontinuities in the extensometer record of the fifth run indicative of cracking were found. A close check of extensometer records of earlier runs also showed no discontinuities which could be interpreted as cracking.

In contrast to Sample A, the crack extended about 0.25 inch from the I.D.; i.e., about half way through the thickness of the wall.

UNCLASSIFIED

Sample C

(U) This sample was given a total of eight runs at peak power levels ranging from 38.5 KW to 75.4 KW with fracture occurring subsequent to the eighth run. Melting problems similar to those observed with previous samples were again evident. After the fourth run, the TaC layer and melted material were machined off the I.D., the sample re-coated with Ta and run four more times.

(U) Since it had not been definitely established in the previous samples when the observed cracking occurred, the system was opened after each run and this sample was examined closely for any evidence of cracking. The fracture was determined to have occurred on cooling during the eighth run both by visual observation and by a study of the extensometer records. The details of each run are given below.

Run 1

No temperature data was obtained on this run which was 6 seconds in duration with a peak power of 38.5 KW. Melting started 2 seconds into the test.

Run 2

This run was of 3.0 seconds duration with a peak power of 50.2 KW. Melting started at 1.0 second when the I.D. thermocouple reading was 2000°F. At power shutdown, the I.D. thermocouple reading was 2250°F, the center was 1840°F and the O.D. was 1650°F.

Run 3

Melting occurred 0.5 seconds into a 5.0 second test with a peak power of 65.0 KW. The I.D. thermocouple reading at the onset of melting was 1960°F. At power shutdown, the I.D. thermocouple was 2880°F, the center was 2370°F and the O.D. was 2090°F.

Run 4

Melting occurred in this run at 0.4 seconds, at which time the power curve had not yet peaked out. The maximum power attained

UNCLASSIFIED

just prior to the onset of melting was 75.4 KW, while the I.D. thermocouple reading was 1190°F. Considerable arcing occurred prior to melting. Power shutdown occurred at 2.5 seconds; the I.D. thermocouple reading was 2330°F, the center was 1490°F and the O.D. was 1200°F.

Because of the severe melting problems, the sample was removed from the test chamber and the TaC layer machined off the I.D. surface. A new Ta layer was deposited and the thermocouples spot welded in approximately their original positions.

#### Run 5

The heating characteristics for this run were considerably improved over the previous run, undoubtedly due to the removal of the previously melted I.D. surface. Peak power was 64.8 KW.

"New" melting occurred at 1.0 second when the inside thermocouple reading was 1680°F. The test duration was 3.0 seconds at which time the I.D. thermocouple was 2340°F, the center was 1630°F, and the O.D. was 1420°F.

#### Run 6

This run was made in an attempt to induce cracking into the sample by following the test conditions of Run 5, Sample B. The run time was 15.3 seconds with a peak power level of 70 KW. Melting started at 0.5 second when the I.D. thermocouple was reading 1460°F. At power shutdown, the I.D. thermocouple was 3320°F, the center was 3200°F and the O.D. was 3110°F. No cracks were found. Based on this test, it was concluded that perhaps fracture in Sample B had not occurred on the fifth run but during an earlier run.

#### Run 7

Inducing fracture by shutting down the power supply when the temperature differential was at a maximum was attempted using a peak power of 73.4 KW. The temperature difference was monitored

UNCLASSIFIED

visually from thermocouple traces during the test duration of 6.0 seconds. Post-test examination of the thermocouple traces showed that the maximum  $\Delta T$  had occurred at 1.6 seconds, long before power shutdown. The entire sample was hot at power shutdown, the I.D. thermocouple reading 3290°F, the center reading 2590°F and the O.D. reading 2360°F. These test conditions did not cause cracking to occur.

The typical melting problems were also encountered with melting starting at 0.4 seconds when the I.D. thermocouple was reading 1280°F.

#### Run 8

Test conditions used in Run 7 were duplicated except that power shutdown was pre-set at 1.6 seconds, at which time the I.D. thermocouple was reading 1930°F, the center was 1060°F and the O.D. was 850°F. The heating portions of these two runs were nearly identical up to power shutdown.

At 3.7 seconds (during cooling) the continuity of the extensometer trace was interrupted. The type of behavior observed is typical of cracking of the test sample. Post-test examination showed that the sample had cracked in two places nearly 180 degrees apart during this run. The cracks extended from the I.D. about two-thirds of the way to the O.D.

UNCLASSIFIED

DOCUMENT CONTROL DATA - R & D		
1. CONTRACT OR GRANT NUMBER N00019-68-1-0010		
2. REPORT TITLE Development and Demonstration of an $N_2O_4$ Injector		
3. PERIOD OF REPORT 1 April 1968 through 15 August 1968		
4. AUTHOR(S) A. C. Carter and A. S. Bell		
5. REPORT DATE October 1968	6. TOTAL NO. OF PAGES 14	7. NO. OF PAGES 14
8. CONTRACT OR GRANT NO. N00019-68-1-0010	9. DOES THIS REPORT COVER: None	
10. PROJECT NO. 3.58	11. OTHER REPORT NO. (If any other numbers that may be assigned this report) None	
12. STATEMENT In addition to security requirements which must be met, this document is subject to special export controls and each transmittal to foreign governments or foreign nationals may be made only with prior approval of AFRL/ASST/SHIN-01, Edwards, California 93523		
13. SUPPLEMENTARY NOTES None	14. SPONSORING/MONITORING AGENCY Air Force Rocket Propulsion Laboratory Air Force Systems Command Edwards, California	
15. ABSTRACT (U) A fifteen-month program was conducted to develop and demonstrate a single-element coaxial injector with $N_2O_4$ at the 3000lbf thrust level. The optimum injector configuration and one variant was employed in multiple-start, long-duration ablative chamber tests. The durability of the final injector configuration was demonstrated by over 460 seconds of operation in 44 starts, including hot restarts without discrepancies. Three basic configurations of the coaxial injector concept, with geometric variations, were tested to evaluate parameters controlling performance and injector/chamber compatibility, together with demonstrating the inherent dynamic stability of the injector. All contract design goals were met or exceeded.		

(variant)



14	KEY WORDS	LINK A		LINK B		LINK C	
		ROLE	AT	ROLE	AT	ROLE	AT
	<p><math>N_2O_4/N_2H_4</math> Injector Injector Performance Post Boost Propulsion</p>						

UNCLASSIFIED

Security Classification